

Technological advances in catheter-based cardiac therapies

René van Es

Technological advances in catheter-based cardiac therapies

© 2016 René van Es

ISBN 978-94-6233-393-2

Cover: René van Es

Layout: wenz iD.nl / Wendy Schoneveld

Printed by: Gildeprint Drukkerijen, Enschede

The research described in this thesis was supported by grants of the Dutch Heart Foundation (2003B07304 and 2010T025). Publication of this dissertation was made possible by the Dutch Heart Foundation.

Further financial support for publication of this dissertation by CART-Tech B.V., St. Jude Medical B.V., Stichting Cardiovasculaire Biologie, ChipSoft B.V., Pfizer B.V., Servier Nederland Farma B.V., Biologics Delivery Systems™, Johnson and Johnson Medical Company is gratefully acknowledged.

Technological advances in catheter-based cardiac therapies

Technologische vooruitgang van
katheter gebaseerde therapieën in het hart

(met een samenvatting in het Nederlands)

Proefschrift

ter verkrijging van de graad van doctor
aan de Universiteit Utrecht op gezag van de rector magnificus,
prof.dr. G.J. van der Zwaan, ingevolge het besluit van het college
voor promoties in het openbaar te verdedigen
op donderdag 29 september 2016 des middags te 4.15 uur

door

René van Es

geboren op 1 maart 1987
te Coevorden

Promotoren: Prof.dr. P.A.F.M. Doevendans
Prof.dr. S.A.J. Chamuleau

Copromotoren: Dr. F.H.M. Wittkamp
Dr.ir. F.J. van Slochteren

CONTENTS

Chapter 1	General Introduction	9
-----------	----------------------	---

PART I CARDIAC REGENERATIVE THERAPY

Chapter 2	Multimodality infarct identification for optimal image guided intramyocardial cell injections	25
Chapter 3	Three dimensional fusion of electromechanical mapping and magnetic resonance imaging for real-time navigation of intramyocardial cell injections in a porcine model of chronic myocardial infarction	45
Chapter 4	Real-Time correction of respiratory induced cardiac motion during electro anatomical mapping procedures	63
Chapter 5	Intramyocardial therapy: A novel accurate and fast method to target the infarct border zone	77
Chapter 6	High Resolution Systematic Digital Histological Quantification of Cardiac Fibrosis and Adipose Tissue in Phospholamban p.Arg14del Mutation Associated Cardiomyopathy	97
Chapter 7	A Systematic Comparison of Cardiovascular Magnetic Resonance and High Resolution Histological Fibrosis Quantification in a Chronic Porcine Infarct Model	115

PART II CARDIAC ABLATION

Chapter 8	Novel method for electrode-tissue contact measurement with multi-electrode catheters	137
Chapter 9	Feasibility of multi-electrode contact measurement as predictor of long-term success with circular pulmonary vein electroporation ablation	151
Chapter 10	Acute and long-term effects of full-power electroporation ablation directly onto the esophagus	163
Chapter 11	General Discussion	177

APPENDICES

Nederlandse samenvatting	188
Dankwoord	194
Publicatielijst	198
Curriculum Vitae	200

Chapter 1



General Introduction

Technology has become increasingly important in healthcare. In this thesis we present novel technological approaches to improve different catheter based therapies in the heart. In the first part of this thesis we focus on catheter navigation strategies to optimize cardiac regenerative therapies. In the second part, the focus is on assessing contact between the catheter and tissue to increase the efficacy of catheter ablation therapy.

PART I CARDIAC REGENERATIVE THERAPY

Ischemic heart disease

Worldwide, 1 of every 3 deaths in 2013 was caused by cardiovascular disease with ischemic heart disease being responsible for almost half of these deaths.^{1,2} Annually, more than 1 million myocardial infarctions are treated in the European union. Current treatment strategies in the acute phase of myocardial infarction include: opening the blocked coronary artery to restore myocardial perfusion, and pharmacological anticoagulation therapy. Over the past decades, the short-term mortality of patients after myocardial infarction has tremendously decreased, contributing to a significant increase in heart failure. Medical therapeutics for heart failure, such as beta-blockers, angiotensin converting enzyme inhibitors and diuretics, aim for symptom relief and are not a cure. The only definitive cure for heart failure is heart transplantation, but is only considered for patient suffering from end-stage heart failure.

Cardiac regenerative therapy

Up until the studies of Beltrami et al. and Quaini et al., the heart was considered to be a post-mitotic organ.^{3,4} Moreover, by studying variations in Carbon-14 levels in the DNA of cardiomyocytes, Bergmann and colleagues proved the presence of cardiomyocyte renewal.⁵ Even though these studies have shown that the heart is capable of self-renewal, the heart itself is unable to compensate for the great loss of cardiomyocytes after an ischemic event. Therefore, therapies aiming at regeneration of the heart have been a vastly studied subject. Over the past decade cardiac regenerative therapy has shown to be safe and the results are promising.^{6,7} The current cardiac regenerative therapies lead to a 3-4% increase in left ventricular ejection fraction. In contrast to classic medical therapy for ischemic heart failure, cardiac regenerative therapy aims at repairing the myocardial function by the application of biological materials to the damaged myocardium.

Since the beginning of cardiac regenerative therapy, biologicals such as stem cells or growth factors have been administered to the heart using a variety of different injection and transplantation techniques. The different techniques for administration include: intra venous injection, surgical epicardial injection, intracoronary infusion and intramyocardial injections.⁸⁻¹⁰ While intravenous injection of biologicals is the easiest and most inexpensive delivery strategy, nonspecific tissue targeting and risk of micro embolisms make it an unpopular choice. Van der Spoel and colleagues showed that there was little difference in delivery efficiency between surgical epicardial injections, intramyocardial injections and intra coronary injections.¹¹ In all study groups, only about only 10% of the delivered Indium-111 labeled cells was found in the heart 4 hours after injection. Surgical epicardial injections require a surgical approach and the technique

can be easily applied during open chest procedures such as a coronary artery by-pass graft procedure. This invasive approach however, is not desirable in patients that do not undergo open-chest surgery. Both intramyocardial injections and intracoronary infusions are considered minimally invasive. The latter technique is technically less challenging and can be performed faster. After an ischemic event, caused by a coronary artery occlusion, infusion of the cells into that same artery allows for precise targeting of the injured myocardium. The infusion of stem cells directly into the coronary artery does however lead to an acute reduction in coronary flow, suggesting obstruction of the micro-circulatory blood flow and a risk of micro infarctions.¹² Furthermore, intracoronary infusion of stem cells requires patent coronary arteries, which is often a problem in patients suffering from chronic ischemic heart disease. Moreover, with the recent introduction of hydrogels to increase the retention, intramyocardial injections, endocardial or epicardial, are the only options to deliver the therapy.^{13,14} Since the epicardial route for intramyocardial delivery requires a more invasive approach, catheter based delivery of intramyocardial therapy seems to be the most suitable delivery strategy for these patients.

Intramyocardial injections

Precise targeting of intramyocardial injections is believed to be important for the success of the therapy. In 1996 Ben-Haim and colleagues introduced the first non-fluoroscopic navigation and mapping system.¹⁵ The magnetic 3-dimensional tracking technology was later incorporated in the NOGA®XP system to facilitate endocardial mapping and the delivery of therapeutics directly to the injured myocardium. The so-called NOGA procedure starts with creating a left ventricular endocardial surface map by acquiring at least 60 separate points throughout the left ventricle.¹⁶ At each of those points, depolarization potentials and wall motion are measured and stored. Thereafter, the created map is used to determine the location of the myocardial infarct. In a subsequent injection procedure (using a special injection catheter with an extendable needle), this map is used to navigate to the infarct border zone to deliver multiple injections. Several studies have been performed to compare the endocardial NOGA maps with different cardiac imaging modalities such as echocardiography, PET, SPECT and MRI.¹⁷⁻²⁰ A comprehensive review of Gyöngyösi and Dib showed considerable variations in NOGA measurements at sites with a specific infarct transmuralty.¹⁶ The studies comparing NOGA with several 3D imaging modalities did not use systematic image registration techniques and were typically based on a manual comparison of bulls-eye images. While such comparisons may give insight in the difference in NOGA parameters measured at either healthy or completely infarcted myocardium, detailed analyses are not possible. In recent years, several research groups have developed and tested alternative techniques to guide intramyocardial therapy.^{21,22} The developed techniques are based on the online fusion of images of a 3D imaging modality, such as MRI, CT, SPECT/CT or PET, with fluoroscopic images or mapping techniques.

Challenges

As with other medical therapies, the challenge with cardiac regenerative therapy is to make the therapy more effective. For cardiac regenerative therapy, improvement strategies include: 1. development of compounds that are more effective, 2. increasing the retention so that the injected compound stays where it is needed for an extended period of time for more therapeutic

effect, and 3. ensure that these injections are delivered to the correct location. Properties of such a location include the availability of nutrients and oxygen to enable survival of the cells, and close proximity to the damaged myocardium.²³ It is widely accepted that the infarct border zone is the location fitting those requirements.^{24–26}

To deliver the compounds to the infarct border zone it first must be identified. With NOGA being the clinical reference standard for intramyocardial therapy, the optimal NOGA parameters to identify the infarct border zone need to be determined. Therefore, NOGA has to be systematically compared with the gold standard imaging for non-invasive infarct identification, late gadolinium enhanced MRI. Furthermore, research into new alternative technologies for intramyocardial delivery based on this gold standard imaging may be of great importance.

Moreover, other factors that may affect the injection accuracy of intramyocardial injection techniques need to be investigated and resolved. For example mapping irregularities induced by cardiac motion caused by breathing of the patient. In the CARTO® mapping and navigation system for cardiac ablation therapy, analogous to the NOGA® XP system, an option for respiratory gating is incorporated. The NOGA system does not have this option. With cardiac regenerative therapy, respiratory induced cardiac motion may account for cardiac movement that is larger than the target.

PART II CARDIAC ABLATION

Atrial fibrillation

Atrial fibrillation is a common supraventricular cardiac arrhythmia, characterized by uncoordinated atrial activation and contraction, resulting in an irregular heartbeat.²⁷ Atrial fibrillation be caused by either structural or electrophysiological abnormalities. Patients with atrial fibrillation have a 2, 3 and 5 fold increased risk of dementia, heart failure and stroke, respectively.^{28–30} Rate or rhythm control are the primary treatment options for patients with atrial fibrillation. Rate control focuses on decreasing the ventricular rate to an acceptable level and is accomplished with pharmacologicals such as beta blockers, calcium channel antagonists, digoxin or amiodarone.³¹ Rhythm control in patients suffering from atrial fibrillation can be achieved using anti arrhythmic drugs or catheter/surgical ablation. The latter two approaches aim at creating a physical boundary to prevent the propagation of erratic supraventricular electrical signals. In this part of the thesis, the focus is on catheter-based therapy for atrial fibrillation.

Catheter ablation

In 1979, Vedel and colleagues discovered that a cardioversion shock, accidentally delivered via a catheter positioned at atrioventricular node, led to complete heart block. In the years thereafter, Gonzales et al. performed the first successful closed chest atrioventricular node ablations in dogs.³² In 1982, the first closed chest catheter ablation procedure in humans was performed by Gallagher et al.³³ Typically, 200-400 Joules direct current (DC) shocks were applied via the distal 2 mm electrode of a 6 French catheter. The large current density around that small electrode, led to electrolysis and the formation of a vapor globe. The vapor globe electrically isolates the electrode leading to arcing (a spark), explosive evaporation and a pressure wave.³⁴ In those days,

the mechanism by which the direct current shocks resulted in the formation of lesions (interruption of conduction) was unknown. One theory suggested that the pressure waves led to barotrauma and damage to the conductive tissue.³⁵ Another theory suggested that the damage was caused by the passage of a high current density through the myocardium.³⁶ By the end of the 1980s, Rowland and colleagues introduced a low power DC ablation technique for His bundle DC ablation, to eliminate arcing.^{37,38} Around the same time, however, the first paper on cardiac radio-frequency ablation was published.³⁹ Radio-frequency (RF) ablation of the atrioventricular node was reported to be safe and effective. In the 1990s, the more elegant RF ablation technique became the standard energy source for cardiac ablation.

In 1998, Haïssaguerre et al. discovered that arrhythmic atrial triggers often originated from the pulmonary veins, and that these foci could be ablated with RF application.⁴⁰ Since then, ablation of the pulmonary vein ostia has become the most important strategy for catheter ablation for atrial fibrillation. With this ablation strategy, the pulmonary vein antra are electrically isolated from the left atrium to prevent atrial capture by triggers from the pulmonary veins. Such electrical isolation is created by a continuous circular line of sequential RF ablation lesions around the pulmonary vein antrum. Discontinuities in the ablation lesion line may be associated with electrical pulmonary vein reconnection.⁴¹ Multiple studies have shown that good electrode-tissue contact is imperative for effective lesion formation with RF energy.^{42,43} Recently, two circular multi-electrode RF ablation catheters were introduced.^{44,45} With these catheters, the complete pulmonary vein antrum perimeter can be targeted at once. However it may be extremely challenging to achieve good contact for all electrodes simultaneously; multiple applications with different catheter positions are often required.⁴⁶

The 3-month success rate of pulmonary vein isolation is low. A study by Das et al. in which all patients underwent a repeat electrophysiological study 2 months after the index radio-frequency pulmonary vein isolation showed reconnections in 25% of the ablated veins.⁴⁷ In a different study by Kuck et al., a repeat electrophysiological study at 3 months revealed conduction gaps in 70% of the patients, in whom complete pulmonary vein isolation was accomplished during the index procedure.⁴⁸ In addition, the Efficacy I study showed the presence of one or more conduction gaps in 65% of the patients at three months follow up.⁴⁹ The 5-year success rate of RF catheter ablation is around 60% and often requires more than one procedure.⁵⁰

Irreversible electroporation

Electroporation, the formation of pores in the cellular membrane through the application of an electric field, is often used in the biotechnological and medical field to allow compounds, such as genes or drugs to cross the otherwise impermeable cell membrane.^{51,52} Chang and colleagues were the first to visualize the formed pores, and they found that these pores with sizes up to 120 nm were formed rapidly (within 40 ms) after the electric application.⁵³

The first law of Joule states that the passage of an electric current through a conductor (tissue) releases heat. This implies that heat is also generated with (irreversible) electroporation and the question was raised whether the effects of irreversible electroporation could be attributed to electroporation alone. In 2005, Davalos and colleagues used a mathematical model that suggested that even with small surface area needles as ablation electrodes, irreversible electroporation can be performed without reaching the thermal ablation limit of 50°C.⁵⁴

Irreversible electroporation as a modality for non-thermal ablation of cardiac tissue was first described in 2007.⁵⁵ In that study, 8-32 pulses of 1500-2000 V with a duration of 100 μ s were applied, epicardially between two 4 cm long electrodes, to the atria of 5 swine. No tissue heating was observed and histologically clear demarcations between the ablation lesion and healthy tissue were seen without signs of charring. Wittkamp and colleagues were the first to apply circular irreversible electroporation to the heart.⁵⁶ In that study, the safety and feasibility of non-thermal irreversible electroporation for the creation of lesions in pulmonary vein ostia was investigated. Irreversible electroporation pulses were applied between all electrodes of a circular decapolar catheter and a skin patch using a standard monophasic defibrillator (Lifepak 9, Physio-Control Inc). In both pulmonary vein ostia of 10 pigs, maximally 4 pulses of 200J were delivered. Adverse events were neither observed during the acute procedure nor during survival of the animals the 3 weeks thereafter. After 3 weeks the animals were electrophysiologically reexamined and decreased electrogram amplitudes were observed at the ablation sites. No signs of pulmonary vein stenosis were observed fluoroscopically. The study suggested that irreversible electroporation can safely be used to create lesions in the ostia of the pulmonary veins. A subsequent study of the same team was conducted to investigate the relation between the magnitude of the irreversible electroporation application and the resulting lesion depth.⁵⁷ A single 200J irreversible electroporation application delivered to the epicardium using a 20mm circular catheter-like decapolar device resulted in a median lesion depth of 5.2mm, deep enough for pulmonary vein isolation. Subsequent studies of the same group addressed several safety aspects of irreversible electroporation for cardiac ablation. A study with an excessive number (10) of applications per pulmonary vein ostium showed the absence of pulmonary vein stenosis, 3 months after irreversible electroporation ablation, in contrast, considerable stenosis occurred after conventional RF ablation in control ostia.⁵⁸ A safety study, in which the irreversible electroporation impulse was applied directly on the epicardium on top of a coronary artery showed no clinically relevant damage to the arteries.⁵⁹ In addition, this study showed no signs that the blood flow in these arteries affected lesion formation. Tissue samples of this study revealed intact nerves inside the ablated myocardium. A subsequent study demonstrated that the phrenic nerve was not, or only transiently affected by irreversible electroporation.⁶⁰ A later study also showed that minimally invasive epicardial ablation was feasible and safe with irreversible electroporation.⁶¹

Challenges

In the past, DC catheter ablation had been performed via a single distal 2mm electrode of a 6F catheter. As described above, the combination of high current with a small electrode surface area led to arcing and an explosion. The new generation of circular multi-electrode catheters offers a significantly larger electrode surface area. This larger surface area enables the delivery of high currents without arcing. Since the electric resistance of blood is about 4 fold lower than that of myocardial tissue, electrode-tissue contact will be important for effective irreversible electroporation ablation. With circular multi-electrode catheters it is difficult, if not impossible, to mechanically determine the electrode-tissue contact for each individual electrode. Therefore, other methods are required to measure electrode-to-tissue contact for such catheters.

Safety aspects are extremely important when introducing a new therapy into medical practice.

Over the past years, our group has investigated many safety aspects of irreversible electroporation ablation. With radiofrequency ablation, the formation of atrio-esophageal fistula is a rare but lethal complication.^{62–64} In humans, the esophagus is located very close to the posterior left atrium. Applying thermal energy to that part of the atrium as is done during electrical isolation of both inferior pulmonary veins can then lead to esophageal damage. The effects of irreversible electroporation on the esophagus still are unknown. Before irreversible electroporation can be used as a modality for cardiac ablation, its effect on the esophagus needs to be investigated.

OUTLINE OF THESIS

Part 1 Optimizing navigation for cardiac regenerative therapy

In the first part of this thesis we focus on improving navigation strategies for cardiac regenerative therapies. The key point in this part is getting the therapy exactly to the position in the heart where the expected effects are maximal, with the use of a catheter suitable for intramyocardial injections. In **Chapter 2** we describe a method to enable the fusion of MRI images and NOGA maps to optimize intramyocardial injections. Subsequently, in **Chapter 3** we use the same approach to retrospectively compare late gadolinium enhanced MRI images with electro-anatomical mapping to find the optimal NOGA parameters to define the infarct border zone. Respiratory induced cardiac motion is an important cause of registration mismatches when fusing two or more imaging modalities. In **Chapter 4** we describe a technical solution that enables real-time correction of electro anatomical maps during mapping procedures, in order to reduce mapping errors and subsequent registration mismatches. Since electro anatomical mapping systems are expensive and the procedures with these devices are laborious, we have developed a software tool that facilitates intramyocardial injections based on late gadolinium enhancement MRI images. This tool, CARTBox2, enables the fusion of target defined on pre-procedural MRI images with live fluoroscopy during the injection procedure. In **Chapter 5**, we compare CARTBox2 with the clinical standard for intramyocardial injections, the NOGA®XP system. Identifying the target area for cardiac regenerative therapy is imperative. In **Chapter 6**, we describe a systematical approach to systematically analyze histological fibrosis in transverse heart slices. In **Chapter 7**, we use the same histological analysis method and systematically compare histology with MRI to find the optimal MRI parameters to identify the target area on MRI images.

Part 2 Optimizing irreversible electroporation catheter ablation

The second part of this thesis focuses on the improvement of catheter-based irreversible electroporation ablation. Electrode-tissue contact is an important factor for irreversible electroporation to be effective. In **Chapter 8**, we describe an electrical method to assess electrode-tissue contact that can be applied to multi-electrode catheters. In a subsequent study (**Chapter 9**), we directly compared this method with the standard clinical protocol for determining electrode-tissue contact for pulmonary vein isolation in a porcine study with long-term follow-up. The safety aspects of irreversible electroporation need to be clear before its introduction into clinical practice. With radio-frequency ablation, the formation of atrio-esophageal fistula is a rare but lethal complication. In **Chapter 10**, we describe a study in which we directly targeted the esophagus with irreversible electroporation. The short and long-term effects on the esophagus were studied endoscopically and histologically.

REFERENCES

1. Correction Naghavi M, Wang H, Lozano R, et al.: Global, regional, and national age-sex specific all-cause and cause-specific mortality for 240 causes of death, 1990-2013: A systematic analysis for the Global Burden of Disease Study 2013. *The Lancet Elsevier Ltd*, 2015; 385:117–171.
2. Mozaffarian D, Benjamin EJ, Go AS, et al.: Heart Disease and Stroke Statistics—2016 Update: A Report From the American Heart Association. *Circulation*. 2015;.
3. Beltrami AP, Urbanek K, Kajstura J, Yan S-M, Finato N, Bussani R, Nadal-Ginard B, Silvestri F, Leri A, Beltrami CA, Anversa P: Evidence that human cardiac myocytes divide after myocardial infarction. *The New England journal of medicine* 2001; 344:1750–1757.
4. Quaini F, Urbanek K, Beltrami AP, Finato N, Beltrami CACA, Nadal-Ginard B, Kajstura J, Leri A, Anversa P: Chimerism of the transplanted heart. *The New England journal of medicine* 2002; 346:5.
5. Bergmann O, Bhardwaj RD, Bernard S, et al.: Evidence for Cardiomyocyte Renewal in Humans. 2016; 324:98–102.
6. Clifford DM, Fisher SA, Brunskill SJ, Doree C, Mathur A, Watt S, Martin-Rendon E: Stem cell treatment for acute myocardial infarction. *Cochrane database of systematic reviews (Online)* 2012; 2:CD006536.
7. Jeevanantham V, Butler M, Saad A, Abdel-Latif A, Zuba-Surma EK, Dawn B: Adult bone marrow cell therapy improves survival and induces long-term improvement in cardiac parameters: A systematic review and meta-analysis. *Circulation* 2012; 126:551–568.
8. Fukushima S, Sawa Y, Suzuki K: Choice of cell-delivery route for successful cell transplantation therapy for the heart. *Future cardiology* 2013; 9:215–227.
9. Brunskill SJ, Hyde CJ, Doree CJ, Watt SM, Martin-Rendon E: Route of delivery and baseline left ventricular ejection fraction, key factors of bone-marrow-derived cell therapy for ischaemic heart disease. *European Journal of Heart Failure* 2009; 11:887–896.
10. van der Spoel TIG, Lee JC-T, Vrijsen K, Sluijter JPG, Cramer MJM, Doevendans P a, van Belle E, Chamuleau S a J: Non-surgical stem cell delivery strategies and in vivo cell tracking to injured myocardium. *The international journal of cardiovascular imaging* 2011; 27:367–383.
11. Van der Spoel TIG, Vrijsen KR, Koudstaal S, Sluijter JPG, Nijssen JFW, de Jong HW, Hoefer IE, Cramer MJM, Doevendans PA, van Belle E, Chamuleau SAJ: Transendocardial cell injection is not superior to intracoronary infusion in a porcine model of ischaemic cardiomyopathy: A study on delivery efficiency. *Journal of Cellular and Molecular Medicine* 2012; 16:2768–2776.
12. Gyöngyösi M, Hemetsberger R, Wolbank S, et al.: Delayed Recovery of Myocardial Blood Flow After Intracoronary Stem Cell Administration. *Stem Cell Reviews and Reports* 2011; 7:616–623.
13. Bastings MMC, Koudstaal S, Kieltyka RE, Nakano Y, Pape ACH, Feyen DAM, van Slochteren FJ, Doevendans PA, Sluijter JPG, Meijer EW, Chamuleau SAJ, Dankers PYW: A fast pH-switchable and self-healing supramolecular hydrogel carrier for guided, local catheter injection in the infarcted myocardium. *Advanced Healthcare Materials* 2014; 3:70–78.
14. Pape ACH, Bakker MH, Tseng CCS, Bastings MMC, Koudstaal S, Agostoni P, Chamuleau SAJ, Dankers PYW: An Injectable and Drug-loaded Supramolecular Hydrogel for Local Catheter Injection into the Pig Heart. *Journal of visualized experiments : JoVE* 2015; :e52450.
15. Ben-Haim S a, Osadchy D, Schuster I, Gepstein L, Hayam G, Josephson ME: Nonfluoroscopic, in vivo navigation and mapping technology. *Nature medicine* 1996; 2:1393–1395.
16. Gyöngyösi M, Dib N: Diagnostic and prognostic value of 3D NOGA mapping in ischemic heart disease. *Nature Publishing Group Nature Publishing Group*, 2011; 8:393–404.
17. Kornowski R, Fuchs S, Shiran A, Summers N, Pietruszewicz M, Ellahham S, Goldstein SA, Leon MB: Catheter-based electromechanical mapping to assess regional myocardial function: A comparative analysis with transthoracic echocardiography. *Catheterization and Cardiovascular Interventions* 2001; 52:342–347.
18. Wiggers H, Bøtker HE, Sjøgaard P, Kalltoft A, Hermansen F, Kim WY, Krusell L, Thuesen L: Electromechanical mapping versus positron emission tomography and single photon emission computed tomography for the detection of myocardial viability in patients with ischemic cardiomyopathy. *Journal of the American College of Cardiology* 2003; 41:843–848.

19. Keck A, Hertting K, Schwartz Y, et al.: Electromechanical mapping for determination of myocardial contractility and viability. *Journal of the American College of Cardiology* 2002; 40:1067–1074.
20. Perin EC, Silva G V., Sarmiento-Leite R, Sousa ALS, Howell M, Muthupillai R, Lambert B, Vaughn WK, Flamm SD: Assessing myocardial viability and infarct transmural extent with left ventricular electromechanical mapping in patients with stable coronary artery disease: Validation by delayed-enhancement magnetic resonance imaging. *Circulation* 2002; 106:957–961.
21. Tomkowiak MT, Klein AJ, Vigen KK, Hacker T a, Speidel M a, VanLysel MS, Raval AN: Targeted transendocardial therapeutic delivery guided by MRI-x-ray image fusion. *Catheterization and cardiovascular interventions : official journal of the Society for Cardiac Angiography & Interventions* 2011; 78:468–478.
22. Dauwe DF, Nuyens D, De Buck S, et al.: Three-dimensional rotational angiography fused with multimodal imaging modalities for targeted endomyocardial injections in the ischaemic heart. *European Heart Journal Cardiovascular Imaging* 2014; 15:900–907.
23. Duran JM, Taghavi S, Berretta RM, Makarewich CA, Sharp T, Starosta T, Udeshi F, George JC, Kubo H, Houser SR: A Characterization and Targeting of the Infarct Border Zone in a Swine Model of Myocardial Infarction. *Clinical and Translational Science* 2012; 5:416–421.
24. Nguyen PK, Lan F, Wang Y, Wu JC: Imaging: Guiding the Clinical Translation of Cardiac Stem Cell Therapy. *Circulation Research* 2011; 109:962–979.
25. Orlic D, Kajstura J, Chimenti S, Jakoniuk I, Anderson SM, Li B, Pickel J, McKay R, Nadal-Ginard B, Bodine DM, Leri A, Anversa P: Bone marrow cells regenerate infarcted myocardium. *Nature* 2001; 410:701–705.
26. Segers VFM, Lee RT: Biomaterials to enhance stem cell function in the heart. *Circulation Research* 2011; 109:910–922.
27. January CT, Wann LS, Alpert JS, et al.: 2014 AHA/ACC/HRS guideline for the management of patients with atrial fibrillation: A report of the American college of Cardiology/American heart association task force on practice guidelines and the heart rhythm society. *Journal of the American College of Cardiology* 2014; 64:e1–e76.
28. Kannel WB, Wolf PA, Benjamin EJ, Levy D: Prevalence, incidence, prognosis, and predisposing conditions for atrial fibrillation: population-based estimates. *The American Journal of Cardiology* 1998; 82:2N – 9N.
29. Wolf PA, Abbott RD, Kannel WB: Atrial fibrillation: a major contributor to stroke in the elderly. The Framingham Study. *Archives of internal medicine* 1987; 147:1561–1564.
30. Miller PSJ, Andersson FL, Kalra L: Are cost benefits of anticoagulation for stroke prevention in atrial fibrillation underestimated? *Stroke*. 2005, pp. 360–366.
31. Halsey C, Chugh A: Rate Versus Rhythm Control for Atrial Fibrillation. *Heart Failure Clinics Elsevier Inc*, 2016; 12:193–203.
32. Gonzales R, Scheinman M, Margaretten W, Rubinstein M: Closed-chest electrode-catheter technique for His bundle ablation in dogs. *American journal of physiology* 1981; 241:H283–H287.
33. Gallagher JJ, Svenson RH, Kasell JH, German LD, Bardy GH, Broughton A, Critelli G: Catheter Technique for closed-chest ablation of the atrioventricular conduction system. *The New England journal of medicine* 1982; 306:194–200.
34. Bardy GH, Coltorti F, Stewart RB, Greene HL, Ivey TD: Catheter-Mediated Electrical Ablation - the Relation between Current and Pulse Width on Voltage Breakdown and Shock-Wave Generation. *Circ Res* 1988; 63:409–414.
35. Ward DE, Davies M: Transvenous high energy shock for ablating atrioventricular conduction in man. Observations on the histological effects. *British heart journal* 1984; 51:175–178.
36. Ward DE, Camm a J: The current status of ablation of cardiac conduction tissue and ectopic myocardial foci by transvenous electrical discharges. *Clinical cardiology* 1986; 9:237–244.
37. Ahsan AJ, Cunningham D, Rowland E, Rickards AF: Catheter Ablation Without Fulguration: Design and Performance of a New System. *Pacing and Clinical Electrophysiology* 1989; 12:131–135.
38. Rowland E, Cunningham D, Ahsan A, Rickards A: Transvenous ablation of atrioventricular conduction with a low energy power source. *British heart journal* 1989; 62:361–366.

39. Huang SK, Bharati S, Graham AR, Lev M, Marcus FI, Odell RC: Closed chest catheter desiccation of the atrioventricular junction using radiofrequency energy. A new method of catheter ablation. *Journal of the American College of Cardiology* 1987; 9:349–358.
40. Haissaguerre M, Jais P, Shah DC: Spontaneous initiation of atrial fibrillation by ectopic beats originating in the pulmonary veins. 1998; 339 SRC -:659–666.
41. Kowalski M, Grimes MM, Perez FJ, Kenigsberg DN, Koneru J, Kasirajan V, Wood MA, Ellenbogen KA: Histopathologic characterization of chronic radiofrequency ablation lesions for pulmonary vein isolation. *Journal of the American College of Cardiology Elsevier Inc.*, 2012; 59:930–938.
42. Wittkamp FHM, Nakagawa H: RF catheter ablation: Lessons on lesions. *PACE - Pacing and Clinical Electrophysiology* 2006; 29:1285–1297.
43. Ikeda A, Nakagawa H, Lambert H, Shah DC, Fonck E, Yulzari A, Sharma T, Pitha J V., Lazzara R, Jackman WM: Relationship between catheter contact force and radiofrequency lesion size and incidence of steam pop in the beating canine heart: Electrogram amplitude, impedance, and electrode temperature are poor predictors of electrode-tissue contact force and lesion. *Circulation: Arrhythmia and Electrophysiology* 2014; 7:1174–1180.
44. Tuan J, Ng GA: Ablation of right ventricular outflow tract tachycardia using a novel multipolar irrigated ablation catheter (nMARQ). *Heart Rhythm Elsevier*, 2014; 11:502–505.
45. Wijffels MCEF, Van Oosterhout M, Boersma LVA, Werneth R, Kunis C, Hu B, Beekman JDM, Vos MA: Characterization of in vitro and in vivo lesions made by a novel multichannel ablation generator and a circumferential decapolar ablation catheter. *Journal of Cardiovascular Electrophysiology* 2009; 20:1142–1148.
46. Laish-Farkash A, Khalameizer V, Fishman E, Cohen O, Yosefy C, Cohen I, Katz A: Safety, efficacy, and clinical applicability of pulmonary vein isolation with circular multi-electrode ablation systems: PVAC® vs. nMARQ™ for atrial fibrillation ablation. *Europace* 2015; :euv258.
47. Das M, Wynn GJ, Morgan M, Lodge B, Waktare JEP, Todd DM, Hall MCS, Snowdon RL, Modi S, Gupta D: Recurrence of Atrial Tachyarrhythmia during the Second Month of the Blanking Period is Associated with More Extensive Pulmonary Vein Reconnection at Repeat Electrophysiology Study. *Circulation: Arrhythmia and Electrophysiology* 2015; 8:846–852.
48. Kuck K-H, Hoffmann BA, Ernst S, Wegscheider K, Treszl A, Metzner A, Eckardt L, Lewalter T, Breithardt G, Willems S: Impact of Complete Versus Incomplete Circumferential Lines Around the Pulmonary Veins During Catheter Ablation of Paroxysmal Atrial Fibrillation: Results From the Gap-Atrial Fibrillation-German Atrial Fibrillation Competence Network 1 Trial. *Circulation Arrhythmia and electrophysiology* 2016; 9:e003337.
49. Neuzil P, Reddy VY, Kautzner J, Petru J, Wichterle D, Shah D, Lambert H, Yulzari A, Wissner E, Kuck KH: Electrical reconnection after pulmonary vein isolation is contingent on contact force during initial treatment: Results from the EFFICAS i study. *Circulation: Arrhythmia and Electrophysiology* 2013; 6:327–333.
50. Teunissen C, Kassenberg W, van der Heijden JF, Hassink RJ, van Driel VJHM, Zuithoff NPA, Doevendans PA, Loh P: Five-year efficacy of pulmonary vein antrum isolation as a primary ablation strategy for atrial fibrillation: a single-centre cohort study. *Europace : European pacing, arrhythmias, and cardiac electrophysiology : journal of the working groups on cardiac pacing, arrhythmias, and cardiac cellular electrophysiology of the European Society of Cardiology* 2016;.
51. Neumann E, Schaefer-Ridder M, Wang Y, Hofschneider PH: Gene transfer into mouse lyoma cells by electroporation in high electric fields. *The EMBO journal* 1982; 1:841–845.
52. Neuman E, Kakorin S, Toensing K: Fundamentals of electroporative delivery of drugs and gens. 1999; 48:3–16.
53. Chang DC, Reese TS: Changes in membrane structure induced by electroporation as revealed by rapid-freezing electron microscopy. *Biophysical journal* 1990; 58:1–12.
54. Davalos R V., Mir LM, Rubinsky B: Tissue ablation with irreversible electroporation. *Annals of Biomedical Engineering* 2005; 33:223–231.
55. Lavee J, Onik G, Mikus P, Rubinsky B: A novel nonthermal energy source for surgical epicardial atrial ablation: Irreversible electroporation. *Heart Surgery Forum* 2007; 10:96–101.
56. Wittkamp FH, van Driel VJ, Van Wessel H: Feasibility of Electroporation for the Creation of Pulmonary Vein Ostial Lesions. 2010; :302–309.

57. Wittkamp FHM, Van Driel VJ, Van Wessel H, Neven KGEJ, Gründeman PF, Vink A, Loh P, Doevendans PA: Myocardial lesion depth with circular electroporation ablation. *Circulation: Arrhythmia and Electrophysiology* 2012; 5:581–586.
58. Van Driel VJHM, Neven KGEJ, Van Wessel H, Du Pré BC, Vink A, Doevendans PAFM, Wittkamp FHM: Pulmonary vein stenosis after catheter ablation electroporation versus radiofrequency. *Circulation: Arrhythmia and Electrophysiology* 2014; 7:734–738.
59. Du Pré BC, Van Driel VJ, Van Wessel H, Loh P, Doevendans PA, Goldschmeding R, Wittkamp FH, Vink A: Minimal coronary artery damage by myocardial electroporation ablation. *Europace* 2013; 15:144–149.
60. van Driel VJHM, Neven K, van Wessel H, Vink A, Doevendans PAFM, Wittkamp FHM: Low vulnerability of the right phrenic nerve to electroporation ablation. *Heart rhythm : the official journal of the Heart Rhythm Society Elsevier*, 2015; 12:1838–1844.
61. Neven K, van Driel V, van Wessel H, van Es RR, Doevendans PA, Wittkamp F: Myocardial Lesion Size After Epicardial Electroporation Catheter Ablation After Subxiphoid Puncture. *Circulation: Arrhythmia and Electrophysiology* 2014; 7:728–733.
62. Pappone C, Oral H, Santinelli V, et al.: Atrio-esophageal fistula as a complication of percutaneous transcatheter ablation of atrial fibrillation. *Circulation* 2004; 109:2724–2726.
63. Barbhaiya CR, Kumar S, John RM, Tedrow UB, Koplan B a., Epstein LM, Stevenson WG, Michaud GF: Global Survey of Esophageal and Gastric Injury in Atrial Fibrillation Ablation. *Journal of the American College of Cardiology American College of Cardiology Foundation*, 2015; 65:1377–1378.
64. Scanavacca MI, D'Ávila A, Parga J, Sosa E: Left atrial-esophageal fistula following radiofrequency catheter ablation of atrial fibrillation. *Journal of Cardiovascular Electrophysiology* 2004; 15:960–962.

PART I

Cardiac regenerative therapy

Chapter 2



Multimodality infarct identification for optimal image guided intramyocardial cell injections

Netherlands Heart Journal 2014;22(11):493–500

Frebus J. van Slochteren¹, René van Es¹, Stefan Koudstaal^{1,5}, Tycho I.G. van der Spoel¹, Joost P.G. Sluijter^{1,5}, Jasper Verbree², Raymon H.R. Pruijm², Josien P.W. Pluim³, Tim Leiner¹, Pieter A. Doevendans^{1,5}, Steven A.J. Chamuleau^{1,5}

¹ Department of Cardiology, University Medical Center Utrecht, The Netherlands

² Department of Technical Medicine, University of Twente, Enschede, The Netherlands

³ Imaging Sciences Institute, University Medical Center Utrecht, The Netherlands

⁴ Department of Radiology, University Medical Center Utrecht, The Netherlands

⁵ Interuniversity Cardiology Institute of the Netherlands (ICIN), Utrecht, The Netherlands

ABSTRACT

Background

Intramyocardial cell injections in the context of cardiac regenerative therapy can currently be performed using electromechanical mapping (EMM) provided by the NOGA®XP catheter injection system. The gold standard technique to determine infarct size and location however is late gadolinium enhanced magnetic resonance imaging (LGE-MRI). In this article we describe a practical and accurate technique to co-register LGE-MRI and NOGA®XP dataset during the injection procedures to ultimately perform image guided injections to the border zone of the infarct determined by LGE-MRI.

Materials and methods

LGE-MRI and EMM were obtained in 3 pigs with chronic myocardial infarction. MRI and EMM datasets were registered using the in-house developed 3D CartBox image registration toolbox consisting of three steps: 1) landmark registration, 2) surface registration, and 3) manual optimization. The apex and the coronary ostia were used as landmarks.

Results

Image registration was successful in all datasets, and resulted in a mean registration error of $3.22 \pm 1.86\text{mm}$ between the MRI surface mesh and EMM points. Visual assessment revealed that the locations and the transmural extent of the infarctions measured by LGE-MRI only partly overlap with the infarct areas identified by the EMM parameters.

Conclusions

The 3D CartBox image registration toolbox enables registration of the EMM on pre-procedurally acquired MRI during the catheter injection procedure. This allows the operator to perform real-time image guided cell injections into the border zone of the infarct as assessed by LGE-MRI. 3D CartBox thereby for the first time enables standardization of the injection location for cardiac regenerative therapy.

INTRODUCTION

Previous studies have shown that injection of stem/progenitor cells into the border zone of the infarcted area in the context of cardiac regenerative therapy helped to stimulate cardiac repair and protection via cell-to-cell contact and secretion of paracrine factors.¹⁻⁷ However, therapeutic effects may rely on the delivery and retention of the regenerative therapeutics on a location where oxygen and nutrients are available to enable survival.⁸ Hence, accurate identification of viable tissue in proximity of the infarct is of great importance. Via intramyocardial injection catheters stem/progenitor cells or biomaterials can be injected minimally invasive into the myocardium. Injection locations can be chosen based on tissue viability measures obtained from electromechanical mapping (EMM), or a-priori knowledge about the infarct location.⁹ The NOGA®XP intramyocardial injection system¹⁰ provides a three dimensional (3D) magnetic tracking technology and allows for the assessment of local electrical and mechanical tissue characteristics. Local unipolar (UV) and bipolar (BV) depolarization potentials and relative catheter tip displacements (Linear Local Shortening, LLS) are measured at multiple locations on the left ventricular (LV) endocardium. These measurements are interpolated to obtain a three-dimensional reconstruction which is used to guide cell injections. This technique is currently used in clinical practice.¹¹⁻¹⁶ Measurements can however not be performed in regions that are susceptible for arrhythmias and measurements are interpolated in regions where no measurements are taken. Furthermore, cut-off values of EMM parameters to identify areas with different viability/perfusion/transmurality vary greatly between studies.¹⁵ Altogether this approach is not reproducible, and prone to errors regarding accurate and detailed identification of the infarct border zone. Since the non transmural border zone of the infarction is believed to be the preferred delivery site of the stem cell therapeutics,¹ it is crucial for it to be optimally defined during the injection procedure. We hypothesize that combining the gold standard measure of infarct size and location by late gadolinium enhanced magnetic resonance imaging (LGE-MRI) or other MRI techniques¹⁷ and practical guidance (NOGA®XP) would further optimize the cell delivery location, and lead to a uniform injection strategy. This approach enables accurate selection and targeting of the infarct border zone with a distinct infarct transmurality with a value between 0 and 100%. In this study we describe the development of a practical software toolbox (3D CartBox) that enables real-time image guided cell injections. 3D CartBox registers NOGA®XP catheter positions on pre-procedurally acquired MRI images to perform intramyocardial injections to locations with an a priori identified distinct infarct transmurality. In addition 3D CartBox can be used to further specify the definition of border zone of the infarct.⁸

MATERIALS AND METHODS

3D CartBox is a Matlab-based software toolbox to register NOGA®XP catheter positions on an endocardial surface mesh derived from MRI. Prior to registration two image processing steps are necessary: 1) Data acquisition, and 2) Data pre-processing as illustrated in Figure 1. 3D CartBox is used for the registration and consists of three phases: 1) initial registration, 2) Iterative Closest Point (ICP) registration, and 3) manual registration. After the registration process post

processing is performed to visualize the data in bullseye plots. In the development process described in this study the 3D CartBox toolbox was applied to data of 3 pigs with a chronic myocardial infarction. The study design is illustrated in Figure 2. The algorithms used in 3D CartBox and in the pre- and post-processing steps are explained in detail in the supplementary data.

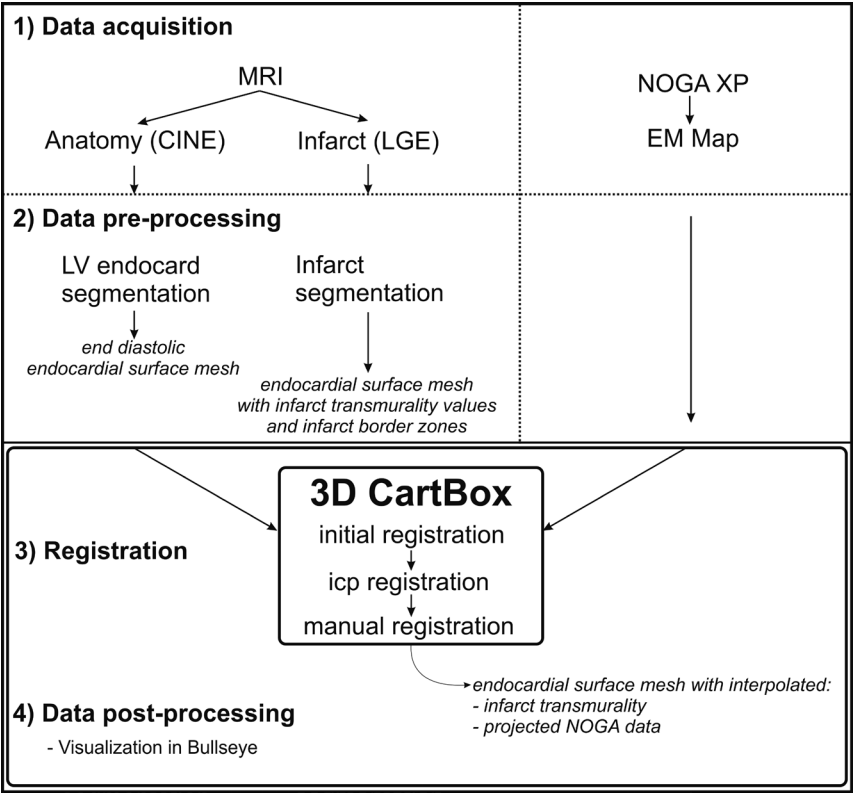


Figure 1 Workflow of the image processing steps that are necessary to use the 3D CartBox toolbox.

Animals

All experiments were performed in accordance with the “Guide for the Care and Use of Laboratory Pigs” prepared by the Institute of Laboratory Animal Resources and with prior approval by the Animal Experimentation Committee of the Faculty of Medicine, Utrecht University, the Netherlands. Three 6-month old female Dalling Landrace pigs (60-70 kg; Instituut voor dierhouderij en diergezondheid (IDDLO), Lelystad, the Netherlands) were pre-treated with clopidogrel 75 mg/day for 3 days and amiodarone 400mg/day for 10 days. In all pigs myocardial infarction (MI) was induced by 75 minutes of percutaneous balloon occlusion of the proximal left circumflex coronary artery as previously described.¹⁸ Eight weeks after MI the experiments were performed as shown in Figure 2.

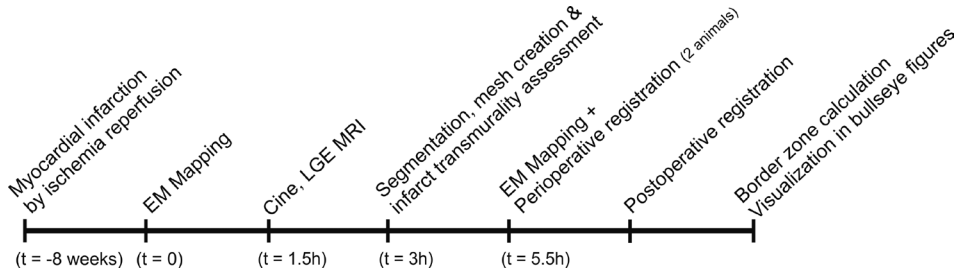


Figure 2 Time line of the experiments. The second mapping procedure was performed in two pigs.

Data acquisition

The in vivo MRI images were acquired using a 1.5 Tesla Philips Medical Systems Achieva scanner. The MRI sequences for the CINE and the LGE MRI acquisitions are described in the supplementary data. The NOGA®XP system (Biosense Webster, Cordis, Johnson & Johnson, USA) version 1.1.43 was used equipped with a 7 French NOGA mapping catheter (Biosense Webster, Cordis, Johnson & Johnson, Diamond Bar, USA) for the mapping. The LV was entered via the left carotid artery, and retrograde passage through the aortic valve. Readout of the catheter tip location was done in end-diastole using R-wave triggering. Thereby providing only end-diastolic tip locations for registration. Electrocardiograms were filtered at 30–400 Hz (bipolar) and 1–240 Hz (unipolar). The EMM datasets were acquired in consideration of the criteria for good electromechanical mapping.¹⁵ Points acquired in the left and right coronary ostia and the apex served as anatomical landmarks and are used for the first registration step. The apex location was taken as the most outward point that was reached in the apical region confirmed by fluoroscopy. To obtain data from the NOGA®XP system in a real time fashion, the system was modified to enable read-only access from an external computer running 3D CartBox.

Data pre-processing

Data pre-processing consists of 1) segmentation of the left ventricle using the CINE images, 2) segmentation of the infarct using the LGE images, 3) calculation of the infarct transmural, 4) projection of the infarct transmural on the endocardial surface mesh derived from the end diastolic CINE images, and 5) calculation of the infarct transmural border zone preferred to use for cell injections. The details of the pre-processing steps are described in the supplementary data.

Registration

During initial registration the raw NOGA®XP dataset and the MRI datasets are registered coarsely based on the anatomical landmarks using a closed-form least squares approach.^{19,20} Used anatomical landmarks are the left and the right coronary ostia and the apex as previously described.²¹ After acquiring points in all regions of the left ventricular endocardium, an iterative closest point (ICP) algorithm²² was applied to optimize the registration. If necessary the registration was manually optimized by adjusting the registration interactively. The algorithm used for the registration are explained in detail in the supplementary data. The accuracy of the

registration was expressed by the registration error being the mean \pm standard deviation of the shortest distance from each EMM point to the cine mesh surface as previously described.²¹ The relevance of the used registration error measure is pointed out in the supplementary data. To prevent interference by EMM points that were not located in the cine mesh (e.g. LV outflow tract), these points were excluded for ICP registration, error calculation, and further processing.

Perioperative image guidance

In this study perioperative registration is performed in two animals. After initial registration the acquired EMM points are visualized in the freely rotatable 3D endocardial surface mesh with projected infarct transmural data. In addition the MR images are displayed as shown in Figure 3 E and F. Newly acquired NOGA[®]XP measurement points appear on the screen. Free rotation of the mesh and the MR images during the image guided procedure assures correct positioning of the needle before cell injection.

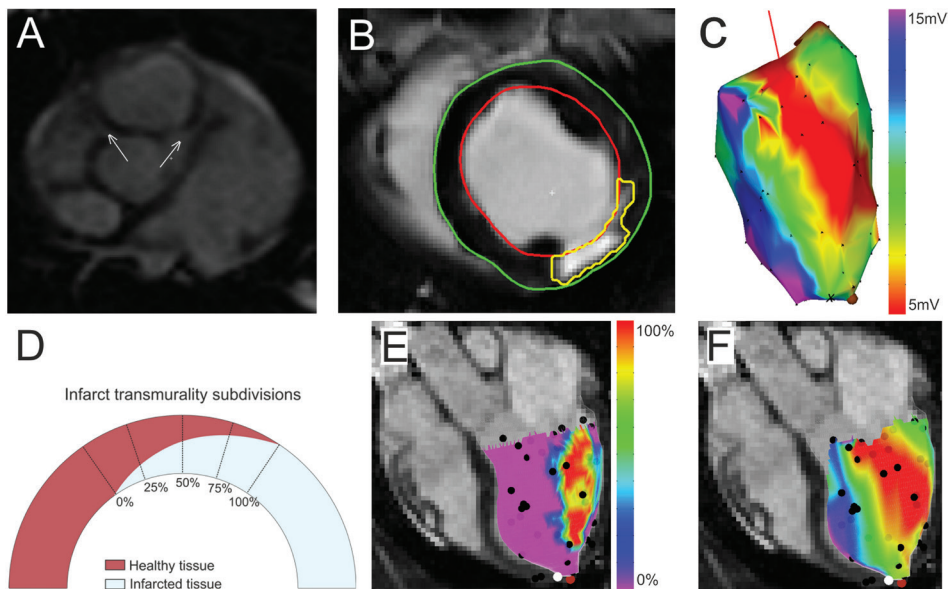


Figure 3 Short axis BTFE image with coronary ostia (A). Segmentation of the epicardium (green), endocardium (red), scar area (yellow) on the short axis LGE scans (B). NOGA[®]XP representation of unipolar voltage map (C). Subdivision of infarct transmural (D). Infarct transmural superimposed on cine mesh (E). Unipolar voltage projection superimposed on cine mesh (F). Colored dots are: NOGA measurement points (black), the apex (white), annotated location (brown).

Post-processing

For visualization purposes both the infarct transmural values and the infarct border zones, as well as the EMM data were projected on the 3D endocardial surface mesh and bullseye plots using customized software.

Statistical analysis

All data is presented as mean \pm standard deviation (SD). A one-way ANOVA test was used to assess difference between the number of points/cm² in the different infarct transmural area. $P < 0.05$ was considered significant.

RESULTS

Data pre-processing

MRI findings are listed in Table 1. The mean LV ejection fraction was $42 \pm 1\%$. All LGE datasets showed a clear fibrotic area as shown in Figure 3b. The LV ejection fraction shows that 8 weeks after MI the pigs had mild heart failure, and a similar infarct size ($27.5 \pm 3.5\%$ of total LV area). The 75-100% infarct transmural area was the smallest, and was absent in one pig. Infarct transmural area was assessed and subdivided in areas with 0, 0-25, 25-50, 50-75, and 75-100% transmural area as illustrated in Figure 3d. The mean endocardial surface areas in these subdivisions respectively were: 73.6 ± 19.7 , 7.2 ± 1.0 , 9.5 ± 2.6 , 5.8 ± 2.8 , and 4.6 ± 5.2 cm², thereby covering 72.5 ± 5.1 , 7.2 ± 0.5 , 9.6 ± 2.9 , 6.4 ± 4.4 , and $4.3 \pm 4.3\%$ of the total LV endocardial surface area. The locations of the coronary ostia could be identified on the cine images (Figure 3a). In all three pigs we were able to acquire EMM points in, or in the vicinity of the coronary ostia. The mean number of EMM points was 66.3 ± 14.2 .

Table 1 Results of cine and late enhancement magnetic resonance imaging of 3 animals. Data are expressed as mean \pm SD

LV end-diastolic volume (ml)	128 ± 19
LV end-systolic volume (ml)	75 ± 11
LV ejection fraction (%)	42 ± 1
Myocardium volume (ml)	118 ± 18
Infarct volume (ml)	17 ± 3
LV area (cm ²)	101 ± 21
Infarct area 0 % transmural area (cm ²)	73.6 ± 19.7 ($72.5 \pm 5.1\%$)
Infarct area 0 - 25 % transmural area (cm ²)	7.2 ± 1.0 ($7.2 \pm 0.5\%$)
Infarct area 25 - 50 % transmural area (cm ²)	9.5 ± 2.6 ($9.6 \pm 2.9\%$)
Infarct area 50 - 75 % transmural area (cm ²)	5.8 ± 2.8 ($6.4 \pm 4.4\%$)
Infarct area 75 - 100 % transmural area (cm ²)	4.6 ± 5.2 ($4.3 \pm 4.3\%$)

Registration

The registration results are listed in Table 2. Perioperative registration was performed in two pigs to test the real time use of the 3D CartBox toolbox (Figure 2). During the real time EMM procedures the cine mesh was successfully merged with the EMM based upon the anatomical landmarks and ICP. After application of ICP the mean surface registration error was 3.27 ± 1.93 mm. No manual optimization of the registration was applied to the datasets. After exclusion of

points located outside the cine mesh the mean registration error was 3.22 ± 1.86 mm. A cine mesh with projected infarct transmural and UV are shown in Figure 3e and 3f. Figure 3c shows the corresponding NOGA®XP EMM. The average coverage of EMM points in the different infarct transmural areas was 0.76 ± 0.44 points/cm². There was no significant difference between the number of points/cm² in each infarct transmural area of all the different animals ($p=0.96$).

Table 2 Three dimensional electromechanical mapping and image registration results of 3 animals. Data are expressed as mean \pm SD.

Electromechanical mapping points			
Total number of points	192		
Points per animal	66.3 ± 14.2		
Distance EMM points to MRI mesh surface (mm)			
All EMM points	3.27 ± 1.93 mm based on 192 points		
All EMM points in cine mesh	3.22 ± 1.86 mm based on 183 points		
Points per infarct transmural area			
0%	53.3 ± 11.7	0.8 ± 0.3 points/cm ²	ns (p=0.96)
0 - 25%	6.0 ± 3.6	0.8 ± 0.5 points/cm ²	
25 – 50%	6.0 ± 3.0	0.7 ± 0.4 points/cm ²	
50 – 75%	2.6 ± 1.5	0.4 ± 0.1 points/cm ²	
75 – 100%	4.5 ± 4.1	0.9 ± 1.2 points/cm ²	

Post processing

To evaluate the projection of the EMM data on the endocardial surface mesh Figure 4 shows bulls eye figures of the UV and BV as represented by the NOGA®XP system (a, e) and after projection on the cine mesh (b, f). Figure 4g represents the projection of LSS. From the comparison with the infarct transmural depicted in Figure 4c it can be observed that there is limited agreement between the EMM parameters and infarct transmural. The 50% infarct transmural border zone determined by LGE-MRI is projected on the bullseye figures of the infarct transmural (c), UV (b), BV (f), and LLS (g). From these images it can be observed that the border zones of low UV and BV values show alignment with the 50% infarct transmural border zone. Figure 4d and h show the projection of the 50% infarct transmural border zone on the endocardial surface mesh as it is visualized during image guided cell injection procedures.

DISCUSSION

In this study, the feasibility of perioperative integration of electromechanical data acquired with the NOGA®XP system with MRI data was shown for the first time. The in-house developed 3D CartBox image registration toolbox has allowed us to register the EMM dataset on a surface mesh derived from end-diastolic CINE MRI images in real time with a mean surface registration error of 3.27 ± 1.93 mm. The three main findings of this study were: 1) real-time use of the

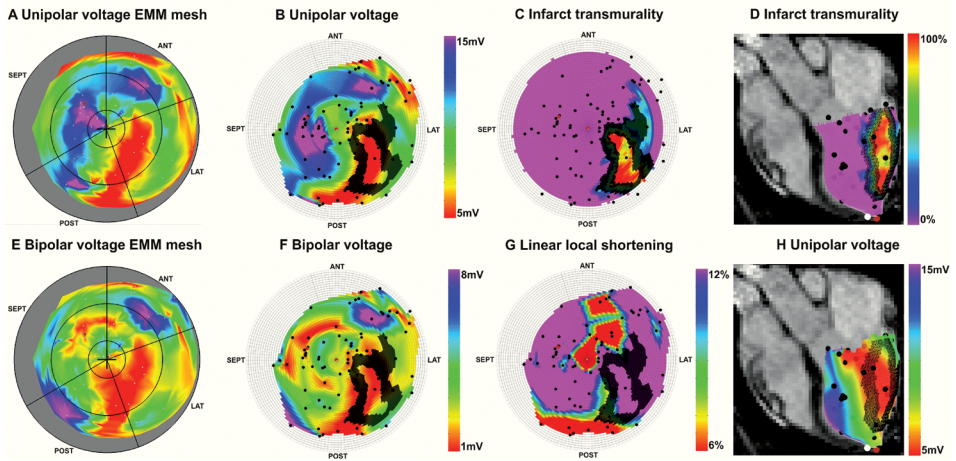


Figure 4 Typical bullseye plots of the NOGA system: Unipolar voltage (A), Bipolar voltage (E). And data projected on the cine mesh: Unipolar voltage (B), Bipolar voltage (F), Infarct transmural (C), Linear local shortening (G). Infarct transmural and unipolar voltages projected on the endocardial surface mesh placed in an end diastolic long axis cine MRI image (D and H). D and H represent the operator view during the image guided injection procedure. Colored dots are: NOGA measurement points (black), the apex (white), annotated location (brown). The black overlay in images B, C, D, F, G, H is a projection of the 50% infarct transmural border zone.

toolbox was feasible. 2) Visually a discrepancy was found between infarct assessment by EMM and LGE-MRI. 3) The 3D CartBox toolbox can be of additional value for infarct assessment during cardiac cell injection procedures.

Data acquisition and pre-processing

The LV ejection fraction in Table 1 showed that 8 weeks after MI the pigs had mild heart failure, and a similar infarct size. The absence of a transmural infarction in one pig is most likely induced by the different response to the ischemia reperfusion procedure due to biological variation. The number of points in the EMM (66.3 ± 14.2) just fulfilled the criteria for good electromechanical mapping as published.¹⁵ During the mapping procedure the EMM points were acquired homogeneously spread over the endocardium, as was confirmed by the number of points each area with a distinct infarct transmural presented in Table 2, and as can be observed from the distribution of EMM points in Figure 4.

Registration

Although acquiring more EMM points might have been beneficial for the registration, the homogeneous distribution of EMM points over the endocardium has secured a correct registration. Due to the longer acquisition time of the LGE images, gated LGE scans did not exactly represent the end diastolic phase. To assure use of the end diastolic ventricular shape for registration we chose to use the end diastolic frame of the cine images for mesh creation, registration and projection of the EMM data. The exclusion of EMM points that were not located in the cine mesh was done to prevent registration based on EMM points that were located in

areas of the LV that were not visualized with MRI. Of the three cases in this study totally 9 mapping points were discarded for this reason. Consequently the registration using all EMM points has a slightly higher registration error: $3.27 \pm 1.93\text{mm}$ compared to $3.22 \pm 1.86\text{mm}$ for the map without the excluded points. Although this difference does not affect registration, it does prevent erroneous projection of EMM parameters on the cine mesh. The 10 times higher weighing of the apex during landmark registration and restriction of the ICP algorithm to 10 degrees in the sagittal plane, and 20 degrees in the transverse and coronal planes were chosen empirically. The resulting surface registration error of $3.22 \pm 1.86\text{mm}$ was less than the value reported in research where CARTO merge was used.²¹ The remaining error can be caused by respiratory induced motion of the heart during the EMM procedure. The NOGA®XP system does not compensate for this.

Post-processing

A high similarity is observed between the EMM maps produced by the NOGA®XP system and the EMM data projected on the cine mesh. The projection of the EMM data on the endocardial surface mesh via linear interpolation results in an accurate projection of the true endocardial surface measurements (Figure 4 a-b, and e-f). From visual assessment it can be inferred that agreement between the infarct identification by EMM (Figure 4 b, f, e) and LGE-MRI (Figure 5 c) is the best with UV, and poor with both BV and LLS. Although it cannot be ruled out completely, the small registration error makes it unlikely that this was the main origin of the poor agreement. Another explanation might be the occurrence of endocardial conducting tissue in regions with an infarct, mimicking normal tissue, or extension of the low voltage regions to neighboring areas of non-transmural infarction through interpolation. Acquiring more points during the mapping procedure in the border zone may solve this problem, provided that this area is known, and not susceptible to arrhythmias due to catheter manipulation. Based on the rationale that 100% transmurally infarcted myocardium is not a location where the stem cells are supplied with sufficient oxygen and nutrients,¹ and in regions with 0% transmural infarction there is no use for stem cells, we have chosen to show the 50% infarct transmural border zone on the bullseye figures in Figure 4b-d and 4f-h. Visual assessment shows that the EMM parameters only partly identify the 50% infarct transmural border zone assessed by the gold standard LGE-MRI infarct assessment technique. The 3D CartBox toolbox enables accurate targeting of infarct border zones with a distinct infarct transmural at any percentage between 0 and 100% transmural determined by LGE-MRI. Thereby 3D CartBox for the first time enables objective specification of the target locations for intramyocardial injections in the context of cardiac regenerative therapy.

Clinical implications

Incorrect injections of stem cells into the myocardium might jeopardize the success of cardiac regenerative therapy.⁸ The combination of the gold standard fibrosis imaging technique for infarct and infarct border zone identification, and a catheter navigation technique to guide injections is a crucial step to target the infarct border zone more accurately. This approach could lead to shorter injection procedures, less necessity for the use of fluoroscopy to confirm the injection location, and less radiation for the patient and the physician. The workflow of 3D CartBox includes: MRI, segmentation, and EMM. Altogether this approximately takes 3 hours, including

the injections. Thereby it is a clinically feasible solution. Real-time integration of LGE-MRI during cardiac cell injection procedures could be a key to harnessing the full therapeutical effects of cardiac stem cell therapy. The 3D CartBox toolbox enables the use of all parameters (perfusion, fibrosis, myocardial wall thickening, myocardial tissue tagging) from a pre-procedural acquired MRI or other imaging modality (SPECT/CT) to guide the cell injection procedures. The 3D CartBox toolbox for image guided cardiac cell injections is rewarded with the BMM valorization grant, and will be made commercially available via the newly founded spin-off company CART-Tech: 'Technical solutions to improve cardiac regenerative therapy'.

Limitations

The use of the coronary ostia for landmark registration is potentially dangerous for the patient and therefore not suitable for clinical use of the toolbox, although clinical use of this method has been reported in literature.²¹ For clinical application of the toolbox in the future we aim to use other fiducial points. The 3 pigs used in this study was found not to be sufficient to perform a quantitative analysis of the overlap between the infarct areas identified by EMM and LGE-MRI or perform a detailed analysis of the thresholds of the NOGA parameters in the areas with different infarct transmuralities. A new study must be performed to explore these aspects by applying 3D CartBox to a larger dataset. Although during all procedures the criteria for good electromechanical mapping were adhered to, acquiring more points might have resulted in a lower registration error. During the mapping procedure small respiratory induced excursions of the catheter tip could be observed. Since the NOGA®XP system did not compensate for respiratory induced motion of the cathetertip, this most likely affected the registration. Compensation for respiratory motion might be beneficial for future applications.

Conclusion

We have developed the 3D CartBox toolbox for real time registration of EMM and MRI data that combines the gold standard diagnostic imaging techniques and highly accurate cardiac navigation to guide cardiac cell injection procedures. The 3D CartBox toolbox shows promising results but more research is necessary to specify the optimal injection location in order to maximize the improvement of cardiac function by cardiac regenerative therapy.

Acknowledgements

Authors would like to acknowledge Merel Schurink, Marlijn Jansen, Maringa Emons and Joyce Visser for excellent technical assistance and animal care, and Thijs Dijkgraaf for his assistance with the read-only access to the NOGA system from an external computer. Many thanks as well for Dries Feyen for reading and correcting the manuscript.

Funding sources

This work was supported by the Netherlands Heart Foundation '[2003B07304 and 2010T025]', BSIK program "Dutch Program for Tissue Engineering", '[grant 6746]', and a Bekalis price (PD). This research is part of the Project P1.04 SMARTCARE of the research program of the BioMedical Materials institute, co-funded by the Dutch Ministry of Economic Affairs and the Nederlandse Hartstichting.

REFERENCES

1. Orlic D, Kajstura J, Chimenti S, *et al.* Bone marrow stem cells regenerate infarcted myocardium. *Nature*. 2003;410(April):701-5.
2. Smits AM, Laake LWV, Ouden KD, *et al.* Human cardiomyocyte progenitor cell transplantation preserves long-term function of the infarcted mouse myocardium. *Cardiovasc Res*. 2009;83(3):527-35.
3. Beltrami AP, Barlucchi L, Torella D, *et al.* Adult cardiac stem cells are multipotent and support myocardial regeneration. *Cell*. 2003;114(6):763-76.
4. Loffredo FS, Steinhauser ML, Gannon J, *et al.* Bone marrow-derived cell therapy stimulates endogenous cardiomyocyte progenitors and promotes cardiac repair. *Cell Stem Cell*. 2011;8(4):389-98.
5. Quevedo HC, Hatzistergos KE, Oskoue BN, *et al.* Allogeneic mesenchymal stem cells restore cardiac function in chronic ischemic cardiomyopathy via trilineage differentiating capacity. *Proc Natl Acad Sci USA*. 2009;106(33):14022-7.
6. Dimmeler S, Zeiher AM, Schneider MD. Unchain my heart: the scientific foundations of cardiac repair. *J Clin Invest*. 2005;115(3):572-83.
7. Robbers LFHJ, Nijveldt R, Beek AM, *et al.* Intracoronary infusion of mononuclear cells after PCI-treated myocardial infarction and arrhythmogenesis: is it safe? *Neth Heart J*. 2012;20(3):133-7.
8. Duran JM, Taghavi S, Berretta RM, *et al.* A characterization and targeting of the infarct border zone in a Swine model of myocardial infarction. *Clin Transl Sci*. 2012;5(5):416-21.
9. Kumar A, Haralampus CA, Hughes M, *et al.* Assessment of safety, accuracy, and human CD34+ cell retention after intramyocardial injections with a helical needle catheter in a porcine model. *Catheter and Cardiovasc Interv*. 2013;81(6):970-7.
10. Ben-Haim SA, Osadchy D, Schuster I, *et al.* Nonfluoroscopic, in vivo navigation and mapping technology. *Nat Med*. 1996;2(12):1393-5.
11. van Ramshorst J, Atsma DE, Beeres SLMA, *et al.* Effect of intramyocardial bone marrow cell injection on left ventricular dyssynchrony and global strain. *Heart*. 2009;95(2):119-24.
12. van Ramshorst J, Antoni ML, Beeres SLMA, *et al.* Intramyocardial bone marrow-derived mononuclear cell injection for chronic myocardial ischemia: the effect on diastolic function. *Circ Cardiovasc Imaging*. 2011;4(2):122-9.
13. Perin EC. Assessing Myocardial Viability and Infarct Transmurality With Left Ventricular Electromechanical Mapping in Patients With Stable Coronary Artery Disease: Validation by Delayed-Enhancement Magnetic Resonance Imaging. *Circulation*. 2002;106(8):957-61.
14. Gyöngyösi M, Lang I, Dettke M, *et al.* Combined delivery approach of bone marrow mononuclear stem cells early and late after myocardial infarction: the MYSTAR prospective, randomized study. *Nat Clin Pract Cardiovasc Med*. 2009;6(1):70-81.
15. Gyöngyösi M, Dib N. Diagnostic and prognostic value of 3D NOGA mapping in ischemic heart disease. *Nat Rev Cardiol*. 2011;8(7):393-404.
16. van Ramshorst J, Bax JJ, Beeres SLMA, *et al.* Intramyocardial bone marrow cell injection for chronic myocardial ischemia: a randomized controlled trial. *JAMA*. 2009;301(19):1997-2004.
17. de Jong S, van Veen TaB, de Bakker JMT, *et al.* Monitoring cardiac fibrosis: a technical challenge. *Neth Heart J*. 2012;20(1):44-8.
18. van Slochteren FJ, Teske AJ, van der Spoel TIG, *et al.* Advanced measurement techniques of regional myocardial function to assess the effects of cardiac regenerative therapy in different models of ischaemic cardiomyopathy. *Eur Heart J Cardiovasc Imaging*. 2012;13(10):808-18.
19. Arun KS, Huang TS, Blostein SD. Least squares fitting of two 3D point sets. *IEEE Trans on Pattern Anal Mach Intell*. 1987;PAMI-9(5):698-700.
20. Umeyama S. Least-squares estimation of transformation parameters between two point patterns. *IEEE Trans on Pattern Anal Mach Intell*. 1991 1991;13(4):376-80.
21. Wijngaalen AP, Van der Geest RJ, Van Huls Van Taxis CFB, *et al.* Head-to-head comparison of contrast-enhanced magnetic resonance imaging and electroanatomical voltage mapping to assess post-infarct scar characteristics in patients with ventricular tachycardias: real-time image integration and reversed registration. *Eur Heart J*. 2010;32(1):104-14.

22. Besl PJ, McKay ND. A Method for Registration of 3-D Shapes. IEE transactions on pattern analysis and machine intelligence. 1992;14(2).
23. Heiberg E, Sjögren J, Ugander M, *et al.* Design and validation of Segment—freely available software for cardiovascular image analysis. BMC Med Imaging. 2010;10(1):1-13.
24. Heiberg E, Engblom H, Engvall J, *et al.* Semi-automatic quantification of myocardial infarction from delayed contrast enhanced magnetic resonance imaging. Scand Cardiovasc J. 2005;39(5):267-75.

SUPPLEMENTAL MATERIAL

Supplementary data

In this supplementary data we describe the workflow and the algorithms that are used to perform image guided cell injections using the 3D CartBox image registration toolbox. The subsequent steps of 3D CartBox that are discussed are illustrated in Figure 1 of the main text. All steps of the workflow were applied to an *in vivo* dataset. A phantom dataset was used to optimize the registration algorithms used. Of each step both the purpose and the algorithms used are discussed and illustrated with images.

Data acquisition

The *in vivo* MRI images were acquired using a 1.5 Tesla Philips Medical Systems Achieva scanner with a commercially available 5 channel phased array cardiac coil. All scans were made using ECG gating. The cine and LGE scans were respectively made with 25 and 1 (end diastolic) phases per cardiac cycle, at the same slice positions and with the same slice orientation. The cine scans were made using Balanced Fast Field Echo (BTFE) with repetition time [TR]/echo time [ET] = 2.9 ms/1.45 ms. Flip angle = 55°, Voxel size = 2.43 x 2.43 mm, field of view [FOV] = 35 x 35 cm, 144 x 144 matrix, 5mm slice thickness, 30 phases/R to R interval. LGE scans were made with [TR]/[ET] = 4.61ms/1.41 ms, Flip angle = 15°, Voxel size = 1.36 x 1.36 mm, field of view [FOV] = 35 x 35 cm, 256 x 256 matrix, 5mm slice thickness. The phantom study was performed using a non-rotational symmetric bottle. MR images were acquired using a 3.0T scanner (Philips Medical Systems). Short axis images were made, repetition time [TR]/ echo time [ET] = 2.84ms/1.42 ms. Flip angle = 55°, Voxel size = 1.36x1.36 mm, field of view [FOV] = 35x35 cm, 256x256 matrix, 5 mm slice thickness.

Data preprocessing

Purpose

To assess the infarct transmural form the LGE scans and project infarct transmural values on the endocardial surface mesh of the left ventricle in order to guide catheter injections based on infarct transmural data. Assign an infarct transmural border zone to use for cell injections.

Method

Segmentation of the left ventricle on the short axis CINE and LGE MRI data is done in the end diastolic phase in approximately 20 slices located from apex to base. The segmentations are done automatically and checked on the long axis images using the freely available software Segment version 1.9 R2507 (<http://segment.heiberg.se>)²³ available for Matlab (MATLAB 2012a, The MathWorks Inc., Natick, MA, 2012). Segmentations are done to create a 3D surface mesh (cine mesh) of the left ventricular endocardium for surface registration and projection of the acquired data. Subsequently the myocardial infarct was segmented on the LGE images using the area based semi-automatic segmentation.²⁴ If necessary both the left ventricle and the infarct segmentations were manually adjusted by an experienced radiologist (TL). The results of the infarct segmentation process in one slice is illustrated in Figure 3b. Area based infarct transmural values are calculated in 80 circumferential segments of all slices using the bullseye

function of segment. The results of the infarct transmural assessment are illustrated in Figure S1a. The infarct transmural data was projected on the CINE derived endocardial surface mesh using the TriScatteredInterp function of Matlab. The CINE derived surface mesh with projected infarct transmural data is illustrated in Figure S1b. The infarct transmural data projected on the endocardial surface mesh is used to calculate the infarct border zone using an in house developed treatment planning algorithm. The infarct border zone is defined as a 1 cm wide area over the 50% infarct transmural isoline. Furthermore the endocardial surface mesh is used for registration of the EMM points, image guided injection procedures, and post processing. Landmark locations used for initial registration are the coronary ostia and apex locations. These locations were selected manually in the end-diastolic frames of the cine images using customized Matlab software.

Registration

Purpose

To combine the EMM dataset and the MRI dataset in order to 1) guide the EMM catheter based on the transmural values derived from LGE MRI data and 2) combine the EMM and the LGE dataset for comparison and optimize the threshold values of the EMM parameters for areas with a different infarct transmural. The initial registration step is used for a coarse alignment of the EMM and CINE MRI mesh. The iterative closest point registration is used to fit the EMM points to the endocardial surface.

Method

Initial registration

Two sets of three 3D points consisting of the two locations of the coronary ostia and the apex measured from CINE MRI (p_{MRI}) and EMM (p_{EMM}) serve as registration landmarks, and are used as input for the initial registration algorithm. The order of the landmarks in both sets of points is the same. The initial registration algorithm is adapted from algorithms published^{19,20} and consists of nine steps:

- 1: Calculate the centroid (c) of each point set: $p_{cMRI} = \frac{1}{3} \sum_{i=1}^3 p_{MRI_i}$ $p_{cEMM} = \frac{1}{3} \sum_{i=1}^3 p_{EMM_i}$
- 2: Translate both sets of points to the origin: $q_{MRI} = p_{MRI_i} - p_{cMRI}$ $q_{EMM} = p_{EMM_i} - p_{cEMM}$
- 3: Calculate the 3x3 matrix H: $H = \sum_{i=1}^3 q_{MRI_i} \cdot q_{EMM_i}^t$
- 4: Calculate the singular value decomposition of H: $H = UDV^T$
- 5: Multiply the determinants of V and U: $X = \det(V) \cdot \det(U)$
- 6: Determine the S matrix dependent of X: $S = \begin{cases} I & \text{if } X = 1 \\ \text{diag}(1, 1, -1) & \text{if } X = -1 \end{cases}$
- 7: Determine the Rotation matrix: $R = USV^T$

8: Determine the translation vector:

$$T = p_{EMM} - R \cdot p_{MRI}$$

9: Apply R and T to the EMM dataset:

$$allpoints_{EMM} = (R \cdot allpoints_{EMM}) + T$$

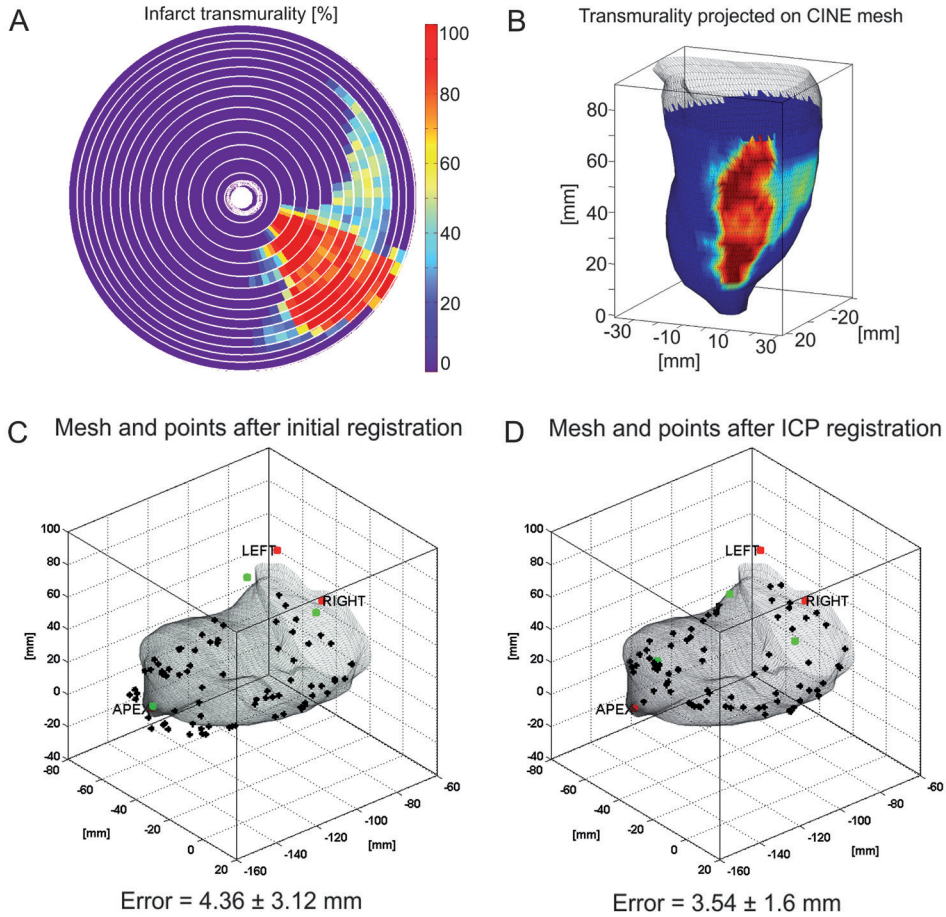


Figure S1 The result of the area based infarct transmural assessment by segment (A). The transmural projection on the CINE mesh (B). 3D endocardial surface meshes with EMM points show the results after initial registration of an *in-vivo* dataset using the apex and left and right coronary ostia as landmarks (C). And ICP registration (D) of an *in-vivo* dataset.

For optimal registration of the apex the algorithm was adapted to apply 10 times higher weighing of the apex compared to the coronary ostia by adding points to the apex location. After applying the rotation matrix and translation vector to (p_{EMM}) and the complete set of all the EMM points ($allpoints_{EMM}$), the orientation and location of (p_{EMM}) and ($allpoints_{EMM}$) is similar to the (p_{MRI}) point set. The result of the initial registration of an *in-vivo* EMM dataset is illustrated in Figure S1c and can be used as input for the second step of 3D CartBox.

Iterative closest point registration

The second registration step incorporated in 3D CartBox is the Iterative Closest Point Method (ICP).^{21,22} In this method the coarsely registered $3 \times n$ point set of the CINE MRI (p_{MRI}) and a $3 \times m$ point set of the EMM (p_{EMM}) are used as input. The ICP algorithm consists of three steps that are iteratively executed.

1: For all points in the EMM dataset compute the closest point in the MRI dataset using the distance function d : $d(MRI, p_{EMM_i}) = \min_{j \in \{1, \dots, n\}} \|p_{MRI_j} - p_{EMM_i}\|$

Let C be the resulting set of m closest points for each of the points in the EMM set. To align the EMM to the MRI dataset a transformation (T) consisting of both a rotation (R) and a translation (T) is necessary. For each point the transformation is: $T(p_{EMM_i}) = R \cdot p_{EMM_i} + T$, and per set of closest points the resulting distance after the transformation can be calculated: $p_{MRI_i} - T(p_{EMM_i}) = p_{MRI_i} - (R \cdot p_{EMM_i} + T)$. To calculate the rotation and translation to minimize the registration error, an error function needs to be optimized:

2: Optimize error function: $argmin_{R,T} f(R,T) = \frac{1}{m} \sum_{i=1}^m \|p_{MRI_i} - (R \cdot p_{EMM_i} + T)\|^2$

3: Apply the translation to the EMM dataset: $p_{EMM_{new}} = R \cdot p_{EMM} + T$

After the third step of the ICP process the first step of the ICP process is executed again using the results of the third step. These three steps are iteratively executed until the criteria to finish the process are reached. In 3D CartBox the finalization criteria are set to a maximum number of iterations (100) or a resulting sum squared error (SSE) below $1 \cdot 10^{-15} \text{mm}$. Using ICP the registration is based upon the points in the (p_{EMM}) point set that are closest to the points in the (p_{MRI}) point set. The results of the ICP registration in an in-vivo dataset are shown in Figure S1d, and cross sectional views of the registration are shown in Figure S2.

Manual registration

Because ICP does not take into account the anatomical correctness of the registration the results of the ICP algorithm need to be checked and approved by the user. This is incorporated into the 3D CartBox workflow. In this way the rotations and translations that are suggested by the ICP algorithm are controlled, to be correct and beneficial for the registration. To allow experienced physicians to optimize the registration based on anatomy or additional landmarks that are acquired during the EMM procedure, 3D CartBox facilitates a manual manipulation of the registration. This can be done by adjusting the rotation and translation of (p_{EMM}) interactively with six degrees of freedom. These are rotation and translation in the sagittal, coronal, and transverse plane. Rotations were limited to respectively 10, 20 and 20 degrees to prevent excess rotations.

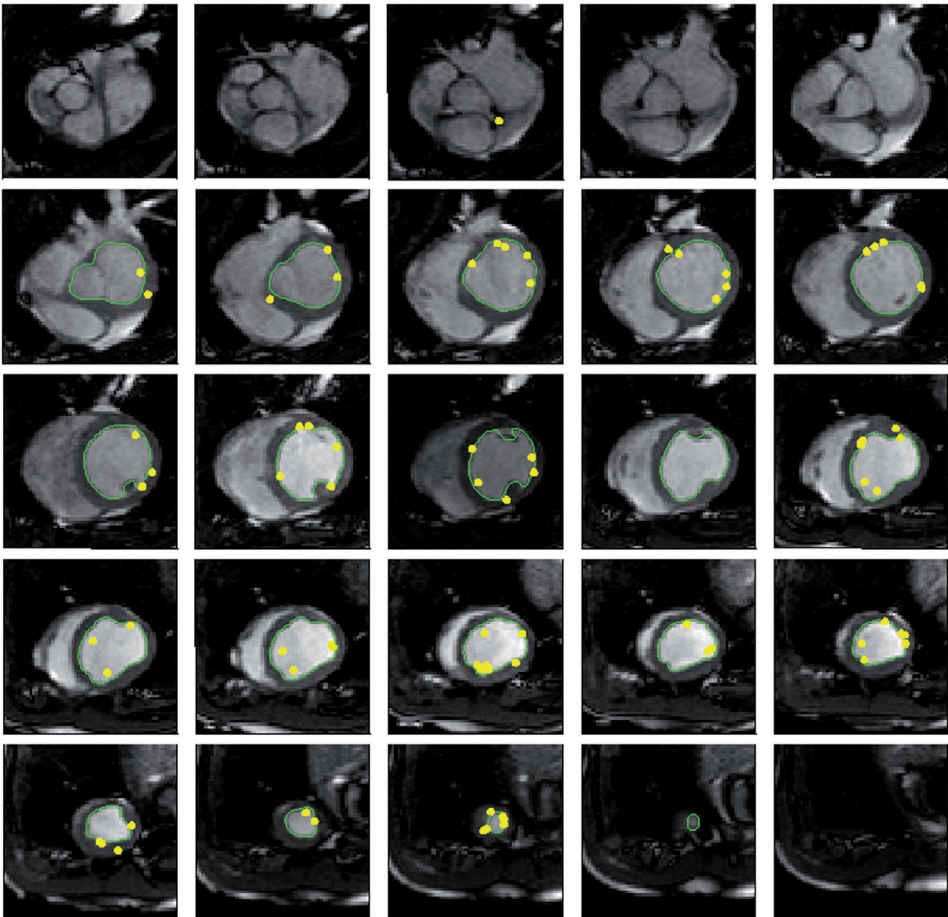


Figure S2 Cross sectional view of the final registration results of an in vivo dataset. The green line represents the endocardial surface mesh and the yellow points are the EMM points.

POST PROCESSING

Purpose

Present data using clinical standard visualization techniques.

Method

Create bullseye plots.

Error assessment

The accuracy of the registration was expressed by the registration error being the mean \pm standard deviation of the shortest distance from each EMM point to the cine mesh surface. To

show the relevance of this measure a cross sectional view of the registration is shown in Figure S2. The registration error of the registration shown in Figure S2 is 3.54 ± 1.6 and was based on 79 EMM points.

Chapter 3



Three dimensional fusion of electromechanical mapping and magnetic resonance imaging for real-time navigation of intramyocardial cell injections in a porcine model of chronic myocardial infarction

International Journal of Cardiovascular Imaging 2016 May;32(5):833-43.

Frebus J. van Slochteren¹, René van Es¹, Mariann Gyöngyösi², Tychon I.G. van der Spoel¹, Stefan Koudstaal¹, Tim Leiner⁴, Pieter A. Doevendans^{1,5}, Steven A.J. Chamuleau^{1,5}

¹ Department of Cardiology, University Medical Center Utrecht, The Netherlands

² Medical University of Vienna, Department of Cardiology, Vienna, Austria

⁴ Department of Radiology, University Medical Center Utrecht, The Netherlands

⁵ Interuniversity Cardiology Institute of the Netherlands (ICIN), Utrecht, The Netherlands

ABSTRACT

For cardiac regenerative therapy intramyocardial catheter guided cell transplantations are targeted to the infarct border zone (IBZ) i.e. the closest region of viable myocardium in the vicinity of the infarct area. For optimal therapeutic effect this area should be accurately identified. However late gadolinium enhanced magnetic resonance imaging (LGE-MRI) is the gold standard technique to determine the infarct size and location, electromechanical mapping (EMM) is used to guide percutaneous intramyocardial injections to the IBZ. Since EMM has a low spatial resolution, we aim to develop a practical and accurate technique to fuse EMM with LGE-MRI to guide intramyocardial injections. LGE-MRI and EMM were obtained in 17 pigs with chronic myocardial infarction created by balloon occlusion of LCX and LAD coronary arteries. LGE-MRI and EMM datasets were registered using our in-house developed 3D CartBox image registration software toolbox to assess: (1) the feasibility of the 3D CartBox toolbox, (2) the EMM values measured in the areas with a distinct infarct transmural (IT), and (3) the highest sensitivity and specificity of the EMM to assess IT and define the IBZ. Registration of LGE-MRI and EMM resulted in a mean error of 3.01 ± 1.94 mm between the LGE-MRI mesh and EMM points. The highest sensitivity and specificity were found for UV <9.4 mV and bipolar voltage <1.2 mV to respectively identify IT of ≥ 5 and ≥ 97.5 %. The 3D CartBox image registration toolbox enables registration of EMM data on pre-acquired MRI during the EMM guided procedure and allows physicians to easily guide injections to the most optimal injection location for cardiac regenerative therapy and harness the full therapeutic effect of the therapy.

INTRODUCTION

Cardiac regenerative therapy for ischemic heart disease (IHD) targets local cardiac protection and regeneration by means of vasculogenesis, cardiomyogenesis, and matrix support.¹ Previous studies have shown that injection of stem/progenitor cells into the border zone of the infarcted area, stimulates cardiac repair via cell-to-cell contact and secretion of paracrine factors.²⁻⁵ Therapeutic effects may importantly rely on the delivery and retention of the regenerative therapeutics on a location where oxygen and nutrients are available to enable survival. Hence, accurate identification of viable tissue in proximity of the myocardial infarct (MI) the infarct border zone (IBZ) is therefore of great importance. The gold standard technique to assess infarct size and location is late gadolinium enhancement (LGE) MRI.

Currently percutaneous intramyocardial cell injections are performed using the NOGA®XP electromechanical mapping (EMM) technique to identify the location of the infarction and the surrounding viable area. This technique measures local unipolar (UV) and bipolar (BV) electrical depolarization potentials and relative catheter tip displacements (Linear Local Shortening, LLS), to assess the local electrical and mechanical tissue characteristics and guide minimal invasive intramyocardial injections. A 3D magnetic tracking technique is used to create a three-dimensional interpolated reconstruction of the LV endocardium⁶ and perform measurements and injections at multiple locations on the endocardium. Prior studies have investigated the relations between myocardial viability/perfusion/infarction and NOGA®XP parameters by comparing bullseye representations of the parameters.⁷⁻⁹ Other studies in the field of electrophysiology have shown beneficial effects of the integration of electroanatomical mapping (EAM) and LGE-MRI for location of foci of ventricular arrhythmia enabling accurate targeting of ablations.¹⁰⁻¹² Different from the ablations, the injection locations in the context of cardiac regenerative therapy have no inherent reference (e.g. cessation of arrhythmia) of the correct location for the therapy. Since the infarcted myocardium is highly susceptible for arrhythmias upon catheter contact, and the mapping procedure is time-consuming, EMM measurements do not completely cover the endocardium and data is interpolated in regions where no measurements are acquired. Moreover, in prior studies to assess the relation between viability/perfusion/infarction and NOGA®XP parameters, different definitions of these parameters are used, and consequently in literature a large variance of threshold values of the NOGA®XP parameters to accurately target IBZ can be found.⁷

Since the non-transmurally infarcted border zone of the infarcted area is believed to be the preferred delivery site of the regenerative therapeutics,² it is crucial to be optimally defined during the injection procedure. We have developed the 3D CartBox image integration toolbox to fuse NOGA®XP EMM and MRI data in a real time fashion.¹³ With this technique we can combine the gold standard infarct imaging technique and local measures of myocardial electrical activity in order to more specifically determine the areas that are most suitable for cell injections. In this study we perform a retrospective in depth 3D multimodality analysis of the myocardial infarction areas with different infarct transmuralities in a porcine model of chronic myocardial infarction using 3D CartBox. Thereby we aim to evaluate the performance of the NOGA system to identify regions with a specific infarct transmuralinity (IT) and wall thickening (WT) as measured using MRI.

METHODS

Animals

For this study 2 animal models were used. In model 1 (LCX) myocardial infarction (MI) was induced by 75 minutes of proximal left circumflex coronary artery (LCX) balloon occlusion as previously described.¹⁴ Three 6-month old female Daland Landrace pigs (60-70 kg; IDDLO, Lelystad, the Netherlands) were pre-treated with clopidogrel 75 mg/day for 3 days and amiodarone 400mg/day for 10 days. Experiments in Utrecht were performed accordance with the "Guide for the Care and Use of Laboratory Pigs" prepared by the Institute of Laboratory Animal Resources and with prior approval by the Animal Experimentation Committee of the Faculty of Medicine, Utrecht University, the Netherlands. In model 2 (LAD) MI was induced in 14 3-months old domestic pigs by 90 minutes of percutaneous balloon occlusion of the left anterior descending coronary artery (LAD) after the second diagonal branch, followed by reperfusion. Pigs were pre-treated with clopidogrel (300 mg) and aspirin (250 mg) one day before procedure, and treated with daily dose of 75 mg clopidogrel and 100 mg aspirin. The experiments were performed in accordance with the "Guide for the Care and Use of Laboratory Pigs" prepared by the Institute of Laboratory Animal Resources and with prior approval by The Experimental Animal Care and Use Committee at the Faculty of Animal Science of the University of Kaposvar (Hungary).

The experiments were performed as shown in Figure 1. Both animal models have a period between the myocardial infarction and the therapy of more than 3 weeks so that a chronic infarct can be expected.¹⁵

Data acquisition

For both models, the NOGA®XP system (Biosense Webster, Cordis, Johnson & Johnson, USA) version 1.1.43 was used equipped with a 7 French NOGA mapping catheter (Biosense Webster, Cordis, Johnson & Johnson, Diamond Bar, USA) for the mapping procedure.

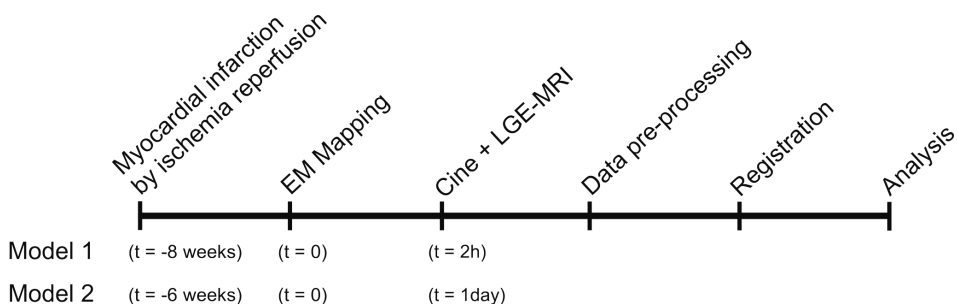


Figure 1 Time line of the experiments of model 1 (LCX), and model 2 (LAD)

The left ventricle (LV) was entered via the left carotid artery (LCX model) and the femoral artery (LAD model), and retrograde passage through the aortic valve. The catheter tip location is tracked throughout the complete cardiac cycle. Data storage is triggered on the R-wave, providing only end diastolic measurement values and points for registration. Electrocardiograms were filtered at 30–400 Hz (bipolar) and 1–240 Hz (unipolar). The EMM datasets were acquired in consideration of the criteria for good electromechanical mapping.⁷

In the LCX model MRI images were acquired using a 1.5T Philips Medical systems Achieva scanner with a surface cardiac array coil. BFFE Cine scans were made to assess cardiac function, and for registration of the NOGA map on the end diastolic endocardium. The settings during the MRI acquisitions were as follows. BFFE: repetition time [TR]/echo time [ET] = 2.9 ms/1.45 ms. Flip angle = 55°, Voxel size = 2.43 x 2.43 mm, field of view [FOV] = 35 x 35 cm, 144 x 144 matrix, 5mm slice thickness, 30 phases/R to R interval, electrocardiographic gated. LGE: repetition time [TR]/echo time [ET] = 4.61ms/1.41 ms, Flip angle = 15°, Voxel size = 1.36 x 1.36 mm, field of view [FOV] = 35 x 35 cm, 256 x 256 matrix, 5mm slice thickness. In the LAD model MRI images were acquired using a 1.5T Siemens Avanto scanner with a body surface coil. BFFE: repetition time [TR]/echo time [ET] = 41.85 ms/1.18 ms. Flip angle = 68°, Voxel size = 1.4 x 1.4 mm, field of view [FOV] = 35 x 25 cm, 256 x 176 matrix, 8mm slice thickness, 25 phases/R to R interval, electrocardiographic gated. LGE: repetition time [TR]/echo time [ET] = 577ms/1.18 ms, Flip angle = 50°, Voxel size = 1.4 x 1.4 mm, field of view [FOV] = 35 x 25 cm, 256 x 180 matrix, 8mm slice thickness. Cine and LGE scans were made at the same positions with the same orientation. In both models Gadovist contrast agent (0.2mmol/ml) was used for the LGE scans with a dose of 15ml/kg. The scan was made 15 minutes after intravenous infusion of the Gadovist.

Data pre-processing

Segmentation of the left ventricle on the short axis CINE and LGE MRI data is done in the end diastolic phase in approximately 20 slices located from apex to base. The segmentations are done automatically and checked on the long axis images using the freely available software Segment version 1.9 R2507 (<http://segment.heiberg.se>)¹⁶ available for Matlab (MATLAB 2012a, The MathWorks Inc., Natick, MA, 2012). Segmentations are done to create a 3D surface mesh (cine mesh) of the LV endocardium for surface registration and projection of the acquired data. Furthermore the local wall thickening (WT) of the myocardium was assessed using the CINE images. The myocardial infarct was segmented on the LGE images using the area based semi-automatic segmentation.¹⁷ If necessary both the LV and the infarct segmentations were manually adjusted by an experienced radiologist. Area based IT values were calculated in 80 circumferential segments of all slices using the bullseye function of Segment.¹⁷ The IT data was projected on the CINE derived endocardial surface mesh using the TriScatteredInterp function of Matlab. The endocardial LV surface mesh is used for registration of the EMM points, image guided injection procedures, and post processing of the EMM and MRI data.

Image registration

Registration of the NOGA®XP and the MRI datasets was performed using a modified 3D CartBox image integration toolbox.¹³ Instead of using anatomical landmarks for registration, we applied a standard rotation to align the NOGA®XP and the MRI coordinate systems. Hereafter we performed a rigid body translation and rotation of the NOGA®XP dataset based on the apex location. The remaining error after rigid body translation and rotation was caused by a slight difference of the supine positions of the animals during the EMM and MRI procedures. The registration error was minimized further by an iterative closest point (ICP) algorithm.¹⁸ The ICP algorithm was restricted to small rotations around the apex in the sagittal, coronal, and transverse plane of respectively 10, 20 and 20 degrees to prevent excess rotations. If necessary the

registration was manually optimized by adjusting the registration interactively with six degrees of freedom: rotation and translation in the sagittal, coronal, and transverse planes. Before the registration was finalized the shape of the LV endocardial surface mesh and the EMM points was visually checked to minimize the registration error due to end diastolic volume (EDV) differences caused by the different timing between EMM and LGE-MRI acquisitions. The registration error was expressed by the mean and standard deviation of the closest distance between the EMM points and the cine mesh surface.¹² To prevent influences of EMM points located outside the cine mesh (e.g. LV outflow tract), these points were excluded for registration, and further processing. The result of the registration of a typical dataset is shown in Figure 2.

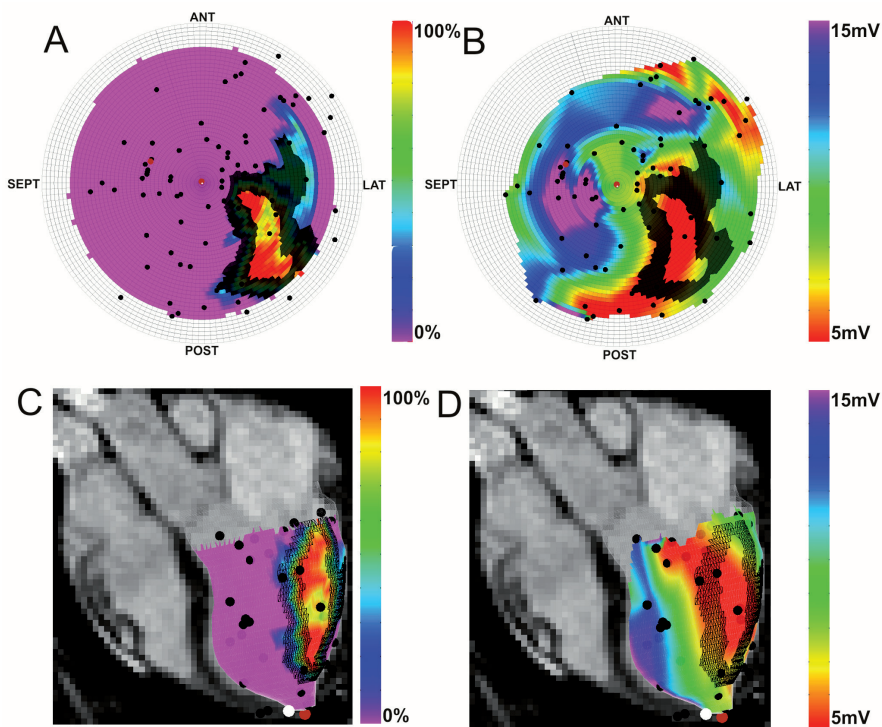


Figure 2 Typical images of bullseyes (A, B) and endocardial surface meshes (C, D). The color scale reflects the value of the infarct transmurality (A and C), Unipolar voltage (B and D). The black dots indicate the measurement locations of the EMM. Brown and white dots respectively represent the injection locations, and the location of the apex. The dark hashed areas indicate the infarct border zone as calculated by the automatic infarct border zone calculation algorithm. ANT = anterior LAT = lateral, POST = posterior, SEPT = septum.

Analysis

The optimal thresholds of the EMM parameters to assign areas with a distinct IT were established by determining the largest area under the curve (AUC) of receiver operating characteristic (ROC) curves. ROC curves were created by automatically subdividing the IT and EMM data into 40

subsequent regions with the IT threshold ranging from ≤ 0 to $\leq 100\%$ with a step size of 2.5%, and 40 subsequent regions of the EMM parameters. For UV the range was set to 0mV to 25mV with a step size of 0.62 mV, for BV the range was set to 0mV to 12mV with a step size of 0.3 mV, for LLS the range was set to -32% to 48% with a step size of 2% and for WT the range was set to -5mm to 15mm with a step size of 0.5 mm. To analyze the tissue that is identified by the specific UV and BV values, the infarct area was divided in 5 areas with a distinct IT: [0%], (0-25%], (25-50%], (50-75%], (75-100%]. The classification of the IT threshold areas is shown in Table 1. To assess the capacity, and find the optimal threshold of UV and BV to distinguish areas with a distinct IT, the UV and BV values were analyzed in all IT areas. Furthermore the most distinctive threshold of WT to assess IT and LSS to assess WT were determined by respectively analyzing the WT values in areas with a distinct IT, and analyzing the LLS values in areas with a distinct WT. This analysis provides insight into the possible use of myocardial deformation assessment by MRI as an alternative technique to identify the IBZ, and assess LSS to represent myocardial deformation. To prevent misinterpretation of collagen rich low voltage areas in the valvular plane with no infarct, and therefore no LGE contrast, we excluded the basal layers of the heart from the analysis.

Table 1 Division of transmural areas. IT = Infarct Transmurality.

Infarct area 0 % IT	All healthy tissue. IT = 0% (includes 0% only)
Infarct area 0 - 25 % IT	IT > 0% to IT < or = 25% (does not include 0% and includes 25%)
Infarct area 25 - 50 % IT	IT > 25% to IT < or = 50% (does not include 25% and includes 50%)
Infarct area 50 - 75 % IT	IT > 50% to IT < or = 75% (does not include 50% and includes 75%)
Infarct area 75 - 100 % IT	IT > 75% to IT < or = 100% (does not include 75% and includes 100%)

Statistics

Statistics were performed using IBM SPSS Statistics (Version 20.0, IBM Corporation, Armonk, New York, United States). All data is presented as mean \pm standard deviation (SD). The differences between the animal models were tested using a student t-test. The differences between the points/cm² of each area were calculated using the Kruskal Wallis test. We compared the EMM parameters to the IT measured by LGE-MRI per measurement point using a linear mixed model analysis to calculate the amount of IT that can be explained by the EMM parameters. For IT, the amount of residual variance (σ^2) within the animals and the variance (intercept, τ) between animals were calculated (null model). Next, EMM parameters were added to the model (full model). Variance explained by the input parameter, R^2 , was calculated as 100% minus the ratio of the full and null models (equation 1).¹⁹ Hence, R^2 represents the reduction in variance of the outcome parameter (IT) after adding input parameters (EMM; UV, BV, LLS).

$$R^2 = 1 - \frac{\sigma_{full}^2 + \tau_{00full}}{\sigma_{null}^2 + \tau_{00null}} \quad (1)$$

RESULTS

Animals

In all animals the myocardial infarction was in a chronic state at the time of the treatment. In the LCX model the infarct was located in the midlateral wall (3 animals). In the animals that underwent an LAD occlusion the infarct was located apicoseptally and mid-apical anterior (14 animals). All LGE-MRI datasets showed a clear hyper intense area on LGE-MRI, and cardiac function was decreased with a mean LV ejection fraction (LVEF) of $42 \pm 8.7\%$. The LCX and LAD models showed an LVEF of $35.7 \pm 3.9\%$ and $43.3 \pm 3.9\%$, respectively ($p=0.05$). The infarct volumes of both models was not different 16.1 ± 2.2 ml and 15.4 ± 4.4 ml for the LCX and LAD model, respectively ($p=0.75$). MRI data is presented in Table 2.

Table 2

LV end-diastolic volume (ml)		123.6 \pm 32.6			
LV end-systolic volume (ml)		72.8 \pm 26.4			
LV stroke volume (ml)		50.7 \pm 11.5			
LV ejection fraction (%)		42.0 \pm 8.7			
LV ejection fraction (%) per model	($p=0.05$)	35.7 \pm 3.9	(model 1)	43.3 \pm 9	(model 2)
Heart rate		92.7 \pm 20.7			
Myocardium volume (ml)		111 \pm 15.6			
Infarct volume (ml)		15.6 \pm 4.1			
Infarct volume (ml) per model	($p=0.75$)	16.1 \pm 2.2	(model 1)	15.5 \pm 4.4	(model 2)
LV area (cm ²)		102.7 \pm 13.8			
Infarct area 0 % IT (cm ²)		68.2 \pm 12.8		(66.1 \pm 6.1 %)	
Infarct area 0 - 25 % IT (cm ²)		10.6 \pm 3.2		(10.5 \pm 3.3 %)	
Infarct area 25 - 50 % IT (cm ²)		6.5 \pm 3.5		(6.3 \pm 3.4 %)	
Infarct area 50 - 75 % IT (cm ²)		6.4 \pm 2.2		(6.4 \pm 2.6 %)	
Infarct area 75 - 100 % IT (cm ²)		10.9 \pm 7.3		(10.5 \pm 6.3 %)	
Infarct areas (cm ²) per model					
Infarct area 0 % IT (cm ²)	($p = 0.72$)	72.6 \pm 22.1	(model 1)	67.3 \pm 10.9	(model 2)
Infarct area 0 - 25 % IT (cm ²)	($p = 0.54$)	12.4 \pm 4.8	(model 1)	10.2 \pm 2.9	(model 2)
Infarct area 25 - 50 % IT (cm ²)	($p = 0.24$)	10.2 \pm 4.5	(model 1)	5.7 \pm 2.9	(model 2)
Infarct area 50 - 75 % IT (cm ²)	($p = 0.88$)	3.7 \pm 3.7	(model 1)	11.7 \pm 6.5	(model 2)
Infarct area 75 - 100 % IT (cm ²)	($p = 0.38$)	3.8 \pm 3.9	(model 1)	12.4 \pm 6.7	(model 2)

Results of cine and late enhancement magnetic resonance imaging of 17 animals. Data are expressed as mean \pm SD. The infarct area size of both models is tested using a student t-test. IT = Infarct Transmurality.

Data acquisition

The LGE-MRI datasets showed a clear myocardial infarction without microvascular obstruction as assessed by the myocardial infarct segmentation algorithm. The mean endocardial surface

area in the [0%], (0-25%), (25-50%), (50-75%), (75-100%) IT subdivisions respectively was: $68.2 \pm 12.8\text{cm}^2$, $10.6 \pm 3.2\text{cm}^2$, $6.5 \pm 3.5\text{cm}^2$, $6.4 \pm 2.2\text{cm}^2$, and $10.9 \pm 7.3\text{cm}^2$ thereby covering $66.1 \pm 6.1\%$, $10.5 \pm 3.3\%$, $6.3 \pm 3.4\%$, $6.4 \pm 2.6\%$ and $10.5 \pm 6.3\%$ of the total LV endocardial surface area. Although it is not significant, the animal models show a marked difference in the sizes of the areas with a distinct infarct transmural. The infarct of the LCX model has a larger portion in the 0-50% IT region whereas the LAD model has a larger portion in the 50-100% IT region. MRI data is presented in Table 2. The mean number of EMM points in the EMM acquisitions was 152.3 ± 55 . All EMM parameters are displayed in Table 3.

Table 3 Three dimensional electromechanical mapping and image registration results of 17 animals.

Electromechanical mapping points				
Total number of EMM points	2867			
EMM points used for registration	2590			
Points per animal	152.3 ± 55			
Registration error (mm)	3.01 ± 1.94			
Registration error (mm) per model ($p = 0.32$)	3.22 ± 1.87	(model 1)	3.0 ± 1.82	(model 2)
Points used for projection and analysis				
Total number of EMM points	1581			
Points per animal	93 ± 27.2			
Points per infarct transmural area used for projection and analysis				
0% IT	50.2 ± 18.4	0.7 ± 0.3 points/cm ²		
0 - 25% IT	9.7 ± 6.2	0.9 ± 0.5 points/cm ²		
25 – 50% IT	8.0 ± 4.3	1.4 ± 0.7 points/cm ²		(p < 0.05)
50 – 75% IT	6.3 ± 5.6	0.9 ± 0.6 points/cm ²		
75 – 100% IT	18.7 ± 14.2	1.5 ± 0.8 points/cm ²		

Data are expressed as mean \pm SD. The registration error of both models is tested using a student t-test. The differences between the points/cm² of each area are calculated using the Kruskal Wallis test. IT = Infarct Transmurality.

Image registration

The registration data is summarized in Table 3. The total number of EMM points in the 17 datasets was 2867. After exclusion of points outside the mesh, the total number of points that are used for registration and projection of EMM parameters on the endocardial surface mesh was 2590. The EMM points acquired during the mapping procedure were aimed to be as homogeneously distributed over the endocardial surface as possible to assure optimal registration of the EMM and MRI cine mesh. The resulting mean registration error of all datasets was $3.01 \pm 1.94\text{mm}$ and the mean registration error of the LCX and LAD models were 3.22 ± 1.87 and 3.0 ± 1.82 ($p = 0.32$), respectively. The EMM point density was significantly higher in the regions with 25-50% and 75-100% IT ($p < 0.05$).

Analysis

ROC curves of the EMM parameters are shown in Figure 3. For each EMM parameter the ROC with the highest AUC to detect areas with IT $\geq 0\%$ are shown (Figure 4). UV best determines IT $\geq 5\%$ (AUC = 0.77) when using a threshold of $\leq 9.38\text{mV}$ with a sensitivity of 0.82 and specificity of 0.64. The mixed model analysis showed that UV explained 15 % of IT (Table 4). BV best determines IT $\geq 97.5\%$ (AUC = 0.81) when using a threshold of $\leq 1.2\text{mV}$ with a sensitivity of 0.83 and specificity of 0.67. From the mixed model analysis it is appreciated that BV explains 10% of IT (Table 4). The lowest AUC is found for LLS (AUC = 0.67) to distinguish IT $\geq 100\%$ by LLS $\leq 8\%$ (sensitivity = 0.65, specificity = 0.6). Correspondingly the mixed model analysis also shows that only 3% of IT is explained by LLS (Table 4). Furthermore we have assessed the relations between LLS and WT, and between IT and WT. LLS most accurately discerns regions with IT of 100% as was shown in Figure 3C and is poorly related to local WT (Figure 5). The ROC curve in Figure 5A shows that LLS $<12\%$ distinguishes WT $\geq 2\text{mm}$ with sensitivity = 0.77 and specificity = 0.52. Nevertheless an analysis of the WT and IT both measured by MRI shows that WT is related to local IT. In Figure 6 it is shown that WT determines IT $\geq 12.5\%$ (AUC = 0.81) when using a threshold of $\leq 2\text{mm}$, with a sensitivity of 0.77 and specificity of 0.73.

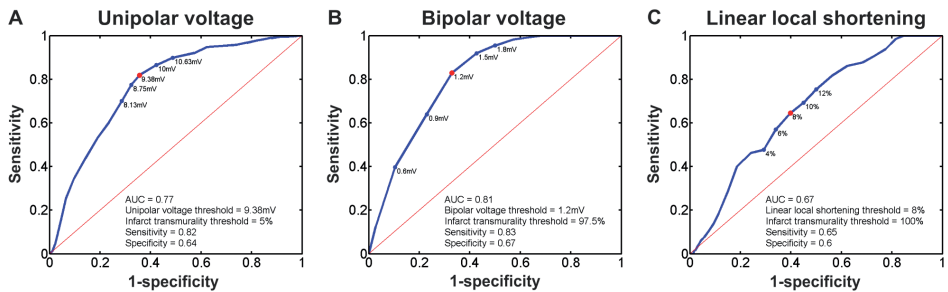


Figure 3 ROC curves for the unipolar voltage (A), bipolar voltage (B), linear local shortening (C) with the highest AUC. The corresponding thresholds of the respective parameters, and the infarct transmuralty are annotated in the figures. The red dot marks the highest sensitivity and specificity.

Table 4	
Parameter	R ²
UV	15%
BV	10%
LLS	3%

Comparison of EMM parameters with infarct transmuralty; R² = explained variance of myocardial fibrosis by the regarding parameter

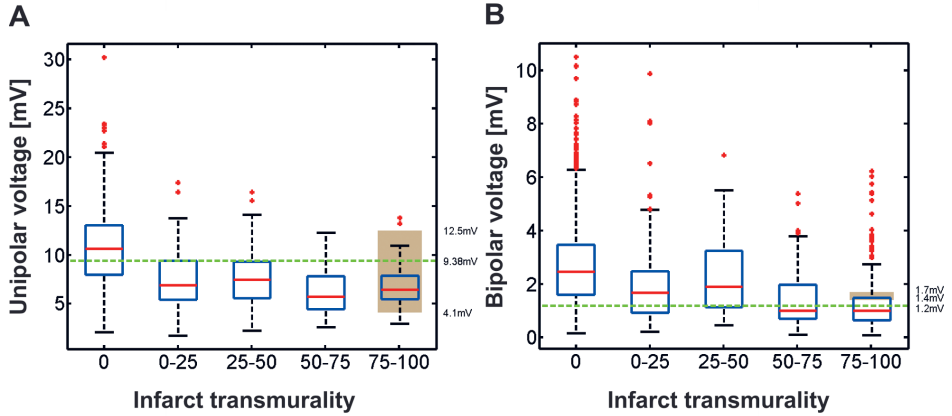


Figure 4 Box plots of the distribution of the unipolar voltage (A), bipolar voltage (B) values in the areas with a distinct infarct transmuralty. Boxes represent the 25-75% percentiles and the red line in the boxes represents the median value. Red dots are outliers ($>3 \times$ SD from the mean value). The green line represents the value with the highest AUC as shown in Figure 1. The grey area represents the range of the threshold values reported in literature to distinguish core infarct. Numbers on the right annotate the range of the threshold values and the value of the green line.

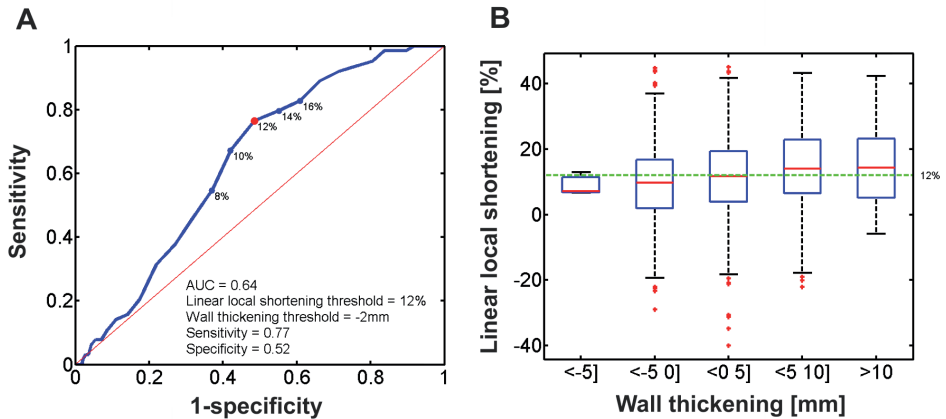


Figure 5 ROC curve for Linear local shortening with the highest AUC (A). The corresponding thresholds for wall thickening and linear local shortening are annotated in the figure. Box plots of the distribution of the linear local shortening values compared to wall thickening (B). Boxes represent the 25-75% percentiles and the red line in the boxes represents the median value. Red dots are outliers ($>3 \times$ SD from the mean value). The green line represents the value with the highest AUC.

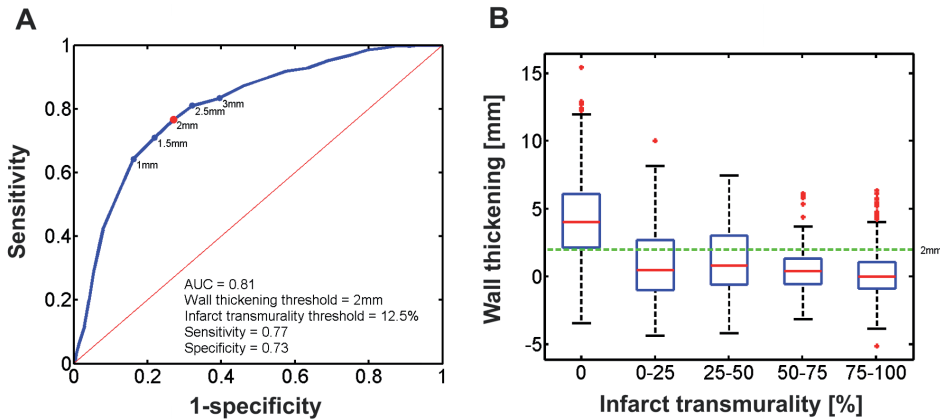


Figure 6 ROC curve for wall thickening with the highest AUC (**A**). The corresponding thresholds for wall thickening and infarct transmural are annotated in the figure. Box plots of the distribution of the wall thickening values compared to infarct transmural. Boxes represent the 25-75% percentiles and the red line in the boxes represents the median value. Red dots are outliers ($>3 \times$ SD from the mean value). The green line represents the value with the highest AUC.

DISCUSSION

In this study we have retrospectively applied the 3D CartBox image integration toolbox to a dataset of 17 pigs with a chronic MI. For the first time we have used 3D CartBox in a larger group resulting in a mean surface registration error of 3.01 ± 1.94 mm. In contrast to earlier studies using a manual segmental comparison,^{7,9} this technique enabled an accurate in depth analysis of the electromechanical properties of infarct areas. The six main findings of this study are: 1) The use of 3D CartBox is feasible. 2) UV and BV do distinguish infarcted and healthy tissue, but have less sensitivity to clearly identify regions with a distinct IT value based on LGE-MRI. 3) LLS and WT are differently affected by IT. 4) WT is affected in the infarct areas, but does not reflect areas with different IT values. 5) Integrated EMM and LGE-MRI images have the potential to guide intramyocardial injections more accurately than the on-table EMM and off-table LGE-MRI alone. 6) The applied EMM-LGE-MRI fusion software can be used for clinical applications of real-time image guided intramyocardial injections in the future.

Animals

This study was conducted in a multicenter fashion using two different animal models. However not significant, in the LCX model the sizes of the 100% transmurally infarcted regions were smaller (Table 2). One animal with an LCX infarct had no 75-100% IT area 8 weeks after MI. Most likely this was caused by lower ischemia time of 75 minutes which causes less irreversible cardiomyocyte cell death. In the 90 minutes LAD occlusion model all pigs had a transmural infarction 6 weeks after MI. No microvascular obstructions were detected in the pigs as could be expected based on literature.²⁰ Because clear infarcts with different IT regions were established in both animal models, all datasets qualified to be used for further analysis.

Data acquisition

Although data of the two centers were recorded using different imaging equipment, data acquisition protocols were identical, and therefore image registration and analysis could be performed using the 3D CartBox toolbox using standard image formats for MRI (DICOM) and NOGA®XP (SQL database).

Image registration

Due to a low spatial resolution of the EMM, the EMM surface meshes never reflect the exact LV surface and therefore a registration error will always occur. In both models the EMM and MRI acquisitions were performed within 2 hours (LCX) and 1 day (LAD). A longer time between EMM and LGE-MRI acquisitions increases the chance of a difference in cardiac load/filling during the EMM and MRI procedures, which can cause an increase of the registration error. Since we did not observe a significant difference between the registration errors of the different models, we believe that the load/filling difference during EMM and LGE-MRI acquisitions was minimal. In this study we have used the standard rotation to align the NOGA®XP and MRI coordinate systems, instead of initial registration based on anatomical landmarks.¹³ Since the pigs were in supine position during both the EMM and MRI procedures the orientation of the animal in during the EMM and MRI procedures could be standardized to minimize the remaining registration error. To prevent erroneous rotations by the subsequent ICP and manual optimization steps of the registration, we have secured that rotations during the manual optimization steps did not exceed 5 degrees. The resulting registration error is $3.01 \pm 1.94\text{mm}$, which is clinically acceptable and even slightly better than the values reported in studies where CARTO® was used: $3.83 \pm 0.57\text{mm}^{12}$ or $4.3 \pm 3.2\text{ mm}^{11}$. The SD of the registration error might be affected by the regularity of the heart rate during the EMM procedures resulting in end diastolic LV surface alterations in the EMM acquisition, or respiratory induced motion of the heart. The NOGA®XP system does not compensate for this. From Table 3 it can be observed that the EMM points are not homogeneously distributed over the areas with a different IT. The highest point density is found in the area with 75-100% IT. This most likely is caused by the targeted search for the infarct area with the EMM catheter during the mapping procedure or the preference of the catheter for aneurysms located in the core infarct.

Analysis

As already visually noticed,^{10,12} infarcted areas measured by LGE-MRI do not always overlap with infarct areas identified by EMM. In our data we have found that EMM has the highest sensitivity and specificity to identify infarct transmuralities of $\geq 5\%$ and $\geq 97.5\%$ by electric signals $UV < 9.38\text{mV}$ and $BV < 1.2\text{mV}$ respectively as is shown in Figure 3. The different sensitivity for different areas most likely is caused by the detection of far field depolarization signals by a single electrode (UV), which are filtered out by the subtraction of two electrode signals that are positioned within 2mm on the catheter (BV). Infarcted tissue in the vicinity of the measurement decreases UV in a larger area whereas BV is only affected by the local tissue. UV therefore performs best to identify areas that are located more at the borders of the infarct, whereas BV is more eligible to identify areas that are located at the infarct core. The linear mixed model analysis presented in Table 4 showed poor overlap between the EMM parameters and the IT

based on LGE-MRI. The large range of the EMM parameters in each area with a distinct IT (Figure 4) emphasizes that the EMM parameters do not accurately reflect IT. This variance might partly be induced by the registration error or the difference between infarct assessment by EMM and LGE-MRI. Since the administration-scanning procedure of the LGE-MRI scan is performed accurately and according to clinical standard, it is expected that the LGE-MRI scans are correct and therefor used as a reference in this study. Potential error sources are the measurements of low depolarization values on healthy tissue due to limited wall contact or measurement of high depolarization values on infarcted tissue caused by far field signals or the presence of local patch of healthy tissue. Since irregular points in the EMM dataset are usually re-examined by the operator, this effect is expected to be a small source of error. On a cellular level depressed electrical activity in the myocardium adjacent to the infarct might play a role.^{15,21} The inhomogeneous distribution of wall stress during the remodeling process causes the myocardium to enter the transient phase of collagen deposition. In the transient phase uptake of gadolinium and the decreased electrical function might be out of phase. Unfortunately studies using a comparable registration algorithm in the field of electrophysiology either did not calculate the ROC curves,¹² or did not perform a detailed analysis of the areas with a different IT.^{10,11} The wide range of threshold values represented in literature⁷ to identify core infarct as shown by the gray area in Figure 4 results from the use of different definitions of viability/perfusion/transmurality and the use of multiple absolute (PET, echocardiography, histology) and relative (SPECT) techniques to identify this, in combination with a manual segmental comparison to EMM data.⁹ To be able to target the hibernating tissue that is mechanically depressed and electrically active, the LLS parameter was introduced to measure local relative cathetertip movements caused by cardiac deformation. Areas with severely depressed movements (LLS) and a maintained UV or BV should present the hibernating tissue in the IBZ. Strikingly Figure 5 illustrates that there is no relation between LLS and the local WT.⁹ This is most likely caused by the definition of LLS being: *'the change in distance between an index point and all its recorded surrounding points from late diastole to maximum systole'*.²² A weighing is applied to emphasize points within a distance of 8-15mm.²² Consequently for a point in an area with small number of points or points moving due to tethering of the tissue, LLS is based on points located more distantly, or based on a false perception, causing erroneous LLS values. To correctly assess cardiac deformation by LLS a higher point density is necessary. In summary, the identification of the IBZ by EMM can be improved by using fusion software to combine EMM and LGE-MRI. Strategies to more optimally identify the IBZ based on LGE-MRI might be helpful to increase the effects of cardiac regenerative therapy.

Clinical implications

Advanced ROC analysis revealed cutoff values of UV <9.38mV and BV <1.2mV to respectively distinguish areas with $\geq 5\%$ and $\geq 97.5\%$ IT. For clinical perspective we have shown that EMM is an adequate tool to distinguish transmurally infarcted myocardium from normal myocardium. For more detailed quantification of transmuralty, we propose to incorporate LGE-MRI data. This may be of interest in view of targeting the exact border zone.²³ The 3D CartBox toolbox for image registration can be used to further specify the most optimal injection location for cardiac regenerative therapy based on LGE-MRI.

Limitations

For both BV and LLS we found that the acquisition of more EMM measurement points would probably have given more insight into the full potential of the BV and LLS parameters. Furthermore the retrospective design of this study and lack of histological data made it impossible to perform a detailed comparison between EMM, LGE-MRI, and histology. In prior studies using coarse registration techniques a good agreement was found between EMM and histology²⁴ and between LGE-MRI and histology.²⁵⁻²⁷ Such a study is necessary to assess the accuracy of LGE-MRI guided injections and will be performed in a 3D fashion in the near future. During the mapping procedure small respiratory induced excursions of the catheter tip were observed. Since the NOGA®XP system does not compensate for respiratory induced motion of the cathetertip, this most likely affected the registration accuracy. Compensation for respiratory motion might be beneficial for future applications.

Conclusion

We are the first to perform robust 3D registration and an in depth comparison of the NOGA®XP EMM parameters and IT measured by LGE-MRI to determine the infarct identification characteristics of EMM. We found that the 3D CartBox image registration toolbox enables multimodality infarct identification and can be used for further specification of the most optimal injection locations for cardiac regenerative therapy.

Acknowledgments

This work was supported by the Netherlands Heart Foundation '[2003B07304 and 2010T025]', BSIK program "Dutch Program for Tissue Engineering", '[Grant 6746]', and a Bekalis price (PD). This research is part of the Project P1.04 SMARTCARE of the research program of the BioMedical Materials institute, co-funded by the Dutch Ministry of Economic Affairs and the Nederlandse Hartstichting.

Compliance with ethical standards

Funding

This work was supported by the Netherlands Heart Foundation '[2003B07304 and 2010T025]', BSIK program "Dutch Program for Tissue Engineering", '[Grant 6746]', and a Bekalis price (PD). This research is part of the Project P1.04 SMARTCARE of the research program of the BioMedical Materials institute, co-funded by the Dutch Ministry of Economic Affairs and the Nederlandse Hartstichting.

Conflict of interest

F.J. van Slochteren is cofounder of CART-Tech B.V.

REFERENCES

1. Dimmeler S, Zeiher AM, Schneider MD (2005) Unchain my heart : the scientific foundations of cardiac repair. *The Journal of Clinical Investigation* 115 (3):572-583. doi:10.1172/JCI200524283.572
2. Orlic D, Kajstura J, Chimenti S, Bodine DM, Leri A, Anversa P (2001) Bone marrow stem cells regenerate infarcted myocardium. *Nature* 410 (April):701-705
3. Smits AM, Laake LWV, Ouden KD, Schreurs C, Szuhai K, van Echteld CJ, Mummery CL, Doevendans PA, Goumans M-J (2009) Human cardiomyocyte progenitor cell transplantation preserves long-term function of the infarcted mouse myocardium. *Cardiovascular Research* 83 (3):527-535. doi:10.1093/cvr/cvp146
4. Beltrami AP, Barlucchi L, Torella D, Baker M, Limana F, Chimenti S, Kasahara H, Rota M, Musso E, Urbanek K, Leri A, Kajstura J, Nadal-Ginard B, Anversa P (2003) Adult cardiac stem cells are multipotent and support myocardial regeneration. *Cell* 114 (6):763-776
5. Loffredo FS, Steinhauser ML, Gannon J, Lee RT (2011) Bone marrow-derived cell therapy stimulates endogenous cardiomyocyte progenitors and promotes cardiac repair. *Cell stem cell* 8 (4):389-398. doi:10.1016/j.stem.2011.02.002
6. Gyöngyösi M, Lang I, Dettke M, Beran G, Graf S, Sochor H, Nyolczas N, Charwat S, Hemetsberger R, Christ G, Edes I, Balogh L, Krause KT, Jaquet K, Kuck K-H, Benedek I, Hintea T, Kiss R, Préda I, Kotevski V, Pejkov H, Zamini S, Khorsand A, Sodeck G, Kaider A, Maurer G, Glogar D (2009) Combined delivery approach of bone marrow mononuclear stem cells early and late after myocardial infarction: the MYSTAR prospective, randomized study. *Nature clinical practice Cardiovascular medicine* 6 (1):70-81. doi:10.1038/ncpcardio1388
7. Gyöngyösi M, Dib N (2011) Diagnostic and prognostic value of 3D NOGA mapping in ischemic heart disease. *Nature Reviews Cardiology* 8 (7):393-404. doi:10.1038/ncardio.2011.64
8. Perin EC, Silva GV, Sarmento-Leite R, Sousa ALS, Howell M, Muthupillai R, Lambert B, Vaughn WK, Flamm SD (2002) Assessing Myocardial Viability and Infarct Transmurality With Left Ventricular Electromechanical Mapping in Patients With Stable Coronary Artery Disease: Validation by Delayed-Enhancement Magnetic Resonance Imaging. *Circulation* 106 (8):957-961. doi:10.1161/01.CIR.0000026394.01888.18
9. Pavo N, Jakab A, Emmert MY, Strebingen G, Wolint P, Zimmermann M, Ankersmit HJ, Hoerstrup SP, Maurer G, Gyöngyösi M (2014) Comparison of NOGA Endocardial Mapping and Cardiac Magnetic Resonance Imaging for Determining Infarct Size and Infarct Transmurality for Intramyocardial Injection Therapy Using Experimental Data. *PLoS ONE* 9 (11):e113245-e113245. doi:10.1371/journal.pone.0113245
10. Codreanu A, Odille F, Aliot E, Marie P-Y, Magnin-Poull I, Andronache M, Mandry D, Djabballah W, Régent D, Felblinger J, de Chillou C (2008) Electroanatomic characterization of post-infarct scars comparison with 3-dimensional myocardial scar reconstruction based on magnetic resonance imaging. *Journal of the American College of Cardiology* 52 (10):839-842. doi:10.1016/j.jacc.2008.05.038
11. Desjardins B, Crawford T, Good E, Oral H, Chugh A, Pelosi F, Morady F, Bogun F (2009) Infarct architecture and characteristics on delayed enhanced magnetic resonance imaging and electroanatomic mapping in patients with postinfarction ventricular arrhythmia. *Heart Rhythm* 6 (5):644-651. doi:10.1016/j.hrthm.2009.02.018
12. Wijnmaalen AP, Geest RJVD, Van Huls Van Taxis CFB, Siebelink H-mJ, Kroft LJM, Bax JJ, Reiber JHC, Schalij MJ, Zeppenfeld K (2010) Head-to-head comparison of contrast-enhanced magnetic resonance imaging and electroanatomical voltage mapping to assess post-infarct scar characteristics in patients with ventricular tachycardias : real-time image integration and reversed registration. *European Heart Journal* 32 (1):104-114. doi:10.1093/eurheartj/ehq345
13. Van Slochteren FJ, Van Es R, Koudstaal S, Van Der Spoel TIG, Sluijter JPG, Verbree J, Pruijm RHR, Pluim JPW, Leiner T, Doevendans PA, Chamuleau SAJ (2014) Multimodality infarct identification for optimal image guided intramyocardial cell injections. *Netherlands Heart Journal Article in press*
14. van der Spoel TIG, Vrijsen KR, Koudstaal S, Sluijter JPG, Nijssen JFW, de Jong HW, Hoefer IE, Cramer M-JM, Doevendans PA, van Belle E, Chamuleau SAJ (2012) Transendocardial cell

- injection is not superior to intracoronary infusion in a porcine model of ischaemic cardiomyopathy: a study on delivery efficiency. *Journal of Cellular and Molecular Medicine* 16 (11):2768-2776. doi:10.1111/j.1582-4934.2012.01594.x
15. Holmes JW, Borg TK, Covell JW (2005) Structure and Mechanics of Healing Myocardial Infarcts. *Annual Reviews of Biomedical Engineering* 7:223-253. doi:10.1146/annurev.bioeng.7.060804.100453
 16. Heiberg E, Sjögren J, Ugander M, Carlsson M, Engblom H, Arheden H (2010) Design and validation of Segment—freely available software for cardiovascular image analysis. *BMC medical imaging* 10 (1):1-13. doi:10.1186/1471-2342-10-1
 17. Heiberg E, Engblom H, Engvall J, Hedström E, Ugander M, Arheden H (2005) Semi-automatic quantification of myocardial infarction from delayed contrast enhanced magnetic resonance imaging. *Scandinavian cardiovascular journal : SCJ* 39 (5):267-275. doi:10.1080/14017430500340543
 18. Umeyama S (1991) Least-squares estimation of transformation parameters between two point patterns. *IEEE Transactions on Pattern Analysis and Machine intelligence* 13 (4):376-380
 19. Snijders TAB BR (2012) *Multilevel Analysis: An Introduction to Basic and Advanced Multilevel Modeling*. 2nd ed. London. Sage Publications,
 20. Ghugre NR, Ramanan V, Pop M, Yang Y, Barry J, Qiang B, Connelly KA, Dick AJ, Wright GA (2011) Quantitative tracking of edema, hemorrhage, and microvascular obstruction in subacute myocardial infarction in a porcine model by MRI. *Magnetic Resonance in Medicine* 66 (4):1129-1141. doi:10.1002/mrm.22855
 21. Fomovsky GM, Holmes JW (2010) Evolution of scar structure , mechanics , and ventricular function after myocardial infarction in the rat. *American Journal Of Physiology Heart and Circulation Physiology* 298:221-228. doi:10.1152/ajpheart.00495.2009
 22. Psaltis PJ, Worthley SG (2009) Endoventricular Electromechanical Mapping - The Diagnostic and Therapeutic Utility of the NOGA ® XP Cardiac Navigation System. *Journal of Cardiovascular Translational Research* 2:48-62. doi:10.1007/s12265-008-9080-7
 23. Romero J, Kahan J, Kelesidis I, Makani H, Wever-Pinzon O, Medina H, Garcia MJ (2013) CMR imaging for the evaluation of myocardial stunning after acute myocardial infarction: a meta-analysis of prospective trials. *European heart journal cardiovascular Imaging* 14 (11):1080-1091. doi:10.1093/ehjci/jet040
 24. Wolf T, Gepstein L, Dror U, Hayam G, Shofti R, Zaretzky a, Uretzky G, Oron U, Ben-Haim Sa (2001) Detailed endocardial mapping accurately predicts the transmural extent of myocardial infarction. *Journal of the American College of Cardiology* 37 (6):1590-1597
 25. Pop M, Ghugre NR, Ramanan V, Morikawa L, Stanis G, Dick AJ, Wright GA (2013) Quantification of fibrosis in infarcted swine hearts by ex vivo late gadolinium-enhancement and diffusion-weighted MRI methods. *Physics in Medicine and Biology* 58 (15):5009-5028. doi:10.1088/0031-9155/58/15/5009
 26. Kim RJ, Fieno DS, Parrish TB, Harris K, Chen EL, Simonetti O, Bundy J, Finn JP, Klocke FJ, Judd RM (1999) Relationship of MRI delayed contrast enhancement to irreversible injury, infarct age, and contractile function. *Circulation* 100 (19):1992-2002
 27. Amado LC, Gerber BL, Gupta SN, Rettmann DW, Szarf G, Schock R, Nasir K, Kraitchman DL, Lima JA (2004) Accurate and objective infarct sizing by contrast-enhanced magnetic resonance imaging in a canine myocardial infarction model. *Journal of the American College of Cardiology* 44 (12):2383-2389. doi:10.1016/j.jacc.2004.09.020

Chapter 4



Real-Time correction of respiratory induced cardiac motion during electro-anatomical mapping procedures

Medical & Biological Engineering & Computing 2016 pp1-9

René van Es¹, Frebus J. van Slochteren^{1,2}, Sanne J. Jansen of Lorkeers¹, Roos Blankena^{1,3}, Pieter A. Doevendans¹, Steven A.J. Chamuleau¹

¹ Department of Cardiology, University Medical Center Utrecht, The Netherlands

² Interuniversity Cardiology Institute of the Netherlands (ICIN), Utrecht, The Netherlands

³ Faculty of Science and Technology, Department of Technical Medicine, University of Twente, Enschede, The Netherlands

ABSTRACT

Introduction

Treatment planning during catheter interventions in the heart is often based on electromechanical tissue characteristics obtained by endocardial surface mapping (ESM). Since studies have shown respiratory induced cardiac motion of over 5mm in different directions, respiratory motion may cause ESMs artifacts due to faulty interpolation. Hence, we designed and tested a real time respiration-correction algorithm for ESM.

Methods

An experimental phantom was used to design the correction algorithm which was subsequently evaluated in 5 pigs. A piezo respiratory belt transducer was used to measure the respiration. The respiratory signal was inserted to the NOGA[®]XP electromechanical mapping system via the ECG leads. The results of the correction were assessed by measuring the displacement of a reference point and the registration error of the ESM on a CMR scan before and after correction.

Results

In the phantom experiment, the reference point displacement was 6.5mm before and 1.1mm after correction, the registration errors were 2.8 ± 2.2 mm and 1.9 ± 1.3 mm respectively. In the animals the average reference point displacement (apex) was reduced from 2.6 ± 1.0 mm before to 1.2 ± 0.3 mm after correction ($P < 0.05$). The in vivo registration error of the ESM and the CMR scan did not significantly improve.

Conclusion

Even though the apical movement appreciated in pigs is small, the correction algorithm shows a decrease in displacement after correction. Application of this algorithm omits the use of the time consuming respiratory gating during ESM, and may lead to less respiratory artifacts in clinical endocardial mapping procedures.

INTRODUCTION

Treatment planning during catheter interventions in the heart is often based on electromechanical tissue characteristics^{1,2} obtained by endocardial surface mapping (ESM). ESM systems determine the exact, real time 3 dimensional (3D) location of the catheter tip inside the heart using an electrical or magnetic field, induced in the thorax of the patient^{2,3}. Measurements of the local depolarization potentials and relative cardiac wall motion are performed on the endocardium and stored with their respective 3D locations to create a 3D reconstruction of the endocardium. Data is interpolated in the areas that are spatially located between the acquired mapping points to reconstruct a continuous endocardial surface.

During the ESM procedure the patient is usually awake and breathing freely. Respiratory induced cardiac motion (RICM) leads to spatial errors in the ESM. A low spatial resolution of ESM together with the RICM induced spatial artifacts may cause inaccurate positioning of endocardial ablations or intramyocardial injections in the context of cardiac regenerative therapy. Studies in patients using different cardiac imaging modalities report RICM ranging up to a centimeter during free breathing, mainly in the caudal-cranial direction⁴⁻⁸. Since a sub-centimeter precision is often required for effective therapy, a technique to overcome interference of RICM during ESM procedures is desirable.

Fusion of ESM data with surface meshes obtained from pre-procedurally acquired 3D imaging data from e.g. CMR or SPECT/CT has recently gained more interest in order to optimize catheter interventions⁸⁻¹³. Since registration of the imaging modalities is done using landmark or surface registration, minimization of the spatial error is of great importance. RICM artifacts can lead to a misalignment in the registration process, therefore compensation for RICM without the use of respiratory gating¹⁴ will reduce procedure time and improve registration accuracy.

In this study we introduce a novel technique to correct for the effect of RICM during ESM procedures without the need for respiratory gating. The NOGA®XP (Biosense Webster, Cordis, Johnson & Johnson, version 1.1.43) intramyocardial injection system was used which provides a 3D magnetic tracking of the catheter and measurement of local electrical and mechanical tissue characteristics. Since the NOGA®XP system is not able to measure respiration a simple add-on was developed to enable respiratory registration through available electro cardiogram (ECG)-leads.

We identified the effect of RICM on the ESM accuracy during mapping procedures by comparing ESM data with gold standard CMR derived surface meshes in a porcine study. The goal was twofold: 1) to minimize RICM artifacts in constructed ESM and 2) to decrease the registration error in the fusion of ESMs with CMR.

METHODS

Respiration and NOGA measurements

A piezo respiratory belt transducer (UFI Model 1132 Pneumotrace II™) was connected to an ECG input of the NOGA®XP system (Figure 1). The respiratory signal was represented on the NOGA®XP system as a baseline shift of the connected ECG channel. Prior to the experiment

the potentiometer in the device was adjusted so that the connected ECG channel showed a clear baseline drift. The NOGA®XP system stores end diastolic 3D location of each acquired location in the local database using the build-in ECG R-wave triggering. The NOGA®XP system records a 12-lead ECG with a length of 2.5s per measured point. The sample rate of the signal is 1 kHz. The NOGA®XP ECG filter settings were optimized to allow visualization of respiratory signals in the 0.05-0.5Hz range. An external computer was used to access the ECG data on the NOGA®XP system via a shared folder. The NOGA®XP database was accessed through a SQL-server with read-only permissions.

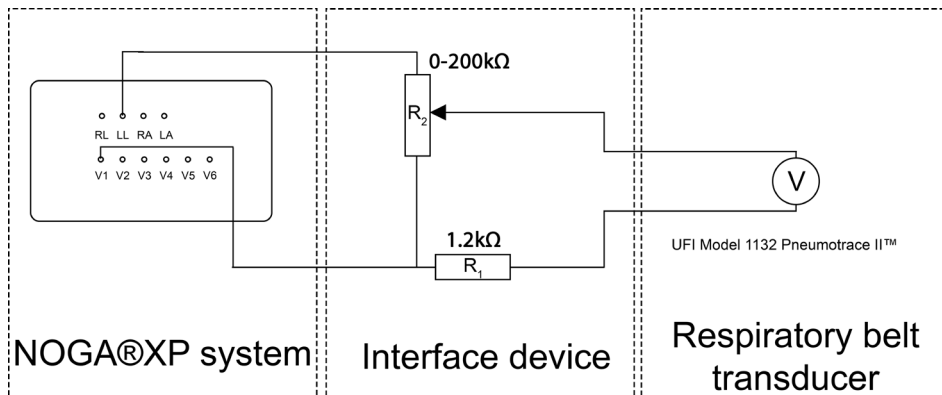


Figure 1 Circuit of the system used to connect a respiratory belt transducer to the ECG leads of Noga®XP system to instigate ECG baseline drift in the V1 ECG channel. The interface device used to alter the voltage, delivered by the respiratory belt transducer, is shown in the center panel. The interface device is connected to the left leg (LL) and V1 ECG channels on the NOGA®XP P PUI box. The respiratory belt transducer is connected to the interface device using a regular BNC connector.

Phantom experiment

A non-rotational symmetric bottle was mapped from the inside in a stationary position. Thereafter, the phantom was mounted on a test lung that was connected to a ventilator. The ventilator tidal volume was set to induce a 15mm motion of the phantom in primarily one direction. To acquire a reference measurement, the 7 French NOGA®XP mapping catheter (Biosense Webster, Cordis, Johnson & Johnson, Diamond Bar, USA) was fixed to the phantom while ventilating the test lung. Hereafter the phantom was mapped on the inside while ventilating the test lung. During the mapping procedures an ECG simulator was connected to the NOGA®XP system to enable triggered data acquisition. The ECG simulator was set to simulate normal sinus rhythm at 80 beats/minute.

Porcine experiments

All animal experiments were conducted in accordance with the national guidelines on animal care and with prior approval by the Animal Experimentation Committee of the Faculty of Medicine, Utrecht University, the Netherlands. Five female Dallas land race pigs were subjected

to a 90 minute left anterior descending balloon occlusion and subsequent reperfusion 8 weeks before the measurements.

A respiratory belt transducer was attached around the abdomen in the sub-thoracic region, where maximal respiratory induced abdominal movement could be measured. The transducer was connected to the ESM system as described before. The ventilator was set to a frequency of 12 breaths per minute with a tidal volume of 800ml and a 2:1 expiration to inspiration ratio. The NOGA®XP catheter was inserted into the left ventricle (LV) via the left carotid artery and retrograde passage through the aortic valve. First, the catheter was positioned in the LV apex and a reference measurement was performed containing at least 60 measurements to assure measurements in all phases of the respiratory cycle. Secondly, in an independent procedure, a complete map of the LV was made. After the mapping procedures a CMR scan was made. The animals were euthanized after finishing the experiments.

CMR

In vivo CMR was performed under anesthesia on a clinical 3T scanner (Achieva TX, Philips Healthcare, Best, the Netherlands) with a 32-channel receiver coil. ECG-gated Cine images were made with Voxel size = 2x2mm, Flip Angle = 45 degrees, Slice Thickness = 8mm, Field of view = 320x320mm, Repetition time [TR] = 3.2ms, Echo Time [TE] = 1.6ms, and 30 Phases/R to R interval. End-diastolic frames of the Cine images were segmented using the freely available software Segment version 1.9 R3262 (<http://segment.heiberg.se>)¹⁵. An end diastolic endocardial surface mesh was generated and used for the registration of the NOGA®XP mapping points. The mesh creation and registration was performed using the in-house developed 3D CartBox and was based on a standard rotation and translation followed by an angle limited iterative closest point procedure and manually corrected if necessary¹³.

Correction algorithm

A detailed overview of the correction algorithm is shown in Figure 2. As a first step a reference measurement was performed to assess the RICM. In the phantom experiment the catheter tip was mounted at a fixed surface location during movement of the phantom. In the *in vivo* experiments the catheter was positioned in the LV apex during the reference measurements. In both experiments at least 60 measurements were used for the reference measurement. It was assured that points and measurements were located in every phase of the respiratory cycle. Storage of the 3D location of the catheter-tip is triggered at t=2s in the stored ECG. For the respiratory analysis, the ECG signal containing the respiratory data was fitted with a 5th order polynomial function over the 1.5-2.5s interval to eliminate R-wave artifacts and signal noise (MATLAB 2013a version 8.1, The MathWorks Inc.). The data was split into an inspiratory and expiratory part based on the slope (θ) of the respiratory signal at t=2s (Figure 2A). For both parts the position is defined in the X, Y, and Z direction.

For each direction a 2nd order polynomial function is fitted using a least squares approach (Eq.1) (e.g. Figure 3B, E). The six resulting functions were thereafter used during the mapping procedure to calculate the correction of every acquired point based on the value (ξ) and θ of the respiratory signal (Eq.2).

$$f_c = ax^2 + bx + c \quad (\text{Eq.1})$$

Equation 1. The 2nd order polynomial function that was used to fit the data acquired during the reference measurement. This was done for each direction for both the inspiratory and expiratory data. f_c represents the measured values in, parameters a , b and c are determined and used to subsequently calculate the correction during the mapping procedure.

$$\begin{bmatrix} X_c \\ Y_c \\ Z_c \end{bmatrix} = \begin{bmatrix} X_m \\ Y_m \\ Z_m \end{bmatrix} - \begin{bmatrix} f_x(\xi) \\ f_y(\xi) \\ f_z(\xi) \end{bmatrix} \quad (\text{Eq.2})$$

Equation 2. The equation that was used to correct the acquired mapping data, $f_x(\xi)$ represents the polynomial function best fitting the X-coordinate data from the reference measurement shown in Eq.1, ξ represents the y-value measured in the normalized respiratory signal. The corrected and measured X- coordinate is represented by X_c and X_m , respectively.

Analysis and statistics

The algorithm is used to relocate measurement points to their location at maximal expiration. To assess the effects of the RICM correction, the root mean squared error (RMSE) of the geometrical distance from all points of the reference measurement to the point acquired at maximal expiration was calculated. The same end-expiratory location was used for both the uncorrected and corrected RMSE. Maximal apical displacement represents the maximal range of all apical locations during the reference measurement, i.e. the distance between the point at maximal expiration and the point furthest from that. Both RMSE and the maximal apical displacement are expressed in mm. The registration error is calculated as mean distance of each mapping point to the CMR end diastolic endocardial surface mesh after registration of the NOGA®XP ESM with the endocardial surface mesh generated from CINE CMR. The registration error is expressed as mean \pm standard deviation in millimeters. Paired t-tests were used to compare original with corrected data, $p < 0.05$ was considered to be statistically significant.

RESULTS

Respiratory Registration

Recording respiratory signals on a precordial ECG lead was performed successfully. The respiratory induced baseline shift in ECG lead V1 during the phantom and *in vivo* experiments is shown in Figures 3A and 3D, respectively.

Phantom experiment

In the motionless phantom 142 position were mapped, in the moving phantom 70 and 118 points were respectively acquired during the reference and mapping measurements. In the reference measurement the derived motion of the phantom was 15mm in the Z direction and 2mm in the

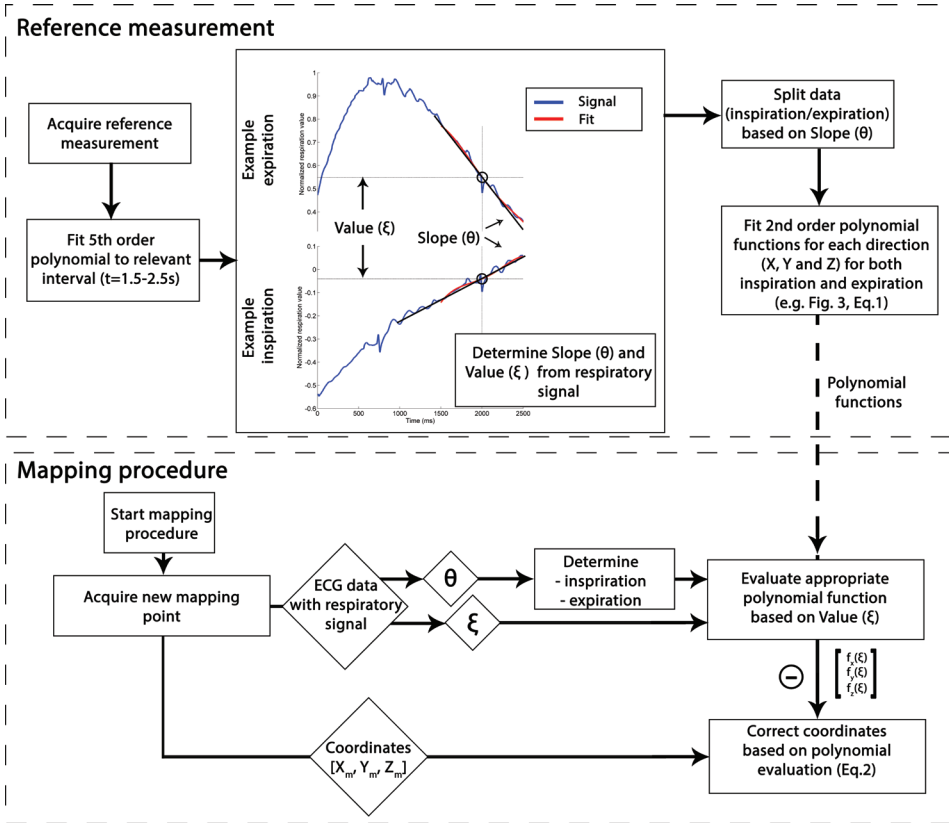


Figure 2 The upper panel shows the flow chart of the algorithm that was used to determine the correction parameters from the reference measurement. The bottom how these parameters were used to correct acquired point during the mapping procedure. θ =slope, ξ =y-value, X_m = measured coordinate.

X and Y directions (Figure 3B). The result of the correction algorithm on the motion of the reference measurement is shown in Figure 3C. The registration error of the ESM on the CMR was 2.0 ± 1.4 mm when no respiratory motion was applied to the phantom (Figure 4A). With motion, the registration error was 2.8 ± 2.2 mm before and 1.9 ± 1.3 mm after correcting for the motion (Figure 4B, 4C and 5B, Table 1). The RMSE in the reference measurement was 6.5 mm before and 1.1 mm after correction (Figure 5A).

Porcine experiments

In five animals (83 ± 6 kg) on average 91 (range: 75-101) reference points were acquired in the apex, the mean number of points in the left ventricular maps was 80 (range: 63-90). In four animals the baseline shift in the respiratory signal was successfully recorded. The RICM correction algorithm was able to correct for the respiratory induced apical movement (Figure 5A, Table 1). The average apical displacement (RMSE) was reduced by 51 % from 2.6 ± 1.0 mm before to 1.2 ± 0.3 mm after correction ($p < 0.05$). The maximal apical displacement was reduced

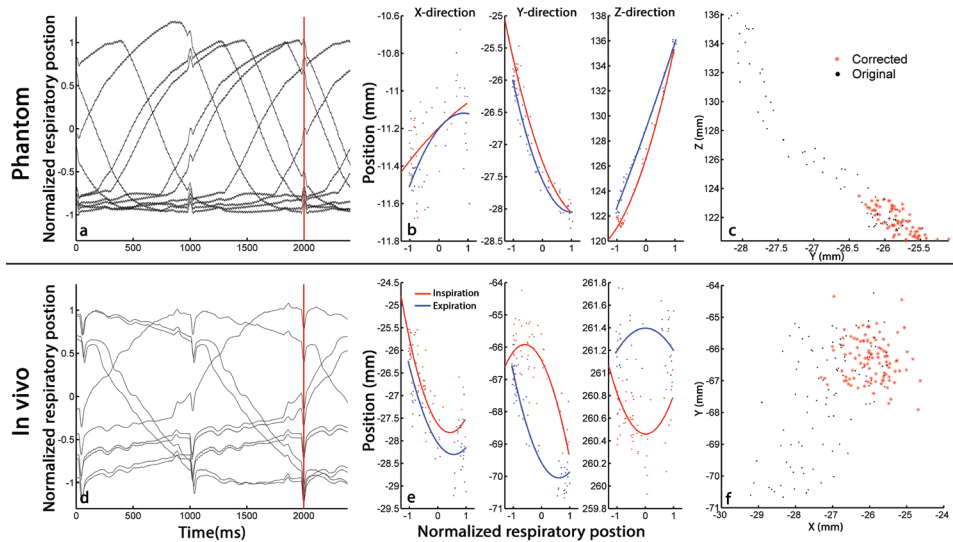


Figure 3 **a/d** Example of the first 10 registered respiratory signals recorded on the precordial ECG V1 lead in the phantom and *in vivo* experiments, respectively. The respiratory position is determined at time point $t=2s$ (red line), the end-diastolic phase (R-wave). **b/e** The recorded 3-dimensional (X,Y and Z) data of all ($n=77$ and $n=100$, respectively) mapped reference points with the fitted 2nd order polynomial functions for inspiration (red) and expiration (blue). Note the differences in scale on the vertical axis. **c/f** Reference measurement before (black) and after correction (red). This is a 2-dimensional representation of the 3D data in the two directions that show the largest variation.

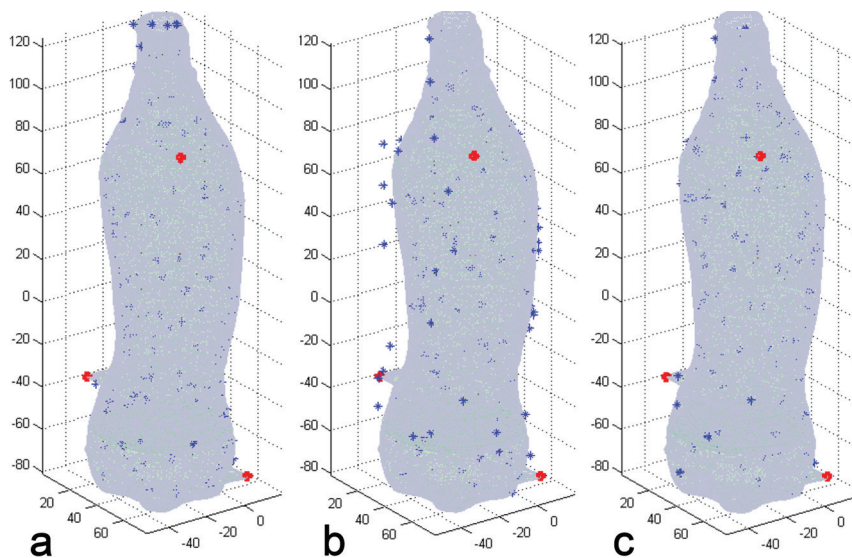


Figure 4 **a** The registration of acquired ESM points (blue) to the MRI derived surface mesh (light blue) where no motion was applied to the phantom. Landmark points (red) were fixed to the external surface of the phantom (registration error $2.0 \pm 1.4mm$). **b** The uncorrected registration with applied motion (registration error $2.8 \pm 2.2mm$). **c** The corrected registration with applied motion (registration error $1.9 \pm 1.3mm$).

by 34% from 3.7 ± 1.1 mm before to 2.3 ± 0.5 mm after correction ($p=0.09$). A representative example of acquired apical reference points is shown in Figure 3F. The registration error was not significantly ($p=0.62$) reduced from 3.8 ± 0.5 mm to 3.7 ± 0.4 mm (mean \pm SEM) after correction.

Table 1 Individual results of all experiments

	Apex movement RMSE(mm)		Apex maximal displacement (mm)		Registration error (mm)	
	Original	Corrected	Original	Corrected	Original	Corrected
Phantom	6.5	1.1	14.0	2.02	2.8 ± 2.2	1.9 ± 1.2
Animal#1	2.3	1.0	3.4	1.95	4.6 ± 2.2	4.4 ± 2.0
Animal#2	1.3	0.9	2.6	1.67	3.6 ± 1.6	3.8 ± 1.5
Animal#3	2.7	1.6	5.5	2.62	3.6 ± 1.7	3.3 ± 1.4
Animal#4	4.1	1.7	3.3	3.06	3.3 ± 1.6	3.4 ± 1.7

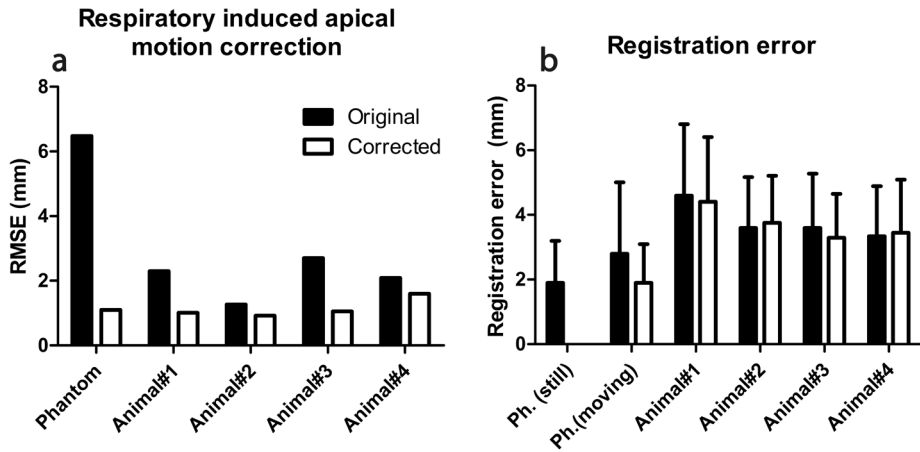


Figure 5 **a** The RMSE error of the reference measurement before and after correction. **b** The registration error of the ESM map and the MRI derived endocardial surface mesh before and after correction. The phantom where no motion was applied (Ph. still) was not corrected. Ph. = phantom

DISCUSSION

Measuring RICM with the NOGA®XP system is feasible using our in-house developed customized interface. In a phantom experiment, the correction algorithm showed to be effective in reducing the RMSE of the reference measurement and the registration error of the NOGA®XP ESM and the CMR dataset. In the porcine experiments RICM of the LV apex was smaller than values reported in human studies. Our correction algorithm is however capable to significantly reduce (34%) the apical displacement throughout the respiratory cycle. The reduction in registration error of corrected ESM data on the CMR data was minimal. This most likely is due to the minimal amount of RICM observed in this porcine model. One animal was excluded from analysis due to a malfunctioning respiration transducer.

Multiple studies into RICM report movement of the human heart in the range of one centimeter⁴⁻⁸. In the present study, the maximal apical displacement measured was 3.7 ± 1.1 mm. An explanation for this difference might be found in the difference of thoracic anatomy between humans and pigs. The thoracic anatomy of the pig might lead to reduced RICM. Furthermore, to explore the RICM of pigs we setup a single experiment in which we increased the tidal volume. We observed a 120% increase (3.3 to 7.3 mm) of RICM (maximal apical displacement) of the apex upon a 20% increase (800 to 950 ml) in tidal volume. Although a tidal volume of 800 ml was used during the experiments the design and validation of the RICM algorithm can be done accurately with the used setup.

Multiple commercially available ESM systems offer the option to use respiratory gating in addition to ECG gating during ESM procedures. This inevitably leads to longer procedure times since mapping points are only acquired during a short phase of the respiratory cycle, usually the end-expiratory phase¹⁴. Furthermore, respiratory gating in free breathing patients may be unreliable since respiratory cycles are never identical. This leads to different residual volumes and thus to different positions of the heart during end-expiration. Our respiratory correction algorithm allows the acquisition of mapping points during the whole respiratory cycle. By uncoupling inspiration and expiration, and take both the slope (θ) and value (ξ) into account during the analysis, the algorithm is able to minimize problems associated with breath to breath variability in tidal volume. Since the algorithm depends on reference measurements, subject specific breathing characteristics, such as depth and rate of breathing, are considered in the algorithm. Additionally, using these characteristics, abnormal breaths during the mapping procedure can be identified automatically and excluded if necessary.

Data acquisition

Acquiring respiration data with the NOGA®XP system using ECG input ports is feasible since our customized device uses only one of the precordial leads (e.g. V1), which are often unused during mapping/injection procedures. The use of an ECG lead as an input for the respiratory signal ensures synchronicity of the stored signals and location data. For use in a clinical setting a dedicated solution is desirable to allow different settings of, for example, the filter settings. In this study, no difficulties in visualizing neither the ECG signals nor the respiratory signals were found.

Limitations

All experiments were performed with the animal connected to a ventilator, therefore respiration curves were predictable and similar throughout the entire procedure. RICM in the porcine model is minimal, and as a result it is difficult to predict the effect of RICM on the registration error in a clinical situation.

Clinical perspective

Many imaging modalities, such as late gadolinium enhancement CMR, provide detailed information about the infarct location and its characteristics. Combining or fusing ESM data with for example late gadolinium enhancement CMR may improve therapeutic outcome^{9,10,13}. The registration error between ESMs and for example MRI data is typically around 3mm in animals and humans (e.g. $3.22 \pm 1.86 \text{ mm}$ ¹³ and $3.8 \pm 0.6 \text{ mm}$ ¹⁶, respectively). Since RICM in patients is often much larger⁴⁻⁸, correction of RICM will probably lead to fewer registration artifacts and therefore to more accurate multimodality catheter diagnosis and treatment. The validation of the correction algorithm in this study was performed retrospectively. However, the correction algorithm is intended to be used in real time during ESM mapping procedures. For example, the reference measurement takes about 1-2 minutes, calculating parameters needed for the subsequent procedure requires less than 2 seconds on a modern computer. During the actual mapping procedure, calculating the correction for a single acquired point requires a few milliseconds. Use of the correction algorithm in real time will therefore not affect the length of the ESM procedure.

CONCLUSION

The correction of RICM during ESM procedures by our correction algorithm is feasible and can be incorporated in commercially available systems. In contrast to the phantom experiments, the suggested RICM correction method was of less additional value during porcine experiments due to minimal RICM in the porcine model. Nevertheless, during patient procedures RICM correction can be of additional value to obtain an anatomically correct map and allow a more optimal registration with respiratory gated cardiac imaging data. A new clinical study must be performed to investigate the clinical benefit of RICM correction.

Acknowledgments

We kindly acknowledge Grace Croft, Marlijn Jansen, Evelyn Velema, Joyce Visser, Merel Schuurink, Martijn van Nieuwburg and Gerard Marchal for their assistance with the animal experiments. We would like to thank Joep van Oorschot, Jaco Zwanenburg and Martijn Froeling for performing the CMR experiments.

REFERENCES

1. de Groot NM, Bootsma M, van der Velde ET, Schalij MJ: Three-dimensional catheter positioning during radiofrequency ablation in patients: first application of a real-time position management system. *J Cardiovasc Electrophysiol* 2000; 11:1183–1192.
2. Ben-Haim S a, Osadchy D, Schuster I, Gepstein L, Hayam G, Josephson ME: Nonfluoroscopic, in vivo navigation and mapping technology. *Nat Med* 1996; 2:1393–1395.
3. Wittkampf FH, Wever EF, Derksen R, Wilde a a, Ramanna H, Hauer RN, Robles de Medina EO: LocaLisa: new technique for real-time 3-dimensional localization of regular intracardiac electrodes. *Circulation* 1999; 99:1312–1317.
4. Shechter G, Ozturk C, Resar JR, McVeigh ER: Respiratory Motion of the Heart From Free Breathing Coronary Angiograms. *IEEE Trans Med Imaging* 2004; 23:1046–1056.
5. Jagi R, Moran JM, Kessler ML, Marsh RB, Balter JM, Pierce LJ: Respiratory Motion of The Heart and Positional Reproducibility Under Active Breathing Control. *Int J Radiat Oncol Biol Phys* 2007; 68:253–258.
6. Holland E, Goldfarb W, Edelman R: Diaphragmatic and Cardiac Motion during Suspended Breathing : Preliminary Experience and Implications for Breath-hold. :483–489.
7. Qi XS, White J, Rabinovitch R, Merrell K, Sood A, Bauer A, Wilson JF, Miften M, Li XA: Respiratory organ motion and dosimetric impact on breast and nodal irradiation. *Int J Radiat Oncol Biol Phys* 2010; 78:609–617.
8. Roujol S, Anter E, Josephson ME, Nezafat R: Characterization of respiratory and cardiac motion from electro-anatomical mapping data for improved fusion of MRI to left ventricular electrograms. *PLoS One* 2013; 8:1–9.
9. Tao Q, Milles J, Van Huls Van Taxis C, Lamb HJ, Reiber JHC, Zeppenfeld K, Van Der Geest RJ: Toward magnetic resonance-guided electroanatomical voltage mapping for catheter ablation of scar-related ventricular tachycardia: A comparison of registration methods. *J Cardiovasc Electrophysiol* 2012; 23:74–80.
10. Reddy VY, Malchano ZJ, Holmvang G, Schmidt EJ, D’Avila A, Houghtaling C, Chan RC, Ruskin JN: Integration of cardiac magnetic resonance imaging with three-dimensional electroanatomic mapping to guide left ventricular catheter manipulation: Feasibility in a porcine model of healed myocardial infarction. *J Am Coll Cardiol* 2004; 44:2202–2213.
11. Dickfeld T, Tian J, Ahmad G, Jimenez A, Turgeman A, Kuk R, Peters M, Saliaris A, Saba M, Shorofsky S, Jeudy J: MRI-Guided ventricular tachycardia ablation: integration of late gadolinium-enhanced 3D scar in patients with implantable cardioverter-defibrillators. *Circ Arrhythm Electrophysiol* 2011; 4:172–184.
12. Dauwe DF, Nuyens D, De Buck S, et al.: Three-dimensional rotational angiography fused with multimodal imaging modalities for targeted endomyocardial injections in the ischaemic heart. *Eur Heart J Cardiovasc Imaging* 2014; 15:900–907.
13. Van Slochteren FJ, Van Es R, Koudstaal S, et al.: Multimodality infarct identification for optimal image guided intramyocardial stem cell injections. *Netherlands Hear J* 2014; 22:493–500.
14. Beinart R, Kabra R, Heist KE, Blendea D, Barrett CD, Danik SB, Collins R, Ruskin JN, Mansour M: Respiratory compensation improves the accuracy of electroanatomic mapping of the left atrium and pulmonary veins during atrial fibrillation ablation. *J Interv Card Electrophysiol* 2011; 32:105–110.
15. Heiberg E, Sjögren J, Ugander M, Carlsson M, Engblom H, Arheden H: Design and validation of Segment—freely available software for cardiovascular image analysis. *BMC Med Imaging* 2010; 10:1.
16. Wijnmaalen AP, Van Der Geest RJ, Van Huls Van Taxis CFB, Siebelink HMJ, Kroft LJM, Bax JJ, Reiber JHC, Schalij MJ, Zeppenfeld K: Head-to-head comparison of contrast-enhanced magnetic resonance imaging and electroanatomical voltage mapping to assess post-infarct scar characteristics in patients with ventricular tachycardias: Real-time image integration and reversed registration. *Eur Heart J* 2011; 32:104–114.

Disclosure of potential conflicts of interest

This research forms part of the Project P1.04 SMARTCARE of the research program of the BioMedical Materials Institute, co-funded by the Dutch Ministry of Economic Affairs, Agriculture and Innovation. The financial contribution of the Nederlandse Hartstichting (NHS) is gratefully acknowledged. Author F.J. van Slochteren is cofounder of CART-Tech B.V..

Ethical approval: "All applicable international, national, and/or institutional guidelines for the care and use of animals were followed."

Chapter 5



Intramyocardial therapy: A novel accurate and fast method to target the infarct border zone

Submitted

René van Es¹, Hans T van den Broek ¹, Mira van der Naald¹, Leon de Jong^{1,2}, Eliane Nieuwenhuis^{1,2}, Adriaan O. Kraaijeveld¹, Pieter A. Doevendans^{1,3}, Steven A.J. Chamuleau¹, Frebus J. van Slochteren¹

¹ Dept of Cardiology, Div Heart and Lungs, University Medical Center Utrecht, The Netherlands

² MIRA Institute for Biomedical Engineering and Technical Medicine, University of Twente, Enschede, The Netherlands

³ Netherlands Heart Institute, Utrecht, The Netherlands

ABSTRACT

Objectives

In this study we have compared the clinical standard for intramyocardial injections, the NOGA system, with CARTBox2 in terms of injection accuracy into the infarct border zone (IBZ), procedure time, fluoroscopy time and dose, and arrhythmogenicity.

Background

For the optimal application of cardiac regenerative therapy in ischemic heart disease, targeting of the correct location to perform intramyocardial injections is of the utmost importance. The general consensus is that this treatment is best delivered to the IBZ. We have developed software that enables the visualization of MRI defined targets on live fluoroscopic images.

Methods

Ten pigs (60-75kg) were subjected to a 90 minute balloon occlusion of the LAD. Four weeks later, a late gadolinium enhanced (LGE) MRI scan was performed. Subsequently, 10-16 injections were delivered in the IBZ using either the NOGA system or CARTBox2. The primary endpoint was the distance of the injections to the IBZ. Secondary endpoints were total procedure time, fluoroscopy time and dose and number of ventricular arrhythmias.

Results

The average distance of the injections to the IBZ was similar for NOGA (-0.7 ± 2.2 mm) and CARTBox2 (0.5 ± 3.2 mm), ($p=ns$). The procedure time with CARTBox2 (69 ± 12 minutes) was significantly shorter than with NOGA (150 ± 12 minutes) ($p < 0.001$). The fluoroscopy time with NOGA (18.7 ± 11.0 minutes) was significantly lower than with CARTBox2 (43.4 ± 6.5 minutes; $p = 0.0003$). Procedures with CARTBox2 caused less ventricular arrhythmias than NOGA ($p=ns$).

Conclusions

CartBox2 is an accurate and fast vendor independent system to facilitate intramyocardial injections based on gold standard non-invasive LGE-MRI fibrosis imaging.

INTRODUCTION

Trans-endocardial delivery of stem cells or other therapeutic products in the context of cardiac regenerative therapy for the treatment of ischemic heart disease (IHD) has become increasingly popular.^{1,2} It is generally accepted that the best location to inject such products is the infarct border zone (IBZ).^{3,4} Currently the NOGA®XP platform (Biosense Webster Cordis, Johnson & Johnson, USA) is the clinical standard to perform intramyocardial injections.⁵

The NOGA system is used to create a map of the left ventricle (LV) using a dedicated catheter which is equipped with a tip coil to provide 3D magnetic tracking and navigation.⁶ Whilst navigating over the LV endocardial wall, measurements of unipolar and bipolar depolarization voltages and local wall deformation (local linear shortening) are performed. The 3D map, containing these parameters, is constructed by acquiring at least 60 homogeneously spread measurements (mapping points) over the LV endocardium.⁷ Subsequently, these parameters are used to determine the location of the infarct and the IBZ, and a target line is defined to emphasize the region of interest during the injection procedure.

Accurate identification of the infarct and IBZ is crucial for the effectiveness of cell therapy. Multiple studies have compared NOGA with other imaging modalities to investigate the ability of NOGA to accurately identify the infarct and IBZ.⁸⁻¹⁰ The overlap between NOGA acquired maps and gold standard late gadolinium enhanced (LGE) MRI is often suboptimal, especially in the IBZ.⁸ Moreover, the NOGA system requires the use of expensive catheters, extensive user training and is time-consuming. To overcome this problem, multiple approaches have been taken to enable intramyocardial injections without using the NOGA system, these systems are usually based on other imaging modalities (e.g. LGE-MRI, SPECT/CT or PET).^{11,12} These systems however, rely on an external online system to fuse and visualize the relevant data onto live X-ray fluoroscopy (XRF) images during the injection procedure.

We have designed the CARTBox2 (CB2) software that is XRF- and catheter-vendor independent and facilitates treatment planning for intramyocardial injections based on LGE-MRI. CB2 processes the LGE-MRI dataset and provides a treatment dataset which contains the targets for injections as well as anatomical information, and can be fused with XRF. Thereby, CB2 enables gold standard LGE-MRI images to be visualized on real-time XRF images. In a porcine model of myocardial infarction we compared CB2 with the NOGA system in terms of injection accuracy to target the IBZ, total XRF time and dose, procedure time and arrhythmogenicity.

METHODS

Animals

All experiments were performed in accordance with the “Guide for the Care and Use of Laboratory Animals” prepared by the Institute of Laboratory Animal Resources and with prior approval by the Animal Experimentation Committee of the Faculty of Medicine, Utrecht University, the Netherlands.

For this study, 14 six months old female Daland landrace pigs (60-75kg) were subjected to a myocardial infarction by a 90 minute occlusion of the left anterior descending (LAD) artery distal

to the second diagonal branch, according to a previously described protocol.¹³ After ischemia/reperfusion, the animals were housed in stables for four weeks and checked daily by the veterinary staff. Pigs were randomized to undergo endocardial injections in the IBZ using either the NOGA system or CB2 (Figure 1).

Prior to ischemia/reperfusion (I/R) all animals were pre-treated with amiodarone for 10 days (1200mg/day), clopidogrel for 3 days (75mg/day), acetylsalicylic acid for 1 day (320mg) and a 5mg buprenorphine patch for 1 day. After I/R, amiodarone, clopidogrel and acetylsalicylic acid were continued until the end of the study in daily doses of 800mg, 75mg and 80mg, respectively. The buprenorphine patch was removed after 6 days.

At the start of both the I/R and injection procedure, anesthesia was induced by an intramuscular injection of ketamine (10mg/kg), midazolam (0.4mg/kg) and atropine (0.5mg). After intubation and transport to the operating theater maintenance anesthesia was set to continuous infusion of 0.5 mg/kg/h midazolam, 2.5 µg/kg/h sufentanil and 0.1 mg/kg/h pancuronium. Before starting the procedures, 300 mg amiodarone and heparin (100 IE/kg after positioning the sheaths and 50 IE/kg every 2 hours) were administered. Pigs were mechanically ventilated with a positive pressure ventilator with FiO₂ 0.5, 10ml/kg tidal volume and a frequency of 12/minute under continuous capnography. An additional arterial line was inserted in a small peripheral artery in the hind limb for continuous stable arterial pressure monitoring.

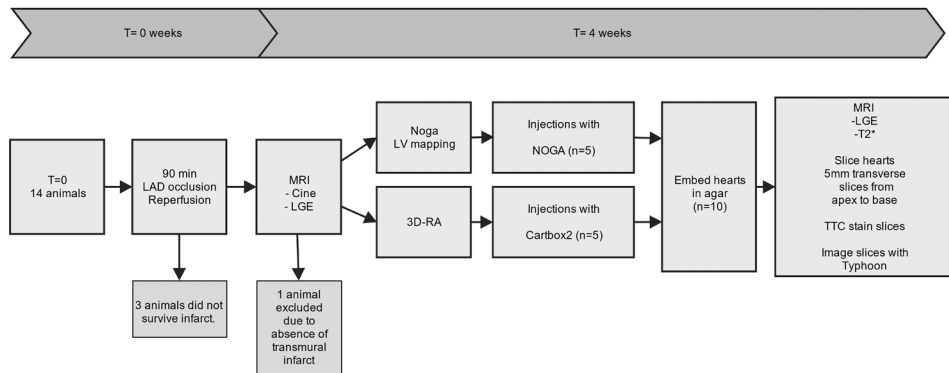


Figure 1. Experimental study design

A total of 14 animals were subjected to a myocardial infarction, ten animals underwent the injection procedure. Five animals were randomized into the NOGA-arm, whilst 5 animals were randomized to the CARTBox2 group. All ten hearts were embedded and analyzed.

Ischemia/reperfusion injury

The internal carotid artery was accessed through an 8F sheath. The internal diameter of the LAD artery was measured after the second diagonal branch in both an anterior-posterior and left anterior oblique view using XRF. A suitable percutaneous coronary intervention (PCI) balloon was positioned after the second diagonal branch and inflated for 90 minutes. XRF was used to confirm proper positioning and occlusion of the balloon. In case of cardiac arrhythmias amiodarone

(150 mg, up to 3 boli) and if necessary adrenaline were infused and the animal was defibrillated using 150-200J biphasic shocks with intermittent chest compressions until return of return of spontaneous circulation.

Pre and peri injection procedure

Four weeks after I/R, before the injection procedure, all animals underwent an MRI scan to visualize the infarct and IBZ (MRI parameters are listed in the supplementary data). For the injections we used a mixture of 10% ureido-pyrimidinone gel, super paramagnetic iron oxide (SPIO) particles (15µg/ml; Sinerem, Guerbet, France) and fluorescent beads (10.000 beads/ml, 580/em605, Molecular Probes Invitrogen).¹⁴⁻¹⁶ In each animal 10-16 injections were deployed, and per injection 0.2ml of the mixture was injected.

Successful insertion of the injection needle into the endocardium was defined as the creation of an extra-systole on the ECG signals upon needle ejection. Needle depth was set to half of the myocardial wall thickness in the IBZ measured on MRI. In case of cardiac arrhythmias 150mg of amiodarone was infused.

Ventricular arrhythmia monitoring

In the last 8 animals that entered the study, ECG leads of a Holter device (Fysiologic ECG Services, Amsterdam, The Netherlands) were attached to the chest of the animals to enable continuous recording of leads V1 and V5 during the mapping and injection procedures. ECG recordings were analyzed by two investigators. For the mapping procedure and each separate injection, the total number of premature ventricular contractions (PVCs), non-sustained ventricular tachycardias (VTs) and sustained VTs were counted. A PVC was defined as a single ectopic complex, a doublet was counted as 2 PVCs. Non-sustained VTs were defined as 3 or more consecutive ventricular complexes with a frequency more than 100/min with a total duration shorter than 30 seconds. Sustained VTs were defined as a VT with a total duration more than 30 seconds.

NOGA mapping and injection procedure

In the NOGA group an 8F sheath was placed in the right femoral artery. Under XRF guidance, the NOGAStar® mapping catheter (Biosense Webster) was introduced into the LV after retrograde passage through the aortic valves. Using the NOGA system (SW version 1.1.43), at least 100 points were mapped covering the complete LV endocardium. After the mapping procedure, the infarct was identified by setting bipolar voltages maps to a range of 0.5-1.5mV. The maps were filtered to remove internal points. A design line (preferred injection location) was manually drawn on the 1mV area (green) around the infarct using the NOGA system software. Subsequently, the Myostar® (Biosense Webster) injection catheter was introduced into the LV. Injections were targeted to this virtual line. All injections were marked in the NOGA map.

CARTBox2

Preparation

In the CARTBox 2 group, endo- and epicardial contours were manually segmented in the LGE-MRI images using the freely available software Segment version 2.0 R4265 (<http://segment.org>).

heiberg.se).¹⁷ Subsequently, the infarct was automatically segmented with Segment based on the Full Width at Half Maximum algorithm (Figure 2). With CB2, in the segmented LGE-MRI images, the preferred injection position was defined as the 1-20% transmural infarcted zone around the infarct. Sixteen targets, equally distributed over the septal and anterior side of the infarct, were manually selected and programmed into DICOM images using CB2. A 3D rotational angiography (3D-RA) roll scan was performed (Allura FD 20, Philips Healthcare, The Netherlands; parameters in supplementary data). The resulting 3D-RA images were semi-automatically fused with the treatment images based on skeletal and cardiac anatomy using Interventional Tools (R8.8.1) on the Philips workstation. Simultaneously, an 8F sheath was placed in the right femoral artery.

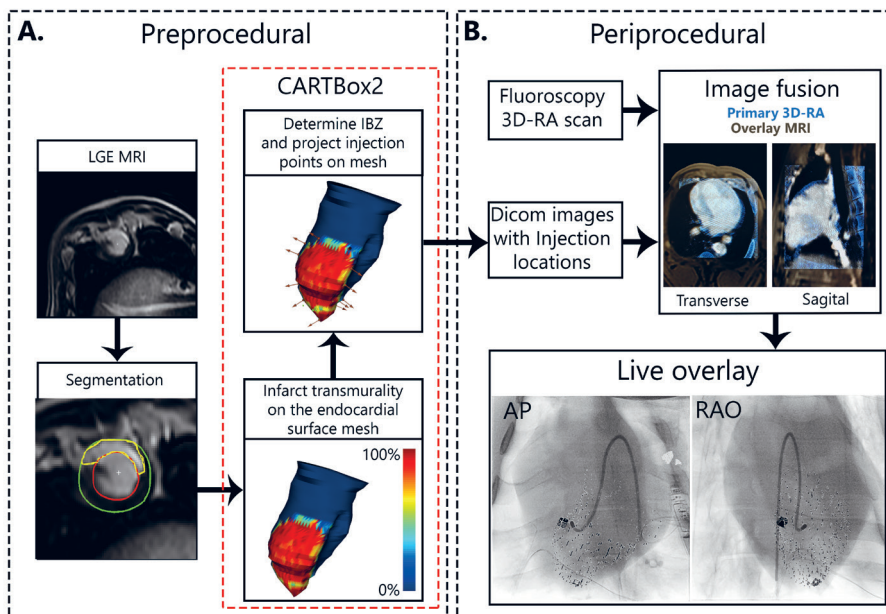


Figure 2. CARTBox2 workflow

Panel A. The preprocedural steps include the acquisition of an LGE-MRI scan of the left ventricle. The endocardium, epicardium and infarct are then segmented. Using CARTBox2, from these segmentations, the scar transmuralty is calculated and projected onto the endocardial surface mesh. Subsequently, the IBZ is calculated and the injection locations are defined and projected onto the mesh (brown arrows), these locations are imbedded into the MRI Dicom images. **Panel B.** After acquiring a 3D-RA scan, the MRI Dicom image is fused with the 3D-RA image based on skeletal anatomy. During the injection procedure, the target locations are visualized on the live fluoroscopic images. LGE-MRI: late gadolinium enhanced magnetic resonance image; IBZ: infarct border zone; 3D-RA: 3-dimensional rotational angiography; AP: anterior-posterior; RAO: right anterior oblique

Injections

After the image fusion, the Myostar® (Biosense Webster) injection catheter was introduced into the LV. The injection targets were displayed one by one on XRF (Figure 2), and moved

automatically with the XRF images upon rotation or angulation of the C-arm. Injections were aimed at the targets displayed on XRF. Correct targeting of a displayed point was verified by inspecting the catheter location from at least 2 fluoroscopic angles at least 30 degrees apart.

Histological processing

After the injection procedure, gadolinium was administered (GadoVist 0.2ml/kg) and 15 minutes later the animals were euthanized with a bolus injection of 20ml 7.5% KCL i.v.. The pericardial sac was removed and the heart was flushed using water. The proximal aorta was dissected approximately 1 cm above the aortic valves. Three sutures were used to position the heart in a plastic tank (17x15x15 cm, WxDxH). A 4 mass % agarose solution at 55 C was used to embed the heart. First the ventricles and atria were filled for support during cutting; secondly space around the heart was filled with the agarose solution. Two rods were placed in the agarose solution next to the heart. The container was then cooled to 4-7°C to allow complete gelation of the agarose.

After complete gelation of the agarose ex-vivo LGE and T2* MRI scans were performed (parameters in supplementary data). Thereafter the embedded heart was cut into 5 mm thick transversal slices starting at the apex using a Berkel® slicer. The cuts were angulated similar to the angulation of short-axis ex-vivo MRI acquisitions. After cutting, the slices were stained in a 1 mass % dissolved 2,3,5-triphenyltetrazoliumchloride (TTC) solution. Both sides of every slice were photographed and scanned with GE Healthcare Typhoon 9410 variable mode scanner set at 2 channels (ch.1 532nm, filter:580BP30; ch.2 633nm, filter:610BP30) with an image resolution of 0.1x0.1mm.

Data analysis

The scar was segmented in the Typhoon images. The TTC and ex-vivo LGE-MRI images were used for verification of the exact infarct location and morphology. From the same images the injection positions were annotated. The distance of each injection to the 1-20% transmural infarct was measured along the endocardial contour. The depth of each injection and the wall thickness were measured perpendicular to the endocardial contour.

Statistical analysis

All normally distributed data are presented as mean \pm standard deviation and non-normally distributed data as median [interquartile range]. A Shapiro-Wilk test was used to test the data for normality. With all repeated measurements per animal, a mean per animal was used for comparison. Injection duration, XRF time and DAP on the anterior and septal sides of the infarction were compared for both groups using a paired student t-test, injections on the apical or basal side of the infarction were excluded for this analysis. Continuous variables with a normal distribution were compared with a two tailed unpaired t-tests, continuous variables with a non-normal distribution were compared with a Mann-Whitney u test. Categorical data was compared using a chi-square test. A sub-analysis was performed in which, time, fluoroscopy time and dose and arrhythmia data of failed injection attempts were excluded. No-outlier analysis was performed. A p-value of <0.05 was considered to be statistically significant. All analyses were performed using SPSS (IBM® SPSS® Statistics, version 23).

RESULTS

Myocardial infarction was induced successfully in 14 animals. One animal died during the infarct induction, one animal died in the night following infarct induction. One animal was euthanized one week after infarct induction after reaching the ‘humane’ end-point due to congestive heart failure. Eleven animals survived to 4 weeks (Figure 1). One animal was excluded from the study after the MRI scan due to absence of a clear infarct and IBZ. Baseline characteristics were balanced between the two study groups (Table 1).

Table 1 Baseline characteristics.

Parameter	NOGA (n=5)	CARTBox2 (n=5)	p-value
Body weight (kg)	72.7±6.4	70.5±5.1	0.559
LV mass (gr)	132±14	120±19	0.309
Infarct size (gr)	11.4±4.0	15.0 ±6.0	0.300
Ejection fraction (%)	52.6±8.7	46.9±4.4	0.236
End diastolic volume (ml)	127±27	126±27.5	0.950
End Systolic volume (ml)	61±20	67±17	0.658

All parameters except body weight were measured using MRI.

Mapping procedure

In the 5 animals which underwent electromechanical mapping with the NOGA system 135±57 points were acquired per map (e.g. Figure 3A). The average NOGA mapping procedure duration was 90.0±9.2 minutes. The average XRF time and dose during mapping was 12.9±9.9 minutes and 18.2±19.0 Gy·cm², respectively. A total of 157±62 PVCs and 78±56 non-sustained VTs were observed during the mapping procedure.

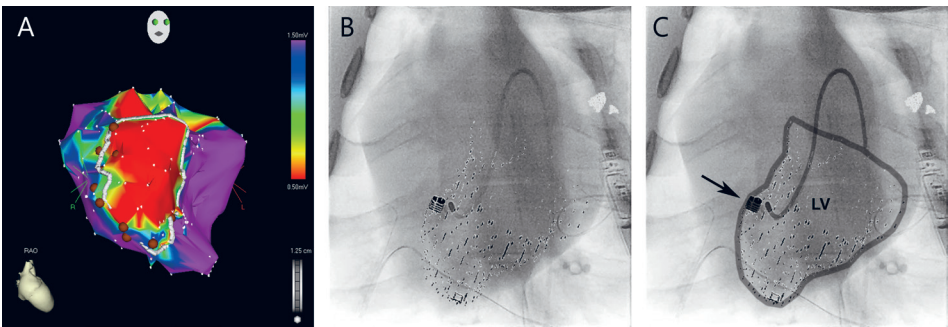


Figure 3. Examples of NOGA and CARTBox injection procedure

A. Example of a NOGA bipolar voltage map (color scale: 0.5-1.5mV) in right anterior oblique view, with design line (white) to indicate the infarct border zone. The injections are shown as brown circles. **B.** Anterior-posterior X-ray fluoroscopy image fused with the CARTBox2 modified MRI scan. The left ventricular endocardium (small dots) and the injection target (large dot). **C.** The same image as shown in B, the endocardial wall and catheter are visually enhanced. The arrow indicates the injection target defined on late gadolinium enhanced MRI.

Intramyocardial injections

A total of 118 injections were performed in 10 animals using the NOGA system (5 animals, 58 injections; e.g. Figure 3A) or the CB2 system (5 animals, 60 injections; e.g. Figure 3B&C). During histological analysis, 8.0 ± 1.2 ($71 \pm 16\%$) and 9.2 ± 3.1 ($75 \pm 15\%$) ($p=0.45$) injections were found in each heart in the NOGA and CB2 group, respectively. There was no significant difference in the injection distances, measured from the injections to the 1-20% transmural IBZ, between the study groups (Figure 4). The average injection depth was 2.9 ± 1.5 mm and 3.4 ± 1.0 mm ($p=0.59$) for NOGA and CB2, respectively. The injection depth relative to the wall thickness is shown in Figure 4C.

Procedure duration

There was no significant difference in the time required for injections between the study groups (Table 2). The total procedure time for CB2, including the 3D-RA and injection time, was significantly shorter ($p<0.001$) than the total NOGA procedure, including both the time required for mapping and injections.

XRF time and dose during injections

In the CB2 group, the average 3D-RA roll scan radiation dose was 5.6 ± 1.6 Gy·cm². Significantly more XRF time and dose was used with the CB2 procedures (Table 2).

Ventricular arrhythmia monitoring

In 8 animals, Holter recordings were successfully analyzed. In the NOGA and CB2 groups, respectively 2 and 1 animal(s), suffered a sustained VT during the injection procedure that required cardioversion. Procedures with CB2 showed a smaller amount of PVCs and non-sustained VTs than NOGA procedures (Table 2).

Sub-analyses

The first 2 animals, one in both groups, were excluded from the anterior-septal comparison due to absence of per injection data (i.e. time). With CB2, injections on the anterior side of the infarction required significantly more XFR time than injections on the septal side ($p=0.04$; Table 3). This effect was not observed with the NOGA injections. With both NOGA and CB2 there was no significant difference in the injection accuracy between injections positioned on the anterior side or septal side of the infarct area.

In the CB2 group, 4 injection attempts in 3 animals were excluded for a sub-analysis. These attempts were ceased because the operator could not reach the target. The sub-analysis shows a substantial reduction in every procedural parameter (Supplementary Data, Table 1).

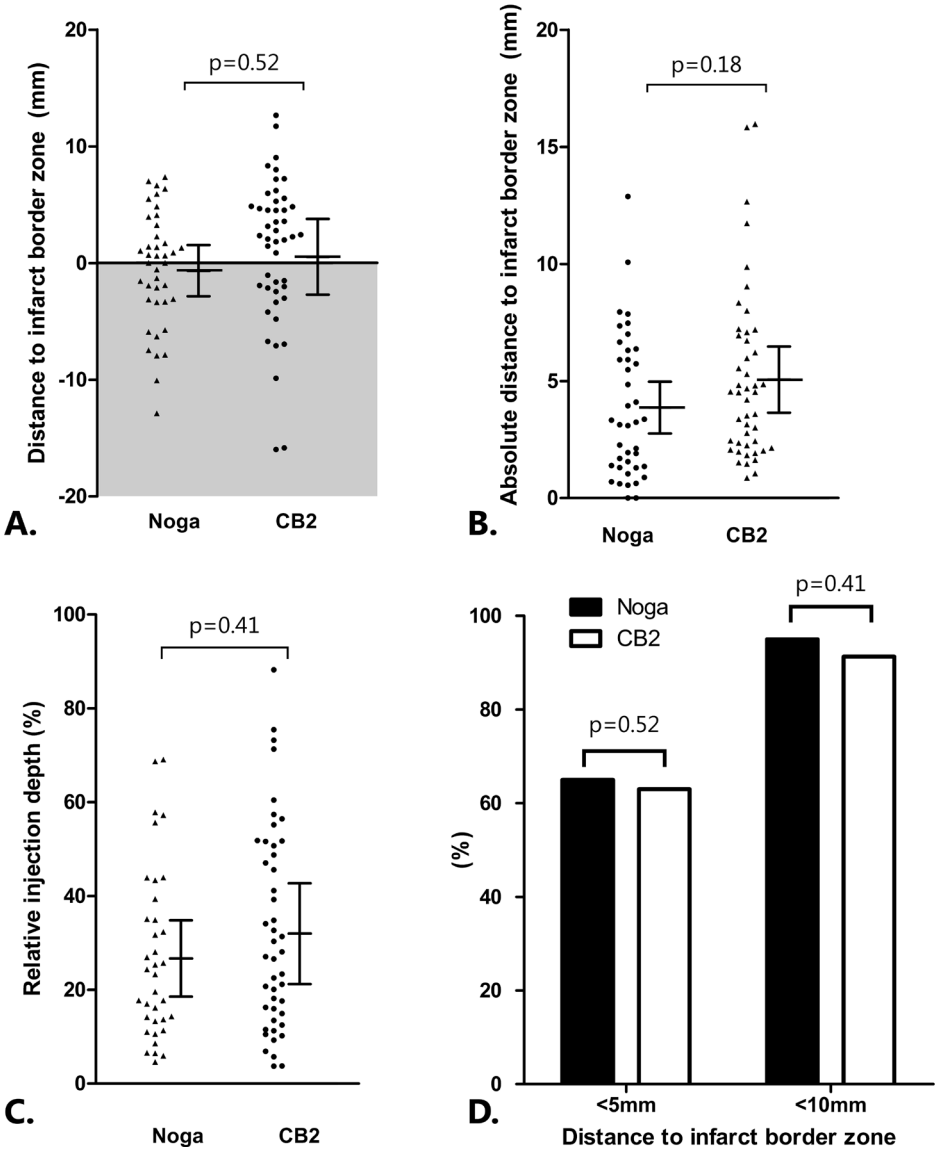


Figure 4. Details of injections.
A-C. The dots represent individual injections with NOGA (n=40) and CB2 (n=46). The error bars show the mean and standard deviation of the injections in each animal. **A.** The gray area indicates the infarct area. **C.** The injection depth relative to the myocardial wall thickness. **D.** Shows the percentage of injections that was within 5 or 10mm from the infarct border zone.

Table 2 Injection procedure parameters

Parameter	NOGA (n=5)	CARTBox2 (n=5)	p
Injection procedure			
Time (min)	60.2±16.7	69.2±11.9	0.355
Total XRF time (min)	6.1±6.2	43.4±6.5	<0.001
Total DAP (Gy·cm ²)	11.2±18.0	64.2±49.0	0.071
PVCs (#)†	239±100	283±10	0.42
Non-sustained VTs (#)†	41.5±11.7	74.3±35.0	0.13
Per injection			
Time (min/injection)	5.4±1.8	6.0±1.4	0.55
Total XRF time (min/injection)	0.5±0.5	3.7±0.8	<0.001
Total DAP (Gy·cm ² /injection)	0.9±1.4	5.4±3.6	0.031
PVCs (#)†	21.0±7.3	20.3±1.1	0.86
Non-sustained VTs (#)†	3.7±0.5	5.2±2.1	0.21
Total procedure (mapping/3D-RA + injections)			
Total time (min)	150.2±12.4	69.2±11.9	<0.001
Total XRF time (min)	18.7±11.0	43.4±6.5	0.003
Total DAP (Gy·cm ²)*	29.4±35.7	69.8±49.0	0.174
PVCs (#)†	396±138	283±10	0.20
Non-sustained VTs (#) †	120±68	74.3±35.0	0.28

DAP: dose area product; XRF: X-ray fluoroscopy; PVC: premature ventricular contraction; VT: ventricular tachycardia †: holter recording and analysis were performed only in the last 8 animals (2 x 4)

Table 3. Details of Anterior-Septal subanalysis

	NOGA			CARTBox2		
	Anterior	Septal	p-value	Anterior	Septal	p-value
Number Injected	24	18	-	20	23	-
Duration (min)	6.0±2.6	4.9±1.9	0.54	8.0±3.0	4.0±0.6	0.06
XRF time (min)	0.8±0.7	0.4±0.4	0.27	5.3±1.8	2.4±0.6	0.04
DAP (Gy·cm ²)	1.4±2.0	0.9±1.2	0.32	8.0±6.7	3.2±3.0	0.12
Injection Found	18	17	-	20	22	-
Distance to IBZ	-0.4±5.3	-1.6±3.3	0.83	-1.46±5.9	1.21±3.5	0.35

DISCUSSION

To the best of our knowledge, this is the first study in which an XRF and catheter independent technique is used for the real-time visualization of injection targets during intramyocardial injections performed with XRF. In this study we have compared the CARTBox2 software to the current standard technique for intramyocardial injections in a large animal model of myocardial infarction. We have shown that CB2 is able to accurately guide intramyocardial injections to the infarct border zone using live fusion of XRF and LGE-MRI. Due to the absence of a mapping procedure with CB2, the procedure time with CB2 was significantly shorter than with NOGA. The total XRF time and dose were significantly higher with CB2, but are comparable with a typical PCI. The number of PVCs and non-sustained VTs was lower in the CB2 group, but not significantly different from the NOGA group.

Injection accuracy

It is generally accepted that the IBZ is the most optimal location for the injection of stem cells or other products for the treatment of focal ischemic cardiomyopathy. There is no consensus on the exact location in terms of transmural. In this study, in the CB2 group, we set the target at 1-20% infarct transmural to assure histological retrieval of the IBZ and to avoid the transmural sections of the infarct. We found neither a statistically significant nor a clinically relevant difference in the IBZ targeting accuracy of both intramyocardial injections methods. The injections with NOGA tended to be located on the inside of the IBZ (-0.7 ± 2.2 mm), while injections with CB2 were on the outside of the IBZ (0.5 ± 3.2 mm). This small difference might be caused by the slightly different region that is targeted with the 1-20% transmural by CB2 compared to the 0.5-1.5mV setting with NOGA. Previous studies showed large variability in NOGA bipolar values for regions of specific infarct transmural.⁷ Furthermore, in the CB2 group, a small error in the registration between the LGE-MRI and 3D-RA scan will lead to targeting error for all injections during that procedure.

Other studies that have developed and tested image fusion systems to guide intramyocardial injections have reported injection accuracies of comparable magnitudes. Tomkowiak and colleagues have designed a system to register and overlay LGE-MRI images on live XRF. In that study the target was defined as a 20mm region around the infarct, the reported injection accuracy is -0.9 ± 5.0 mm (mean \pm SD).¹² Dauwe and colleagues have designed a system that fuses and overlays XRF with LGE-MRI, CT or ^{18}F -FDG-PET/CT. In that study the target zone was defined as the IBZ, the reported targeting accuracies are -2.3 ± 0.8 mm, 2.2 ± 0.8 and 0.0 ± 1.1 mm (mean \pm SEM) for XRF fused with MRI, CT and PET/CT, respectively.¹¹ Comparing the reported injection accuracy numbers for LGE-MRI based XRF interventions of the aforementioned studies suggests that the performance of CB2 is similar or slightly better. Whether such a difference is clinically relevant has to be investigated in future studies.

Procedure duration

Injections with the NOGA system require the laborious construction of a detailed electro anatomical map. Using CB2 such a roadmap is not required. The use of CB2 does require the acquisition and segmentation of a LGE-MRI scan, both are however performed prior to the

injection procedure and therefore do not increase Cath Lab procedure time. With CB2, a 3D-RA roll scan is acquired during the Cath lab procedure which on average takes less than one minute. Since the registration of the LGE-MRI with 3D-RA can be performed during the insertion of the arterial access sheaths, it does not increase overall procedure time. In this study we found no significant difference in the time required for the intramyocardial injections between both systems. Due to the absence of the mapping procedure with CB2, procedures performed with CB2 were significantly shorter.

XRF time and dose

Injections performed with CB2 required significantly more XRF time in comparison with the NOGA system. The DAP was not significantly higher with CB2 which may suggest that the XRF angulation and rotation with CB2 required less XRF energy and thus a lower DAP. With the NOGA system being a non-fluoroscopic navigation system, XRF guidance is only required for passing the aortic valve and for the initial mapping points. We were unable to find any literature that reports on XRF usage during NOGA procedures. However, the experience in our own center is that XRF is commonly used during the mapping and injection procedures to gain insight in catheter position and movement.

The average reported dose for a PCI is in the range of 70-150 Gy·cm².^{18,19} Data of the present study showed that the XRF dose with CB2 procedures is similar or lower than an average PCI.

Ventricular arrhythmia monitoring

During the NOGA procedure, more ventricular arrhythmias were observed; the difference with CB2 procedures was not significant. Holter recordings were performed in only 8/10 study animals. The aforementioned studies of Tomkowiak and Dauwe only report on major ventricular arrhythmias suffered during the injection procedures. Dauwe and colleagues report that 3/5 animals required cardioversion in the NOGA group vs. 1/10 animals injected with their own system.¹¹ Tomkowiak and colleagues report that no sustained arrhythmias were observed.¹² In the present study 2/5 and 1/5 animals required cardioversion during the NOGA and CB2 injections, respectively. The number of ventricular arrhythmias per injection was similar between both study groups, suggesting that the NOGA mapping procedure is responsible for the higher total number of ventricular arrhythmias. Due to the large variation in PVCs in the NOGA group and with non-sustained VTs in both groups, no significant differences between both methods were observed.

Limitations

To accurately identify the IBZ during the mapping procedure with NOGA, we mapped this region in higher detail (i.e. more mapping points). This led to a prolonged mapping procedure, where the typical clinical NOGA mapping procedure takes about 45 minutes⁷, the mapping time in this study was 90 minutes. However, substituting the mapping time in our study with the optimal value of 45 minutes still leads to a significantly longer procedure time for NOGA (103.2±13.6 minutes) compared to CB2 (70.0±12.7 minutes; p=0.004).

In this study a single plane XRF device was used. The use of a biplane XRF device would have obviated the need to rotate the C-arm multiple times to verify the catheter position, saving much

procedure time. It is therefore likely that the total injection time with CB2 would have been considerably shorter if a biplane XRF setup had been used.

With NOGA, the target was shown as a line around the infarct (Figure 3A). To simplify visualization with CB2, the injection targets were shown one by one on the XRF overlay (Figure 3B&C). The latter approach of visualizing a single point instead of a line, forced the operator to maneuver the catheter to that exact point. This has inevitably led to an increased procedure time whenever a target was difficult to reach, as was shown in the sub-analysis (Supplementary Table 1). Instead of changing focus to a reachable target, time was spent on reaching difficult targets. For future procedures using CB2, we would recommend visualizing the target as a line that extends at least a few centimeters in either direction along the target zone.

Since the NOGA map is constructed from points that are acquired on the LV endocardium using a catheter, the target region is always reachable with the catheter. In contrast, targets selected with CB2, are selected manually from LGE-MRI without taking the physical reachability of the target into account. Careful selection of target points during the treatment planning phase can prevent selection of points at locations that are extremely difficult to reach. This is substantiated by the fact that in the CB2 group, injections on the anterior side of the infarction required significantly more XRF time than injection on the septal side. This can be explained by the location of the papillary muscles just next to the anterior IBZ, navigating the catheter to this area from the lateral wall is challenging while an anterior approach requires passing the infarct area itself. Furthermore, the sub-analysis showed that excluding navigation time, XRF time and XRF dose of unsuccessful injection points substantially reduced all these parameters. More experience with treatment planning and CB2 guided injection procedures can solve these planning issues.

Clinical implications

The use of CB2 as an alternative to the NOGA system for intramyocardial injections can significantly shorten the procedure time and can increase Cath Lab capacity. CARTBox2 also obviates the need for expensive dedicated intramyocardial injection systems, both in terms of acquisition and operating (e.g. mapping and injection catheters) costs. The radiation dose involved with CB2 injection procedures is higher than NOGA but does not exceed that of a typical PCI. Furthermore, the information of the (LGE) MRI scan can give more insight into specific infarct or function parameters. With CB2, core infarct or thin myocardial wall sections can be identified and displayed onto live XRF and enables the operator to avoid such areas for intramyocardial injections.

Conclusion

CARTBox2 is a safe and accurate alternative technology for fluoroscopic guidance of intramyocardial therapy. The data of this study shows that the injection procedures performed with CARTBox2 are equally accurate, but quicker, require more fluoroscopy and provoke less arrhythmias than NOGA procedures. The novel CARTBox2 technological strategy enables its use in all cardiology centers that have modern fluoroscopic imaging equipment.

Acknowledgments

We kindly acknowledge Marlijn Jansen, Joyce Visser and Martijn van Nieuwburg for their assistance with the animal procedures. Martijn Froeling and Anke Wassink are greatly acknowledged for their assistance with the acquisition of the MRI scans. Patricia Dankers is acknowledged for her help with the Upy gel. We greatly acknowledge Dave Hopman of Fysiologic BV for his dedication in assisting with the holter analyses and CART-TECH BV for providing software and support during the study.

Disclosures

FJ van Slochteren and SAJ Chamuleau are co-founders of CART-TECH B.V.. The other authors have nothing to disclose.

REFERENCES

1. Ptaszek LM., Mansour M., Ruskin JN., Chien KR. Towards regenerative therapy for cardiac disease. *Lancet* 2012;379(9819):933–42. Doi: 10.1016/S0140-6736(12)60075-0.2. Bartunek J., Vanderheyden M., Hill J., Terzic A. Cells as biologics for cardiac repair in ischaemic heart failure. *Heart* 2010;96(10):792–800. Doi: 10.1136/hrt.2007.139394.
3. Nguyen PK., Lan F., Wang Y., Wu JC. Imaging: Guiding the Clinical Translation of Cardiac Stem Cell Therapy. *Circ Res* 2011;109(8):962–79. Doi: 10.1161/CIRCRESAHA.111.242909.
4. Orlic D., Kajstura J., Chimenti S., et al. Bone marrow cells regenerate infarcted myocardium. *Nature* 2001;410(6829):701–5. Doi: 10.1038/35070587.
5. Psaltis PJ., Worthley SG. Endoventricular electromechanical mapping - The diagnostic and therapeutic utility of the NOGA®XP cardiac navigation system. *J Cardiovasc Transl Res* 2009;2(1):48–62. Doi: 10.1007/s12265-008-9080-7.
6. Ben-Haim S., Osadchy D., Schuster I., Gepstein L., Hayam G., Josephson ME. Nonfluoroscopic, in vivo navigation and mapping technology. *Nat Med* 1996;2(12):1393–5. Doi: 10.1038/nm1296-1393.
7. Gyöngyösi M., Dib N. Diagnostic and prognostic value of 3D NOGA mapping in ischemic heart disease. *Nat Publ Gr* 2011;8(7):393–404. Doi: 10.1038/nrcardio.2011.64.
8. Slochteren FJ., Es R., Gyöngyösi M., et al. Three dimensional fusion of electromechanical mapping and magnetic resonance imaging for real-time navigation of intramyocardial cell injections in a porcine model of chronic myocardial infarction. *Int J Cardiovasc Imaging* 2016;1–11. Doi: 10.1007/s10554-016-0852-x.
9. Pavo N., Jakab A., Emmert MY., et al. Comparison of NOGA endocardial mapping and cardiac magnetic resonance imaging for determining infarct size and infarct transmural for intramyocardial injection therapy using experimental data. *PLoS One* 2014;9(11):1–13. Doi: 10.1371/journal.pone.0113245.
10. Van Slochteren FJ., Van Es R., Koudstaal S., et al. Multimodality infarct identification for optimal image-guided intramyocardial cell injections. *Netherlands Hear J* 2014;22(11):493–500. Doi: 10.1007/s12471-014-0604-2.
11. Dauwe DF., Nuyens D., De Buck S., et al. Three-dimensional rotational angiography fused with multimodal imaging modalities for targeted endomyocardial injections in the ischaemic heart. *Eur Heart J Cardiovasc Imaging* 2014;15(8):900–7. Doi: 10.1093/ehjci/jeu019.
12. Tomkowiak MT., Klein AJ., Vigen KK., et al. Targeted transendocardial therapeutic delivery guided by MRI-x-ray image fusion. *Catheter Cardiovasc Interv* 2011;78(3):468–78. Doi: 10.1002/ccd.22901.
13. Koudstaal S., Jansen SJ., Gho JMIH., et al. Myocardial Infarction and Functional Outcome Assessment in Pigs 2014;(April):1–10. Doi: 10.3791/51269.
14. Bastings MMC., Koudstaal S., Kieltyka RE., et al. A fast pH-switchable and self-healing supramolecular hydrogel carrier for guided, local catheter injection in the infarcted myocardium. *Adv Healthc Mater* 2014;3(1):70–8. Doi: 10.1002/adhm.201300076.
15. Pape ACH., Bakker MH., Tseng CCS., et al. An Injectable and Drug-loaded Supramolecular Hydrogel for Local Catheter Injection into the Pig Heart. *J Vis Exp* 2015;(100):e52450. Doi: 10.3791/52450.
16. Delikatny EJ., Poptani H. MR techniques for in vivo molecular and cellular imaging. *Radiol Clin North Am* 2005;43(1):205–20. Doi: 10.1016/j.rcl.2004.07.004.
17. Heiberg E., Sjögren J., Ugander M., Carlsson M., Engblom H., Arheden H. Design and validation of Segment—freely available software for cardiovascular image analysis. *BMC Med Imaging* 2010;10:1. Doi: 10.1186/1471-2342-10-1.
18. Pantos I., Patatoukas G., Katritsis DG., Efstathiopoulos E. Patient radiation doses in interventional cardiology procedures. *Curr Cardiol Rev* 2009;5(1):1–11. Doi: 10.2174/157340309787048059.
19. Chida K., Saito H., Kagaya Y., et al. Indicators of the maximum radiation dose to the skin during percutaneous coronary intervention in different target vessels. *Catheter Cardiovasc Interv* 2006;68(2):236–41. Doi: 10.1002/ccd.20830.

SUPPLEMENTARY DATA

MRI parameters (pre-injection)

Cine

Repetition time [TR]/echo time [ET] = 3.39 ms/1.69 ms. Flip angle = 60 °, Pixel size = 1.25 x 1.25 mm, [FOV] = 320 x 320 mm, 256 x 256 matrix, 8 mm slice thickness.

Late Gadolinium Enhancement

[TR]/[ET] = 3.64 ms/1.19 ms. Flip angle = 25 °, Pixel size = 1.25 x 1.25 mm, [FOV] = 296 x 296 mm, 256 x 256 matrix, 4 mm slice thickness.

MRI parameters (ex-vivo)

LGE

[TR]/[ET] = 5.53 ms/1.69 ms. Flip angle = 25 °, Pixel size = 1.0 x 1.0 mm, [FOV] = 169 x 169 mm, 176 x 176 matrix, 3 mm slice thickness.

*T2**

[TR]/[ET] = 88.7 ms/15 equally distributed ETs with range 1.9-24.6 ms. Flip angle = 15 °, Pixel size = 0.5 x 0.5 mm, [FOV] = 169 x 169 mm, 320 x 320 matrix, 3 mm slice thickness.

3D-RA parameters

180° rotation in 10.2s, 30fps. Max rotation speed 30°/s. Tube voltage 125kV. 128x128 reconstruction matrix

Supplementary Table 1

Parameter	Noga® XP (n=5)	CARTBox 2 (n=5)	CARTBox 2 (n=5)	Noga vs CB2	Noga vs successful CB2
		All injections	successful injections		
Injection procedure					
Time (min)	60.2±16.7	69.2±11.9	61.2±3.0	0.355	0.06
Total XRF time (min)	6.1±6.2	43.4±6.5	37.9±4.0	<0.001	<0.001
Total DAP (Gy·cm ²)	11.2±18.0	64.2±49.0	57.3±48.0	0.071	0.079
PVCs (#)(n=4) †	239±100	283±10	241±25	0.42	0.97
Non-sustained VTs (#)	41.5±11.7	74.3±35.0	55.8±17.6	0.13	0.23
Per injection					
Time (min/injection)	5.4±1.8	6.0±1.4	5.3±1.4	0.55	0.99
Total XRF time (min/injection)	0.5±0.5	3.7±0.8	3.3±0.8	<0.001	<0.001
Total DAP (Gy·cm ² /injection)	0.9±1.4	5.4±3.6	4.9±3.6	0.031	0.051
PVCs (#)†	21.0±7.3	20.3±1.1	18.3±2.2	0.86	0.53
Non-sustained VTs (#)†	3.7±0.5	5.2±2.1	4.2±1.2	0.21	0.45
Total procedure					
Total time (min)	150.2±12.4	69.2±11.9	61.2±3.0	<0.001	<0.001
Total XRF time (min)	18.7±11.0	43.4±6.5	37.9±3.9	0.003	0.015
Total DAP (Gy·cm ²)*	29.4±35.7	69.8±49.0	62.9±48.2	0.174	0.247
PVCs (#)†	396±138	283±10	241±25	0.20	0.07
Non-sustained VTs (#) †	120±68	74.3±35.0	55.8±17.6	0.28	0.12

DAP: dose area product; XRF: X-ray fluoroscopy; PVC: premature ventricular contraction; VT: ventricular tachycardia †: holter recording and analysis were performed only in the last 8 animals (2 × 4)

Chapter 6



High Resolution Systematic Digital Histological Quantification of Cardiac Fibrosis and Adipose Tissue in Phospholamban p.Arg14del Mutation Associated Cardiomyopathy

PloS ONE 2014;9:e94820

Johannes M.I.H. Gho¹, René van Es¹, Nikolas Stathonikos², Magdalena Harakalova^{1,2}, Wouter P. te Rijdt³, Albert J.H. Suurmeijer⁴, Jeroen F. van der Heijden¹, Nicolaas de Jonge¹, Steven A.J. Chamuleau¹, Roel A. de Weger², Folkert W. Asselbergs^{1,5,6}, Aryan Vink²

¹ Department of Cardiology, Division Heart and Lungs, University Medical Center Utrecht, Utrecht, the Netherlands

² Department of Pathology, University Medical Center Utrecht, Utrecht, the Netherlands

³ Department of Cardiology, University Medical Center Groningen, University of Groningen, Groningen, the Netherlands

⁴ Department of Pathology, University Medical Center Groningen, University of Groningen, Groningen, the Netherlands

⁵ Durrer Center for Cardiogenetic Research, ICIN-Netherlands Heart Institute, Utrecht, the Netherlands

⁶ Institute of Cardiovascular Science, Faculty of Population Health Sciences, University College London, London, United Kingdom

ABSTRACT

Myocardial fibrosis can lead to heart failure and act as a substrate for cardiac arrhythmias. In dilated cardiomyopathy diffuse interstitial reactive fibrosis can be observed, whereas arrhythmogenic cardiomyopathy is characterized by fibrofatty replacement in predominantly the right ventricle. The p.Arg14del mutation in the phospholamban (*PLN*) gene has been associated with dilated cardiomyopathy and recently also with arrhythmogenic cardiomyopathy. Aim of the present study is to determine the exact pattern of fibrosis and fatty replacement in *PLN* p.Arg14del mutation positive patients, with a novel method for high resolution systematic digital histological quantification of fibrosis and fatty tissue in cardiac tissue. Transversal mid-ventricular slices ($n = 8$) from whole hearts were collected from patients with the *PLN* p.Arg14del mutation (age 48 ± 16 years; 4 (50%) male). An in-house developed open source MATLAB script was used for digital analysis of Masson's trichrome stained slides (<http://sourceforge.net/projects/fibroquant/>). Slides were divided into trabecular, inner and outer compact myocardium. Per region the percentage of connective tissue, cardiomyocytes and fatty tissue was quantified. In *PLN* p.Arg14del mutation associated cardiomyopathy, myocardial fibrosis is predominantly present in the left posterolateral wall and to a lesser extent in the right ventricular wall, whereas fatty changes are more pronounced in the right ventricular wall. No difference in distribution pattern of fibrosis and adipocytes was observed between patients with a clinical predominantly dilated and arrhythmogenic cardiomyopathy phenotype. In the future, this novel method for quantifying fibrosis and fatty tissue can be used to assess cardiac fibrosis and fatty tissue in animal models and a broad range of human cardiomyopathies.

INTRODUCTION

A network of extracellular matrix maintains the structural integrity of the myocardium. Due to several etiologies increased deposition of collagen and other extracellular matrix proteins can occur leading to cardiac fibrosis.¹ After myocardial infarction, cardiomyocytes are replaced by connective tissue leading to reparative fibrosis. In contrast, in non-ischemic cardiomyopathies, an increase in collagen synthesis by myofibroblasts results in diffuse interstitial reactive fibrosis. In arrhythmogenic cardiomyopathy (AC), fibrosis is accompanied by an increase of adipocytes leading to so-called fibrofatty replacement.²

Myocardial fibrosis is an important part of the histological characteristics in heart failure (HF) with preserved and reduced ejection fraction and may act as a substrate for cardiac arrhythmias. Adequate detection of the amount and distribution of fibrosis in the heart is important for diagnosis, predicting prognosis, treatment planning and follow-up after therapy.^{3,4} The reference noninvasive standard for indirect detection of myocardial fibrosis is late gadolinium enhancement on cardiac magnetic resonance imaging (MRI).³ Thus far, detailed histological correlation studies to validate this MRI technique are scarce. Histological assessment of cardiac fibrosis is mostly limited by the small amount of tissue available in diagnostic endomyocardial biopsies that only provides regional information.² In addition, quantification of histological fibrosis is usually performed semi-quantitatively, classifying the fibrosis in limited categories.

Phospholamban is a protein in the sarcoplasmic reticulum and acts as a (reversible) inhibitor of the Ca^{2+} pump: sarcoplasmic reticulum Ca^{2+} -ATPase 2a (SERCA2a). On phosphorylation it dissociates from SERCA2a and thereby activates the Ca^{2+} pump. This cascade regulates cardiac relaxation and contractility. Several causal phospholamban (*PLN*) mutations have been described in humans.⁵⁻⁸ The p.Arg14del (c.40_42delAGA) founder mutation in the *PLN* gene has been associated with dilated cardiomyopathy (DCM) and recently also with AC.⁹ Detailed histologic analysis of the pattern of fibrosis and fatty changes in *PLN* mutation associated cardiomyopathies has not been extensively studied and to the best of our knowledge has not been performed on transverse heart slices.

The aim of this study was to determine the exact patterns of fibrosis and fatty changes in the myocardium of patients with the *PLN* p.Arg14del mutation associated cardiomyopathy in relation to their clinical phenotype. This study population was used as proof-of-principle for a novel method of high resolution systematic digital quantification of fibrosis and fatty tissue in transversal cardiac slides. In the future this method may be used for detailed histological quantification and determination of the distribution pattern of cardiac fibrosis in different types of heart disease, in addition it provides a detailed high resolution reference for imaging techniques of cardiac fibrosis.

METHODS

Ethics statement

The study met the criteria of the code of proper use of human tissue that is used in the Netherlands. The study was approved by the scientific advisory board of the biobank of the

University Medical Center Utrecht, Utrecht, the Netherlands (protocol no. 12/387). Written informed consent was obtained or in certain cases waived by the ethics committee when obtaining informed consent was not possible due to death of the patient.

Hearts obtained at autopsy (n = 2) or explantation (n = 6) were collected from patients with the *PLN* p.Arg14del mutation. Based on their initial clinical presentation, patients were divided in two categories: predominantly DCM or AC. Three control hearts, two donor hearts not-used for transplantation and one heart obtained at autopsy of a road accident victim, were used as reference.

We used a systematic methodology for high resolution digital cardiac fibrosis quantification (Figure 1). Hearts were cut in transverse (short-axis) slices of 1 cm thick starting at the apex including both ventricles. Each fourth transverse slice was fixed in formalin and divided into smaller pieces. A map of the heart slice was drawn to annotate the origin of each tissue specimen. Subsequently the samples were embedded in paraffin and Masson's trichrome staining was performed. The slides were scanned at 20X magnification as described previously.¹⁰ Images were extracted using Aperio ImageScope v12.0.0.5039 (Aperio, Vista, CA, USA) as a TIFF file with lossless compression. The images were resized to 10% of their original size for digital analysis.

To analyze the cardiac tissue, slides were divided into several layers: the epicardial area, compact myocardium and non-compact (trabeculated) myocardium (<http://sourceforge.net/projects/fibroquant/>). The epicardial area was defined as the outer region of fatty tissue bordered by the first row of cardiomyocytes. The non-compact myocardial area was defined as the endocardial trabeculated region. The compact myocardium was defined by the area between the trabeculated area and the epicardial area and was artificially divided with an equidistant line in two halves. An equidistant line is one for which every point on the line is equidistant from the nearest points on both the epicardial and trabecular segmentation. In case a midline division was not feasible, e.g., due to a thin wall or originating from the interventricular septum (without epicardium), mean values of the total myocardium were used. Thus, the myocardium was divided in four layers: trabecular myocardium, inner or outer compact myocardium and the epicardium.

In all four layers the percentage of connective tissue (blue), cardiomyocytes (red) and adipose tissue (cells with non stained cytoplasm) was digitally quantified using MATLAB (Release R2012a, The MathWorks, Inc., Natick, Massachusetts, United States). The percentage per region was calculated by separating the Masson's trichrome stained slides into its constituent stains of methyl blue and ponceau-fuchsin by performing colour deconvolution.¹¹ This produces two grayscale images depicting the concentration of the two stainings. The resulting images are filtered using a 2D median filter and further processed using morphological dilation, thresholding and closing operations. The adipose tissue is quantified using a separate function in order to highlight the "chain-link" structure of adipocytes as seen on glass slides. The original image is converted to grayscale and filtered using a 2D median filter. After that a threshold is applied and morphological opening is performed. The median filtered image is then subtracted from the morphologically opened image and the resulting image is further morphologically processed by performing consecutive closing and opening operations. This converts the "chain-link" structure into a black and white image where only the adipose tissue is left. The area of each constituent is determined and a percentage is calculated based on the total area that was processed.¹² The

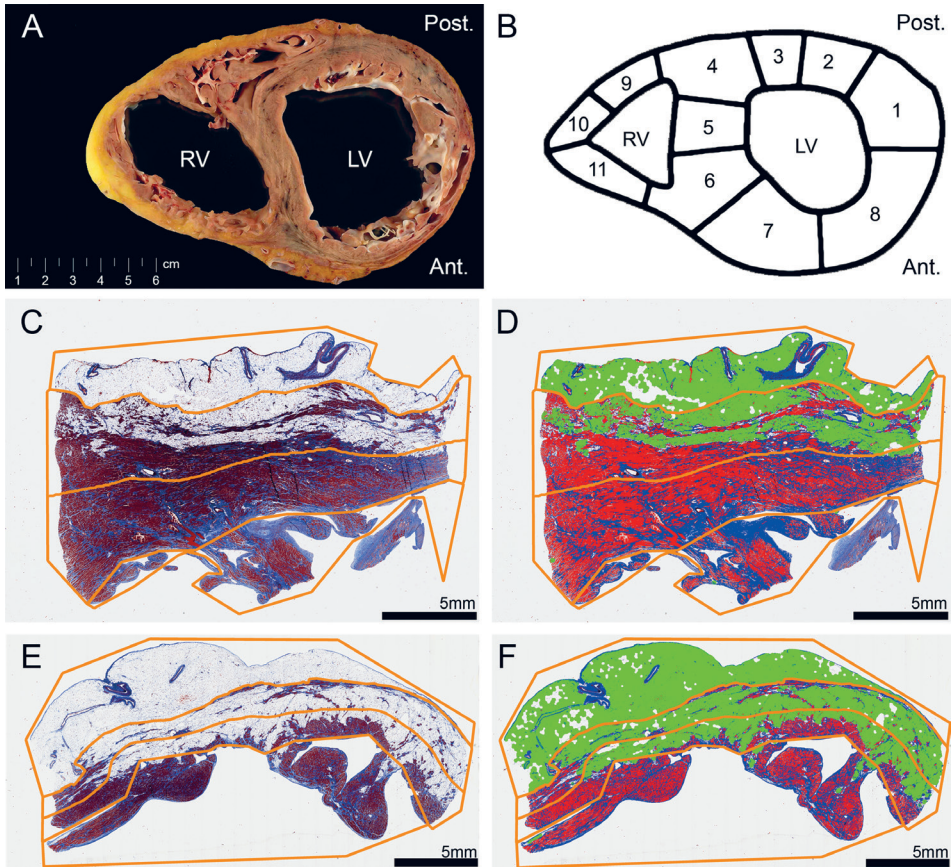


Figure 1 Overview of methodology. LV, left ventricle; RV, right ventricle; Ant., anterior; Post., posterior. **A**, gross showing a transverse heart slice of arrhythmogenic cardiomyopathy. **B**, transverse slice dissection scheme. **C-F**, examples of digital slide processing. Regions of interest are shown in orange lines (defining the epicardium, compact myocardium divided by an equidistant midline and trabeculated part). **C**, slide from the left ventricle posterior wall. **D**, slide C after digital processing. Red: cardiomyocytes. Blue: connective tissue. Pseudo green: adipose tissue. **E**, slide from the right ventricle lateral wall. **F**, slide E after digital processing. Red: cardiomyocytes. Blue: connective tissue. Pseudo green: adipose tissue.

epicardial region was excluded from analysis. The resulting values (percentage fibrosis and fatty tissue) were annotated to the corresponding region in the heart using an automated algorithm (Supplementary Figure S1).

Subsequently the annotated map of the transverse slice is automatically transformed to a standardized schematic overview. The annotated map was translated to a schematic overview by determining the angular properties of each separate section from the middle of the ventricles with a precision of one degree. The results of the quantification (percentage fibrosis or fatty tissue) are displayed using an easily interpretable color scale. Statistics were performed using IBM SPSS Statistics (Version 20.0, IBM Corporation, Armonk, New York, United States).

We compared mean percentages of fibrosis and adipose tissue in different areas between the two clinical phenotypes of AC and DCM and control hearts. The left ventricle was divided into a septal, posterior, posterolateral, lateral, anterolateral and anterior part. The right ventricle was divided into a posterior and anterior part. To compare mean percentages of fibrosis and adipose tissue corrected for surface area per region and condition a repeated measures analysis was performed. After Greenhouse-Geisser correction, interactions between region and condition were explored. Post hoc tests (Tukey HSD) were performed in the absence of a significant interaction.

RESULTS

Clinical characteristics of the patients are summarized in Table 1. Mean age was 48±16 years; 4 (50%) patients were male. Five patients were known with a clinical phenotype of DCM and 3 patients were known with a clinical phenotype of AC. The schematic overviews depict distribution and percentage of fibrosis and adipose tissue for DCM (Figure 2) and arrhythmogenic patients (Figure 3). Mean values of fibrosis and adipose tissue with standard deviations per region and condition (control, AC or DCM) are presented in Supplementary Table S1.

Table 1 Patient characteristics of the *PLN* p.Arg14del mutation carriers

	(n = 8)
Age; mean (SD)	48 (16)
Male sex	4 (50%)
Device	
ICD	4 (50%)
CRT-D	3 (38%)
Left ventricular assist device	4 (50%)
First presenting symptom	
Arrhythmia	4 (50%)
Heart failure	4 (50%)
Heart transplantation	6 (75%)

SD, standard deviation; ICD, implantable cardioverter-defibrillator; CRT-D, cardiac resynchronization therapy defibrillator.

In the 8 heart slices of *PLN* mutation carriers, myocardial fibrosis was mainly observed in the trabecular part of the posterolateral wall of the right ventricle and in the posterolateral (mean >38%) and in lesser extent anterolateral (mean >26%) wall of the left ventricle. In the left ventricle, fibrosis was more pronounced in the outer layer of compact myocardium than in the myocardial layers more closely to the lumen. Mean percentage of fibrosis and adipose tissue is shown in the combined schematic overviews (Figure 4). The septum and ventral wall of the right ventricle revealed the least amount of interstitial fibrosis. Fatty changes of myocardium were predominantly observed in the entire right ventricle wall (mean 37.2±14% and 28.9±4% in AC and 26.1±20% and 24.3±12% in DCM respectively in regions 7 and 8) and in the epicardial side of the compact myocardium of the posterolateral wall of the left ventricle (mean 6.9±5%

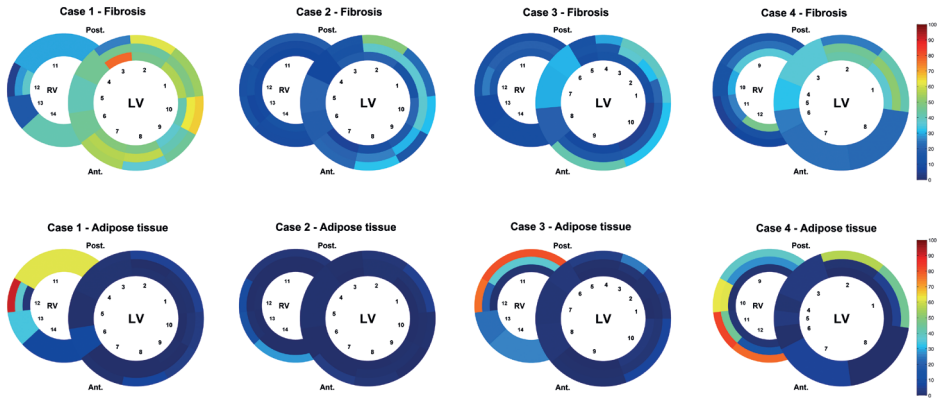


Figure 2 Schematic heart slice overview of patients with a clinical phenotype of dilated cardiomyopathy. The results of the digital quantification in heart slices in percentage of fibrosis or adipose tissue are shown using a color scale. The epicardial fat has been excluded from this overview. LV, left ventricle; RV, right ventricle; Ant., anterior; Post., posterior

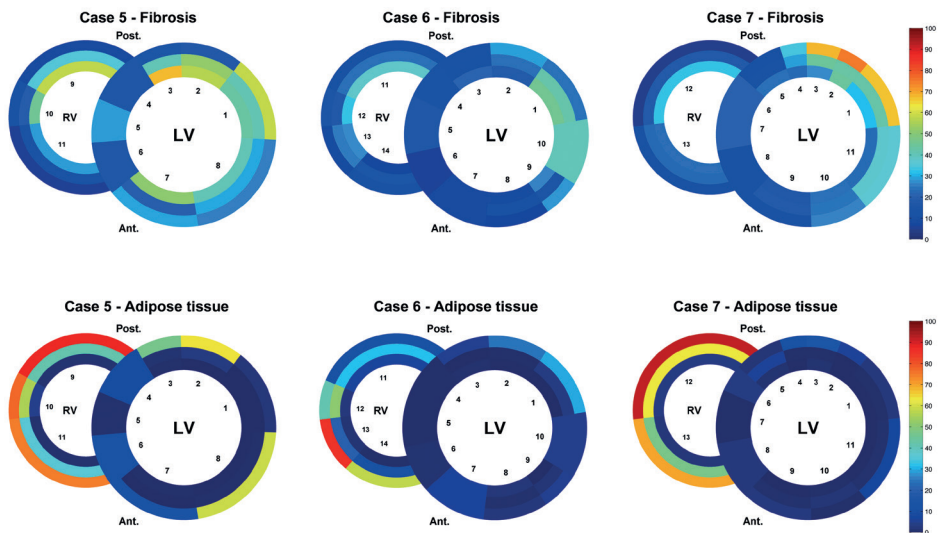


Figure 3 Schematic heart slice overview of patients with a clinical phenotype of arrhythmogenic cardiomyopathy. The results of the digital quantification in heart slices in percentage of fibrosis or adipose tissue are shown using a color scale. The epicardial fat has been excluded from this overview. LV, left ventricle; RV, right ventricle; Ant., anterior; Post., posterior

in AC and $5.8 \pm 6\%$ in DCM in region 1). Overall fatty infiltration of myocardium was more pronounced in the right (mean adipose tissue $>24\%$) than in the left (mean adipose tissue $<11\%$) ventricle. Mean fibrosis in control hearts was less than 6%, mean adipose tissue was 2% or less in the left ventricle myocardium and less than 15% in the right ventricular wall (Figure 5).

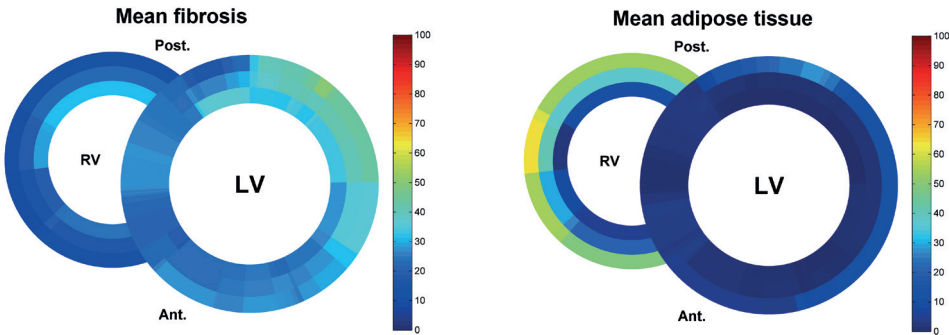


Figure 4 Schematic heart slice overview of patients with the *PLN* p.Arg14del mutation (dilated and arrhythmogenic cardiomyopathy). The results of the mean percentage of fibrosis or adipose tissue are shown using a color scale. In total 102 heart slides of 8 heart slices were used. LV, left ventricle; RV, right ventricle; Ant., anterior; Post., posterior

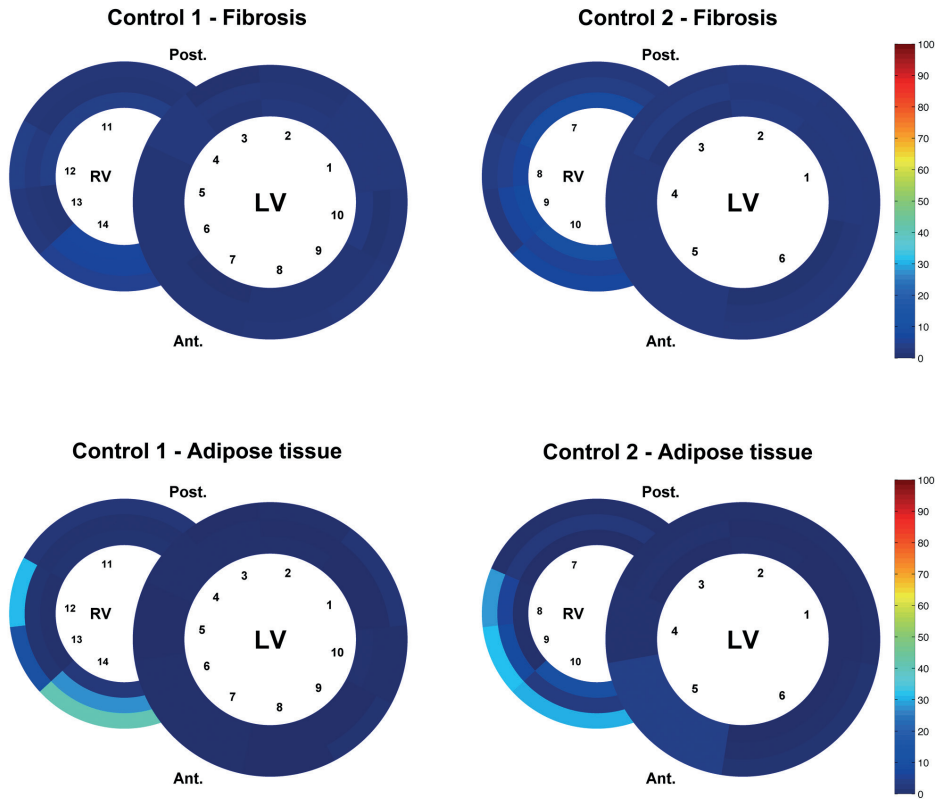


Figure 5 Schematic overview of fibrosis and adipose tissue in heart slices of control hearts. The results of the digital quantification in percentage of fibrosis or adipose tissue are shown using a color scale. The epicardial fat has been excluded from the analysis. LV, left ventricle; RV, right ventricle; Ant., anterior; Post., posterior

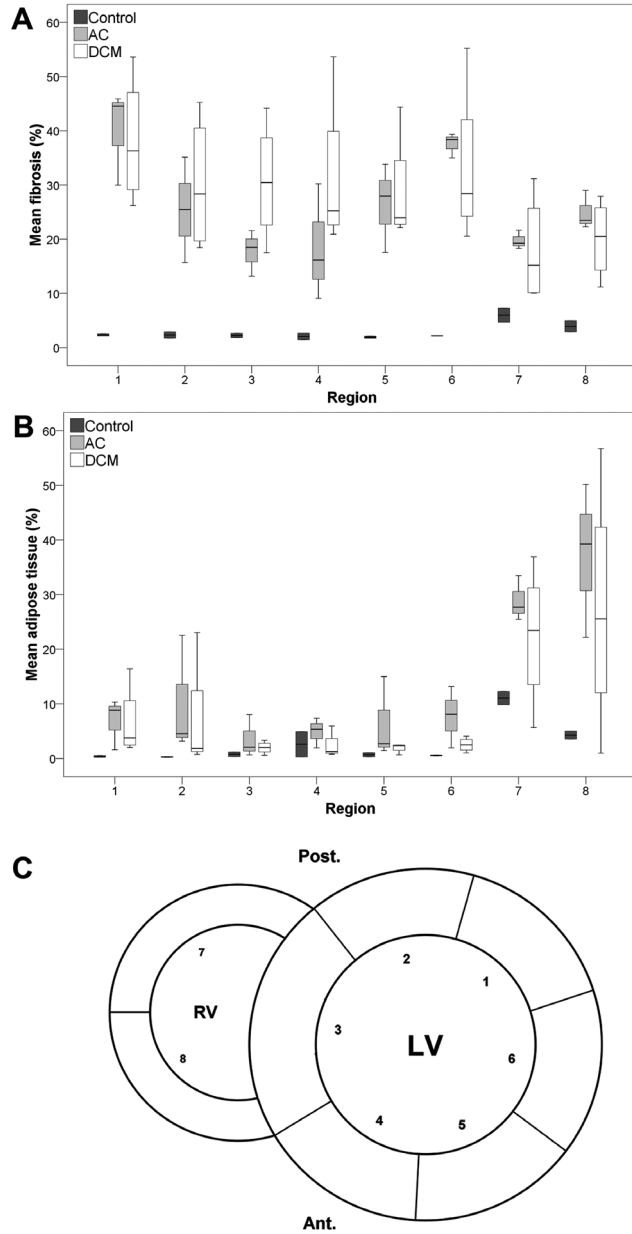


Figure 6 Boxplots of mean fibrosis and mean adipose tissue in the different regions. Boxplots of mean percentage of fibrosis (A) and adipose tissue (B) per condition in 8 regions (C) corrected for surface area. Outliers are represented by small circles or stars. AC, arrhythmogenic cardiomyopathy; DCM, dilated cardiomyopathy; LV, left ventricle; RV, right ventricle; Ant., anterior; Post., posterior; 1 = LV posterolateral wall; 2 = LV posterior wall; 3 = interventricular septum; 4 = LV anterior wall; 5 = LV anterolateral wall; 6 = LV lateral wall; 7 = RV dorsal wall; 8 = RV ventral wall.

Mean connective and adipose tissue per condition and region ($n = 8$, corrected for surface area) is shown in boxplots (Figure 6). Mean values of fibrosis and adipose tissue were log transformed to reduce right-skewness and heterogeneity of variance and a repeated measures analysis was performed. Comparing fibrosis we found a significant interaction between condition and region ($p < 0.001$), therefore post-hoc testing was not performed. For adipose tissue there was no significant interaction between condition and region ($p = 0.470$). We found no significant difference between AC and DCM in pattern of adipose tissue ($p = 0.382$). Compared to controls, we found a higher percentage of adipose tissue in AC ($p = 0.028$) and a trend for a higher percentage of adipose tissue in DCM ($p = 0.126$).

DISCUSSION

To the best of our knowledge this is the first study that provides the exact and detailed pattern of fibrosis and fatty changes in *PLN* p.Arg14del mutation associated cardiomyopathy hearts. For this study we developed a novel method for systematic high resolution digital quantification of different tissue types in the heart. This quantification has been applied to Masson's trichrome stained slides of transverse cardiac slices in *PLN* p.Arg14del mutation associated cardiomyopathies. Interestingly we found an overlap in fibrosis and fatty changes between DCM and AC in *PLN* p.Arg14del mutation carriers. Myocardial fibrosis was mainly observed in the posterolateral wall of the left ventricle and in less extent in the posterolateral wall of the right ventricle. Fatty tissue was more pronounced in the myocardium bordering the epicardium of the right ventricle. We found a significant higher percentage of adipose tissue in AC compared to control hearts ($p = 0.028$).

Phospholamban is a regulator of the SERCA2a pump, important for maintaining Ca^{2+} homeostasis and crucial for cardiac contractility.^{6, 13} Phosphorylation of PLN increases SERCA2a activity, leading to increased cardiac relaxation and contractility for the next beat. The precise pathophysiological mechanism in *PLN* p.Arg14del mutation carriers leading to cardiac fibrosis and heart failure remains unknown. Transgenic mice overexpressing the mutant PLN-R14del showed extensive myocardial fibrosis, myocyte disarray, ventricular dilation and premature death, recapitulating human cardiomyopathy.⁹ Co-expression of the normal and mutant protein in HEK-293 cells resulted in SERCA2a super inhibition. From these results it was inferred that the *PLN* p.Arg14del mutation causes inhibition of the SERCA2a pump and thereby leads to disturbed calcium metabolism and subsequently cardiac dysfunction. These data show that this process of reactive fibrosis develops according to a specific pattern, irrespective of the phenotype of the patients. Our small sample size should thereby be taken into account and because of a significant interaction post-hoc testing was not feasible for comparing the mean fibrosis values. This varying phenotype might be influenced by effect modifiers, e.g., epigenetics or intense endurance exercise.¹⁴ In addition, it has been postulated that the pattern of reactive fibrosis is determined by myocardial stress, microvascular dysfunction and sustained activation of neurohormonal and cytokine systems.¹⁵ Future research is needed to elucidate underlying pathophysiology in *PLN* mutation carriers related to the phenotype.

Previous (not *PLN* mutation specific) histopathological studies have shown similar areas of predilection in AC.¹⁶ At first, affected areas in the right ventricle (RV) were described as the classic triangle of dysplasia, including the RV inflow tract, the apex and the RV outflow tract.¹⁷ Further research revealed that AC is not isolated to the RV. In a clinicopathologic study by Corrado et al. left ventricular involvement was found in 76% of cases with AC affecting both the septum and LV free wall, with a predilection for the posteroseptal and posterolateral areas.¹⁸ A recent MRI study in desmosomal mutation positive patients with AC showed involvement of the basal inferior and anterior right ventricle and the posterolateral left ventricle in AC, supporting the presence of a new biventricular triangle in early AC.¹⁹ Our results support the evidence from experimental animal models that the disease process in AC starts on the epicardial side and extends as a wave-front from the epicardium towards the endocardium.²⁰ Clinical diagnosis of AC is made using International Task Force (revised) criteria, including structural (MRI and echocardiogram), histological (e.g. endomyocardial biopsy), electrocardiographic, arrhythmic and genetic features.² The sensitivity of endomyocardial biopsies from the right ventricular septum in AC is low, according to our findings this might also be the case in *PLN* mutation associated cardiomyopathies.²¹

The method of fibrosis quantification presented here can be used for several applications. First, determination of the fibrosis pattern in the heart could provide an important link for genotype-phenotype relationships in genetic cardiomyopathies. Previous studies have proposed morphometric evaluation of either fibrosis or adipocytes in different tissues.²²⁻²⁴ In our analysis fibrosis and fibrofatty replacement can be assessed simultaneously in layer specific detail. We defined different regions of interest to divide the heart in an epicardial, compact and trabeculated layer. In addition, the pattern of fibrosis can be studied in the different regions of both ventricles. By studying the exact fibrosis pattern throughout the heart, patterns of disease might be discovered thereby elucidating mechanisms of pathophysiology. Numerous disease-causing genes for different cardiomyopathies have been identified during the past two decades and the challenge for the future is to link these genetic mutations to specific patterns of disease in the heart.^{20, 25} In future, AC with different underlying causal mutations could be compared to the *PLN* p.Arg14del mutation carriers with AC.

The second application could be validation of myocardial imaging techniques. The reference noninvasive standard for fibrosis detection is late gadolinium enhancement on MRI.³ Adequate correlation to the gold standard of histology is important. Thus far, correlation studies are mostly done with small endomyocardial biopsies that only represent a fraction of the total myocardium or with triphenyl tetrazolium chloride (TTC) stained heart slides.²⁶ Recently, several novel techniques for fibrosis detection have been proposed, including T_1 -mapping, that also require adequate correlation to histology.^{3, 27} Cardiac MRI images obtained before autopsy or heart transplantation, indicating fibrosis could be divided in similar segments to produce a bullseye for comparison with histopathological quantification. However, some heart failure patients are ineligible for MRI because of implanted devices, such as implantable cardioverter-defibrillator, cardiac resynchronization therapy and left ventricular assist devices.

A third potential application could be systematic fibrosis quantification in animal models, for example in models of ischemic²⁸ or non-ischemic cardiomyopathy²⁹. Effects of novel therapies on myocardial fibrosis can be examined in randomized preclinical trials, by systematically comparing the amount of fibrosis on histology. A standardized preclinical model with induced myocardial infarction can be used to study new therapeutics, such as cell therapy, as a strategy to attenuate cardiac fibrosis and stop progression towards heart failure.^{30, 31}

In conclusion, in *PLN* p.Arg14del mutation associated cardiomyopathy myocardial fibrosis is predominantly present in the left posterolateral wall, whereas fatty changes are more pronounced in the wall of the right ventricle. In the analysed heart slices from *PLN* p.Arg14del mutation carriers with non-ischemic cardiomyopathy we found an overlap in distribution pattern between patients with DCM and AC and a significant higher percentage of adipose tissue in AC compared to control hearts ($p=0.028$). We developed a novel method for systematic high resolution digital histological quantification of fibrosis and fatty tissue in the heart. This method can be used to assess cardiac fibrosis and fatty tissue in a broad range of human cardiomyopathies, animal models and can serve as gold standard for noninvasive imaging techniques.

Acknowledgments

We thank Petra van der Kraak-Homoet for technical assistance. We are also grateful to R.K. Stellato, MSc for statistical advice.

REFERENCES

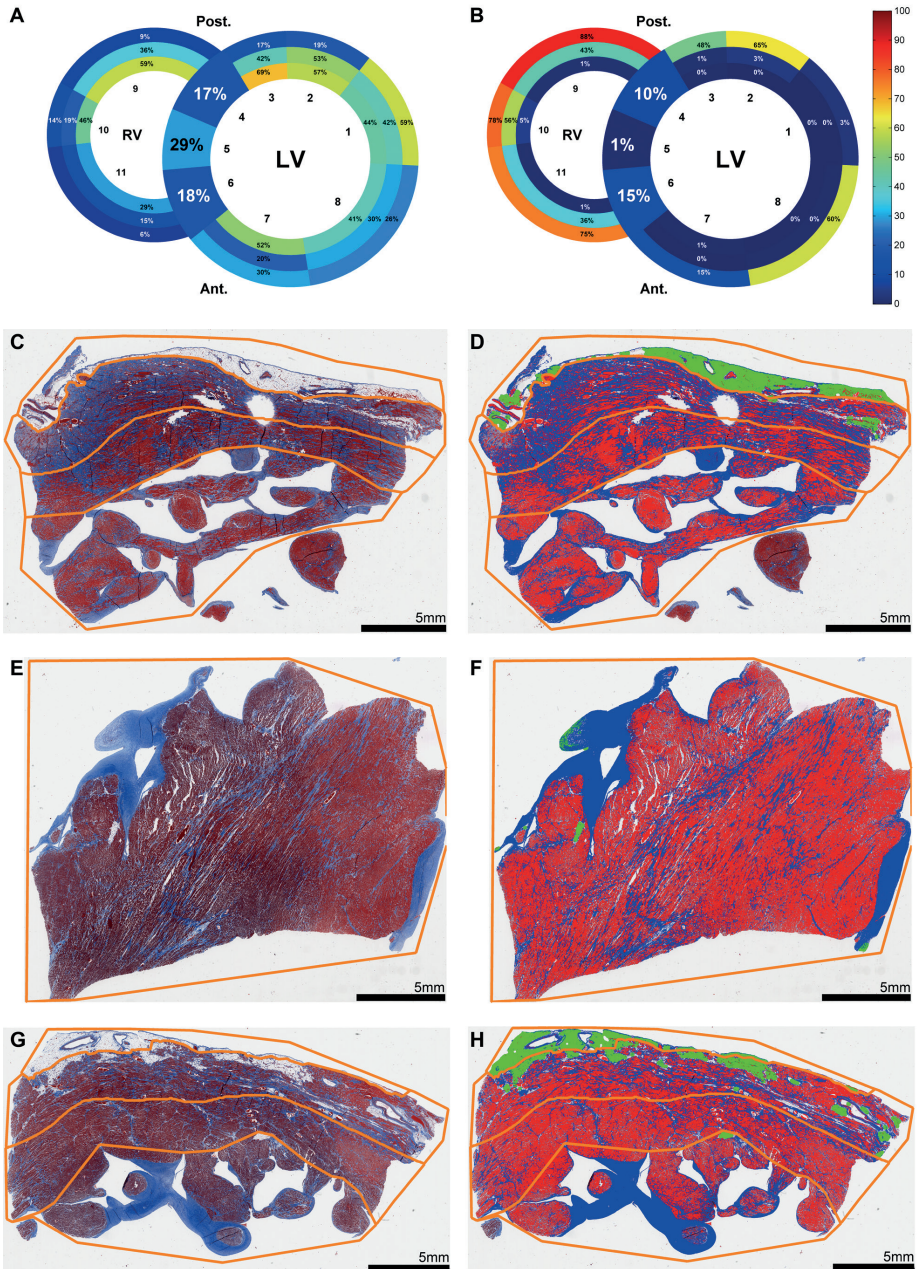
1. Weber KT, Sun Y, Bhattacharya SK, Ahokas RA, Gerling IC. Myofibroblast-mediated mechanisms of pathological remodelling of the heart. *Nat Rev Cardiol.* 2013;10:15-26.
2. Marcus FI, McKenna WJ, Sherrill D, Basso C, Bauce B, Bluemke DA, et al. Diagnosis of arrhythmogenic right ventricular cardiomyopathy/dysplasia: proposed modification of the task force criteria. *Circulation.* 2010;121:1533-41.
3. Mewton N, Liu CY, Croisille P, Bluemke D, Lima JA. Assessment of myocardial fibrosis with cardiovascular magnetic resonance. *J Am Coll Cardiol.* 2011;57:891-903.
4. de Jong S, van Veen TA, de Bakker JM, van Rijen HV. Monitoring cardiac fibrosis: a technical challenge. *Neth Heart J.* 2012;20:44-8.
5. Schmitt JP, Kamisago M, Asahi M, Li GH, Ahmad F, Mende U, et al. Dilated cardiomyopathy and heart failure caused by a mutation in phospholamban. *Science.* 2003;299:1410-3.
6. MacLennan DH, Kranias EG. Phospholamban: a crucial regulator of cardiac contractility. *Nat Rev Mol Cell Biol.* 2003;4:566-77.
7. Haghighi K, Kolokathis F, Pater L, Lynch RA, Asahi M, Gramolini AO, et al. Human phospholamban null results in lethal dilated cardiomyopathy revealing a critical difference between mouse and human. *J Clin Invest.* 2003;111:869-76.
8. Haghighi K, Kolokathis F, Gramolini AO, Waggoner JR, Pater L, Lynch RA, et al. A mutation in the human phospholamban gene, deleting arginine 14, results in lethal, hereditary cardiomyopathy. *Proc Natl Acad Sci U S A.* 2006;103:1388-93.
9. van der Zwaag PA, van Rijsingen IA, Asimaki A, Jongbloed JD, van Veldhuisen DJ, Wiesfeld AC, et al. Phospholamban R14del mutation in patients diagnosed with dilated cardiomyopathy or arrhythmogenic right ventricular cardiomyopathy: evidence supporting the concept of arrhythmogenic cardiomyopathy. *Eur J Heart Fail.* 2012;14:199-207.
10. Huisman A, Looijen A, van den Brink SM, van Diest PJ. Creation of a fully digital pathology slide archive by high-volume tissue slide scanning. *Hum Pathol.* 2010;41:751-7.
11. Ruifrok AC, Johnston DA. Quantification of histochemical staining by color deconvolution. *Anal Quant Cytol Histol.* 2001;23:291-9.
12. Pratt WK. Digital image processing: PIKS Scientific inside. 4th ed. Hoboken, New Jersey: Wiley; 2007.
13. Gustavsson M, Verardi R, Mullen DG, Mote KR, Traaseth NJ, Gopinath T, et al. Allosteric regulation of SERCA by phosphorylation-mediated conformational shift of phospholamban. *Proc Natl Acad Sci U S A.* 2013;110:17338-43.
14. La Gerche A, Burns AT, Mooney DJ, Inder WJ, Taylor AJ, Bogaert J, et al. Exercise-induced right ventricular dysfunction and structural remodelling in endurance athletes. *Eur Heart J.* 2012;33:998-1006.
15. Masci PG, Barison A, Aquaro GD, Pingitore A, Mariotti R, Balbarini A, et al. Myocardial delayed enhancement in paucisymptomatic nonischemic dilated cardiomyopathy. *Int J Cardiol.* 2012;157:43-7.
16. Basso C, Corrado D, Marcus FI, Nava A, Thiene G. Arrhythmogenic right ventricular cardiomyopathy. *Lancet.* 2009;373:1289-300.
17. Marcus FI, Fontaine GH, Guiraudon G, Frank R, Laurenceau JL, Malergue C, et al. Right ventricular dysplasia: a report of 24 adult cases. *Circulation.* 1982;65:384-98.
18. Corrado D, Basso C, Thiene G, McKenna WJ, Davies MJ, Fontaliran F, et al. Spectrum of clinicopathologic manifestations of arrhythmogenic right ventricular cardiomyopathy/dysplasia: a multicenter study. *J Am Coll Cardiol.* 1997;30:1512-20.
19. Te Riele AS, James CA, Philips B, Rastegar N, Bhonsale A, Groeneweg JA, et al. Mutation-positive arrhythmogenic right ventricular dysplasia/cardiomyopathy: the triangle of dysplasia displaced. *J Cardiovasc Electrophysiol.* 2013;24:1311-20.
20. Basso C, Bauce B, Corrado D, Thiene G. Pathophysiology of arrhythmogenic cardiomyopathy. *Nat Rev Cardiol.* 2012;9:223-33.
21. Basso C, Ronco F, Marcus F, Abudurehman A, Rizzo S, Frigo AC, et al. Quantitative assessment of endomyocardial biopsy in arrhythmogenic right ventricular cardiomyopathy/dysplasia: an in vitro validation of diagnostic criteria. *Eur Heart J.* 2008;29:2760-71.

22. Krajewska M, Smith LH, Rong J, Huang X, Hyer ML, Zeps N, et al. Image analysis algorithms for immunohistochemical assessment of cell death events and fibrosis in tissue sections. *J Histochem Cytochem.* 2009;57:649-63.
23. Farris AB, Adams CD, Brousaides N, Della Pelle PA, Collins AB, Moradi E, et al. Morphometric and visual evaluation of fibrosis in renal biopsies. *J Am Soc Nephrol.* 2011;22:176-86.
24. Osman OS, Selway JL, Kepczynska MA, Stocker CJ, O'Dowd JF, Cawthorne MA, et al. A novel automated image analysis method for accurate adipocyte quantification. *Adipocyte.* 2013;2:160-4.
25. Jacoby D, McKenna WJ. Genetics of inherited cardiomyopathy. *Eur Heart J.* 2012;33:296-304.
26. Schalla S, Bekkers SC, Dennert R, van Suylen RJ, Waltenberger J, Leiner T, et al. Replacement and reactive myocardial fibrosis in idiopathic dilated cardiomyopathy: comparison of magnetic resonance imaging with right ventricular biopsy. *Eur J Heart Fail.* 2010;12:227-31.
27. Moon JC, Messroghli DR, Kellman P, Piechnik SK, Robson MD, Ugander M, et al. Myocardial T1 mapping and extracellular volume quantification: a Society for Cardiovascular Magnetic Resonance (SCMR) and CMR Working Group of the European Society of Cardiology consensus statement. *J Cardiovasc Magn Reson.* 2013;15:92.
28. Pop M, Ghugre NR, Ramanan V, Morikawa L, Stanis G, Dick AJ, et al. Quantification of fibrosis in infarcted swine hearts by ex vivo late gadolinium-enhancement and diffusion-weighted MRI methods. *Phys Med Biol.* 2013;58:5009-28.
29. Gho JM, Kummeling GJ, Koudstaal S, Jansen of Lorkeers SJ, Doevendans PA, Asselbergs FW, et al. Cell therapy, a novel remedy for dilated cardiomyopathy: A systematic review. *J Card Fail.* 2013;19:494-502.
30. Elnakish MT, Kuppusamy P, Khan M. Stem cell transplantation as a therapy for cardiac fibrosis. *J Pathol.* 2013;229:347-54.
31. Koudstaal S, Jansen of Lorkeers S, Gho JM, van Hout GP, Jansen MS, Grundeman PF, et al. Myocardial infarction and functional outcome assessment in pigs. *J Vis Exp.* 2014.

Supplementary Figure 1 Schematic overview of Case 6 Arrhythmogenic Cardiomyopathy with ► representative images.

A,B, schematic heart slice overview of mean fibrosis (**A**) and adipose tissue (**B**). Corresponding slide numbers are shown inside the inner rings (n = 11). Mean percentage of fibrosis (**A**) or adipose tissue (**B**) per area have been superimposed on the overview (values rounded to the nearest whole number, values <20% are shown in white to improve readability). **C,E,G**, raw microscopic slide images after Masson's trichrome staining, respectively corresponding to slide 1, 5 and 7. **D,F,H**, corresponding slides after digital processing. Red: cardiomyocytes. Blue: connective tissue. Pseudo green: adipose tissue. The slides depicted in Figure 1C-F are also derived from the same heart, 1C,D correspond to slide 3 and 1E,F correspond to slide 10.

SUPPLEMENTARY MATERIALS



Supplementary Table 1 Mean percentage of fibrosis and adipose tissue per region and condition.

		Control (n=3)		AC (n=3)		DCM (n=5)	
		Mean (%)	SD	Mean (%)	SD	Mean (%)	SD
Fibrosis	Region 1	2.5	0.3	40.1	8.8	38.9	10.5
	Region 2	2.2	0.6	25.4	9.7	31.2	11.3
	Region 3	2.3	0.4	17.7	4.3	33.8	12.0
	Region 4	1.8	0.7	18.5	10.8	34.0	14.4
	Region 5	2.4	0.8	26.4	8.2	30.6	10.2
	Region 6	2.4	0.4	37.6	2.3	34.5	13.5
	Region 7	4.6	1.6	24.9	3.6	23.1	9.3
	Region 8	5.1	2.0	19.7	1.7	19.3	9.2
Adipose tissue	Region 1	0.7	0.7	6.9	4.7	5.8	6.0
	Region 2	0.6	0.6	10.1	10.8	5.7	9.7
	Region 3	0.7	0.4	3.6	3.9	1.8	1.1
	Region 4	2.0	2.5	4.9	2.7	2.5	2.2
	Region 5	0.7	0.4	6.4	7.5	1.9	0.7
	Region 6	0.7	0.2	7.7	5.6	2.4	1.1
	Region 7	7.8	6.1	37.2	14.1	26.1	20.0
	Region 8	14.4	5.9	28.9	4.1	24.3	12.0

Regions correspond to the depicted regions in Figure 6C. AC, Arrhythmogenic Cardiomyopathy; DCM, Dilated Cardiomyopathy; SD, standard deviation.

Chapter 7



A Systematic Comparison of Cardiovascular Magnetic Resonance and High Resolution Histological Fibrosis Quantification in a Chronic Porcine Infarct Model

Submitted

René van Es^{1,*}, Johannes M.I.H. Gho^{1,*}, Frebus J. van Slochteren², Sanne J. Jansen of Lorkeers¹, Allard J. Hauer¹, Joep W.M. van Oorschot³, Pieter A. Doevendans¹, Tim Leiner³, Aryan Vink⁴, Folkert W. Asselbergs^{1,5,6}, Steven A.J. Chamuleau¹

*Contributed equally to this article and are shared first authors

¹ Department of Cardiology, Division Heart and Lungs, University Medical Center Utrecht, Utrecht, the Netherlands

² Interuniversity Cardiology Institute of the Netherlands, Utrecht, the Netherlands

³ Department of Radiology, University Medical Center Utrecht, Utrecht, the Netherlands

⁴ Department of Pathology, University Medical Center Utrecht, Utrecht, the Netherlands

⁵ Durrer Center for Cardiogenetic Research, ICIN-Netherlands Heart Institute, Utrecht, the Netherlands

⁶ Institute of Cardiovascular Science, Faculty of Population Health Sciences, University College London, London, United Kingdom

ABSTRACT

Background

The noninvasive reference standard for myocardial fibrosis detection on cardiovascular magnetic resonance imaging (CMR) is late gadolinium enhancement (LGE). Currently there is no consensus on the preferred method for LGE quantification. Moreover myocardial wall thickening (WT) and strain are measures of regional deformation and function. Aim of this research was to systematically compare *in vivo* CMR parameters, such as LGE, WT and strain, with histological fibrosis quantification.

Methods

Eight weeks after 90 minutes ischemia/reperfusion of the LAD artery, 16 pigs underwent *in vivo* Cine and LGE CMR. Histological sections from transverse heart slices were digitally analysed for fibrosis quantification. Mean fibrosis percentage of analysed sections was related to the different CMR techniques (using segmentation or feature tracking software) for each slice using a linear mixed model analysis.

Results

The full width at half maximum (FWHM) technique for quantification of LGE yielded the highest R^2 of 60%. Cine derived myocardial WT explained 16 to 36% of the histological myocardial fibrosis. The peak circumferential and radial strain measured by feature tracking could explain 15% and 10% of the variance of myocardial fibrosis, respectively.

Conclusions

This novel method to systematically compare CMR image data with digital histological images is feasible. Myocardial WT and strain were only modestly related with the amount of fibrosis. The fully automatic FWHM analysis technique is the preferred method to detect myocardial fibrosis.

BACKGROUND

Myocardial fibrosis has been associated with heart failure and can act as a substrate for cardiac arrhythmias.¹ Following myocardial infarction (MI), loss of cardiomyocytes leads to reparative fibrosis with replacement by connective tissue. Noninvasive assessment of cardiac fibrosis is important for diagnosis, predicting prognosis and treatment planning.² The noninvasive reference standard for fibrosis detection is late gadolinium enhancement (LGE) on cardiovascular magnetic resonance imaging (CMR). Since there is no consensus on the LGE quantification techniques³, a detailed comparison with the reference standard of histological analysis is important. For example, accurate fibrosis quantification can predict reversible myocardial dysfunction after revascularization.^{4,5} Thus far, mainly correlation studies have been performed with small endomyocardial biopsies, triphenyl tetrazolium chloride stained or *ex vivo* hearts.⁶⁻⁸ Studies using whole heart slices are scarce⁹, especially for focal fibrosis. While LGE provides an accurate qualitative measure of fibrosis, it requires contrast administration with potential adverse effects and does not provide a quantitative or direct measurement of cardiac collagen.^{2,10} The result of LGE differs between different imaging studies and by variable intensity threshold settings and thus relies on an adequate imaging protocol. Functional assessment of the local myocardium is typically performed visually on cine CMR images. Quantitative assessment of local myocardial function (e.g., wall thickening) can also be performed with (semi-)automatic segmentation software packages.^{11,12} More recently, feature tracking (FT) has been introduced as a method to assess local myocardial deformation (strain) using cine images without the need for tagged CMR scans.¹³ Feature tracking is relatively quick in post processing, has shown reasonable agreement with tagging CMR when looking at global strain from complete slices and might be usable with different field strengths.¹⁴⁻¹⁶ However, there is debate about the agreement between strain derived from FT and tagging CMR at a segmental level, as multiple studies found poor intra- and interobserver variability for segmental strain.^{14,17-19}

We have recently developed a method for high resolution systematic digital histological quantification of (diffuse and focal) cardiac fibrosis in a whole heart slice²⁰, which can provide a detailed reference for comparing different CMR imaging techniques. The aim of this study was to systematically analyse *in vivo* CMR derived parameters and high spatial resolution digital fibrosis quantification in a chronic porcine infarct model to compare different CMR techniques with myocardial fibrosis assessment. Parameters of interest are: LGE CMR, myocardial strain and wall thickening (WT). Myocardial strain and myocardial WT are respectively assessed by FT and manual segmentation on cine MRI.

METHODS

Animal model

All *in vivo* experiments were conducted in accordance with the Guide for the Care and Use of Laboratory Animals prepared by the Institute of Laboratory Animal Resources. Experiments were approved (protocol no.: 2012.II.09.145) by the local Animal Experiments Committee (DEC) (Utrecht, the Netherlands).

Our protocol regarding a porcine chronic MI model has been described in detail before.²¹ Eight weeks after 90 minutes ischemia/reperfusion of the proximal left anterior descending artery (LAD), 16 Dalland Landrace pigs (79.8±5.8 kg; 6 months old; see Supplementary Table 1) under continuous anesthesia underwent *in vivo* CMR on a clinical 3T scanner (Achieva TX, Software Release 3.2.1, Philips Healthcare, Best, the Netherlands).

CMR

Pigs were positioned supine with a dedicated 32-channel phased-array receiver coil over the chest and scanned using a standardized protocol. For image planning scout images were obtained in short-axis and two-chamber long-axis views. ECG-gated steady-state free precession (SSFP) short-axis (from apex to base of LV) and two chamber long-axis cine images were acquired. Thirty frames were acquired per RR cycle. Cine parameters: echo time (TE)/repetition time (TR) 1.6/3.2ms, 13 slices, slice thickness 8 mm, resolution = 2x2mm, Field of voxel (FOV) = 320x320mm², bandwidth = 1200Hz and flip angle = 45°.

LGE

Late gadolinium enhancement CMR was performed using an inversion recovery 3D-turbo-gradient-echo-technique 15 minutes after an intravenous bolus injection of 0.2 ml/kg gadobutrol (Gadovist, Bayer Healthcare, Berlin, Germany). First, a look-locker scout was performed for the optimal inversion time. Acquisition parameters for the LGE scan: inversion time (TI) = 200-270ms, TE/TR = 1.5/4.7ms, slice thickness = 6mm, spatial resolution = 1.5x1.5mm², FOV = 300x300mm², flip angle = 25°, 63 TFE shots, bandwidth = 300Hz, number of signals averaged = 2, SENSE acceleration = 2.

CMR imaging analysis

Segment

Offline image analysis to derive WT and LGE was performed using Segment software version v1.9 R3590 (<http://segment.heiberg.se>, Medviso AB, Lund, Sweden).¹² In all datasets, the short-axis slice corresponding to the histological slice was selected based on its location, and used for further analysis (Figure 1). In the short-axis cine images, LV endo- and epicardial borders were manually segmented in all time frames. The segmentation of the end-diastolic frame was copied to the corresponding LGE slice (Figure 1C). Manual adjustment of the segmentation was performed if necessary. From the short-axis cine dataset the absolute WT (mm) per image frame of 60 LV segments was exported. The end-systolic absolute WT of each segment was used for further analysis.

Feature Tracking

Cardiac strain analysis by FT was performed using the Image-Arena 2D Cardiac Performance Analysis software toolbox version 1.2 (TomTec Imaging Systems, Unterschleissheim, Germany). The end-diastolic endo- and epicardial contours of the slice were manually traced (Figure 1B) by two authors simultaneously (R.v.E. and J.G.), based on mutual agreement. The mid-lateral point along the endocardial contour was marked as an anatomical reference and data was exported for registration purposes. For all 48 segments, raw data containing circumferential

strain (ϵ_{cc}), radial strain (ϵ_{rr}) and WT (*endo to epi distance*), was exported and used for further analysis (Figure 1E).

Viability analysis

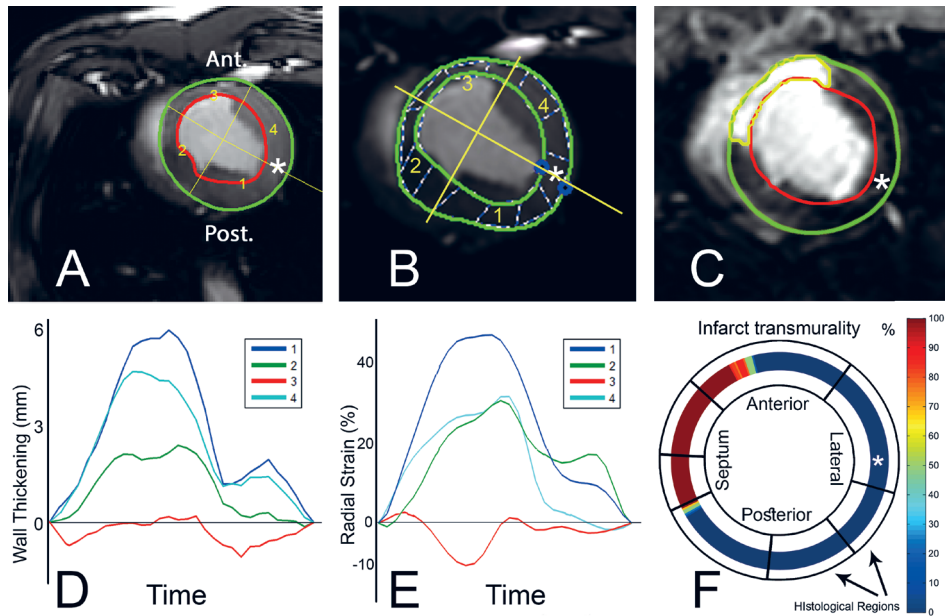


Figure 1 Cardiovascular Magnetic Resonance Analysis Methods

A-C. The endo- and epicardial segmentations of the wall thickening (Segment), feature tracking (Image-Arena) and LGE (Segment) analyses respectively. The asterisk (*) indicates the point in the mid-lateral wall that was used for registration between CMR and histology. **B.** The dashed lines are used by Image-Arena as an aid for visualization of regional deformation. **C.** The automatic FWHM infarct delineation is shown in C (yellow). **D.** Resulting WT patterns of the four segments shown in **A**, the actual WT analysis used 60 sections. **E.** Radial strain analysis of 48 segments averaged to result in 4 segments (Image-Arena); shown in **B**, the actual radial strain analysis used 48 segments. **F.** The %TM data was exported in 360 segments. The digitized annotation map of the LV, as shown in Figure 2B, is then projected onto the LGE exported data for analysis. Note: the four segments in subfigures A, B, D and E were shown as a simplified example. The actual measurements used for further analysis consisted of 60 (**A&D**) and 48 (**B&E**) segments. FWHM = full width at half maximum; LGE = late gadolinium enhancement; LV = left ventricle; %TM = fraction of transmurality; WT = wall thickening.

Segment

For viability analysis of short-axis LGE datasets, scar was delineated using automatic full width at half maximum (FWHM) (Figure 1C), standard deviation (SD) from remote (2, 3 and 5SD) and manually corrected SD from remote (2, 3 and 5SD) algorithms. For the SD methods, the remote healthy myocardium of the lateral wall was selected as remote. Manual corrections of the infarct area after automatic segmentation were performed in the manually corrected subgroups. These corrections were performed based on the expected infarct area in the LAD territory and any obvious artefacts. These regions were manually removed from the segmented scar. The fraction

of area based transmuralty (%TM), the infarct size fraction of the wall thickness, was analysed in 360 equal segments over the LV wall. For myocardial signal intensity (MSI) and each scar delineation method the %TM was exported for further analysis.

Histology

Following CMR, the animals were sacrificed by exsanguination under general anaesthesia and the hearts were excised and cut into transverse (short-axis) 1 cm thick slices from apex to base. Each third transverse slice was fixed in formalin, cut into smaller sections and an overview of the heart slice was drawn to annotate the origin of each tissue specimen (Figure 2A). These sections were embedded in paraffin and stained with Masson's trichrome. The slides were scanned at 20X magnification as described before²². Images were extracted using Aperio ImageScope v.12.0.0.5039 (Aperio, Vista, CA, USA) and resized to 10% for digital analysis.

Histological analysis

Digital histological analysis was performed systematically as previously described, using the in-house developed open source software package Fibroquant (<http://sourceforge.net/projects/fibroquant>).²⁰ The epicardium, defined as the outer region of fatty tissue bordered by the first row of cardiomyocytes, was excluded from further analysis. The remaining myocardium, including the compact and trabeculated region was analysed as a whole. The percentage of connective tissue (blue), cardiomyocytes (red) and adipose tissue (cells with non-stained cytoplasm; pseudo green) was digitally quantified using Fibroquant. The results were annotated to their corresponding heart region (Figure 2A) and transformed to a standardized schematic overview (Figure 2B).

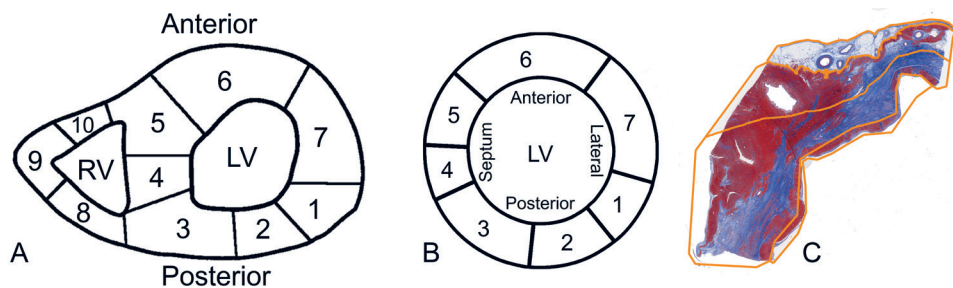


Figure 2 - Digital Histological Analysis Methods

A. Example of map containing the origin of the histological sections in the heart slice of one animal. **B.** The digitized left ventricular annotation map of image A. **C.** The manual tracings of the four regions across the histological myocardial section, corresponding to location 5 in A and B. The orange lines depict the endocardial to epicardial subsegmentation.

Matching MRI with histology

After the construction of the standardized schematic overview, the exported high detail MRI data was averaged over the regions delineated by the histological sections (see example, Figure

1F). A landmark in the mid-lateral wall of all datasets was used as a reference point for registration. This reference was defined as the point opposite both hinge points of the right ventricle (RV).

Statistical analysis

Statistics were performed using IBM SPSS Statistics (Version 20.0, IBM Corporation, Armonk, New York, United States). We compared different CMR techniques with percentages of fibrosis per section using a linear mixed model analysis. For fibrosis, the amount of residual variance (σ^2) within the animals and the variance (intercept, τ) between animals were calculated (null model). Subsequently, CMR parameters were added to the model (full model). R^2 (Snijders & Bosker, 2012), was calculated as 100% minus the ratio of the full and null models (equation 1)^{23,24}, representing the explained variance.

$$R^2 = 1 - \frac{\sigma_{full}^2 + \tau_{00full}}{\sigma_{null}^2 + \tau_{00null}} \quad (\text{eq. 1})$$

RESULTS

Histology

A total of 116 histological sections (16 animals) were successfully stained, segmented (Figure 2C) and analysed (see example, Figure 3A&B). Digital maps with the annotated origins of each histological section were used to construct schematic histological overviews for each animal (see example, Figure 3C). One animal (8 sections) was excluded from further analysis because of lack of histological fibrosis due to a sampling error (Supplementary Figure1), 108 sections remained. Mean fibrosis percentages (15 animals) were log transformed to reduce right-skewness and heterogeneity of variance. Myocardial fibrosis was mainly observed in the anteroseptal wall (Figure 3D), corresponding to the LAD territory. The 8-week old LAD infarct model used in this study yielded fibrosis percentages of 57% at maximum.

Cine CMR analysis

Segment

Myocardial WT curves were successfully extracted for 15 animals in 60 segments. Mean end systolic absolute WT was 2.4 ± 2.4 mm (range -2.1 to 7.2 mm) (Figure 4A, 5A). The explained variance of WT for histological myocardial fibrosis was 36% (Table 1).

Feature tracking

Data of 15 animals was successfully extracted and analysed using 48 segments. After matching the data according to histological sections the mean ϵ_{cc} , ϵ_{rr} and WT were $-12.1 \pm 12.1\%$ (range -38.5 to 24.3%), $26.9 \pm 34.7\%$ (range -26.0 to 171.9%) and -1.6 ± 2.5 mm (range -4.6 to 7.7 mm), respectively (Figure 4B, 5B-D). Feature tracking derived ϵ_{cc} , ϵ_{rr} and WT explained 15%, 10% and 16% of myocardial fibrosis, respectively (Table 1).

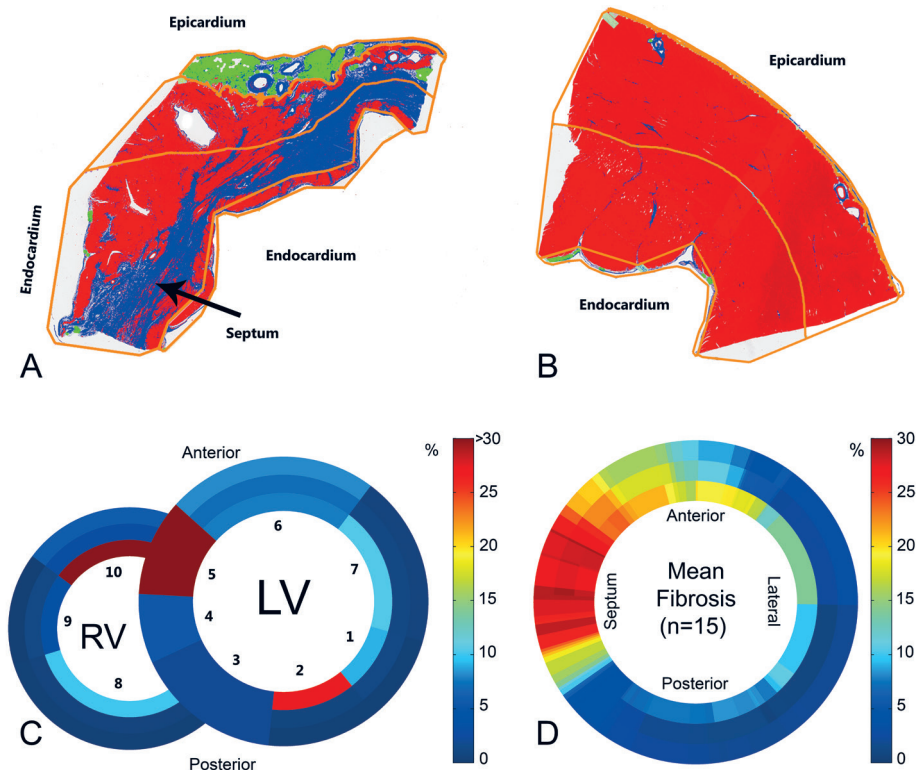


Figure 3 Results of Histological Analysis

A-B. Results of the histological analyses of sections 5 and 7, respectively (Figure 2A&B). Connective tissue (blue), cardiomyocytes (red) and adipose tissue (cells with non-stained cytoplasm; pseudo green). The orange lines indicate the endocardial to epicardial subsegmentation. **C-D.** The colorbar denotes the percentage of fibrosis found based on histology. **C.** Analysis of the whole heart of this animal, the numbers indicated the histological sections, 5 and 7 correspond to subfigures **A** and **B**, respectively. **D.** Mean fibrosis content in the left ventricle of all animals ($n=15$). LV = left ventricle; RV = right ventricle.

Viability CMR analysis

Segment

The mean LGE scar transmural and MSI (15 animals) is shown in Figure 6. The variance between animals was small (range 0 to 0.14) (Table 1). The automatic FWHM algorithm resulted in 60% explained variance for histological myocardial fibrosis. The manually corrected SD from remote methods for LGE analysis yielded an explained variance between 58 - 60%. The variance within animals (σ^2) decreased (0.94 to 0.65) with more stringent automatic segmentation methods (2-5 SD), while it remained similar in the manually edited SD from remote subgroup. The MSI of the LGE images, in which no additional interaction is required, explained the myocardial fibrosis for 52%.

Table 1 Comparison of Wall Thickening, Strain and LGE with Histological Fibrosis

n = 15	σ^2_{full}	τ_{full}	R ²
Cine WT (Segment)	1.07	0.02	36%
Cine WT (Image-Arena)	1.44	0*	16%
Radial Strain	1.54	0*	10%
Circumferential Strain	1.45	0*	15%
2SD	0.94	0.07	41%
3SD	0.82	0.11	46%
5SD	0.65	0.12	55%
2SD Manual Correction	0.66	0.03	60%
3SD Manual Correction	0.63	0.05	60%
5SD Manual Correction	0.65	0.07	58%
FWHM	0.62	0.07	60%
Myocardial signal intensity	0.68	0.14	52%

The null model used in the statistical analysis containing the variance in myocardial fibrosis was expressed as $\sigma^2_{full} + \tau_{full} = 1.71^*$. The full model containing the unexplained variance in myocardial fibrosis after adding explanatory CMR parameters is expressed as $\sigma^2_{full} + \tau_{full}$. The resulting R² value was calculated as (eq. 1).

* = Although all convergence criteria were satisfied, the hessian matrix was not positive definite, as a consequence the residual and random intercept variance were pooled. FWHM = full width at half maximum; LGE = late gadolinium enhancement; R² = explained variance of myocardial fibrosis; SD = standard deviation; σ^2 = intra animal variance; τ = inter animal variance; WT = wall thickening.

Scar transmuralty compared to fibrosis and functional parameters

In the boxplots (Figure 7), the median fibrosis ranged from 1.4% in the segments without LGE to 22.7% in the segments with 75-100% infarct transmuralty using FWHM. Median WT ranged from 4.3 to 0.0mm and ϵ_{cc} and ϵ_{rr} ranged from -15.0% to -7.7% and 40.0% to -1.0% respectively between the infarct transmuralty from 0 to 100%.

DISCUSSION

This study demonstrates a novel systematic method to compare different *in vivo* CMR techniques with high spatial resolution histological analyses in a chronic porcine infarct model. To the best of our knowledge, this is the first time such a systematic comparison has been performed and this method can be readily adapted for use with other imaging modalities such as SPECT, CT, PET and echocardiography. For LGE imaging, we found that the FWHM and the 2, 3 or 5SD from remote methods with manual correction were the best methods to quantify the amount of myocardial fibrosis. Although it is expected that measures of myocardial deformation would be affected in infarcted myocardium, myocardial WT and strain were only modestly related with the amount of myocardial fibrosis.

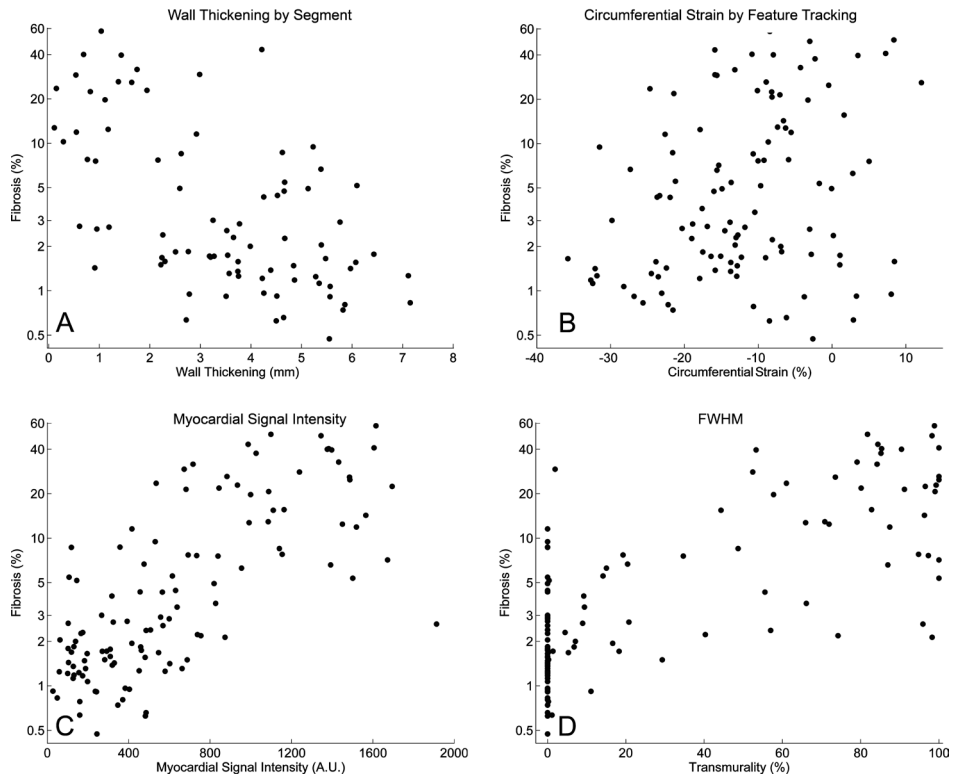


Figure 4 Comparisons of Cardiovascular Magnetic Resonance Parameters and Fibrosis (n = 15)

The dots represent 108 separate sections from 15 animals. R^2 values (explained variance) are derived from a separate linear mixed model analysis. Fibrosis was compared with: **A.** Wall thickening results of the cine analysis (Segment); **B.** Circumferential strain analysis (Image-Arena); **C.** Myocardial signal intensity analysis (Segment); **D.** LGE FWHM analysis (Segment). FWHM = full width at half maximum; LGE = late gadolinium enhancement.

Myocardial WT

The reference standard for the noninvasive assessment of cardiac anatomy and function is CMR². While cine imaging is not intended for fibrosis quantification, MI is associated with a lower amount of WT in the infarct area.⁶ We measured myocardial WT using two different software analysis tools, Segment and Image-Arena. Our analysis shows that WT derived from Segment performs better in explaining myocardial fibrosis compared to Image-Arena ($R^2 = 36\%$ vs. 16%). In Segment, both the endo- and epicardial contours of the selected slice were manually traced in every frame. In Image-Arena the segmentation was performed in only one frame and the tracing in subsequent frames was automatically propagated by the software algorithm. The FT workflow could limit accuracy and cause variability, due to the lack to perform manual adjustments in multiple frames which is inherent to the algorithm. Furthermore, the slightly lower spatial resolution of the FT export compared to the Segment export (48 vs. 60 segments, respectively) may have influenced the results. Additionally, through plane motion and filtering

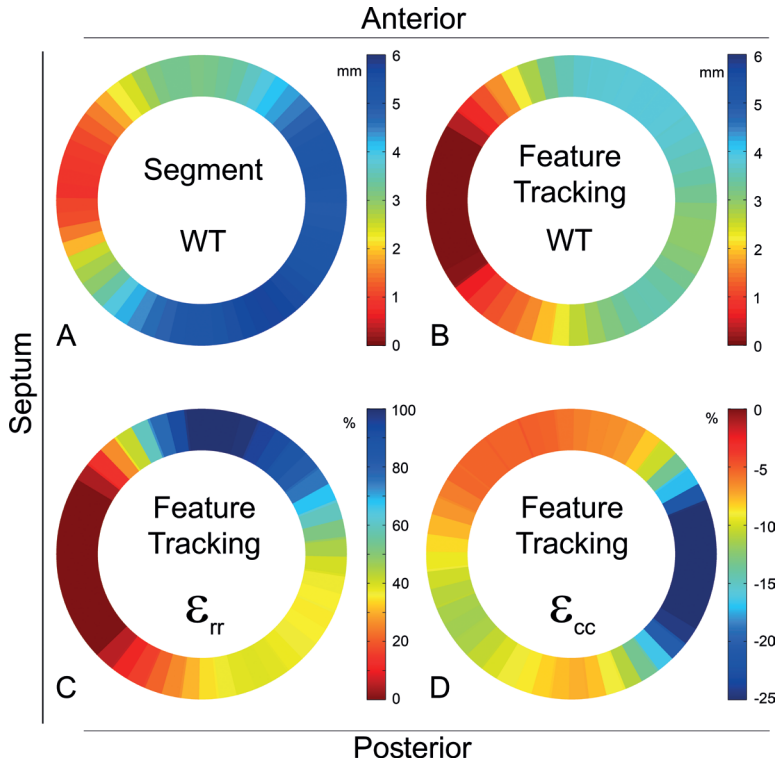


Figure 5 Mean Wall Thickening and Strain Analysis (n = 15)

A. The averaged results of the cine WT analysis (Segment). **B-D.** The averaged results of the feature tracking analysis, the WT, circumferential (ϵ_{cc}) and radial (ϵ_{rr}) strain respectively (Image-Arena). ϵ_{cc} = circumferential strain; ϵ_{rr} = radial strain; WT = wall thickening.

algorithms resulting in loss of detail are likely to introduce erroneously tracked features, thereby affecting the FT results.

Cardiac deformation

In our analysis of the LV slices, both radial and circumferential strain based on FT were poorly associated with myocardial fibrosis ($R^2 = 10\%$ and 15% respectively). As previously described by Cowan et al., differences in strain could occur between two regions indicated as healthy by LGE.¹⁹ From our study it can be concluded that FT based strain imaging is less applicable to identify regional myocardial fibrosis in this experimental infarct model. This might be caused by the fact that strain is not a strictly local phenomenon, but is the resulting deformation caused by the contraction of cardiomyocytes in the vicinity of the infarct. Although local myocardial deformation assessment is not a direct measurement of fibrosis, strain analysis might supply new insights in local cardiac biomechanics after ischemic injury, but rigorous clinical validation is required.

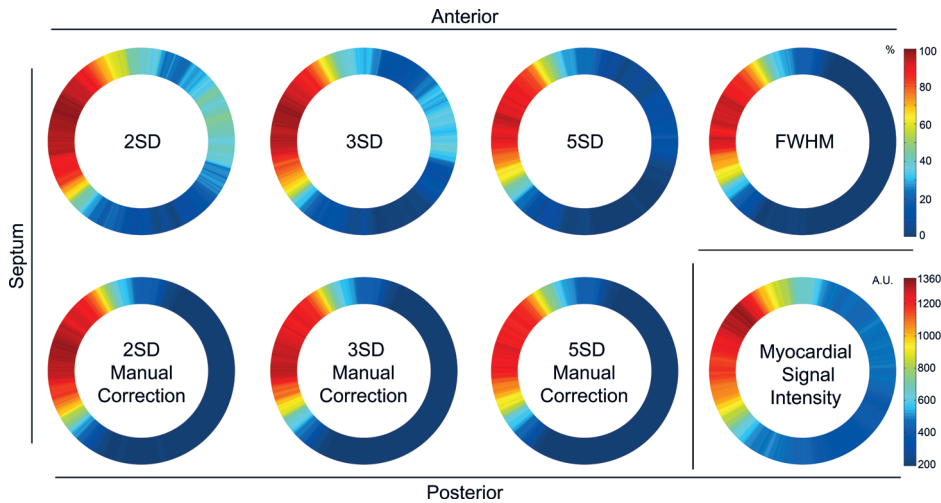


Figure 6 Mean Late Gadolinium Enhancement Analysis (n = 15)

Averaged results of the fraction of transmural in 360 segments for the 2, 3 and 5SD automatic methods, the 2, 3 and 5SD from remote manually corrected subgroup and the fully automatic FWHM analysis. In the bottom right corner, the averaged myocardial signal intensity is shown. A.U. = arbitrary unit; FWHM = full width at half maximum; SD = standard deviation.

Viability

Compared to the reference standard of fibrosis on histology, FWHM and the 2, 3 or 5SD from remote methods with manual correction were the best explanatory variables for variance in fibrosis. The FWHM technique uses half of the maximal signal intensity within the scar region as a threshold to determine the infarct area.²⁵⁻²⁷ The used SD from remote methods delineate scar by pixels with an image intensity higher than the mean plus 2, 3 or 5SD from the mean in a non-infarcted remote region.⁶ Late gadolinium enhancement has been previously validated *ex vivo* using a myocardial signal intensity analysis compared to quantitative histopathological sections with fibrosis to discriminate between healthy myocardium, dense scar and the border zone.⁸ A previous clinical study showed limited reproducibility of the SD from remote techniques with manual correction and found the FWHM technique the most reproducible method.³

In our analysis, the MSI measured from LGE images resulted in worse explanatory values for myocardial fibrosis compared to FWHM (52% vs. 60%). The between animal variance of LGE MSI compared to FWHM was higher (0.14 vs. 0.07) which might be explained by MSI variation due to small differences in gadolinium injection to acquisition time. Because of the improved explanation for myocardial fibrosis and reduced manual interaction needed, FWHM would be the preferred method of choice from this study for infarct quantification on LGE CMR. In diffuse fibrosis, with less distinct LGE or remote areas, the FWHM method could be technically more difficult and T1-mapping might be more promising.⁹

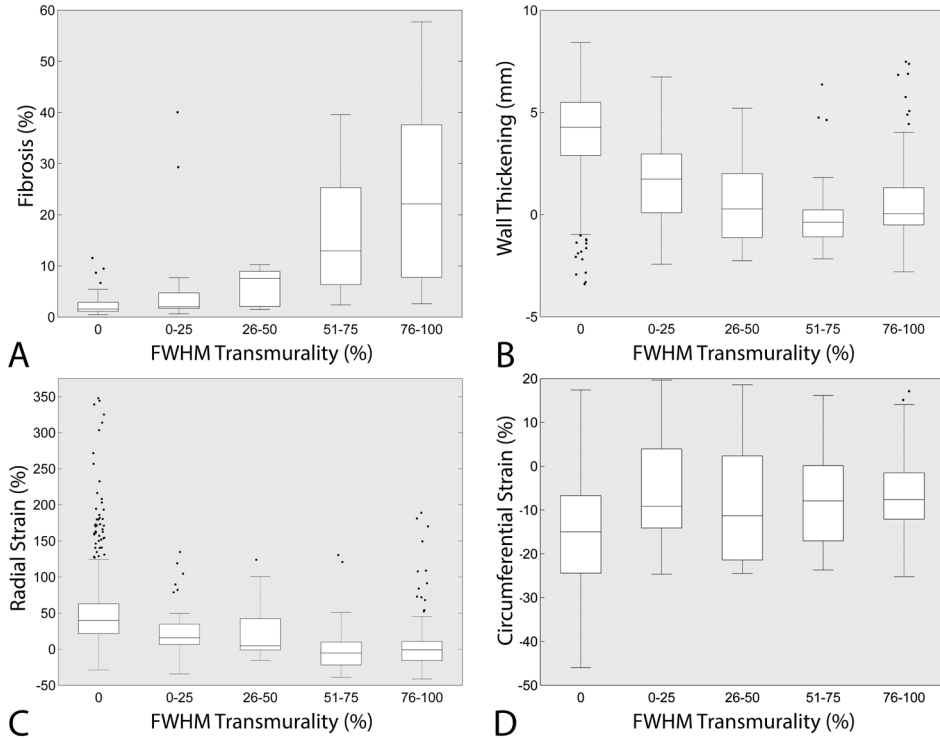


Figure 7 Boxplots of Late Gadolinium Enhancement Scar Transmurality and Fibrosis or Functional Parameters (n = 15)

A-D. Late gadolinium enhancement fraction of transmurality based on the FWHM algorithm divided in different subgroups (0, 0-25, 26-50, 51-75 and 76-100%) compared to fibrosis percentage, wall thickening from feature tracking, and radial or circumferential strain from FT. The dots represent outliers. FT = feature tracking; FWHM = full width at half maximum; WT = wall thickening.

Limitations

The final resolution of the comparison between histology and MRI is determined by the method of histological sections cut from the LV, typically 7 or 8 sections per heart slice in this study. Only one short-axis slice of the CMR images was used and the high detail MRI data was averaged to match exactly with the histology data, leading to a loss of detail, especially along the infarct border zone. For future studies dissection of the entire heart using a (cryo)microtome could be considered to preserve the gross cardiac anatomy. Resulting high resolution images could later be analyzed and subdivided using automated algorithms to allow for a more detailed comparison with high detail imaging modalities.

The selected mid-lateral point was used as a landmark for registration of the different modalities due to a standardized workflow for histological processing as it was used as a starting point for cutting the heart slice into smaller sections.²⁰ For future studies we recommend to use anatomical features (e.g. RV hinge points) as landmarks for image registration.

In the assessment of local cardiac function (e.g., WT, ϵ_{cc} and ϵ_{rr}), next to the known poor intra-

and interobserver variability associated with FT analysis on a segmental level, it is likely that a higher fibrosis percentage would have led to a stronger relation with worsening of functional parameters. The RV was excluded from all comparisons because the conventional analyses applied on the cine and LGE images in this study did not allow an accurate analysis of the right ventricular parameters.

Future implications

The comparison method used in this study could be applied on data from other imaging modalities such as SPECT, PET, CT, echocardiography and other CMR sequences (e.g., T1-mapping) and can also be translated for use with a 3D model. While the proximal LAD ischemia/reperfusion model used in this study produced consequent isolated anteroseptal infarctions, it would be in the interest of external validity to study other infarct sizes and locations using this method. Improved fibrosis detection with CMR will be applicable to a broad clinical spectrum ranging from diagnostic to therapeutic outcomes, including cell therapy, ablation therapy, valvular diseases, cardiomyopathies and ischemic heart disease. For example, precise identification of the fibrotic region allows for accurate therapy guidance to the target area with the aim to ultimately improve clinical outcome for patients.

Conclusions

In conclusion, the novel systematic method to compare high resolution *in vivo* CMR imaging with detailed histological fibrosis data was feasible and can readily be applied to other imaging data. Locally measured functional parameters such as WT, and measures of myocardial deformation derived from FT: radial and circumferential strain related modestly with local myocardial fibrosis, yet can be used to gain insight into local cardiac mechanics. The fully automatic FWHM algorithm applied on the reference standard LGE CMR showed to be preferred to detect myocardial fibrosis in a chronic *in vivo* infarct model.

Acknowledgments

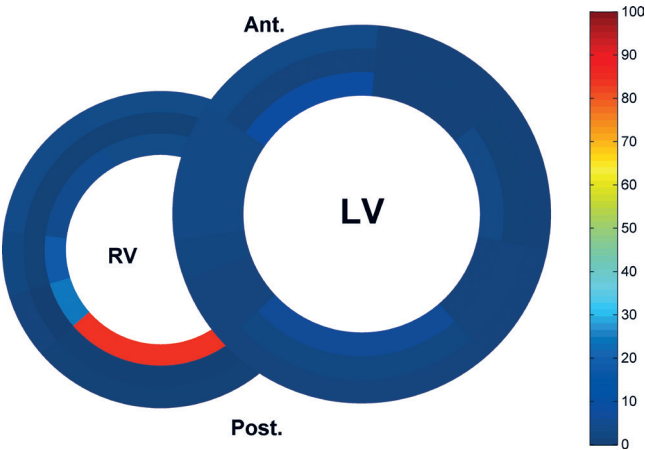
We kindly acknowledge Grace Croft, Marlijn Jansen, Evelyn Velema, Joyce Visser, Merel Schurink, Martijn van Nieuwburg and Gerard Marchal for their assistance with the animal experiments. We would like to thank Jaco Zwanenburg and Martijn Froeling for performing the CMR experiments. We are also grateful to Rebecca Stellato for statistical advice. This research forms part of the Project P1.04 SMARTCARE of the research program of the BioMedical Materials Institute, co-funded by the Dutch Ministry of Economic Affairs, Agriculture and Innovation. The financial contribution of the Nederlandse Hartstichting (NHS) is gratefully acknowledged. FA is supported by UCL Hospitals NIHR Biomedical Research Centre. The contribution of FvS and SC to the project was supported by the TKI LSH framework MRI Guided RegenerAtive ThErapy (MIGRATE) project and with financial support of the NHS and Interuniversity Cardiology Institute of the Netherlands.

REFERENCES

1. Weber KT, Sun Y, Bhattacharya SK, Ahokas RA, Gerling IC. Myofibroblast-mediated mechanisms of pathological remodelling of the heart. *Nat Rev Cardiol* 2013;10:15-26.
2. Mewton N, Liu CY, Croisille P, Bluemke D, Lima JA. Assessment of myocardial fibrosis with cardiovascular magnetic resonance. *J Am Coll Cardiol* 2011;57:891-903.
3. Flett AS, Hasleton J, Cook C et al. Evaluation of techniques for the quantification of myocardial scar of differing etiology using cardiac magnetic resonance. *JACC Cardiovasc Imaging* 2011;4:150-6.
4. Kim RJ, Wu E, Rafael A et al. The use of contrast-enhanced magnetic resonance imaging to identify reversible myocardial dysfunction. *N Engl J Med* 2000;343:1445-53.
5. Bondarenko O, Beek AM, McCann GP, van Rossum AC. Revascularization in patients with chronic ischaemic myocardial dysfunction: insights from cardiovascular magnetic resonance imaging. *Eur Heart J Cardiovasc Imaging* 2012;13:985-90.
6. Kim RJ, Fieno DS, Parrish TB et al. Relationship of MRI delayed contrast enhancement to irreversible injury, infarct age, and contractile function. *Circulation* 1999;100:1992-2002.
7. Malliaras K, Smith RR, Kanazawa H et al. Validation of contrast-enhanced magnetic resonance imaging to monitor regenerative efficacy after cell therapy in a porcine model of convalescent myocardial infarction. *Circulation* 2013;128:2764-75.
8. Pop M, Ghugre NR, Ramanan V et al. Quantification of fibrosis in infarcted swine hearts by ex vivo late gadolinium-enhancement and diffusion-weighted MRI methods. *Phys Med Biol* 2013;58:5009-28.
9. Iles LM, Ellims AH, Llewellyn H et al. Histological validation of cardiac magnetic resonance analysis of regional and diffuse interstitial myocardial fibrosis. *Eur Heart J Cardiovasc Imaging* 2015;16:14-22.
10. Bellin MF, Van Der Molen AJ. Extracellular gadolinium-based contrast media: an overview. *European journal of radiology* 2008;66:160-7.
11. Attili AK, Schuster A, Nagel E, Reiber JH, van der Geest RJ. Quantification in cardiac MRI: advances in image acquisition and processing. *Int J Cardiovasc Imaging* 2010;26 Suppl 1:27-40.
12. Heiberg E, Sjogren J, Ugander M, Carlsson M, Engblom H, Arheden H. Design and validation of Segment—freely available software for cardiovascular image analysis. *BMC Med Imaging* 2010;10:1.
13. Hor KN, Gottliebson WM, Carson C et al. Comparison of magnetic resonance feature tracking for strain calculation with harmonic phase imaging analysis. *JACC Cardiovascular imaging* 2010;3:144-51.
14. Augustine D, Lewandowski AJ, Lazdam M et al. Global and regional left ventricular myocardial deformation measures by magnetic resonance feature tracking in healthy volunteers: comparison with tagging and relevance of gender. *J Cardiovasc Magn Reson* 2013;15:8.
15. Schuster A, Morton G, Hussain ST et al. The intra-observer reproducibility of cardiovascular magnetic resonance myocardial feature tracking strain assessment is independent of field strength. *European journal of radiology* 2013;82:296-301.
16. Khan JN, Singh A, Nazir SA, Kanagala P, Gershlick AH, McCann GP. Comparison of cardiovascular magnetic resonance feature tracking and tagging for the assessment of left ventricular systolic strain in acute myocardial infarction. *European journal of radiology* 2015.
17. Morton G, Schuster A, Jogiya R, Kuty S, Beerbaum P, Nagel E. Inter-study reproducibility of cardiovascular magnetic resonance myocardial feature tracking. *J Cardiovasc Magn Reson* 2012;14:43.
18. Wu L, Germans T, Guclu A, Heymans MW, Allaart CP, van Rossum AC. Feature tracking compared with tissue tagging measurements of segmental strain by cardiovascular magnetic resonance. *J Cardiovasc Magn Reson* 2014;16:10.
19. Cowan BR, Peereboom SM, Greiser A, Guehring J, Young AA. Image Feature Determinants of Global and Segmental Circumferential Ventricular Strain From Cine CMR. *JACC Cardiovascular imaging* 2014.
20. Gho JM, van Es R, Stathonikos N et al. High resolution systematic digital histological quantification of cardiac fibrosis and adipose tissue in phospholamban p.Arg14del mutation associated cardiomyopathy. *PLoS One* 2014;9:e94820.

21. Koudstaal S, Jansen of Lorkeers S, Gho JM et al. Myocardial infarction and functional outcome assessment in pigs. *Journal of visualized experiments : JoVE* 2014.
22. Huisman A, Looijen A, van den Brink SM, van Diest PJ. Creation of a fully digital pathology slide archive by high-volume tissue slide scanning. *Hum Pathol* 2010;41:751-7.
23. Snijders TAB, Bosker RJ. *Multilevel Analysis: An Introduction to Basic and Advanced Multilevel Modeling*. 2nd ed. London: Sage Publications, 2012.
24. LaHuis DM, Hartman MJ, Hakoyama S, Clark PC. Explained Variance Measures for Multilevel Models. *Organizational Research Methods* 2014;17:433-451.
25. Amado LC, Gerber BL, Gupta SN et al. Accurate and objective infarct sizing by contrast-enhanced magnetic resonance imaging in a canine myocardial infarction model. *J Am Coll Cardiol* 2004;44:2383-9.
26. Beek AM, Bondarenko O, Afsharzada F, van Rossum AC. Quantification of late gadolinium enhanced CMR in viability assessment in chronic ischemic heart disease: a comparison to functional outcome. *J Cardiovasc Magn Reson* 2009;11:6.
27. Hsu LY, Natanzon A, Kellman P, Hirsch GA, Aletras AH, Arai AE. Quantitative myocardial infarction on delayed enhancement MRI. Part I: Animal validation of an automated feature analysis and combined thresholding infarct sizing algorithm. *J Magn Reson Imaging* 2006;23:298-308.

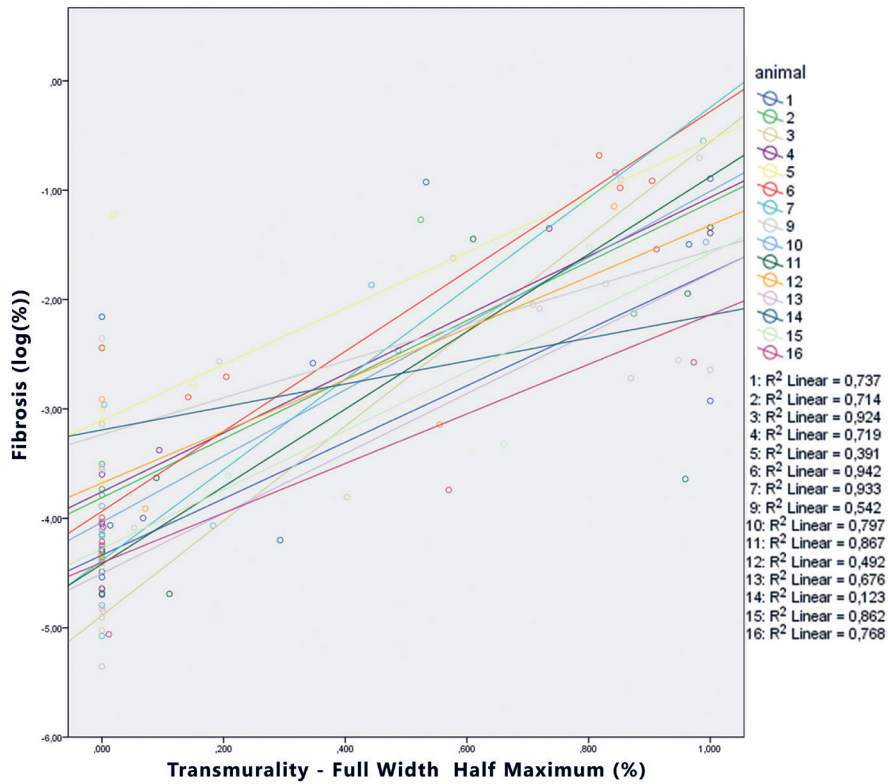
SUPPLEMENTAL MATERIAL



Supplementary Figure 1 Whole heart slice fibrosis analysis, one animal (excluded from analysis due to absence of left ventricular fibrosis). The percentage of fibrosis is shown using a color scale. Ant. = anterior; LV = left ventricle; Post. = posterior; RV = right ventricle.

Supplementary Table 1

	Mean (\pm SD)
Left ventricular ejection fraction (%)	39 (\pm 6)
LV mass (g)	113 (\pm 12)
Infarct size (%)	18 (\pm 4)
Heart rate (bpm)	64 (\pm 21)



Supplementary Figure 2

The dots represent sections from the different animals and regression lines per animal are shown with different colors. Fibrosis was compared with LGE FWHM analysis (Segment). CMR = Cardiovascular Magnetic Resonance; FWHM = full width at half maximum; LGE = late gadolinium enhancement.

PART II

Cardiac ablation

Chapter 8



Novel method for electrode-tissue contact measurement with multi-electrode catheters

Submitted

René van Es¹, John Hauck², Vincent J.H.M.¹, Kars Neven^{1,3,4}, Harry van Wessel¹, Pieter A. Doevendans^{1,5}, Fred H.M. Wittkamp¹

¹ University Medical Center Utrecht- Div. Heart and Lungs, Dept. of Cardiology, Utrecht, Netherlands

² St. Jude Medical AF division, St Paul, MN

³ Dept. of Rhythmology, Alfried Krupp Krankenhaus, Essen, Germany

⁴ Witten/Herdecke University, Witten, Germany

⁵ Netherlands Heart Institute, Utrecht, The Netherlands

ABSTRACT

Introduction

With multi-electrode catheters, measuring contact force (CF) on each electrode is technically challenging. Present electrical methods, like the electrical coupling index (ECI) may yield false positive values in pulmonary veins. We developed a novel method that measures electrode-interface resistance (IR) by applying a very local electrical field between neighboring catheter electrodes while measuring voltage between each catheter electrode and a skin patch.

Methods

In vitro, effects of remote high-impedance structures were studied. In addition, both ECI and IR were directly compared with true electrode-tissue CF. In five pigs, the influence of high-impedance pulmonary tissue on ECI and IR was investigated while navigating the free floating catheter into the caval veins. Inside the left atrium (LA), IR was directly compared with CF. Finally, multi-electrode IR measurements in the LA and inferior pulmonary vein (IPV) were compared.

Results

In vitro, IR is much less affected by remote high-impedance structures than ECI (3% vs 32%, respectively). Both IR and ECI strongly relate to electrode-tissue CF ($r^2=0.84$). In vivo, and in contrast to ECI, IR was not affected by nearby pulmonary tissue. Inside the LA, a strong relation between IR and CF was found. This finding was confirmed by simultaneous multi-electrode measurements in LA and IPV.

Conclusion

Data of the present study suggest that electrode-tissue contact affects the IR while being highly insensitive to remote structures. This method facilitates electrode-tissue contact measurements with circular multi-electrode ablation catheters.

INTRODUCTION

Electroporation ablation for pulmonary vein (PV) isolation has recently been introduced to create continuous and deep circular lesions, with a single high-current application, synchronously delivered via all electrodes of a circular catheter.^{1,2} Like radiofrequency (RF), electroporation ablation is based on the delivery of electrical current from electrode to tissue and therefore electrode-tissue contact is important for effective energy transfer to the tissue.^{3,4}

Electrode-tissue contact can be quantified using mechanical contact force (CF) transducers.^{5,6} This is technically feasible for a single ablation electrode, but extremely challenging if not impossible for multiple electrodes on a single catheter. In addition, such a complex CF sensing solution may significantly increase catheter costs. Moreover, CF although appealing, may not be the optimal parameter to determine electrode-tissue contact. With a catheter tip entrapped in endocardial left atrium (LA) cavities or narrow structures, electrode-tissue contact may be good without much CF.^{7,8} Direct measurement of electrode-tissue contact may therefore be preferable above CF, both for RF ablation as well as for electroporation ablation.

Recently, the electrical coupling index (ECI) has been studied as an electrical method to measure electrode-tissue contact inside the LA.^{9,10} ECI calculates the electrode-tissue impedance by applying a small high frequency electrical drive current between a catheter electrode and a first skin patch while measuring the voltage difference between that electrode and a second patch at a contralateral skin location (Figure 1A).¹¹ Both reactance and resistance are calculated to determine ECI. Reactance relates to the direct metal-electrolyte interface, while resistance is affected by all structures through which the low measuring current is conducted.¹²

Inside the LA cavity, ECI worked well. Within a pulmonary vein, however, high ECI values suggesting good contact have been reported even with a floating electrode,⁹ presumably by too much contribution of nearby high-impedance pulmonary tissue. This tissue is part of the current path between the electrode and the first skin patch and affects the measured voltage between electrode and second skin patch (Figure 1A).

Novel technology

Contribution of remote structures to the measured impedance with ECI can possibly be avoided by concentrating the drive current in a much smaller area around the target electrode. This can be achieved by using a more closely spaced dipole, e.g. by using a neighboring electrode of the target electrode as counter electrode instead of the first skin patch (Figure 1B). With a multi-electrode circular catheter, all electrodes have such a neighboring electrode and this offers the unique opportunity to synchronously measure the interface impedance for every single electrode. In the present study, this novel method to measure interface resistance (IR) was compared to the ECI method both in vitro and in a porcine model. Additionally, IR was directly compared to CF in the same catheter.

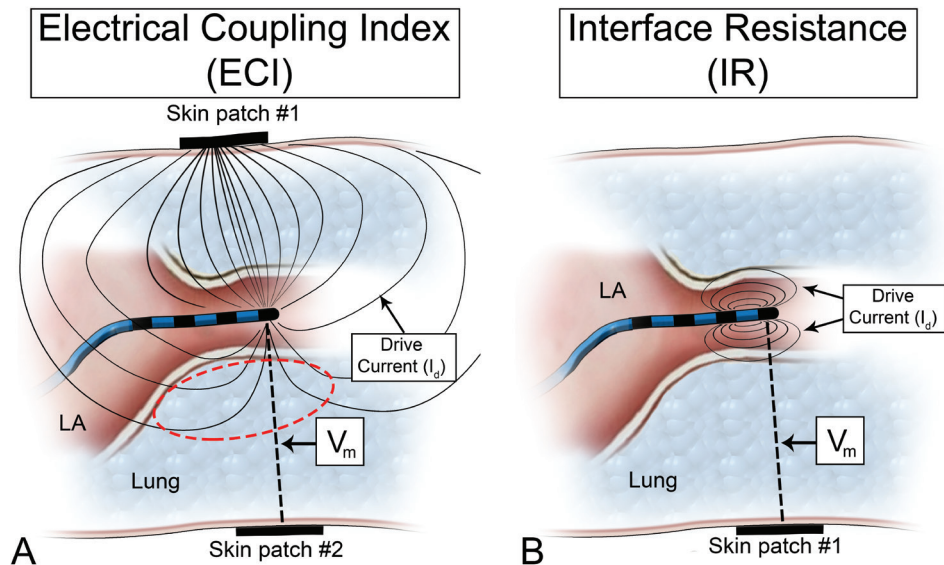


Figure 1 Schematic overview of the two methods to measure impedance that were compared. **(A)** With ECI the drive current (I_d) is applied between a catheter electrode and first skin patch while measuring the voltage (V_m) between the same catheter electrode and a second skin patch. The red dashed line indicated the voltage measurement that is affected by pulmonary tissue. **(B)** With IR the drive current is applied between two neighboring catheter electrodes while measuring the voltage between the same catheter electrode and a skin patch. LA= Left Atrium, ECI = Electrical Coupling index, IR = Interface Resistance, V_m = Voltage measurement, I_d = Drive current.

MATERIALS AND METHODS

In vitro experiments

Experiments were performed in a plastic tank filled with diluted saline with a blood-like conductivity of 6-10 mS/cm.^{11,13} Two indifferent electrodes (Z1 and Z2) were positioned in opposite corners of the tank (Figure 2). For ECI, the drive current was applied between the target electrode and the indifferent electrode Z1 while the resulting voltage difference was measured between the target electrode and the opposite indifferent electrode Z2. For IR, the drive current was applied between the target and a neighboring return electrode while the resulting voltage difference was measured between the target electrode and the indifferent electrode Z2. Both ECI and IR were calculated by dividing the measured voltage difference between the target electrode and Z2 by totally applied current. Consequently, the ECI method that was employed in the present study only measured the resistive component and neglected the small contribution of reactance.¹¹ For all measurements with a circular catheter, electrode 5 was used as target electrode, while electrode 6 was used as counter electrode for the bipolar drive current during IR measurement.

No contact and remote influence

The influence of remote electrically resistive structures was studied by moving an 18-mm diameter circular decapolar catheter with 2-mm electrodes in and out through the center of a 25-mm diameter and a 50-mm long electrically isolating plastic tube (Figure 2A). The measurements started 10 mm above the entrance of the tube (baseline value) and ended 10 mm below the exit of the tube. ECI and IR were measured every 2 mm and calculated relative to baseline values.

Contact and remote influence

Changes in ECI and IR were measured with a 7 French (F) linear catheter (TactiCath™ Quartz 75, St. Jude Medical, Minnetonka, MN) moving towards a section of freshly excised porcine left ventricular tissue. With this catheter, electrode 1 (3.5 mm distal electrode) was used as target electrode while electrode 2 was used as counter electrode (2 mm inter electrode distance) for the bipolar drive current during IR measurement. The catheter was positioned 20 mm above the tissue and was lowered with steps of 2 mm (20-10 mm), 1 mm (10-5 mm), 0.5 mm (5-2 mm) and 0.2 mm (2-0 mm) towards the tissue. This procedure was performed three times. At each position, ECI and IR were measured. Changes in resistance were calculated relative to the baseline value taken at 20 mm distance.

Comparison with contact force

Changes in ECI and IR were measured with a 7 F linear CF sensing catheter (TactiCath™ Quartz 75, St. Jude Medical, Minnetonka, MN), CF readout and impedance data were synchronized. TactiSoft (St. Jude Medical, Minnetonka, MN) software was used to perform CF measurements. A section of freshly excised porcine left ventricular tissue was positioned on the bottom of a tank (Figure 2B). The linear catheter was pressed straight down onto the epicardial side of myocardial tissue >200 times, each time at a slightly different tissue location and with a different CF between 0 and 30 gramforce. For each run, CF and either ECI or IR, were measured. Maximal CF and increase in ECI or IR values relative to the baseline value taken at 20 mm distance were measured for each 'touch down'.

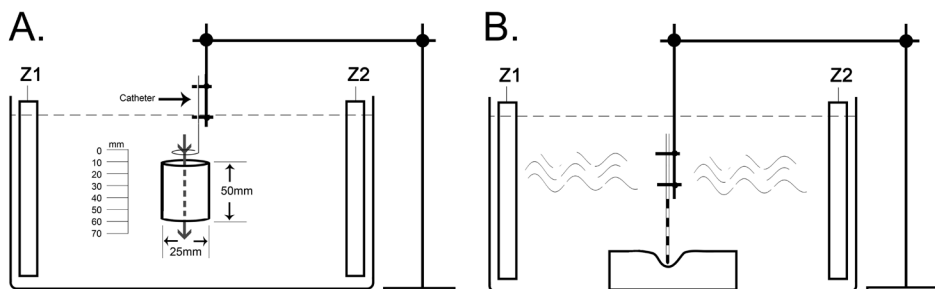


Figure 2 (A) Setup used to measure influence of a nearby high impedance structure (pvc tube) in a non-contact situation. For the IR measurement, the Z1 electrode was used, for the ECI measurement, both Z1 and Z2 electrodes were used. (B) Setup used to measure the force-impedance relation using the ECI and IR methods. The linear contact force sensing catheter was pressed down onto a piece of heart tissue on the bottom of the tank. IR = Interface Resistance, ECI = Electrical Coupling Index

In-vivo porcine studies

All studies were performed after prior approval from the Animal Experimentation Committee of the University Medical Center Utrecht and were performed in compliance with the Guide for the Care and Use of Laboratory Animals.¹⁴ Measurements were performed in five female (80-90 kg) Daland type landrace pigs. All animals were used in conjunction with other studies; no animals were used solely for this study.

Transseptal puncture was performed via the right femoral vein. An 8.5 F deflectable sheath (Agilis, St. Jude Medical, Minnetonka, MN) was used to facilitate access to the LA. Angiography of the IPV was performed in the anterior-posterior direction to fluoroscopically delineate/mark its ostium.

Non-contact

A circular in-plane 12-mm octopolar catheter with 2-mm electrodes (St. Jude Medical, Inc., St. Paul, MN; Figure 3A), inserted via the femoral vein, was moved between the inferior caval vein (ICV), the right atrium (RA), and the superior caval vein (SCV). A presumable floating electrode, electrode 5, was used as target electrode while electrode 6 served as return electrode for IR measurement.

One indifferent skin patch was placed on the shaved back of the animal; a second skin patch, used as return electrode for ECI measurement, was placed on the shaved abdomen. With the catheter inside the RA, a 5-second reference measurement was taken using both methods. Under fluoroscopic guidance, the catheter was then first positioned at least 2 cm into the SCV and then into the ICV above the diaphragm while measurements of ECI and IR were collected during 5 seconds at both locations.

Direct correlation with contact force

Under fluoroscopic guidance a 7 F CF-sensing catheter (Tacticath™ Quartz 75, St. Jude Medical, Minnetonka, MN) was introduced via the Agilis sheath into the LA. In five animals, the catheter tip was pushed against the LA endocardial wall at different locations with varying forces between 0 and 40 gramforce. At each location, the CF was kept stable for at least 2 seconds, while synchronously recording CF and IR.

Multi-electrode measurements

A multi-electrode impedance system was developed to synchronously measure IR at all electrodes of a decapolar catheter: A small bipolar high frequency current of approximately 10 μ A was simultaneously applied between each neighboring electrode pair, i.e. electrodes 1 and 2, electrodes 3 and 4, etc., while the resulting voltage at each electrode was measured relative to the indifferent skin patch on the back of the animal.

A 7 F, 20 mm circular decapolar catheter (St. Jude Medical, Inc., St. Paul, MN; Figure 3B) was introduced into the LA through the Agillis sheath. With the catheter in an apparently floating position in the LA cavity, IR values from all catheter electrodes were acquired and averaged during a 10-second episode. Thereafter, the mean of the 3 lowest averaged IR values was taken as a reference value for non-contact. Under fluoroscopic guidance, the catheter was then positioned in the inferior pulmonary vein (IPV) and again IR values from each of all catheter

electrodes were synchronously acquired and average during a 10-second episode. The mean IR value per electrode was compared to the reference value obtained inside the LA cavity.

Data analysis

All data was processed off-line using Matlab 2012a (The Mathworks, Inc., Natick MA). Data were compared using 2-tailed paired t-tests; a p-value <0.05 was considered statistically significant. The in vitro maximal IR, ECI and CF for each separate measurement ('touch down') were compared. The in vivo CF data was compared with IR by manually selecting phases of stable CF and calculating mean CF and IR over that same period. The results of the in vitro CF experiments were fitted with a power function using the curve fitting tool of Matlab. All data are presented as mean \pm standard deviation.

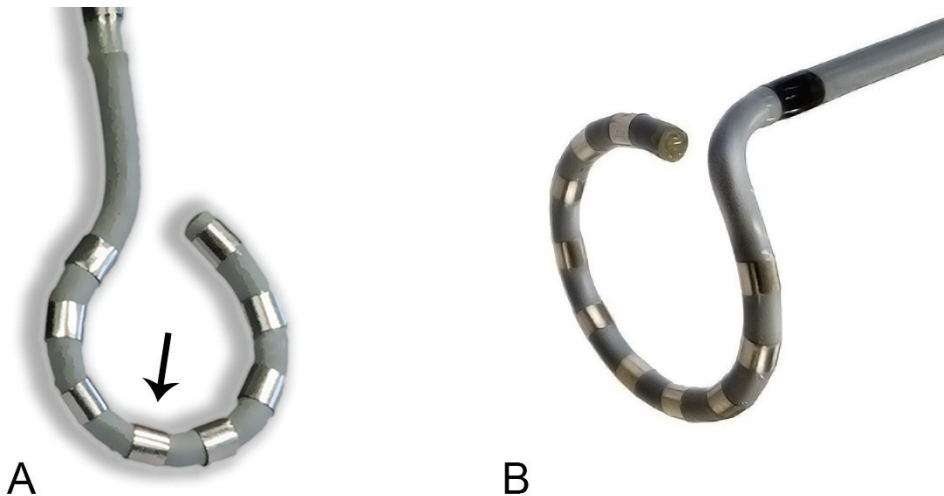


Figure 3 The catheters used to perform the different experiments. **(A)** The octapolar lollipop catheter was used in the first animal experiment. The arrow indicated the electrode that was used during the experiments. **(B)** The 20-mm circular decapolar catheter was used for the remote resistance tube experiments and in the second in vivo experiments.

RESULTS

In vitro experiments

Non contact and remote influence

The reference impedance, measured at 10 mm above the plastic tube, was 96.6Ω and 82.7Ω for the ECI and IR methods respectively. With the catheter in the middle of the tube, ECI and IR had increased by 32.2% and 3.2% respectively (Figure 4A).

Contact and remote influence

At 20 mm distance from the tissue, a resistance of $98.0 \pm 2.3\Omega$ and $43.7 \pm 1.9\Omega$ was measured

with the ECI and IR methods, respectively. At tissue contact, the average increase in impedance was 22.6% ($p < 0.01$) and 30.8% ($p < 0.01$) for the ECI and IR measurement, respectively (Figure 4B).

Comparison with contact force

A total of 237 and 288 measurements were performed with the ECI and IR method, respectively. The fitted power curves for ECI and ER both have a coefficient of determination $r^2 = 0.84$ (Figure 4C).

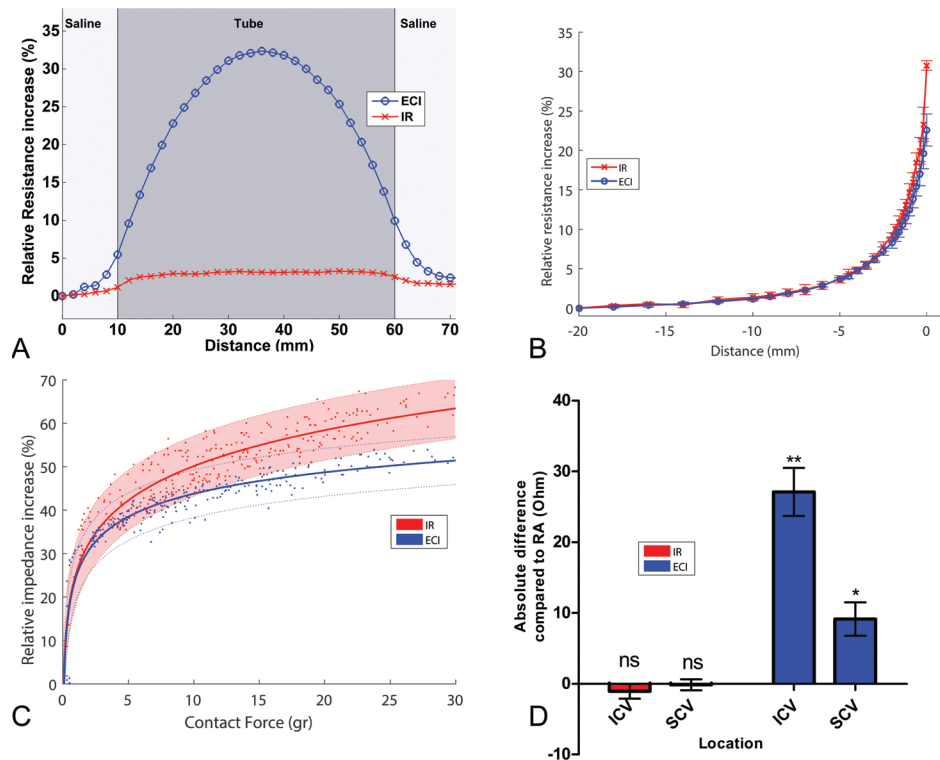


Figure 4 (A) The relative change in measured resistance for both the ECI and IR measurements while moving the catheter through a plastic tube without making contact. The ECI shows a large increase in measured resistance while the IR method was only marginally affected. (B) The relative change in measured resistance for both the ECI and IR measurements while moving the linear TactiCath catheter toward a section of freshly excised porcine myocardium. (C) The increase in measured resistance relative to a measurement performed in a free floating position at 20 mm from the tissue. The lines indicate the fitted line, the dashed lines indicate the 90% confidence interval. The dots represent individual measurements. (D) The results of the in vivo experiment. The measurements in the inferior and superior caval veins were compared with a reference measurement taken in the right atrium.

* $p < 0.05$, ** $p < 0.001$. ECI = Electrical Coupling Index, IR = Interface Resistance, RA = Right atrium, ICV = Inferior Caval Vein, SCV = Superior Caval Vein.

Porcine study

Non contact

ECl and IR values, measured in the RA of 5 animals were $126.5 \pm 9.8\Omega$ and $81.0 \pm 5.7\Omega$. Inside the ICV, ECl and IR values changed by $+27.1 \pm 7.6\Omega$ and $-1.1 \pm 2.3\Omega$, compared to RA values, ($p=0.001$ and $p=0.35$, respectively) (Figure 4D). Inside the SCV, ECl and IR values changed by $+9.1 \pm 5.3\Omega$ and $-0.2 \pm 1.7\Omega$ compared to RA measurements ($p=0.02$ and $p=0.85$, respectively).

Direct relation with contact force

A total of 373 stable episodes of CF-IR measurements were analyzed. Variations in applied force between successive measurements are clearly visible in both CF and IR tracings (e.g. Figure 5A). Beat to beat variations are present in both CF and IR signals and are in phase. There was clear relationship between applied CF and increase in impedance (Figure 5B).

Multi-electrode measurements

Synchronous IR values from all electrode pairs were successfully acquired in all five animals in both the LA and the IPV (e.g. Figure 5C and 5D). There was no significant difference between the non-contact LA reference measurement of $68.5 \pm 2.4\Omega$ and the lowest IR value of $69.6 \pm 4.9\Omega$ ($p=0.71$) measured inside the IPV.

DISCUSSION

In the present study, a novel electrical method for measuring electrode-tissue contact was compared with the present ECl method and with mechanical CF in vitro and in vivo. The novel IR method, that uses an electrical drive current between the target electrode and a closely spaced neighboring electrode, creates a much more localized electrical field than the original ECl method that uses a skin patch as return electrode. Both ECl and IR showed a comparable relative increase in resistance upon approaching and pushing against heart tissue. There is a clear relationship between CF and impedance for both methods. However, the novel IR method is much less susceptible to the presence of remote high impedance structures. Even a completely electrically isolating plastic tube around the catheter only marginally affected IR measurements.

In the porcine study, an in-plane, 12-mm circular octopolar catheter with 2-mm electrodes was moved between both caval veins and the RA. This catheter type was chosen instead of a circular PV catheter to facilitate that the target electrode, electrode 5 at the top of the catheter hoop, would be floating inside the vessels. Despite such floating position however, ECl values inside the ICV increased by approximately 20% relative to the value acquired inside the RA cavity. IR values however, remained unaffected when the floating electrode was moved from the RA cavity to inside the ICV or SCV.

During the multi-electrode measurements, the 20-mm circular catheter was positioned in the proximal IPV. The internal diameter of the proximal IPV is usually larger than the hoop diameter of the catheter used in this study (e.g. Figure 5C), which makes it unlikely that all electrodes had good tissue contact.¹⁵

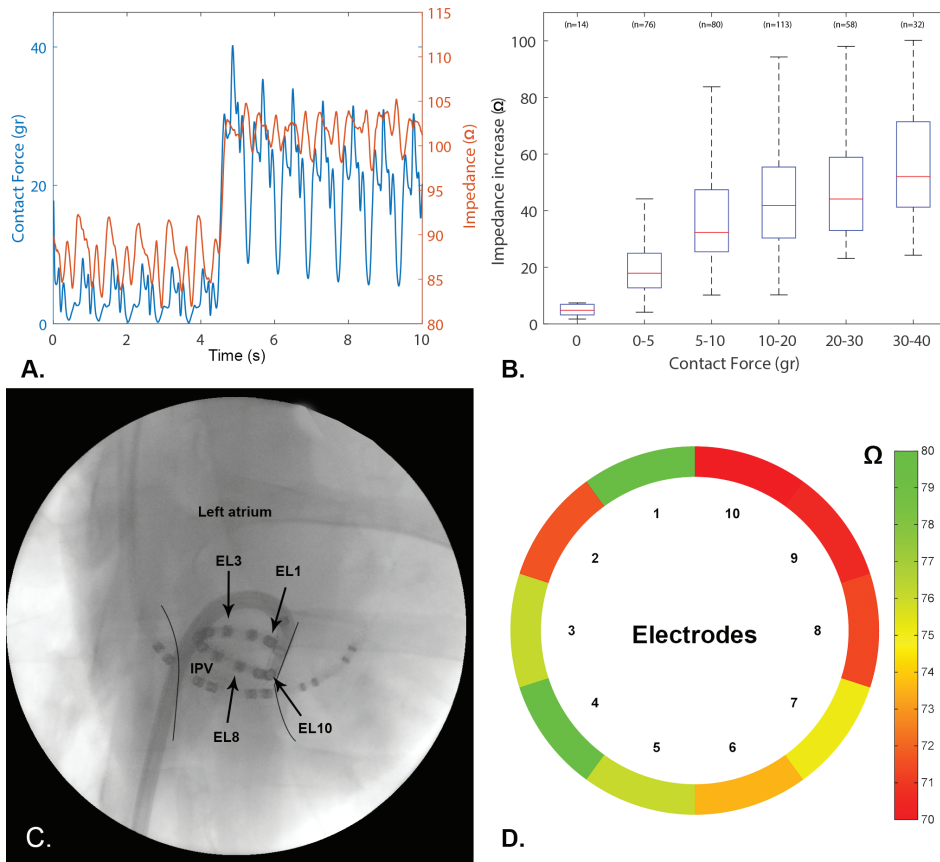


Figure 5 (A and B) Measurement performed in the LA with the linear TactiCath® catheter. **(A)** Example of a 10 seconds combined CF and IR measurement. The catheter was pushed firmer against the LA wall, half way through the measurement the catheter was pushed more firmly against the LA wall. **(B)** Combined CF and IR measurements in the LA of five animals. The number of measurements per bin is stated above the bins. The red lines represent the median value, the boxes represent the inter quartile range and the whiskers represent the range. **(C and D)** Measurements performed with a 20-mm circular decapolar catheter. **(C)** Example anterior-posterior fluoroscopic image of the left atrium. The inferior pulmonary vein (IPV) is delineated by the black lines. **(D)** The measured impedances of the electrodes shown in figure C. The average minimum impedance inside the left atrium was $70.6 \pm 3.2\Omega$. *EL* = Electrode, *IPV* = Inferior Pulmonary Vein.

With the 20-mm circular decapolar catheter inside the proximal porcine IPV, IR values of presumably non-contacting electrodes also did not increase relative to the values obtained from floating electrodes inside the LA cavity. The in vitro finding of a much lower susceptibility of IR (versus ECI) to remote high impedance structures was thus confirmed by data obtained in vivo. This is in line with a more localized electrical field used for IR measurement that includes a smaller portion of surrounding media than with ECI measurement.

In vitro, a strong correlation between applied CF and IR was found. A comparable correlation was observed in the porcine experiments, a change in applied CF immediately affected IR and both CF and IR showed similar beat to beat variations caused by the contracting heart.

Limitations

In this study, a modified ECI method was used for comparison with the novel IR method. The original ECI method uses both the resistive as well as the reactive components of electrode impedance, while the latter component was neglected in the present study. Reactance is determined by the capacitance of the direct metal-electrolyte interface, whereas electrical charge is transferred between electrons and ions.¹¹ The resistive component of electrode impedance is affected by all structures beyond this interface. Therefore, only the latter resistive component can be responsible for higher, and thus erroneous, “good contact” values within PVs as observed in clinical studies with the ECI method. In addition, elimination of reactance facilitated a quick switch between ECI and IR, because only the return electrode had to be switched, which was especially important during in vivo studies.

In the in vivo experiments, a floating state of the target electrode inside the ICD and SCV was not verified. We purposely selected electrode 5 at the top of the “in plane circular” catheter hoop to minimize the risk that this electrode would not be floating inside the SCV and ICD. The same holds true for electrodes with low IR values inside the proximal IPV. The only purpose of those latter studies was to investigate whether an erroneous rise in impedance would be present inside a vessel close to lung tissue. Such rise was not observed which strongly suggests the absence of an effect of remote lung tissue on IR.

In the porcine in vivo experiments, the spread in IR values was much larger than in vitro. In the latter experiments, the CF catheter was pushed against smooth epicardium. In the porcine studies with the TactiCath catheter inside the small LA, it was very hard to avoid catheter insertion into the relatively large and trabeculated LA appendage. This may explain relatively good tissue contact even with low CF and thus a larger variation in IR values in the porcine experiments than in vitro.

Clinical implications

Recently, tissue contact information has attracted great interest, especially for complex procedures like PV isolation. The introduction of CF sensing catheters led to improved procedural success.¹¹ With the introduction of “single shot” circular multi-electrode catheters, reliable mechanical contact assessment around the complete hoop is a technical challenge. Mechanical solutions with more than a few pressure sensors are impossible with presently available technology. The novel IR method may facilitate synchronous and instantaneous measurement of electrode-tissue contact with any multi-electrode catheter design without complex design changes.

IR is a direct measure of the amount of electrode-tissue contact area independent of applied force, hence firmer contact will not increase contact area. CF measures the applied force in grams, not the amount of electrode surface that is in contact with the tissue. Therefore, comparing CF with electrical contact may be regarded as comparing apples and oranges. However, a complete absence of electrical contact should always coincide with zero CF while some CF should always create some electrical contact. However, with the catheter electrode in an endocardial cavity, good electrical contact may also coincide with low CF.⁷ This reasoning may explain the variation in electrical contact at a given level of CF as shown in Figure 5B.

A potential disadvantage of IR as a measure of electrode contact is that IR may not be able to

detect excessive CF. If so, this will be a major drawback for the application of this technique to standard 'straight' ablation catheters. With circular multi-electrode catheters however, excessive contact force is highly unlikely and then measurement of IR may be a very good alternative for CF.

Conclusions

Data of the present study suggest that electrode-tissue contact affects the electrode-interface resistance. This novel method described in this study is highly insensitive to remote structures around a target location. The measuring method does not require any (complex) force transducer and facilitates electrode-tissue contact measurement all around circular multi-electrode ablation catheters.

Acknowledgments

We would like to thank Tessa Kappers, Robin Wesselink and Lieke Hermans for their help with the in vitro work. We kindly acknowledge Grace Croft, Marlijn Jansen, Evelyn Velema, Joyce Visser and Martijn van Nieuwburg for their assistance with the animal experiments.

Conflict of Interest/Disclosures

Fred Wittkamp and Kars Neven are consultants for St. Jude Medical, Inc.. Both Fred Wittkamp and Harry van Wessel are co-inventors of circular electroporation. John Hauck is the inventor of the contact system and was an employee of St. Jude Medical, Inc. at the time of the study. The other authors have no conflicts of interest to disclose.

REFERENCES

1. Wittkamp FHM, Van Driel VJ, Van Wessel H, Neven KGEJ, Gründeman PF, Vink A, Loh P, Doevendans PA: Myocardial lesion depth with circular electroporation ablation. *Circ Arrhythmia Electrophysiol* 2012; 5:581–586.
2. Wittkamp FH, van Driel VJ, Van Wessel H, Hof IE, Gründeman PF, Hauer RN, Loh P: Feasibility of electroporation for the creation of pulmonary vein ostial lesions. *J Cardiovasc Electrophysiol* 2011; 22:302–309.
3. Avitall B, Mughal K, Hare J, Helms RAY, Krum D: The effects of electrode-tissue contact on radiofrequency lesion generation. *PACE - Pacing Clin Electrophysiol* 1997; 20:2899–2910.
4. Wittkamp FHM, Nakagawa H: RF catheter ablation: Lessons on lesions. *PACE - Pacing Clin Electrophysiol* 2006; 29:1285–1297.
5. Yokoyama K, Nakagawa H, Shah DC, Lambert H, Leo G, Aebly N, Ikeda A, Pitha J V., Sharma T, Lazzara R, Jackman WM: Novel contact force sensor incorporated in irrigated radiofrequency ablation catheter predicts lesion size and incidence of steam pop and thrombus. *Circ Arrhythm Electrophysiol* 2008; 1:354–362.
6. Thiagalingam A, D’Avila A, Foley L, Guerrero JL, Lambert H, Leo G, Ruskin JN, Reddy VY: Importance of catheter contact force during irrigated radiofrequency ablation: Evaluation in a porcine ex vivo model using a force-sensing catheter. *J Cardiovasc Electrophysiol* 2010; 21:806–811.
7. Wittkamp FHM, Vonken E-J, Derksen R, Loh P, Velthuis BK, Wever EFD, Boersma LVA, Rensing BJ, Cramer MJ: Pulmonary Vein Ostium Geometry: Analysis by Magnetic Resonance Angiography. *Circulation* 2003; 107:21–23.
8. Wittkamp FHM, Van Oosterhout MF, Loh P, Derksen R, Vonken EJ, Slootweg PJ, Ho SY: Where to draw the mitral isthmus line in catheter ablation of atrial fibrillation: Histological analysis. *Eur Heart J* 2005; 26:689–695.
9. Piorkowski C, Sih H, Sommer P, Miller SP, Gaspar T, Teplitsky L, Hindricks G: First in human validation of impedance-based catheter tip-to-tissue contact assessment in the left atrium. *J Cardiovasc Electrophysiol* 2009; 20:1366–1373.
10. Gaspar T, Sih H, Hindricks G, Eitel C, Sommer P, Kircher S, Rolf S, Arya A, Teplitsky L, Piorkowski C: Use of electrical coupling information in AF catheter ablation: A prospective randomized pilot study. *Hear Rhythm [Internet] Elsevier*, 2013; 10:176–181. Available from: <http://dx.doi.org/10.1016/j.hrthm.2012.10.010>
11. Deno DC, Sih HJ, Miller SP, Teplitsky LR, Kuenzi R: Measurement of electrical coupling between cardiac ablation catheters and tissue. *IEEE Trans Biomed Eng* 2014; 61:765–774.
12. Franks W, Schenker I, Schmutz P, Hierlemann A: Impedance characterization and modeling of electrodes for biomedical applications. *IEEE Trans Biomed Eng* 2005; 52:1295–1302.
13. Geddes LA, Kidder H: Specific resistance of blood at body temperature II. *Med Biol Eng Kluwer Academic Publishers*, 1976; 14:180–185.
14. Institute for Laboratory Animal Research: Guide For the care and use of laboratory animals. 8th Edition. Washington (DC): National Academies Press, 2011,.
15. Van Driel VJHM, Neven KGEJ, Van Wessel H, Du Pré BC, Vink A, Doevendans PAFM, Wittkamp FHM: Pulmonary vein stenosis after catheter ablation electroporation versus radiofrequency. *Circ Arrhythmia Electrophysiol* 2014; 7:734–738.

Chapter 9



Feasibility of multi-electrode contact measurement as predictor of long-term success with circular pulmonary vein electroporation ablation

In preparation

René van Es¹, Vincent J.H.M. van Driel^{1,2}, Kars Neven^{1,3,4}, Harry van Wessel^{1,5},
Pieter A.F. Doevendans^{1,6}, Fred H.M. Wittkamp¹

¹ Department of Cardiology, Division Heart and Lungs, University Medical Center Utrecht, The Netherlands

² Department of Cardiology, Haga Teaching Hospital, The Hague, The Netherlands

³ Department of Rhythmology, Alfried Krupp Krankenhaus, Essen, Germany

⁴ Witten/Herdecke University, Witten, Germany

⁵ St. Jude Medical, Veenendaal, The Netherlands

⁶ Netherlands Heart Institute, Utrecht, The Netherlands

ABSTRACT

Introduction

Electrode-tissue contact is an important predictor for the success of pulmonary vein (PV) isolation. With multi-electrode ablation catheters, measuring electrode-tissue contact force for each individual electrode is technically challenging. In this porcine study, we assessed the feasibility of an electrical measurement of electrode-tissue contact for predicting long-term success of circular PV electroporation ablation.

Methods

Individual electrode interface impedance (EII) of a circular decapolar catheter was measured by applying a small current between pairs of neighboring electrodes while measuring the voltage between each electrode and a skin patch. In 10 pigs, one PV was ablated solely based on interface impedance (EII group), the other PV was ablated using local electrogram information (EP group) with the operator blinded for interface impedance. IRE ablations were performed at 200J. After 3 months, recurrence of conduction was assessed.

Results

A total of 43 IRE applications were delivered in 19 PVs. Acutely no reconnections were observed in either group. After 3 months, 0 vs. 3 ($p = 0.21$) PVs showed recurrence of conduction in the EII and EP groups respectively.

Conclusion

Data of this study suggest that interface impedance predicts effective IRE applications. For the long-term success of electrical PV isolation with circular IRE applications, measurement of electrode interface impedance was at least as good as the classical electrophysiological approach for determining the need for additional IRE applications. Data of this study also suggest that circular IRE is an adequate ablation technique for electrical PV isolation.

INTRODUCTION

Pulmonary vein (PV) isolation is an effective therapy to treat atrial fibrillation. With RF ablation, the success of PV isolation depends amongst others on the quality of catheter electrode-tissue contact during the ablation.¹

Recently, circular irreversible electroporation (IRE) ablation has been introduced as a novel method for PV isolation.² As with radiofrequency (RF) ablation, IRE is based on the delivery of an electrical current from a catheter electrode to the tissue. Electrode-tissue contact will therefore be as important for effective energy transfer with IRE ablation as with RF ablation.³ IRE is capable of creating deep continuous circular lesions.⁴ Such lesions may reduce the incidence of reconnection and perhaps thus also the need for a predefined observation period after ablation. However, measurement of electrode-tissue contact force for each separate electrode of a multi-electrode catheter would be technically extremely challenging. In a previous study, (Chapter 8) we demonstrated a novel electrical method to measure electrode-tissue contact with circular multi-electrode catheters.⁵

In the present long-term porcine study, we evaluated if electrode-contact information during ablation could replace the standard electrophysiological analysis of electrical PV isolation, and obviate the need for a predefined observation period.

METHODS

Animals

All animal experiments were performed with approval from the Animal Experimental Ethical committee of the University Medical Center Utrecht. In 10 Daland landrace pigs (60–75 kg), calcium carbasalate (80 mg/d) and clopidogrel (75 mg/d, after a loading dose of 300 mg) therapy was started three days before the procedure and continued until euthanasia. Amiodarone therapy was started one week before the procedure (600 mg/d) and continued in a 400-mg/d schedule to prevent procedure-related arrhythmias. The animals were intubated and anesthetized according to standard procedures. Transseptal puncture for access to the left atrial (LA) cavity was performed via the right femoral vein. An 8F deflectable sheath (Agilis, St. Jude Medical, Minnetonka, MN, USA) was used to facilitate access to PV ostia.

Study design

Per animal, the value of electrical interface impedance (EII) was studied by presenting this information to the physician for only one of the two PVs. For these veins (Group EII), circumferential EII was the sole parameter to decide about additional energy applications. In the group of PVs that were treated without EII information (Group EP), the decision to ablate was based on classical electrophysiological criteria, like local electrograms that suggested the absence or presence of remaining intact PV sleeve sections, but also on the opinion of the catheterizing physician that he had covered the complete ostial perimeter during IRE applications.

Reference measurement of electrode-tissue contact

A 7F 20-mm circular decapolar deflectable electroporation catheter with 2-mm electrodes (Figure 1A) was introduced via an 8.5F Agilis sheath (St. Jude Medical) into the LA under fluoroscopic guidance. The catheter was connected to a new multi-electrode impedance system (MEIS) that simultaneously measures and displays individual electrode interface impedance of all catheter electrodes.

The catheter was deflected sideways against the LA endocardial wall such that only some of the electrodes were supposed to be in good tissue contact, while the electrodes on the other side of the hoop were lacking any tissue contact. With this catheter position, a reference measurement was taken to establish electrical limits for good and poor contact.

During the subsequent procedure, the degree of electrode-tissue contact between these outer limits was displayed on the screen of the MEIS system by color-coding the individual catheter electrodes depending on measured contact.

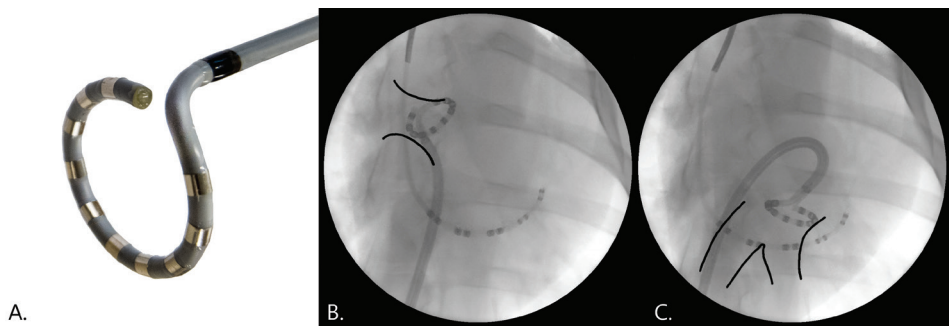


Figure 1. **A.** The 20-mm circular decapolar catheter that was used to perform the ablations. **B** Anterior-posterior fluoroscopic image. The circular catheter is located in the RPV. The black lines indicate the marked RPV ostium as obtained using a fluoroscopic contrast agent. **C** Anterior-posterior fluoroscopic image. The circular catheter is located in the IPV. The black lines indicate the marked IPV ostium. LA: left atrium; IPV: inferior pulmonary vein; RPV: right pulmonary vein.

Pre-ablation procedure

Angiography of the right (RPV) and inferior (IPV) pulmonary veins was performed in the anterior-posterior (AP) direction and the location of PVs and ostia were marked. The circular electroporation catheter was then deployed inside the common tubular PV segment, anatomically guided by the previously obtained PV angiogram and LA geometry as constructed using the NavX™ (St. Jude Medical, Inc.) 3D electroanatomical mapping system. PV entrance and exit conduction were determined using standard electrophysiological criteria. Then, the circular section of the electroporation catheter was gently pulled back and positioned as close as possible to the PV ostium.

Ablation Procedure

The energy (200J) was delivered using a monophasic external defibrillator (Lifepak 9, Physio-Control, Inc.; Redmond, WA). A skin patch (7506, Valleylab Inc.; Boulder, CO) was used as

indifferent electrode. Voltage and current waveforms of each energy application were stored on a digital oscilloscope.² All catheter positions just prior to IRE applications were stored fluoroscopically (Figure 1B & C) and tagged on the NavX™ geometry. Interface impedance of all catheter electrodes was stored continuously.

Post-ablation procedure

Thirty minutes after completing ablation of both veins, bidirectional electrical isolation of both PVs was reanalyzed: The decapolar circular catheter was positioned just distally to the ablation line and the presence of PV potentials was assessed. Bipolar stimulation via all electrode pairs of the circular ablation catheter was applied to detect conducting myocardial sleeve remnants. PV reconnection was presumed if stimulation with 10 mA led to left atrial capture. If such reconnections were found, extra circular IRE ablations were performed in the EP group only.

Follow-up

Three months after ablation, bidirectional electrical isolation of both PVs and the approximate location of the site of reconnection were assessed as described above. Then, all animals were euthanized by exsanguination. The heart was removed and inspected macroscopically.

Data analysis

The perimeter of the PV ostia was divided in 12 equal segments (Figure 2). Using the AP fluoroscopic images, and NavX™ to differentiate anterior from posterior positions, two observers blinded for study outcome allocated the location of each of the 10 electrodes just prior to each IRE application to a single distinct segment. Sites of reconnection determined during the follow-up procedure were allocated to one of possible four sections as indicated in Figure 2.

When multiple IRE applications had been performed in a single PV, the highest recorded electrode impedance per segment was used as the measure of tissue contact.

Subsequently, for each of the 12 segments, an impedance value below the lower reference value was scored as poor; a value above the lower reference value was scored as good. Finally, if one or more of three segments located inside each of the four possible reconnection sections was scored as poor, the entire reconnection section was scored as poor. In the final analysis, four sections per PV were used for further analysis (Figure 2).

Statistical analysis

Data is presented as average \pm standard deviation. The average number of IRE applications in right and inferior PVs and the number of applications in both EII group and EP group PVs were compared using a paired t-test. The total number of PV reconnections in the two groups, and the association between the site of PV reconnection and contact scores were compared using the Fisher exact test. With all tests, a *p*-value of <0.05 was considered to be statistically significant.

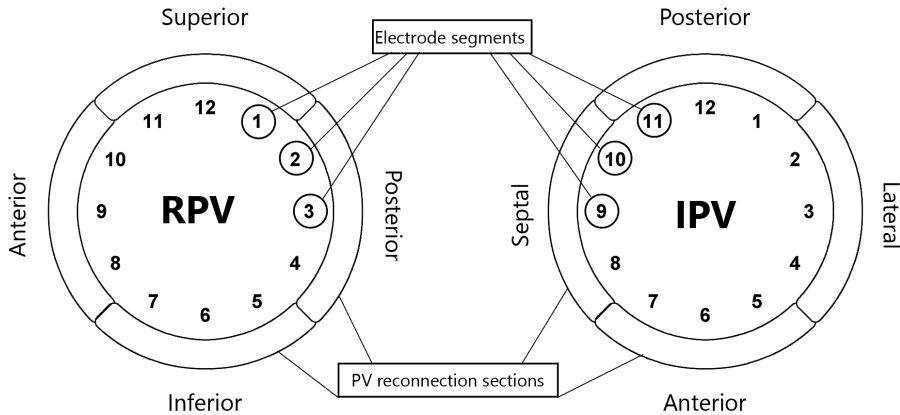


Figure 2. Pulmonary vein segments used for analysis. The right and inferior pulmonary veins were subdivided into 12 equal segments. The locations of all electrodes just prior to the ablation were allocated to one of these segments. During follow-up at three months, per PV, the location of reconnection was allocated to any of the four PV reconnection sections. RPV: right pulmonary vein; IPV: Inferior pulmonary vein; PV: pulmonary vein.

RESULTS

A total of 44 IRE applications were delivered to the 20 PVs of 10 animals, without medical complications (Table 1). None of the IRE applications showed signs of arcing on the captured voltage and current waveforms. In one animal, the MEIS system failed due to a software problem and the procedure in that PV was stopped after one IRE application. Data of this PV was excluded from further analysis. The other PV was ablated according to the protocol for the EP group.

The average impedance values representing poor and good contact were $68.8 \pm 5.7 \Omega$ and $84.3 \pm 9.6 \Omega$ ($p < 0.001$), respectively. In the RPV, 1.8 ± 0.4 and 2.3 ± 1.3 ($p = 0.53$) energy applications were delivered in the EII and EP group, respectively (Table 2). In the IPV, 2.4 ± 0.5 and 2.6 ± 0.5 ($p = 0.58$) energy applications were delivered in the EII and EP group, respectively. There was no significant difference between the number of delivered IRE applications between both groups (Table 2).

PV reconnections

Acute reconnection after a 30-minute observation period was not detected in either group. At follow-up after three months, PV reconnection was found in three EP group PVs; two in the RPV and one in the IPV. In the RPV, both reconnections were located in the anterior segment. In the IPV, the reconnection was located in the anterior lateral segment. No reconnections were found in the EII group. There was a non-significant difference ($p = 0.21$) in the number of PV reconnections between the two groups. In the EP group, there was no significant difference in the number of IRE applications between the PVs with and without the presence of PV reconnection, 1.7 ± 0.6 and 2.3 ± 0.5 ($p = 0.12$), respectively. PV

Table 1 Details of procedures.

Animal #	Vein	Shocks	Group	Position of reconnection
1	<i>RPV</i>	4	EII	-
	<i>IPV</i>	2	EP	-
2	<i>RPV</i>	2	EP	Anterior
	<i>IPV</i>	3	EII	-
3	<i>RPV</i>	2	EII	-
	<i>IPV</i>	3	EP	-
4	<i>RPV</i>	1	EP	Anterior
	<i>IPV</i>	3	EII	-
5	<i>RPV</i>	1	EII	-
	<i>IPV</i>	2	EP	-
6	<i>RPV</i>	2	EP	-
	<i>IPV</i>	3	EII	-
7	<i>RPV</i>	1	EII	<i>excluded</i>
	<i>IPV</i>	2	EP	Lateral
8	<i>RPV</i>	2	EP	-
	<i>IPV</i>	2	EII	-
9	<i>RPV</i>	2	EII	-
	<i>IPV</i>	3	EP	-
10	<i>RPV</i>	2	EP	-
	<i>IPV</i>	2	EII	-

IPV = Inferior pulmonary vein, RPV = right pulmonary vein, EII = group in which the ablations were performed based on electrical contact information, EP = group in which the ablation was performed based on electrophysiological criteria.

Table 2. Number of IRE applications.

	RPV	IPV	<i>p</i> -value
EII group	2.3 ± 1.3	2.6 ± 0.5	0.63
EP group	1.8 ± 0.4	2.4 ± 0.5	0.10
<i>p</i>-value	0.54	0.58	

IRE: irreversible electroporation; IPV: Inferior pulmonary vein; RPV: right pulmonary vein; EII group: the ablations were performed based on electrode interface impedance; EP group: the ablation was performed based on electrophysiological criteria.

reconnections were identified in 2/11 (18%) reconnection sections that were scored as poor contact. PV reconnections were identified in 1/65 (2%) reconnection sections that were scored as good contact. The sections with PV reconnections showed a non-significant association with poor contact scores ($p = 0.05$).

DISCUSSION

In the present porcine study, circular IRE was used to isolate both PVs in 10 animals using either a classical electrophysiological approach or a novel multi-electrode interface impedance measurement to determine the necessity for additional IRE applications. The acute success rate after a 30-minute observation period was 100% for both methods. After three months follow-up, three PVs with recurrent conduction were found in the 10 PVs of the classical approach (EP group) while all nine PVs that were ablated on the basis of electrical contact information (EII group) did not show recurrent conduction. However, this difference did not reach statistically significance. There was no significant difference in the number of IRE applications between the PVs or between the groups.

The absence of any reconnection within the 30-minute observation period suggests that such observation period may be too short with circular IRE ablation. Data of this study suggests that the use of electrical contact information in combination with a 3D navigation system could potentially replace the current electrophysiological approach for both determining electrode-to-tissue contact and the 30-minute observation period.

In the present study, 16/19 (84%) of the ablated PVs showed complete electrical isolation at three months follow-up. In clinical studies, in which complete circumferential PV isolation was accomplished during the index procedure, at a repeat electrophysiological study after two or three months, PV reconnection was observed in 62-70% of the patients.⁶⁻⁸ The relatively high success rate obtained in the present study suggests that circular IRE is a feasible and adequate ablation technique to achieve PV isolation. Future clinical studies have to be performed to show the long-term success rate of IRE PV isolation in humans.

In this study, we observed a non-significant ($p = 0.05$) association between poor contact scores during ablation and recurrent conduction at follow-up. A model with four sections to allocated the sites of PV reconnection was chosen to compensate for inaccuracies due to: (1) a possible difference in animal position between the two procedures; (2) a change of left atrial geometry and PV diameter as a result of growth of the pig⁹; (3) the use of bipolar stimulation to detect PV reconnection; (4) the fact that left atrial capture by stimulation at a site distal to the ablation line does not unequivocally prove the presence of an intact myocardial sleeve at exactly that location. In part the non-significant result of this study will probably be due to the low incidence of reconnection.

With circular multi-electrode catheters, it may be difficult to achieve good electrode-to-tissue contact for all electrodes around the PV antrum perimeter. Therefore, multiple energy applications are usually required to achieve complete circumferential PV isolation with current thermal circular ablation techniques.¹⁰ In the present study, per PV an average of 2.3 IRE applications was needed using a fixed diameter 20-mm circular multi-electrode catheter. The size of the IPV antrum is often larger than 20 mm, thus requiring more IRE applications for circumferential coverage.⁹ Using a circular catheter with a variable hoop diameter, ranging from 17-27 mm, would probably have decreased the number of necessary IRE applications per PV, especially in the IPV.

The availability of real-time contact information may facilitate optimal catheter positioning and obviate the need for laborious testing to evaluate electrode-tissue contact. In addition, usage of

the MEIS system together with a 3D navigation system enables systematical targeting of specific segments of the PV perimeter to ensure complete circumferential coverage during the ablation procedure.

Limitations

In this study, adenosine was not administered to check for acute PV reconnection. Prior studies have shown that adenosine can unmask sites of possible PV reconnection after RF-ablation.^{11,12} Whether adenosine use can unmask potential PV reconnection sites acutely after IRE ablation has yet to be investigated.

Clinical perspective

The MEIS technique enables the real-time visualization of electrode interface impedance for each individual electrode of a circular multi-electrode catheter and facilitates direct feedback to the physician for optimal catheter positioning in the PV antrum. Sufficient electrode-tissue contact during circular electroporation ablation may create continuous and deep lesions that may obviate the need for both electrophysiological analysis of electrical PV isolation as well as a 30-minute observation period after ablation. Further clinical studies are required to demonstrate the benefit of contact information for circular PV isolation with IRE in the clinical setting.

Conclusions

Data of this study and especially the low chronic reconnection rate of 16% suggest that circular IRE ablation is an adequate technique for electrical PV isolation. The absence of any long-term reconnection suggests that the combination of circular electrical contact information and circular IRE ablation may reduce procedure time not only by shorter ablation duration, but also by elimination of the 30-minute observation period after ablation.

REFERENCES

1. Wittkamp FHM, Nakagawa H. RF catheter ablation: Lessons on lesions. *PACE - Pacing and Clinical Electrophysiology*. 2006;29:1285–1297.
2. Wittkamp FH, van Driel VJ, Van Wessel H. Feasibility of Electroporation for the Creation of Pulmonary Vein Ostial Lesions. 2010;302–309.
3. Avital B, Mughal K, Hare J, Helms R, Krum D. The effects of electrode-tissue contact on radiofrequency lesion generation. *PACE - Pacing and Clinical Electrophysiology*. 1997;20:2899–2910.
4. Wittkamp FHM, Van Driel VJ, Van Wessel H, Neven KGEJ, Gründeman PF, Vink A, Loh P, Doevendans PA. Myocardial lesion depth with circular electroporation ablation. *Circulation: Arrhythmia and Electrophysiology*. 2012;5:581–586.
5. van Es R, Van Driel VJHM, Neven KGEJ, Wessel H Van, Hauck J, Doevendans PA, Wittkamp FHM. Novel Multi-Electrode Method for Measurement of Tissue Contact [Internet]. In: Heart Rhythm 36th annual scientific sessions. Boston: Available from: <http://www.abstractsonline.com/pp8/#!/3647/presentation/13296>
6. Das M, Wynn GJ, Morgan M, Lodge B, Waktare JEP, Todd DM, Hall MCS, Snowdon RL, Modi S, Gupta D. Recurrence of Atrial Tachyarrhythmia during the Second Month of the Blanking Period is Associated with More Extensive Pulmonary Vein Reconnection at Repeat Electrophysiology Study. *Circulation: Arrhythmia and Electrophysiology*. 2015;8:846–852.
7. Kuck K-H, Hoffmann BA, Ernst S, Wegscheider K, Treszl A, Metzner A, Eckardt L, Lewalter T, Breithardt G, Willems S. Impact of Complete Versus Incomplete Circumferential Lines Around the Pulmonary Veins During Catheter Ablation of Paroxysmal Atrial Fibrillation: Results From the Gap-Atrial Fibrillation-German Atrial Fibrillation Competence Network 1 Trial. *Circulation Arrhythmia and electrophysiology*. 2016;9:e003337.
8. Neuzil P, Reddy VY, Kautzner J, Petru J, Wichterle D, Shah D, Lambert H, Yulzari A, Wissner E, Kuck KH. Electrical reconnection after pulmonary vein isolation is contingent on contact force during initial treatment: Results from the EFFICAS i study. *Circulation: Arrhythmia and Electrophysiology*. 2013;6:327–333.
9. Van Driel VJHM, Neven KGEJ, Van Wessel H, Du Pré BC, Vink A, Doevendans PAFM, Wittkamp FHM. Pulmonary vein stenosis after catheter ablation electroporation versus radiofrequency. *Circulation: Arrhythmia and Electrophysiology*. 2014;7:734–738.
10. Laish-Farkash A, Khalameizer V, Fishman E, Cohen O, Yosefy C, Cohen I, Katz A. Safety, efficacy, and clinical applicability of pulmonary vein isolation with circular multi-electrode ablation systems: PVAC[®] vs. nMARQ[™] for atrial fibrillation ablation. *Europace* [Internet]. 2015;euv258.
11. Tritto M, De Ponti R, Salerno-Uriarte JA, Spadacini G, Marazzi R, Moretti P, Lanzotti M. Adenosine restores atrio-venous conduction after apparently successful ostial isolation of the pulmonary veins. *European Heart Journal*. 2004;25:2155–2163.
12. Datino T, MacLe L, Qi XY, Maguy A, Comtois P, Chartier D, Guerra PG, Arenal A, Fernández-Avilés F, Nattel S. Mechanisms by which adenosine restores conduction in dormant canine pulmonary veins. *Circulation*. 2010;121:963–972.

Chapter 10



Acute and long-term effects of full-power electroporation ablation directly onto the esophagus

Intactness of the extracellular matrix demonstrates unique ablation characteristics of irreversible electroporation

Submitted

Kars Neven^{1,2,3}, René van Es¹, Vincent J.H.M.¹, Harry van Wessel^{1,4}, Herma H. Fidder⁵, Aryan Vink⁶, Pieter A. Doevendans^{1,7}, Fred H.M. Wittkamp¹

¹ Dept. of Cardiology, University Medical Center Utrecht, Utrecht, The Netherlands

² Dept. of Rhythmology, Alfried Krupp Krankenhaus, Essen, Germany

³ Witten/Herdecke University, Witten, Germany

⁴ St. Jude Medical, Veenendaal, The Netherlands

⁵ Dept. of Gastroenterology, University Medical Center Utrecht, Utrecht, The Netherlands

⁶ Dept. of Pathology, University Medical Center Utrecht, Utrecht, The Netherlands

⁷ ICIN - Netherlands Heart Institute, Utrecht, The Netherlands

ABSTRACT

Background

Esophageal ulceration and fistula are complications of pulmonary vein isolation (PVI) using thermal energy sources. Irreversible electroporation (IRE) is a novel, non-thermal ablation modality for PVI. A single 200 J application can create deep myocardial lesions. Acute and chronic effects of this new energy source on the esophagus are unknown.

Methods

In 8 pigs (± 70 kg), the suprasternal esophagus was surgically exposed. A linear suction device with a single 35 mm long and 6 mm wide protruding linear electrode inside a plastic suction cup was used for ablation. Single, non-arcing, non-barotraumatic, cathodal 100 and 200 J applications were delivered at 2 different sites on the anterior esophageal adventitia. No proton-pump inhibitors were administered during follow-up. Esophagoscopy was performed at days 2 and 7. After euthanasia at day 60, the esophagus was evaluated visually and histologically.

Results

All ablations were uneventful. Esophagoscopy at day 2 showed small white densities in the ablated areas, which appeared to be small intra-epithelial vesicles. No epithelial erythema, erosions or ulcerations were seen. At day 7, all densities had disappeared and all esophaguses appeared completely normalized. After euthanasia, there were no macroscopically visible lesions on the adventitia or epithelium. Histologically, a small scar was observed at the outer part of the muscular layer, whereas the mucosa and submucosa were normal.

Conclusions

Esophageal architecture remains unaffected 2 months after IRE, purposely targeting the adventitia. IRE is a safe modality for catheter ablation near the esophagus.

INTRODUCTION

Thermal catheter ablation may cause collateral damage to extracardiac structures. Various manifestations of esophageal damage, like esophageal ulceration and atrial-to-esophageal fistula, by radiofrequency energy, cryo-energy and various other thermal catheter ablation methods have been described.¹⁻⁵

Circular electroporation ablation via a multi-electrode catheter is a novel, non-thermal ablation technique. A few milliseconds (ms) short high-current density impulse creates microlesions in the cell membrane. The increased cellular permeability results in disruption of cellular hemostasis and ultimately in cell death.^{6, 7} Electroporation ablation has been shown to create sufficiently large and deep lesions for treatment of cardiac arrhythmias.⁸⁻¹⁰ With large and deep lesions in or around pulmonary vein ostia, the risk of esophageal damage may be greater than with currently used thermal ablation methods, like radiofrequency or cryoablation. This risk needs to be assessed before clinical implementation of electroporation ablation.

In the present study, the esophagus was targeted purposely with electroporation ablation, using an energy level capable of creating approximately 7-mm deep lesions in myocardial tissue.¹⁰

METHODS

This porcine study was performed in 8 animals (60-75 kg) after prior approval from the Animal Experimentation Committee of Utrecht University and was in compliance with the Guide for Care and Use of Laboratory Animals.¹¹

Animal preparation

Each pig was intubated and anesthetized following standard procedures. According to the study protocol, 5000 International Units of intravenous heparin were administered. Arterial pressure and capnogram were continuously monitored throughout the whole procedure.

Surgical exposure of the esophagus and electroporation ablation

After a suprasternal incision, an approximately 12-cm long section of the esophagus was surgically exposed. Ablation was performed with a custom linear suction device, comprising a 35 mm long and 6 mm wide linear electrode inside a 42 mm long and 7 mm wide plastic suction cup (Figure 1). The suction device was sucked with a constant partial vacuum of 50-60 cm H₂O parallel to the esophageal axis on the anterior esophageal adventitia and caused firm contact between the metal strip electrode inside the suction cup and esophagus (Figure 2). In the first animal, a single, 6-ms, 100-joules cathodal application was then delivered. In absence of adverse events in the first animal, a single, 6-ms, 200-joules cathodal application was delivered in all other animals, because maximal effect was aimed for. The energy was generated by a monophasic external defibrillator (Lifepak 9, Physio-Control, Inc., Redmond, WA). A large skin patch (7506, Valleylab Inc., Boulder, CO) on the back served as indifferent electrode.

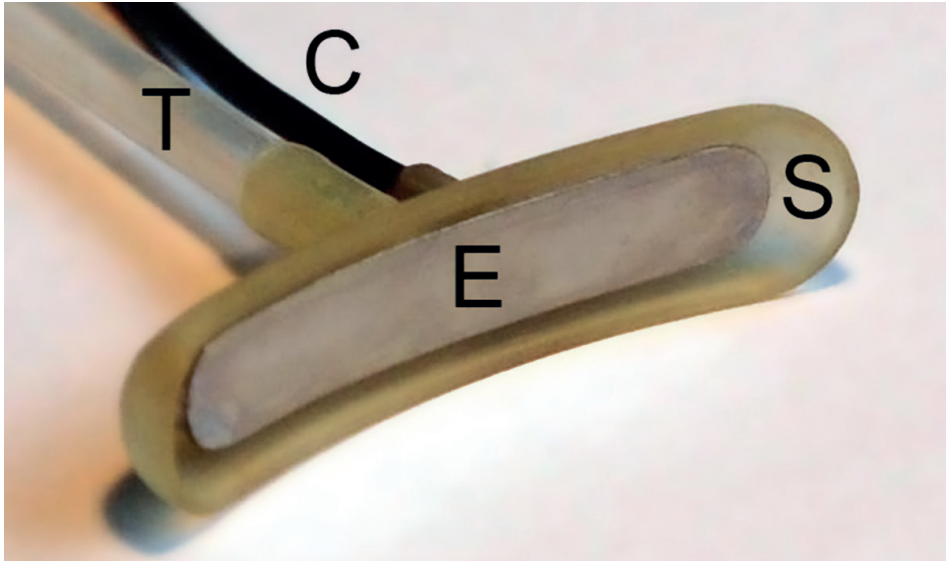


Figure 1 Linear suction device consisting of a 42 mm long and 7 mm wide plastic suction cup (S) connected to a vacuum system by a tube (T) and containing a single 35 mm long and 6 mm wide protruding linear electrode (E) that is connected by a cable (C) to the pulse generator.

The ablation was repeated at a second site on the anterior esophageal adventitia, as described above. Voltage and current waveforms of all applications were recorded as previously described.⁹ With the suction device still in position after the application, both far ends of the device were marked with sutures and surgical clips (for future fluoroscopic identification of the ablated segment).

Follow-up and esophagoscopy

After surgical closure of the wound, the animal was allowed to recover. No proton-pump inhibitors were administered during follow-up. In 5 out of 8 animals, after intubation and anesthesia following standard procedures, esophagoscopy using a video endoscope (Q160AL, Olympus CF, Tokyo, Japan) was performed at days 2 and 7. An experienced gastroenterologist performed the esophagoscopy, and the entire video-endoscopy was digitally saved for post-hoc analysis. The other 3 animals were euthanized at day 2 in order to study the acute effects of electroporation ablation. In these animals, no esophagoscopy was performed. After a 2-month survival period, the remaining 5 animals were again intubated and anesthetized following standard procedures. The thorax was opened by sternotomy, and the animals were euthanized by exsanguination. In all animals, the esophagus was removed and visually inspected, and the areas with ablation lesions were excised, pinned to a support, and fixed in formalin.

Statistical analysis

Continuous variables were expressed as mean \pm standard deviation.

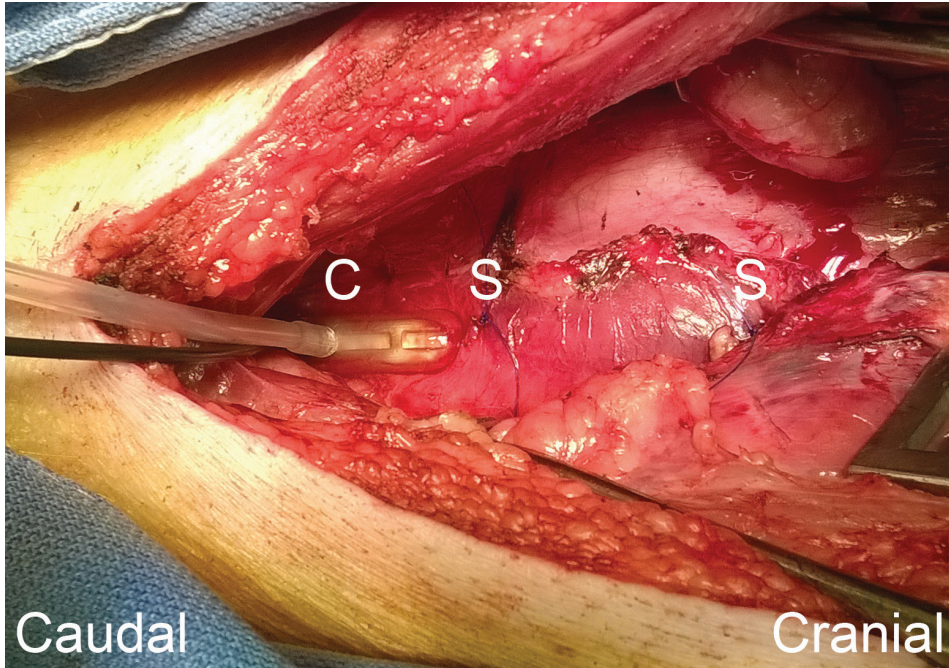


Figure 2 Suction cup (C) placed on the esophageal epithelium. Between the sutures (S), the partial vacuum of the suction cup has resulted in some discoloration of the outer esophageal wall. The suction cup is placed at the second ablation site. After the last ablation, the surgical clips were placed directly next to the sutures.

Results

All recorded voltage and current waveforms were smooth demonstrating the absence of arcing.⁹ Average peak current of the 200-joule applications was 21.2 ± 2.6 amperes (Table).

Visual inspection of the ablation area and the electrode directly after the energy application never revealed any blood clots or charring. Acutely, the suction device caused minimal local hematoma due to bursting of superficial small blood vessels.

All animals survived the procedure and the follow-up period without complications. There were no signs of anorexia, vomiting, weight loss, hematemesis or melena suggesting adverse clinical effects on the esophagus or pain.

Esophagoscopy was guided by fluoroscopic identification of the surgical clips and area of interest. The surgical clips that marked both far ends of the ablation line allowed easy identification of the ablated areas. (Figure 3).

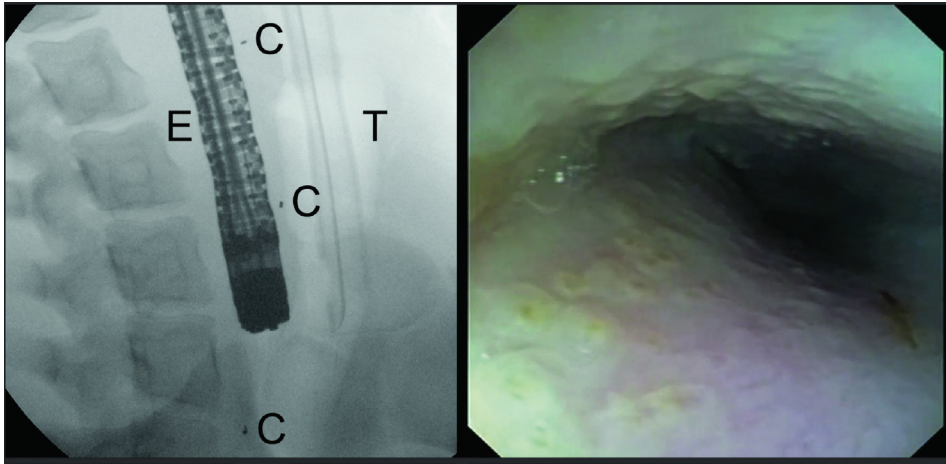


Figure 3 Panel **A**: Fluoroscopic image of an endoscope (E) in the esophagus during esophagoscopy at day 2. An endotracheal ventilation tube (T) is visible. Also, the 3 surgical clips (C) are clearly visible. They mark the far ends of the 2 esophageal ablation sites. Using this fluoroscopic guidance, the gastroenterologist knows exactly where the area of interest is.

Panel **B**: Endoscopic view of an esophageal lesion area at day 2, the distal esophagus is on the far side. Multiple whitish, circumscribed, clear fluid-containing elevations with a diameter of several millimeters, resembling vesicles in the ablated areas (lower left side of panel 3B) and on the opposite esophageal wall (upper side of panel 3B) are seen. No epithelial erythema, erosions or ulcerations were found.

At day 2, esophagoscopy showed normal esophageal motility, no stenosis, and multiple whitish, circumscribed, clear fluid-containing elevations with a diameter of several millimeters, resembling vesicles in the ablated areas and, to a lesser degree, on the opposite esophageal wall. No epithelial erythema, erosions or ulcerations were seen. These findings were macroscopically confirmed (Table, Figure 4). At day 7, esophagoscopy again showed normal esophageal motility and no stenosis. All elevations had disappeared and all esophagi appeared completely normalized (Table). After euthanasia at day 60, there were no macroscopically visible lesions on the adventitia or epithelium. However, the muscular layer showed a scar in all animals (Table).

Three animals were euthanized as planned at day 2. Microscopy of the ablated tissue showed 3 layers: mucosa consisting of non-keratinizing squamous epithelium, submucosa with mucus glands and the muscular layer. An intraepithelial vesicle was present, compatible with the macroscopic observation (Figure 5). Further analysis showed degeneration of the superficial part of the epithelium with intact basal epithelial layers.

The muscular layer showed a lymphohistiocytic inflammatory infiltrate in the outer muscular layer with degeneration of some striated muscle cells. The submucosa in between this inflammatory infiltrate and the epithelial vesicle was unremarkable.

Five animals were euthanized as planned at day 60. A superficial scar was present in the outer part of the esophagus, in the outer part of the muscular layer at the location where the inflammatory infiltrate was observed after 2 days follow-up (Figure 6). The epithelium of the mucosa was intact.

Table showing procedural parameters and outcome of each animal.

Animal Nr.	Pulse Nr.	Energy (Joule)	Voltage (Volt)	Current (Ampere)	Follow-up (days)	Endoscopy/ macroscopy (day 2)	Endoscopy (day 7)	Visible scar (day 60)
1	1	100	1750	15.5	60	vesicles	normal epithelium	yes
	2	100	1725	15.5				
2	1	200	2425	23.0	60	vesicles	normal epithelium	yes
	2	200	2425	23.5				
3	1	200	n/a	n/a	60	vesicles	normal epithelium	yes
	2	200	n/a	n/a				
4	1	200	2450	21.5	60	vesicles	normal epithelium	yes
	2	200	2470	21.0				
5	1	200	2500	21.25	60	vesicles	normal epithelium	yes
	2	200	2500	21.25				
6	1	200	2500	22	2	vesicles*	n/a	n/a
	2	200	2550	21.5				
7	1	200	2575	21.0	2	vesicles*	n/a	n/a
	2	200	2500	22.5				
8	1	200	2450	23.5	2	vesicles*	n/a	n/a
	2	200	2450	23.5				

Voltage and current values are recorded peak values. Nr.: Number; n/a: not available; *: no esophagoscopy was performed in these animals, findings are based on direct visual inspection after termination.

DISCUSSION

One of the worst possible complications of pulmonary vein isolation using currently available ablation techniques is thermal damage to the esophagus, resulting in atrial-to-esophageal fistula. Thermal injury to the esophagus is mainly being caused by catheter ablation on the adjacent left atrial wall, but esophageal heating can also be caused by catheter ablation in the posterior right atrium.¹² The ablation energy (heat or cold) does not stop at the pericardial side of the atrial myocardium, and can cause collateral damage to neighboring structures, like the esophagus.^{1,13} Typically the anterior part of the esophagus at a distance of approximately 25-35 cm from incisors is endangered.¹⁴ Injury to the esophagus can be caused by all presently used ablation modalities: radiofrequency ablation, cryoballoon ablation (Arctic Front™ and Arctic Front Advance™), irrigated radiofrequency multipolar ablation (nMARQ™), duty-cycled phased radiofrequency ablation (PVACTM), visually guided laser balloon catheter (CardioFocus™), catheter ablation by robotic navigation (Sensei™).^{3, 13, 15-19} Several theories have been developed as to why esophageal injury and even atrial-to-esophageal fistula do happen.¹⁷ One theory sees the direct thermal injury with subsequent necrosis of the esophageal wall as the culprit.²⁰⁻²³ Another theory suggests injury to the periesophageal nerves, (increased) gastric acid regurgitation and acid etching of the lesion, leading to formation of ulcers and/or fistula, but the data on this matter is ambiguous.^{23, 24}

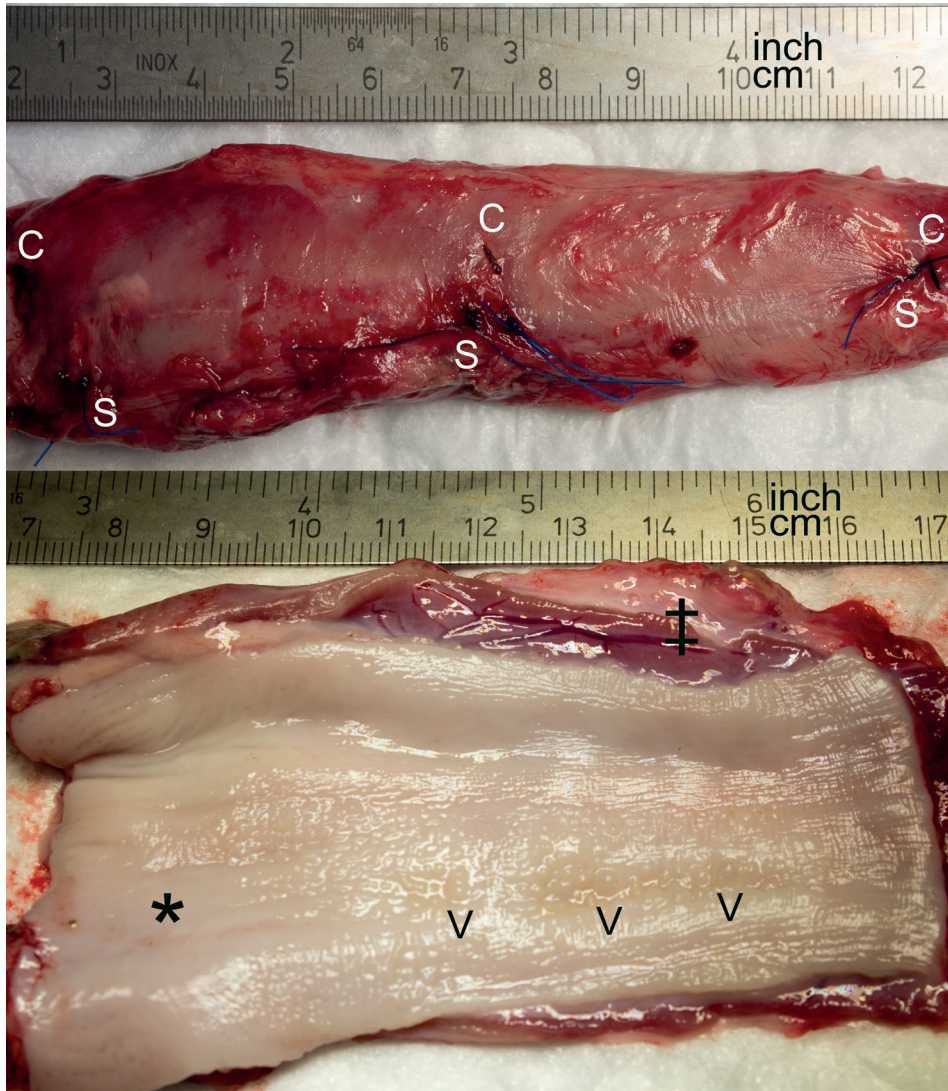


Figure 4 Upper panel: Macroscopy of exterior of esophagus at day 2. Between the surgical clips (C) and the stitches (S), a whitish linear ablation lesion is visible. There are no hematoma or ulcerations. Also, the surface of the outer esophageal wall seems intact. **Lower panel:** Macroscopy of esophageal epithelium at day 2. On the surface of the non-keratinizing squamous epithelium (*) an area with multiple vesicles (V) of various sizes is visible. There are no signs of ulceration. The muscular layer is macroscopically intact (‡).

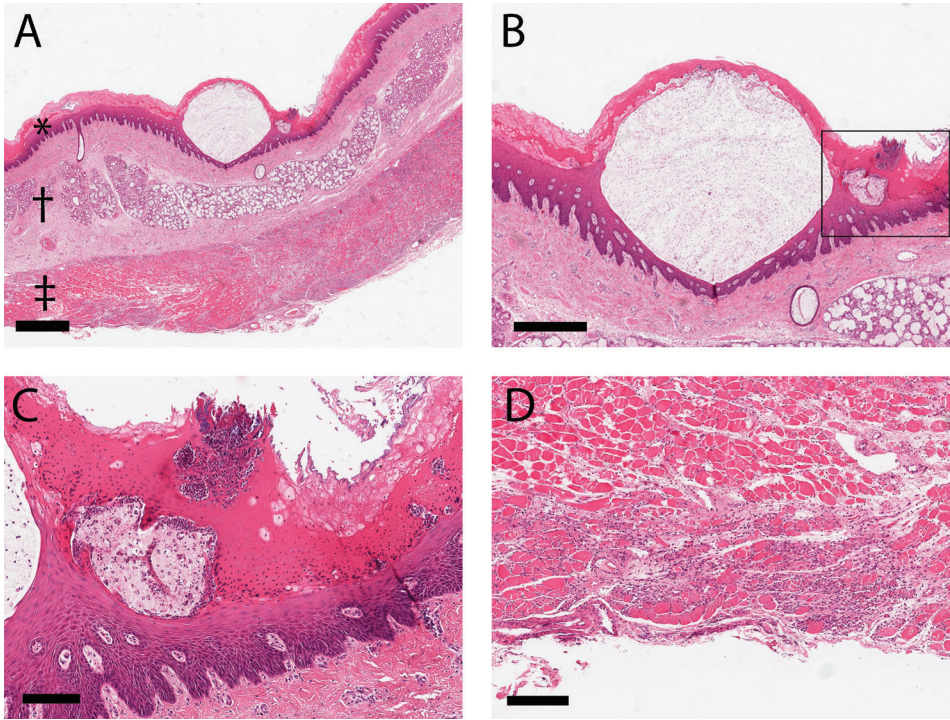


Figure 5 Esophageal electroporation ablation lesion at 2 days follow-up.

A: overview of the wall of the esophagus showing 3 layers (from top to bottom): mucosa consisting of non-keratinizing squamous epithelium (*), submucosa with mucus glands (†) and the muscular layer (‡). An intraepithelial vesicle is present. Hematoxylin and eosin stain, bar = 1 mm. **B:** higher magnification of the vesicle shown in figure A. Bar = 500 μ m. **C:** higher magnification of the rectangle in figure B, showing degeneration of the superficial part of the epithelium with intact basal epithelial layers. Bar = 150 μ m. **D:** higher magnification of the muscular layer of figure A showing an lymphohistiocytic inflammatory infiltrate in the outer muscular layer with degeneration of some striated muscle cells. The submucosa in between this inflammatory infiltrate and the epithelial vesicle is unremarkable. Bar = 300 μ m.

The occurrence of this complication may not be recognized, since there is a delay of up to 6 weeks between pulmonary vein isolation and onset of aspecific symptoms, like dysphagia, chest pain, fever, seizures or cerebrovascular accidents and melena.⁵ Urgent esophageal stenting or operation is indicated, but often the atrial-to-esophageal fistula is lethal.

In 2008, Hong et al. performed esophageal electroporation ablation using a modified, commercially available epicardial ablation clamp as well as radiofrequency ablation.²⁵ Esophageal lesions from electroporation energy were characterized by myocyte and interstitial damage practically identical to the cardiac lesions. The lesions were restricted to the muscle layer. The luminal epithelial layer and the delicate lamina muscularis mucosae (a small rim of smooth muscle cells beneath the epithelial basal layer) were left without pathological changes. In contrast, the radiofrequency ablations compressed the esophageal wall and destroyed the epithelial and muscular layers, and the adventitia.

Irreversible electroporation can create deep myocardial ablation lesions, whilst sparing the coronary arteries and the phrenic nerve.^{10, 26, 27} It can also persistently isolate the pulmonary veins without occurrence of acute or chronic pulmonary vein stenosis.^{9, 28} Due to the combination of deep lesions and the close proximity of the posterior left atrial wall to the esophagus, it is of paramount importance to exclude possible adverse effects on the esophagus. Therefore, this study, purposely targeting the esophagus was conducted. Linear electroporation ablation using 200 joules applications directly on the outer esophageal wall was regarded as a worst-case scenario for human electroporation ablation near the esophagus. Because of the design of the ablation electrode inside a suction cup, optimal electrode-tissue contact is guaranteed. In the absence of a surrounding blood pool or other conducting tissue, the energy delivered is forced to go entirely through the esophageal tissue. The energy application was only delivered when the suction cup was placed and remained firmly attached to the esophagus.

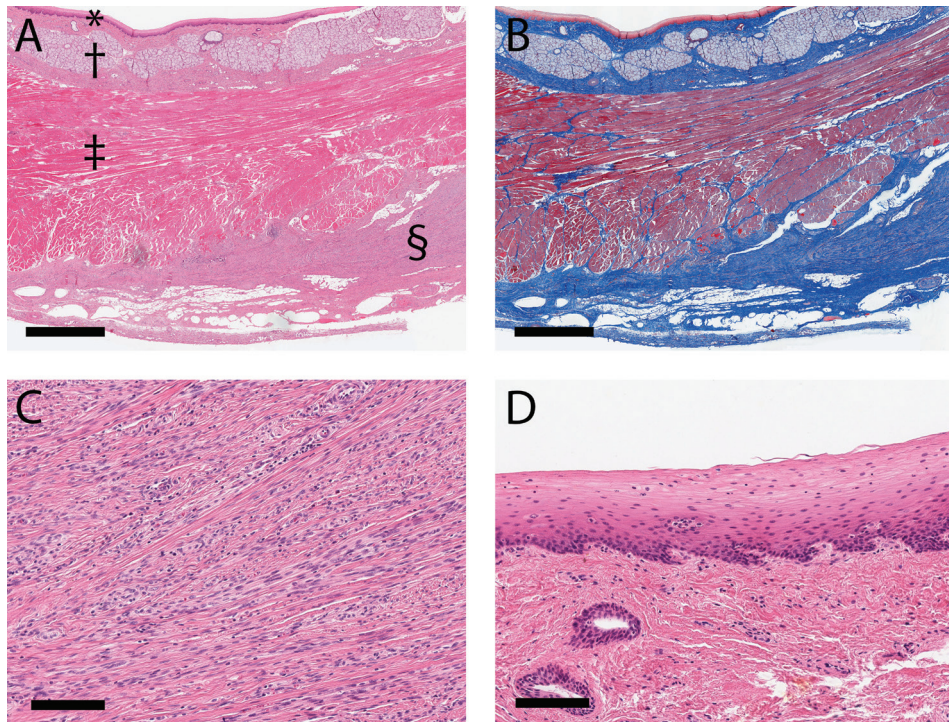


Figure 6 Esophageal electroporation ablation lesion at day 60.

A and **B**: overview of the wall of the esophagus consisting of mucosa (*), submucosa (†) and muscular layer (§). A limited scar is present in the outer part of the esophagus in the outer part of the muscular layer (§) at the location where the inflammatory infiltrate was observed after 2 days follow-up. **A**: hematoxylin and eosin stain, **B**: Masson's trichrome stain. Bar = 1.5 mm. **C**: higher magnification of the scar area of **A** showing myofibroblasts in extracellular matrix. Bar = 100 μ m. **D**: higher magnification of the epithelial layer of **A** showing intact epithelium. Bar = 100 μ m.

Main findings

The main findings of the present study are that direct electroporation ablation on the outer esophageal wall seems to be asymptomatic in pigs, and causes harmless, self-limiting vesicles on the non-keratinizing squamous epithelium at the ablation site. After 7 days and 60 days follow-up, the epithelium has completely normalized. There are no signs of ulceration or other adverse reactions. Microscopy after 2 days and 60 days follow-up shows evidence of ablated muscular tissue, proving that the delivered energy reached its target area. The epithelial layer at 60 days follow-up shows intact epithelium and an intact extracellular matrix, proving that the architecture of the esophageal tissue remains chronically intact.

Irreversible electroporation is the first ablation technique that can create large myocardial ablation lesions without severely damaging the esophagus, acutely or chronically. This can have very important future implications, in the sense that for the first time in the history of cardiac ablation there is a fast and powerful ablation technique available without the feared “flip side of the coin”: collateral damage to surrounding extracardiac structures. The absence of severe esophageal damage after ablating with an energy level able to create approximately 7 mm deep myocardial lesions could mean that safe and very effective myocardial ablation at the posterior side of the atria is within reach.

Tissue specificity of electroporation ablation has been well described in the past. Over the last two decades, reversible electroporation has been intensively pursued as a very promising technique for the treatment of cancer, especially hepatic and prostatic cancer cells are sensitive to electroporation ablation.^{29, 30} On the other hand, blood vessels and nerves are much less susceptible to electroporation ablation.^{27, 31-33} The exact reason for this tissue specificity is unknown.

Limitations

This is an animal study, in which the porcine esophagus was ablated. Although no animal showed signs of esophageal discomfort (anorexia, vomiting, hematemesis) or pain, we cannot exclude that humans would experience discomfort or even pain following electroporation ablation near the esophagus.

Using a porcine animal model, we realize that the effects of electroporation ablation on the human esophagus may be different.

In this study we only investigated one energy setting. However, previous studies have showed that this energy level and mode of delivery can create deep and wide myocardial ablation lesions, able to create transmural lesions.

Conclusions

Esophageal architecture remains unaffected 2 months after electroporation ablation, purposely targeting the adventitia. Data of this study suggests that electroporation ablation is a safe modality for catheter ablation near the esophagus.

Conflict of Interest

Fred Wittkamp and Harry van Wessel are the inventors of circular electroporation. The other authors have no conflicts of interest.

REFERENCES

1. Pappone C, Oral H, Santinelli V, et al. Atrio-esophageal fistula as a complication of percutaneous transcatheter ablation of atrial fibrillation. *Circulation* Jun 8 2004;109:2724-2726.
2. Stockigt F, Schrickel JW, Andrie R, Lickfett L. Atrioesophageal fistula after cryoballoon pulmonary vein isolation. *J Cardiovasc Electrophysiol* Nov 2012;23:1254-1257.
3. Deneke T, Schade A, Diegeler A, Nentwich K. Esophago-pericardial fistula complicating atrial fibrillation ablation using a novel irrigated radiofrequency multipolar ablation catheter. *J Cardiovasc Electrophysiol* Apr 2014;25:442-443.
4. Schmidt B, Metzner A, Chun KR, Leftheriotis D, Yoshiga Y, Fuernkranz A, Neven K, Tilz RR, Wissner E, Ouyang F, Kuck KH. Feasibility of circumferential pulmonary vein isolation using a novel endoscopic ablation system. *Circ Arrhythm Electrophysiol* Oct 2010;3:481-488.
5. Neven K, Schmidt B, Metzner A, Otomo K, Nuyens D, De Potter T, Chun KR, Ouyang F, Kuck KH. Fatal end of a safety algorithm for pulmonary vein isolation with use of high-intensity focused ultrasound. *Circ Arrhythm Electrophysiol* Jun 2010;3:260-265.
6. Teissie J, Golzio M, Rols MP. Mechanisms of cell membrane electroporation: a minireview of our present (lack of ?) knowledge. *Biochimica et biophysica acta* Aug 5 2005;1724:270-280.
7. Lee RC, Zhang D, Hannig J. Biophysical injury mechanisms in electrical shock trauma. *Annual review of biomedical engineering* 2000;2:477-509.
8. Lavee J, Onik G, Mikus P, Rubinsky B. A novel nonthermal energy source for surgical epicardial atrial ablation: irreversible electroporation. *Heart Surg Forum* 2007;10:E162-167.
9. Wittkamp FH, van Driel VJ, van Wessel H, Vink A, Hof IE, Grundeman PF, Hauer RN, Loh P. Feasibility of electroporation for the creation of pulmonary vein ostial lesions. *J Cardiovasc Electrophysiol* Mar 2011;22:302-309.
10. Wittkamp FH, van Driel VJ, van Wessel H, Neven KG, Grundeman PF, Vink A, Loh P, Doevendans PA. Myocardial lesion depth with circular electroporation ablation. *Circ Arrhythm Electrophysiol* Jun 1 2012;5:581-586.
11. Institute for Laboratory Animal Research: Guide for the care and use of laboratory animals. 8th ed. Washington (DC): National Academies Press; 2011.
12. Tsai WK, Koruth J, Reddy VY. Esophageal heating is not limited to left atrial ablation. *Circ Arrhythm Electrophysiol* Feb 1 2014;7:178-179.
13. Scanavacca MI, D'Avila A, Parga J, Sosa E. Left atrial-esophageal fistula following radiofrequency catheter ablation of atrial fibrillation. *J Cardiovasc Electrophysiol* Aug 2004;15:960-962.
14. Halm U, Gaspar T, Zachaus M, Sack S, Arya A, Piorkowski C, Knigge I, Hindricks G, Husser D. Thermal esophageal lesions after radiofrequency catheter ablation of left atrial arrhythmias. *The American journal of gastroenterology* Mar 2010;105:551-556.
15. Ahmed H, Neuzil P, d'Avila A, Cha YM, Laragy M, Mares K, Brugge WR, Forcione DG, Ruskin JN, Packer DL, Reddy VY. The esophageal effects of cryoenergy during cryoablation for atrial fibrillation. *Heart rhythm : the official journal of the Heart Rhythm Society* Jul 2009;6:962-969.
16. Metzner A, Burchard A, Wohlmuth P, et al. Increased incidence of esophageal thermal lesions using the second-generation 28-mm cryoballoon. *Circ Arrhythm Electrophysiol* Aug 2013;6:769-775.
17. Deneke T, Bunz K, Bastian A, Pasler M, Anders H, Lehmann R, Meuser W, de Groot JR, Horlitz M, Haberkorn R, Mugge A, Shin DI. Utility of esophageal temperature monitoring during pulmonary vein isolation for atrial fibrillation using duty-cycled phased radiofrequency ablation. *J Cardiovasc Electrophysiol* Mar 2011;22:255-261.
18. Tilz RR, Chun KR, Metzner A, et al. Unexpected high incidence of esophageal injury following pulmonary vein isolation using robotic navigation. *J Cardiovasc Electrophysiol* Aug 1 2010;21:853-858.
19. von Bary C, Dornia C, Kirchner G, Weber S, Fellner C, Nisenbaum D, Georgieva M, Stroszczyński C, Hamer OW. Esophageal tissue injury following pulmonary vein isolation using the PVAC: assessment by endoscopy and magnetic resonance imaging. *Pacing and clinical electrophysiology : PACE* Apr 2013;36:477-485.

20. Gillinov AM, Pettersson G, Rice TW. Esophageal injury during radiofrequency ablation for atrial fibrillation. *The Journal of thoracic and cardiovascular surgery* Dec 2001;122:1239-1240.
21. Doll N, Borger MA, Fabricius A, Stephan S, Gummert J, Mohr FW, Hauss J, Kottkamp H, Hindricks G. Esophageal perforation during left atrial radiofrequency ablation: Is the risk too high? *The Journal of thoracic and cardiovascular surgery* Apr 2003;125:836-842.
22. Aupperle H, Doll N, Walther T, Kornherr P, Ullmann C, Schoon HA, Mohr FW. Ablation of atrial fibrillation and esophageal injury: effects of energy source and ablation technique. *The Journal of thoracic and cardiovascular surgery* Dec 2005;130:1549-1554.
23. Ripley KL, Gage AA, Olsen DB, Van Vleet JF, Lau CP, Tse HF. Time course of esophageal lesions after catheter ablation with cryothermal and radiofrequency ablation: implication for atrio-esophageal fistula formation after catheter ablation for atrial fibrillation. *J Cardiovasc Electrophysiol* Jun 2007;18:642-646.
24. Martinek M, Hassanein S, Bencsik G, Aichinger J, Schoeffl R, Bachl A, Gerstl S, Nesser HJ, Purerfellner H. Acute development of gastroesophageal reflux after radiofrequency catheter ablation of atrial fibrillation. *Heart rhythm : the official journal of the Heart Rhythm Society* Oct 2009;6:1457-1462.
25. Hong J, Stewart MT, Cheek DS, Francischelli DE, Kirchhof N. Cardiac ablation via electroporation. Conference proceedings : Annual International Conference of the IEEE Engineering in Medicine and Biology Society IEEE Engineering in Medicine and Biology Society Conference 2009;2009:3381-3384.
26. du Pre BC, van Driel VJ, van Wessel H, Loh P, Doevendans PA, Goldschmeding R, Wittkamp FH, Vink A. Minimal coronary artery damage by myocardial electroporation ablation. *Europace* Jan 2013;15:144-149.
27. van Driel VJ, Neven K, van Wessel H, Vink A, Doevendans PA, Wittkamp FH. Low vulnerability of the right phrenic nerve to electroporation ablation. *Heart rhythm : the official journal of the Heart Rhythm Society* Aug 2015;12:1838-1844.
28. van Driel VJ, Neven KG, van Wessel H, du Pre BC, Vink A, Doevendans PA, Wittkamp FH. Pulmonary vein stenosis after catheter ablation: electroporation versus radiofrequency. *Circ Arrhythm Electrophysiol* Aug 2014;7:734-738.
29. Miller L, Leor J, Rubinsky B. Cancer cells ablation with irreversible electroporation. *Technology in cancer research & treatment* Dec 2005;4:699-705.
30. Onik G, Mikus P, Rubinsky B. Irreversible electroporation: implications for prostate ablation. *Technology in cancer research & treatment* Aug 2007;6:295-300.
31. Rubinsky B, Onik G, Mikus P. Irreversible electroporation: a new ablation modality—clinical implications. *Technology in cancer research & treatment* Feb 2007;6:37-48.
32. Maor E, Ivorra A, Leor J, Rubinsky B. The effect of irreversible electroporation on blood vessels. *Technology in cancer research & treatment* Aug 2007;6:307-312.
33. Li W, Fan Q, Ji Z, Qiu X, Li Z. The effects of irreversible electroporation (IRE) on nerves. *PLoS one* 2011;6:e18831.

Chapter 11



General Discussion

PART I CARDIAC REGENERATIVE THERAPY

The success of cardiac regenerative therapy depends on three pillars (1) using the right therapeutic consisting of a biological or compound, (2) making sure the therapeutic stays in the heart long enough to do its job (3) getting the therapeutic to the right location. In this thesis we mainly addressed the latter point and described different technological approaches to optimize the delivery of cardiac regenerative therapy and to improve identification of the target zone.

Optimal delivery

For intramyocardial applications of cardiac regenerative therapy, choosing and reaching the correct injection location is imperative for the therapy to be effective. In completely healthy myocardium, the injection of stem cells or other products serves no direct purpose while in fibrotic tissue, little nutrients and oxygen are available for the materials to survive and the tissue to regenerate. General consensus is that in patients with focal ischemic heart disease, intramyocardial regenerative therapy is best delivered to the infarct border zone. The infarct border zone is defined as the area in between core infarct and healthy tissue. In that area, the myocardium is partly damaged and nutrients and oxygen are available. The clinical non-invasive gold standard for the identification of myocardial fibrosis (and thus: infarct border zone) is late gadolinium enhanced MRI.¹ In **Chapter 2**, we demonstrated a technique to combine NOGA endocardial surface mapping with late gadolinium enhanced MRI. We found that the real-time fusion of MRI and NOGA was feasible and that there were visual discrepancies between the NOGA parameters and MRI images. The technology of fusing MRI and NOGA allows the operator to guide intramyocardial therapy based on both NOGA maps and late gadolinium enhanced MRI scans. In **Chapter 3**, we used same technological approach to fuse MRI and NOGA was used to systematically compare NOGA acquired endocardial surface maps with and late gadolinium enhanced MRI scans retrospectively to find the best NOGA parameters to identify the infarct border zone. Data of these studies showed that the variation in NOGA parameters is substantial for areas of specific infarct transmuralty. The low spatial resolution of the NOGA maps together with movement of the heart due to respiration further worsen this problem. In **Chapter 4**, we described a technological approach to enable real-time correction of respiratory induced cardiac motion for the NOGA system. We attached a respiratory belt transducer to one of the ECG leads; respiration was stored as a baseline drift in that ECG-channel. The results of this porcine study showed a significant reduction in apical displacement after applying the correction algorithm. The effect on left ventricular NOGA maps as a whole was not significant, mainly due to the limited respiratory induced motion of the porcine heart. The technique might however obviate the need for time consuming respiratory-gated mapping and treatment during for example injection or ablation procedures based on endocardial mapping.

In **Chapters 2 and 3** we described the use of CARTBox to fuse and compare NOGA maps with (late gadolinium enhanced) MRI scans. As a next step, CARTBox2 was developed to facilitate guidance of intramyocardial injections using live fluoroscopy fused with late gadolinium enhanced MRI scans obviating the need for expensive catheter tracking technology. In **Chapter 5**, we compared this new system with NOGA, the current clinical reference standard for the delivery of intramyocardial therapy. We showed that the accuracy for targeting the infarct border zone

with CARTBox2 is similar to the NOGA system, but that intramyocardial injection procedures can be performed significantly faster. NOGA is a non-fluoroscopic navigation system, CARTBox2 is a fluoroscopy based injection system, and thus with CARTBox2 procedures fluoroscopy was significantly more used. However, fluoroscopy use with CARTBox2 was similar to an average percutaneous coronary intervention procedure.

Besides optimal targeting of the intramyocardial injections, the injected products should stay where they were injected long enough to be effective. Van den Akker et al. demonstrated that injections with mesenchymal stem cells in the myocardium are swiftly washed out via the venous system.² In the study described in **Chapter 5**, a mixture containing ureido-pyrimidinone (Upy) gel, fluorescent beads and supra paramagnetic particles was used.³⁻⁵ The Upy gel in the mixture ensured that the injections would stay in the myocardial wall long enough for them to be detected during analysis. Future studies, like the study of van der Spoel et al., should be performed to investigate the additional value of the Upy gel to increase retention of injected products.⁶

Target identification

To detect the optimal target zone for cardiac regenerative therapy, the exact location of the infarct has to be identified. As a first step, and for the purpose of histological fibrosis quantification, we developed a software toolbox (FibroQuant) that allows the automatic and systematical analysis of histological sections. In **Chapter 6**, this toolbox was used to determine the myocardial fibrosis and fatty replacement patterns in patients with a mutation in the phospholamban gene. In a subsequent study, described in **Chapter 7**, the toolbox was used to systematically compare high resolution digital histology with late gadolinium enhanced MRI scans to find the best parameters to detect myocardial fibrosis in a porcine model of myocardial infarction. In both studies we separately analyzed 8-14 histological sections from a single whole transverse heart slice. These separate slices were combined after analysis. The chosen methodology inevitably led to decrease in precision. Future studies therefore should use 3D whole heart histology. With this technique transverse heart slices can be analyzed as a whole. Subsequently, these separate slices can be reconstructed to form a 3D histological representation of the heart. The main obstacle for this technique is the cutting and processing of the large histological sections.

Beside improvement of histological analyses, different MRI techniques that may improve identification of the infarct border zone should be explored. Recent studies showed new MRI sequences for fibrosis identification using endogenous contrast.⁷ Such new sequences have to be compared to histology and late gadolinium enhanced MRI scans systematically before being applicable in the field of cardiac regenerative therapy.

Future aspects

More advanced catheter navigation and guidance techniques should be explored. In **Chapter 5**, we introduced a novel technique to enable MRI based fluoroscopic catheter guidance, CARTBox2. The application of CARTBox2 was demonstrated as a software tool to facilitate the guidance of intramyocardial therapy. The technology, on which CARTBox2 is based, can be used for any catheter-based therapy that involves navigation. Possible applications of CARTBox2 include but

are not limited to, cardiac ablations, pacemaker lead placement or endocardial biopsies. Even though the fluoroscopic dose levels are well within acceptable limits, the major disadvantage of this technique is the requirement of fluoroscopy. Therefore, further development of the technology is necessary. An example of advances in this field includes MediGuide™, which fuses 3D magnetic tracking with fluoroscopy. Instead of requiring continuous fluoroscopy to visualize the catheter, with MediGuide™, a single heart beat fluoroscopic movie is acquired on which the catheter, based on 3D magnetic tracking, is continuously superimposed.

Another promising approach is the use of MRI based catheter tracking and guidance technology.⁸ With this approach intramyocardial injection procedures can be performed within the MRI. The catheter can be visualized in real-time whilst navigating to the target. With this approach gold standard non-invasive infarct identification with late gadolinium enhanced MRI or other MRI techniques⁷ can be combined directly with catheter navigation and guidance techniques, eliminating errors that typically occur during image registration. Design and construction of MRI compatible catheters is complex. For this application, either passive or active catheters can be used. Passive catheters rely on MRI visibility based on the intrinsic properties of the materials used, while active catheters use coils or other electronic components to enhance MRI visibility. Active catheters have the advantage of being automatically trackable and tend to cause less image distortion. In the near future, MRI guided intramyocardial injections may prove to be superior to approaches relying on different modalities.

PART II CARDIAC ABLATION

In the second part of this thesis we focused on improving the efficacy of pulmonary vein isolation with irreversible electroporation by using a novel method for measuring electro-tissue contact. In addition, we addressed one of the last remaining safety aspects of irreversible electroporation.

Efficacy

With irreversible electroporation, contact between the catheter electrodes and the cardiac tissue is important for effective transfer of the electric current between electrode and tissue and thus for lesion formation. The electrical resistance of blood is lower than that of tissue. When irreversible electroporation is applied and electrodes are not in contact with tissue, part of the current will dissipate into blood, and lesion formation may be suboptimal or absent. In **Chapter 8**, we introduced a novel method for electrical measurement of electrode-tissue contact by means of the interface impedance, which can be used with circular multi-electrode catheters. This method was compared to another electrical contact measuring method, and to a mechanical method to measure contact force, both in vitro and in a porcine animal model. We showed that the novel method is less susceptible for remote high impedance tissue (e.g. the lungs) than the other electrical method, while being equally 'sensitive' to measure contact. Both in vitro and in vivo, the experiments demonstrated a non-linear relationship between electrical contact and contact force. In a subsequent study, described in **Chapter 9**, we assessed the feasibility of the novel multi-electrode impedance system for predicting long-term success of circular PV electroporation ablation. In that study we showed that the interface impedance predicts effective

irreversible electroporation applications, and that pulmonary vein isolation based on the interface impedance measurements is at least as good as the classical electrophysiological approach for determining the need for additional irreversible electroporation applications.

In the latter study the 3D localization of each individual electrode on the catheter, was ‘manually’ combined with individual electrode contact measurements. This approach allowed for circumferential targeting of the pulmonary vein ostium. The 3D location of ‘good’ electrical contact was marked just prior to irreversible electroporation application. Subsequently, segments without ‘good’ contact during ablation were systematically retargeted. Integration of the electrical contact method into 3D navigation systems, such as NavX™ or MediGuide™ (St. Jude Medical), can make pulmonary vein ablation procedures more effective and possibly shorten procedures considerably.

Safety aspects

With the introduction of new technology into clinical practice, it is important to discuss safety aspects. Currently available technological approaches for pulmonary vein isolation are considered relatively safe. However a complication rate of approximately 6% has been reported.^{9,10} Complications during and after pulmonary vein isolation include, but are not limited to, cardiac perforation, pulmonary vein stenosis, myocardial infarction, pericarditis, esophageal injury, phrenic or vagal nerve injury, stroke or a transient ischemic attack and bleeding.¹¹

Thermal complications

Some of these complications can directly be attributed to the type of energy source used for ablation. Thermal energy (heating or cooling tissue) applied with radio frequency ablation, cryo-balloon ablation, high-intensity focused ultrasound and visually guided laser balloon ablation is not tissue specific and can easily be transferred beyond the intended target area (e.g. pulmonary veins). Organs and tissues near the target location such as the nerves, coronary arteries or the esophagus can therefore unintentionally be ‘ablated’. Consequences of these unintentional ablations can be severe.

Previous studies of our group addressed several safety related topics of irreversible electroporation for cardiac ablation.^{12–15} In **Chapter 10**, we describe the effect of this ablation modality on the esophagus. We hypothesized that applying the ablation energy directly to the external esophagus would reveal the largest possible effect. Data showed that some minor effects were endoscopically visible 2 days after ablation, but these were resolved after one week. Histological analysis after 2 months revealed the presence of a small scar only in the outer part of the muscular layer. The results from this study suggest that irreversible electroporation is a safe modality for catheter ablation in close vicinity to the esophagus.

The seemingly tissue specific characteristics of irreversible electroporation observed in the latter experiment and previous studies^{12–14} require further investigation. Cell size, morphology and orientation, and nearby cells or tissues with different electrical properties have been associated with different responses to (irreversible) electroporation pulses.^{16–18} Whether these cell properties can also explain the observations in the study described in **Chapter 10** and the aforementioned studies has yet to be investigated.

One of the last remaining open ends concerning the safety of irreversible electroporation as a

modality for cardiac ablation is the formation of microbubbles on the electrode surface upon energy delivery. In the early days of direct current ablation in the 1980s multiple studies were conducted into the formation microbubbles.^{19,20} With irreversible electroporation ablation, possible complications due to gas bubble formation are twofold, embolic events and spark (arcing) formatting and a subsequent explosion at the catheter electrodes. In 1985, Rowland and colleagues observed the opacification of the right ventricle directly after direct current discharge.²¹ Holt and colleagues showed that both gas formation and hemolysis were directly proportional to delivered energy.²² Further study needs to be performed into the amount of gas formation and hemolysis after irreversible electroporation with circular catheters.

Future aspects

The large current applied with irreversible electroporation between catheter electrodes and an indifferent skin patch leads to electrical stimulation of skeletal muscles. The resulting contraction of the muscles, comparable with an external defibrillation shock, will necessitate the use of general anesthesia in patients.²³ Even though general anesthesia is increasingly being used during cardiac ablation procedures, associated risks should not be underestimated.^{23–25} To overcome the problem of skeletal muscle contractions, Arena and colleagues have tested high frequency alternating currents for irreversible electroporation.²⁶ In the brain of rats, high frequency irreversible electroporation proved to be able to create lesion without muscle contractions. High frequency irreversible electroporation may prove to be a feasible alternative for cardiac ablation.

FINAL REMARKS

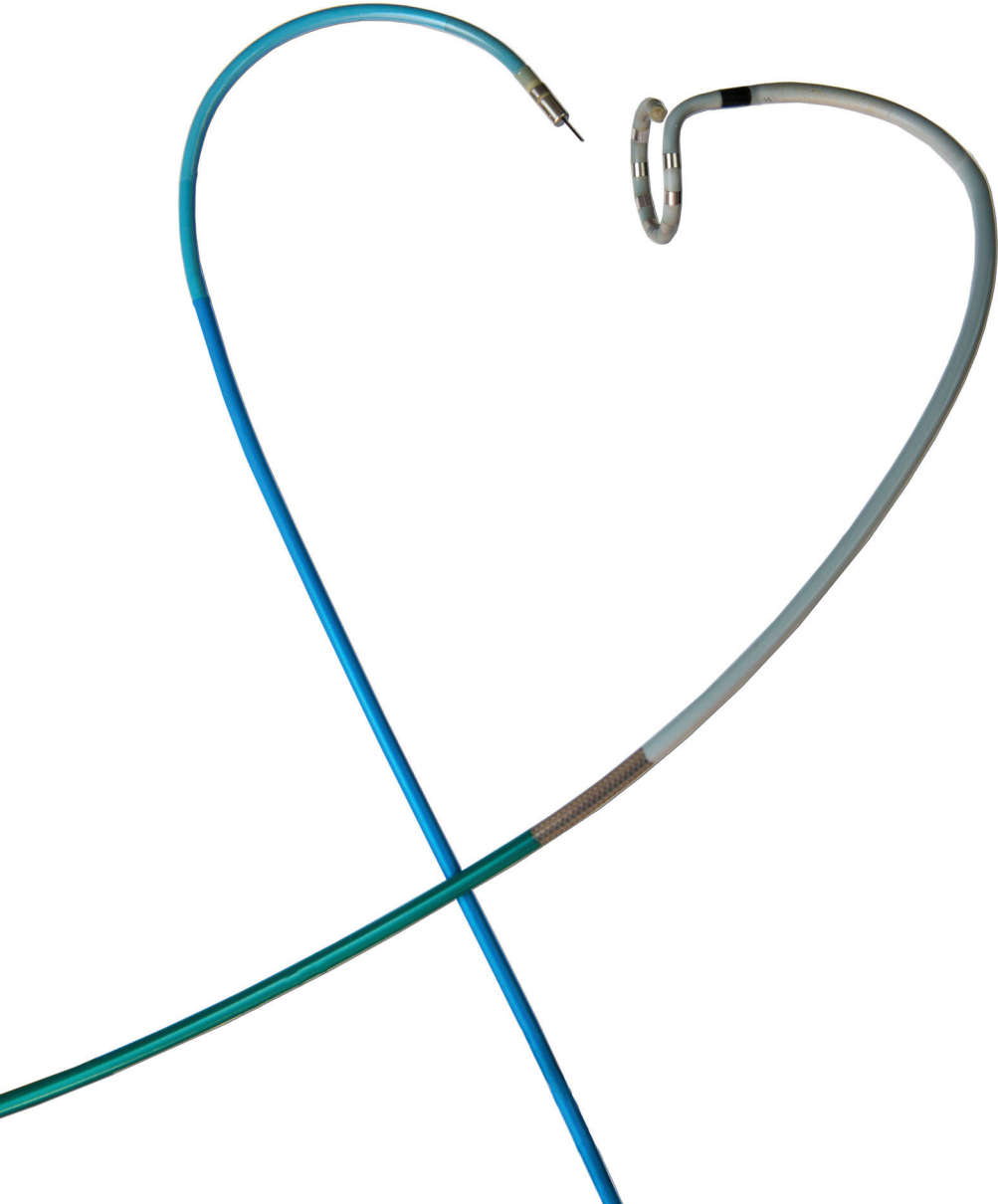
In this thesis we described different novel technological approaches to improve different catheter based therapies. The various technologies were employed to optimize navigation and guidance for delivery of intramyocardial injections and to improve efficacy of irreversible electroporation ablation therapy. The new technologies were all evaluated in preclinical studies. All techniques have proven to be safe, and should as a next step, be evaluated in clinical trials to assess their added value for clinical practice. In that phase of product development, collaboration between academic researchers and medical companies is essential for successful valorization, and should be pursued. Future studies should focus on both improving current technologies and doing research into new technological innovations. Technology will provide the solution to solve current and upcoming problems in the medical field.

REFERENCES

1. Kim RJ, Fieno DS, Parrish TB, et al.: Irreversible Injury , Infarct Age , and Contractile Function. Online 2002; :1992–2002.
2. van den Akker F, Feyen DAM, van den Hoogen P, van Laake LW, van Eeuwijk ECM, Hoefer I, Pasterkamp G, Chamuleau SAJ, Grundeman PF, Doevendans PA, Sluijter JPG: Intramyocardial stem cell injection: go(ne) with the flow. *European Heart Journal* 2016; :ehw056.
3. Bastings MMC, Koudstaal S, Kieltyka RE, Nakano Y, Pape ACH, Feyen DAM, van Slochteren FJ, Doevendans PA, Sluijter JPG, Meijer EW, Chamuleau SAJ, Dankers PYW: A fast pH-switchable and self-healing supramolecular hydrogel carrier for guided, local catheter injection in the infarcted myocardium. *Advanced Healthcare Materials* 2014; 3:70–78.
4. Pape ACH, Bakker MH, Tseng CCS, Bastings MMC, Koudstaal S, Agostoni P, Chamuleau SAJ, Dankers PYW: An Injectable and Drug-loaded Supramolecular Hydrogel for Local Catheter Injection into the Pig Heart. *Journal of visualized experiments : JoVE* 2015; :e52450.
5. Delikatny EJ, Poptani H: MR techniques for in vivo molecular and cellular imaging. *Radiologic Clinics of North America* 2005; 43:205–220.
6. Van der Spoel TIG, Vrijsen KR, Koudstaal S, Sluijter JPG, Nijssen JFW, de Jong HW, Hoefer IE, Cramer MJM, Doevendans PA, van Belle E, Chamuleau SAJ: Transendocardial cell injection is not superior to intracoronary infusion in a porcine model of ischaemic cardiomyopathy: A study on delivery efficiency. *Journal of Cellular and Molecular Medicine* 2012; 16:2768–2776.
7. van Oorschot JWM, Gho JMIH, van Hout GPJ, Froeling M, Jansen of Lorkeers SJ, Hoefer IE, Doevendans P a., Luijten PR, Chamuleau S a. J, Zwanenburg JJM: Endogenous contrast MRI of cardiac fibrosis: Beyond late gadolinium enhancement. *Journal of Magnetic Resonance Imaging* 2014; 00:n/a – n/a.
8. Ratnayaka K, Faranesh AZ, Guttman MA, Kocaturk O, Saikus CE, Lederman RJ: Interventional cardiovascular magnetic resonance: still tantalizing. *Journal of cardiovascular magnetic resonance : official journal of the Society for Cardiovascular Magnetic Resonance* 2008; 10:62.
9. Deshmukh A, Patel NJ, Pant S, et al.: In-hospital complications associated with catheter ablation of atrial fibrillation in the United States between 2000 and 2010: Analysis of 93 801 procedures. *Circulation* 2013; 128:2104–2112.
10. Teunissen C, Kassenberg W, van der Heijden JF, Hassink RJ, van Driel VJHM, Zuithoff NPA, Doevendans PA, Loh P: Five-year efficacy of pulmonary vein antrum isolation as a primary ablation strategy for atrial fibrillation: a single-centre cohort study. *Europace* 2016; :eu439.
11. Calkins H, Kuck KH, Cappato R, et al.: 2012 HRS/EHRA/ECAS Expert Consensus Statement on Catheter and Surgical Ablation of Atrial Fibrillation: Recommendations for Patient Selection, Procedural Techniques, Patient Management and Follow-up, Definitions, Endpoints, and Research Trial Design: A re. *Europace* 2012; 14:528–606.
12. van Driel VJHM, Neven K, van Wessel H, Vink A, Doevendans PAFM, Wittkampf FHM: Low vulnerability of the right phrenic nerve to electroporation ablation. *Heart rhythm : the official journal of the Heart Rhythm Society Elsevier*, 2015; 12:1838–1844.
13. Du Pré BC, Van Driel VJ, Van Wessel H, Loh P, Doevendans PA, Goldschmeding R, Wittkampf FH, Vink A: Minimal coronary artery damage by myocardial electroporation ablation. *Europace* 2013; 15:144–149.
14. Van Driel VJHM, Neven KGEJ, Van Wessel H, Du Pré BC, Vink A, Doevendans PAFM, Wittkampf FHM: Pulmonary vein stenosis after catheter ablation electroporation versus radiofrequency. *Circulation: Arrhythmia and Electrophysiology* 2014; 7:734–738.
15. Neven K, van Driel V, van Wessel H, van Es R, Doevendans P a, Wittkampf F: Myocardial Lesion Size after Epicardial Electroporation Catheter Ablation following Subxiphoid Puncture. *Circulation Arrhythmia and electrophysiology* 2014; .
16. Canatella PJ, Black MM, Bonnicksen DM, McKenna C, Prausnitz MR: Tissue electroporation: quantification and analysis of heterogeneous transport in multicellular environments. *Biophysical journal* 2004; 86:3260–3268.
17. Golberg A, Bruinsma BG, Uygun BE, Yarmush ML: Tissue heterogeneity in structure and conductivity contribute to cell survival during irreversible electroporation ablation by ‘electric field sinks’. *Scientific reports* 2015; 5:8485.

18. Valic B, Golzio M, Pavlin M, Schatz A, Faurie C, Gabriel B, Teissie J, Rols MP, Miklavcic D: Effect of electric field induced transmembrane potential on spheroidal cells: theory and experiment. *Eur Biophys J* 2003; 32:519–528.
19. Bardy GH, Coltorti F, Ivey TD, Alferness C, Rackson M, Hansen K, Stewart R, Greene HL: Some factors affecting bubble formation with catheter-mediated defibrillator pulses. *Circulation* 1986; 73:525–538.
20. Bardy GH, Coltorti F, Stewart RB, Greene HL, Ivey TD: Catheter-Mediated Electrical Ablation - the Relation between Current and Pulse Width on Voltage Breakdown and Shock-Wave Generation. *Circ Res* 1988; 63:409–414.
21. Rowland E, Foale R, Nihoyannopoulos P, Perelman M, Krikler DM: Intracardiac contrast echoes during transvenous His bundle ablation. 1985; :240–243.
22. Holt PM, Boyd EG: Hematologic effects of the high-energy endocardial ablation technique. *Circulation* 1986; 73:1029–1036.
23. Furniss SS, Sneyd JR: Safe sedation in modern cardiological practice. *Heart (British Cardiac Society)* 2015; :1526–1530.
24. Salukhe TV, Willems S, Drewitz I, Steven D, Hoffmann BA, Heitmann K, Rostock T: Propofol sedation administered by cardiologists without assisted ventilation for long cardiac interventions: An assessment of 1000 consecutive patients undergoing atrial fibrillation ablation. *Europace* 2012; 14:325–330.
25. Kottkamp H, Hindricks G, Eitel C, et al.: Deep sedation for Catheter Ablation of atrial fibrillation: A prospective study in 650 consecutive patients. *Journal of Cardiovascular Electrophysiology* 2011; 22:1339–1343.
26. Arena CB, Sano MB, Rossmeisl JH, Caldwell JL, Garcia P a, Rylander M, Davalos R V: High-frequency irreversible electroporation (H-FIRE) for non-thermal ablation without muscle contraction. *BioMedical Engineering OnLine BioMed Central Ltd*, 2011; 10:102.

Appendices



Nederlandse samenvatting

Dankwoord

Publicatielijst

Curriculum Vitae

DEEL 1 OPTIMALISATIE VAN KATHETER NAVIGATIE IN HET HART

Regeneratieve therapie bij ischemische hartziekten, zoals bijvoorbeeld een hartinfarct, richt zich enerzijds op het voorkomen van het verlies van nog meer hartspiercellen en anderzijds op het stimuleren van de groei van nieuwe hartspiercellen. Bij deze therapie worden (stam)cellen, groeifactoren of andere producten toegediend in het hart. De meest optimale injectie locatie bevindt zich in het randgebied van het infarct. Hier komt nog genoeg bloed om de cellen van voedingstoffen en zuurstof te voorzien en er is tevens weefsel aanwezig dat hersteld moet worden.

Deze toediening kan op verschillende manieren plaatsvinden, namelijk via een injectie aan de buitenzijde van het hart, via injectie in de kransslagaderen of via injectie aan de binnenzijde van het hart middels een katheter. De injectie aan de buitenzijde van het hart heeft als voordeel dat je kunt zien waar je injecteert, een groot nadeel van deze techniek is dat het invasief is. Injecties in een kransslagader vinden plaats via een katheter en zijn dus minimaal invasief, daarnaast komt de therapie ook precies daar waar de schade is ontstaan. Echter zijn niet alle vaten geschikt voor deze injecties. Dergelijke injecties kunnen zorgen voor het ontstaan van micro-infarcten, daarom is het niet mogelijk om alle soorten producten te injecteren. De injectie van therapeutische producten via de binnenzijde van het hart met behulp van een katheter heeft als voordeel dat je precies kunt bepalen waar de therapie terecht komt, ook is het mogelijk om bijvoorbeeld gels te injecteren. Daarnaast is deze benadering ook minimaal invasief. In de huidige klinische studies worden stamcellen of andere producten geïnjecteerd met behulp van het NOGA-katheter navigatiesysteem. Met dit systeem wordt eerst de binnenkant van het hart in kaart gebracht met een katheter. Op basis van de verkregen 3D gegevens wordt daarna bepaald waar het infarct zich bevindt en waar de injecties moeten worden geplaatst. Vervolgens worden op die plaatsen met de katheter injecties toegediend.

In de praktijk merken we dat de gemeten locatie van het infarct niet altijd precies overeenkomt met de locatie die we bijvoorbeeld op een MRI-scan gezien hebben. Om dit te onderzoeken hebben we een software toolbox, 3D CARTBox, ontwikkeld waarmee we de data van de NOGA en die van de MRI-scanner met elkaar kunnen combineren en vergelijken. In de studie, beschreven in **hoofdstuk 2**, hebben we 3D CARTBox gebruikt om de NOGA- en MRI-data van 3 dieren met een infarct te combineren. Het doel van de studie was om het gebruik van deze toolbox te testen. Vervolgens hebben we dezelfde toolbox gebruikt om de data van een grotere groep van 17 dieren, retrospectief te vergelijken. Het doel was systematisch te onderzoeken hoe de NOGA-parameters zich verhouden met die gemeten op MRI. De resultaten van deze studie, beschreven in **hoofdstuk 3**, laten zien dat de NOGA-parameters gebruikt kunnen worden om het infarct te identificeren, maar dat zij minder sensitief zijn in gebieden met een specifieke infarct transmuraliteit (infarct dikte als fractie van de totale wanddikte). Hierdoor kan het lastig zijn om het randgebied van het infarct nauwkeurig te identificeren. Daarnaast laat deze studie zien dat 3D CARTBox een nauwkeurige fusie van NOGA en MRI mogelijk maakt die gebruikt kan worden voor klinische MRI geleide intramyocardiale injecties.

De 3D NOGA en MRI-datasets worden opgenomen in een eind diastolische fase van de hartcyclus, hierdoor heeft het hart in beide datasets dezelfde afmetingen. Het hart beweegt bij mensen mee met de ademhaling, hierdoor zijn verschuivingen van het hart tot ruim 1cm in

verschillende richtingen mogelijk. Om er tijdens MRI-scans voor te zorgen dat het hart steeds op dezelfde plaats ligt moet de patiënt bij iedere scan volledig uitademen. Tijdens een NOGA-procedure is de patiënt wakker en kan vrij ademen. Omdat een NOGA-procedure ruim een uur duurt, liggen de gemeten punten allemaal op een verschillende plaats in de ademhalingscyclus. Deze verschuiving kan ervoor zorgen dat er bij het combineren van de NOGA-data en MRI-scans een klein verschil ontstaat tussen beide datasets. Omdat het niet mogelijk is om de patiënt bij elke meting te laten uitademen of alleen te meten tijdens de uitadem fase, hebben we een correctie systeem ontwikkeld. Dit systeem bestaat uit een borstband waarmee we de ademhaling kunnen meten, deze is via een ecg-kanaal verbonden met het NOGA-systeem. Voordat we de NOGA-procedure beginnen doen we een referentie meting, hierbij doen we continu metingen, tijdens de ademhaling. Op basis van deze meting kunnen we een voorspelling geven van waar het hart zich bevindt tijdens een specifiek punt van de ademhalingscyclus. Vervolgens kunnen we tijdens de procedure, met behulp van deze informatie én de dan gemeten ademhaling, een correctie uitvoeren op de meting in het hart. In **hoofdstuk 4** beschrijven wij een fantoom- en dierstudie waarin we deze nieuwe techniek testen. De fantoomstudie liet zien dat het algoritme goed in staat is om een door ademhaling bewegend meetpunt stabiel te houden. In een volgende dierstudie hebben we ook laten zien dat het algoritme werkt en toepasbaar is tijdens een NOGA-procedure. We hebben echter niet kunnen aantonen dat het verschil tussen de NOGA en MRI-data kleiner wordt.

Verdere doorontwikkeling van 3D CARTBox heeft geleid tot CARTBox2, een software tool waarmee het mogelijk is om planning te doen op basis van MRI-beelden. In deze MRI-beelden, waarin het infarct duidelijk zichtbaar is, kan de gewenste injectie positie nauwkeurig worden aangegeven. Tijdens de injectie procedure kunnen deze bewerkte beelden worden gecombineerd met de doorlichtingsbeelden die standaard worden gebruikt om de katheter zichtbaar te maken. Door gebruik te maken van een externe software tool is het mogelijk deze beelden te gebruiken met alle apparatuur die MRI-beelden ondersteunt. Omdat alle katheters zichtbaar zijn op doorlichtingsbeelden, zijn er geen speciale katheters nodig. CARTBox2 is dus volledig onafhankelijk van de gebruikte doorlichtingsapparatuur en katheters. In de studie die is beschreven in **hoofdstuk 5**, hebben we de injectienauwkeurigheid van CARTBox2 vergeleken met die van het NOGA-systeem. Naast de injectienauwkeurigheid, hebben we ook de procedure duur, de hoeveelheid straling en het aantal hartritme stoornissen gemeten. De studie is uitgevoerd in twee groepen van vijf dieren, allen met een infarct. Vier weken na het induceren van een infarct hebben we per dier 10-16 injecties geplaatst met het NOGA-systeem dan wel CARTBox2. De randzone van het infarct, waar het infarct 1-20% van de wanddikte beslaat, was hierbij gedefinieerd als doelgebied. Na de injecties is het hart verwijderd voor nader onderzoek. Hierna, hebben we van alle injecties de afstand tot dit doelgebied gemeten. De resultaten van deze studie laten zien dat de injecties met beide technieken erg dicht in de buurt van het doel komen, injecties met NOGA liggen gemiddeld 0.7 ± 2.2 mm aan de binnenzijde van het infarct en injecties met CARTBox2 liggen gemiddeld 0.5 ± 3.2 mm buiten het infarct. Omdat CARTBox2 gebaseerd is op de combinatie van MRI en doorlichting, is de hoeveelheid straling hoger dan bij NOGA, dat is gebaseerd op magnetische tracking. De hoeveelheid straling bij CARTBox2 is echter lager dan bij een gemiddelde dotterprocedure. Omdat bij de CARTBox2 procedures direct kan worden begonnen met de injecties, en het hart dus niet eerst in kaart hoeft te worden gebracht, zijn

deze procedures korter dan die met het NOGA-systeem. Wel moet er voor CARTBox2 eerst een MRI-scan worden gemaakt, maar dit kan ook enige tijd voor de procedure al gedaan worden. Tijdens deze studie hebben wij geen verschillen gezien in het aantal hartritmestoornissen die optraden door het bewegen van de katheter in het hart. Uit deze studie kunnen we concluderen dat CARTBox2 een accuraat en fabrikant onafhankelijk systeem is om intramyocardiale injecties uit te voeren op basis van gouden standaard MRI-afbeeldingen.

De studies beschreven in hoofdstukken 2-5 komen voort uit de wens om de nauwkeurige informatie van de MRI-scan te kunnen gebruiken tijdens een injectie procedure. Door het infarct nauwkeurig in beeld te brengen met een MRI hopen we tijdens de injectie procedure de therapie op een meer effectieve plaats te brengen. Hierbij is het essentieel dat het infarct op de MRI-scan correct wordt geïdentificeerd. Studies waarbij men MRI-scans heeft vergeleken met histologie zijn veelal gebaseerd op een grove vergelijking of op een vergelijking van losse monsters. Om de vergelijking tussen MRI en histologie op een nauwkeurige en systematische manier te kunnen uitvoeren hebben we eerst een protocol ontwikkeld om de histologie in één transversale hartplak systematisch in kaart te brengen. In **hoofdstuk 6** beschrijven we dit protocol en gebruiken we dit om de verschillen in fibrosepatronen tussen verschillende patiëntgroepen in kaart te brengen. Het protocol bestaat uit 4 stappen: 1) het snijden van coupes uit de hartplak en de herkomst hiervan vastleggen, 2) het kleuren van de coupes met Masson trichroom om het gezonde weefsel en infarct weefsel te kunnen onderscheiden, 3) het uitvoeren van een automatische analyse waarbij de hoeveelheid gezond hartspierweefsel, fibrotisch weefsel en vetweefsel per coupe bepaald wordt, 4) de resultaten overzetten naar de originele oriëntatie zoals dit was in de hartplak. De resulterende dataset geeft vervolgens een eenvoudig inzicht in de distributiepatronen van de verschillende weefsels in de hartplak. In **hoofdstuk 7** hebben we deze methode vervolgens gebruikt om de histologie, van een hartplak van 16 dieren met een infarct, systematisch te vergelijken met een MRI-scan van deze zelfde plak. In deze studie hebben we de hoeveelheid fibrose vergeleken met de aankleuring op de MRI-scan, daarnaast hebben we ook gekeken of de beweging van de hartwand hiermee gecorreleerd was. De aankleuring van het infarct op de MRI-scan is met bepaalde algoritmes op verschillende manieren (automatisch) te kwantificeren. De studie heeft laten zien dat het automatische algoritme (FWHM; Full Width at Half Maximum) het best presteerde, daarnaast heeft het als groot voordeel dat er geen interactie van de gebruiker nodig is en dus de kans op fouten kleiner wordt. De wandbewegingen bleken minder goed in het voorspellen van de hoeveelheid fibrose en tevens waren er grote onderlinge verschillen tussen verscheidene softwareprogramma's. De resultaten hebben ertoe geleid dat we het FWHM-algoritme gebruikt hebben in de CARTBox2-studie.

DEEL 2 OPTIMALISATIE KATHETER ABLATIES IN HET HART

Hartritmestoornissen vormen een belangrijke oorzaak van ziekte en overlijden bij mensen. De meest voorkomende vorm van een hartritmestoornis is boezemfibrilleren. Bij boezemfibrilleren trekken de boezems niet meer normaal samen na stimulatie vanuit de sinusknoop, maar gebeurt dit snel en onregelmatig door stimuli van elders in de boezems. Door deze chaotische

samentrekking wordt het bloed niet meer actief de hartkamers ingepompt, hierdoor stroomt het bloed langzamer of komt zelfs stil te staan op bepaalde plaatsen in de boezems. Omdat langzaam stromend bloed makkelijker kan stollen en bloedpropjes kan vormen, is een beroerte één van de mogelijke gevolgen van onbehandeld boezemfibrilleren. Omdat de kamers van het hart worden geactiveerd door de boezems, trekken de kamers vaak snel en onregelmatig samen. Hierdoor ervaart de patiënt hartkloppingen, tevens kan het hart minder effectief pompen met als gevolg dat patiënten sneller kortademig en moe worden.

De behandeling van boezemfibrilleren kan met medicatie en/of katheterablatie gebeuren. De meest voorkomende oorsprong van de stimuli, die de boezems onregelmatig doen samentrekken, zijn de longvenen (vaten die vanuit de longen naar het hart gaan). Bij katheterablatie (longvenenablatie) worden de longvenen elektrisch geïsoleerd van het hart. Op die manier kunnen de elektrische stimuli vanuit de longvenen het hart niet meer bereiken. Momenteel worden deze ablaties vooral uitgevoerd met behulp van radiofrequente energie, dit zorgt voor lokale warmte en leidt tot celdood. Met een katheter worden puntlaesies gemaakt op de overgang van de longvene naar boezem, door meerdere van dit soort laesies te maken isoleert men het vat. Deze techniek heeft vaak een onvoldoende lange termijn werkzaamheid (door onvoldoende laesiediepte en/of -grootte) en geeft kans op complicaties.

In de afgelopen 8 jaar heeft onze onderzoeksgroep een nieuwe ablatiemethode ontwikkeld (irreversibele electroporatie), waarbij wel goede laesies gemaakt konden worden, en zo goed als geen complicaties optraden. Electroporatie werkt op basis van een korte sterke elektrische puls tussen de katheter en een huidelektrode, hierdoor ontstaan kleine gaatjes in de cellen vlak bij de katheter. De cellen zullen hiervan dood gaan en worden vervangen door niet geleidend littekenweefsel. Op deze manier kunnen we de longvenen van de boezem isoleren. Bij electroporatie werken we met een ronde katheter met meerdere elektroden, daarmee kan de gehele longvene in één keer rondom worden geïsoleerd. Het is hierbij wel belangrijk dat alle elektroden goed tegen het weefsel aanliggen. Bij radiofrequente ablaties gebuikt men hiervoor een druksensor in de tip van de katheter. Bij electroporatie ablatie maken we gebruik van een ronde katheter met 10-14 elektroden, omdat zoveel druksensoren niet in deze katheter passen is deze manier van contact meten niet mogelijk. In **hoofdstuk 8** beschrijven we een elektrische methode om contact te meten. Deze meting is gebaseerd op het principe dat bloed elektriciteit beter geleid dan weefsel dat doet. Door een kleine stroom te sturen tussen de verschillende buurelektroden en tegelijk de spanning te meten van elke elektrode naar de huidelektrode, kunnen we de weerstand tussen de elektroden berekenen. Als de katheter los in de boezem ligt zal de weerstand lager zijn dan wanneer de elektroden tegen de longvene aanliggen. In de studie hebben we contactwaarden in een proefopstelling gemeten en deze vergeleken met de afstand van de elektrode tot een bepaald object. Ook hebben we de contactwaarden bepaald bij verschillende krachten waarmee de elektrode tegen weefsel is gedrukt. Deze fantoomproeven hebben laten zien dat er een duidelijk relatie is tussen afstand en contactwaarde en tussen uitgeoefende druk en de contactwaarde. In dierproeven hebben we vervolgens een katheter gebruikt met een druksensor, hierop hebben we ook onze contactmeting aangesloten. Op die manier konden we tegelijk druk en elektrisch contact meten. Daarna hebben we de sensor met verschillende drukken tegen de binnenkant van de linkerboezem gedrukt. Vervolgens hebben we de druk en het elektrisch contact gemeten en deze met elkaar vergeleken. Ook bij deze

proeven zagen we een duidelijk verband tussen uitgeoefende druk en elektrisch contact. Uit deze studie concluderen we dat deze methode goed bruikbaar is als contactmeetmethode bij ronde meerpolige katheters.

In een vervolgstudie, beschreven in **hoofdstuk 9**, hebben we longvenen ablaties uitgevoerd in een diermodel. Bij 10 dieren hebben we in elk dier bij één longvene een electroporatie ablatie uitgevoerd met behulp van de contactmeting, en de andere longvene met behulp van lokale metingen van elektrische activiteit van het hart. Op die manier konden we onderzoeken of het gebruik van de contactmeting had geleid tot een betere isolatie. Om dit te controleren hebben 3 maanden na de ablaties gemeten of de longvenen nog steeds geïsoleerd waren. In de groep waarbij we de contactmeting niet hebben gebruikt waren 7 van de 10 longvenen nog steeds geïsoleerd. In de groep waarbij we het contact wel hebben gemeten waren 9 van de 9 venen nog steeds geïsoleerd. Eén dier van die laatste groep is geëxcludeerd omdat de contactmeting niet werkte en de ablatie halverwege is afgebroken. Deze resultaten suggereren dat de contactmeting van toegevoegde waarde is bij electroporatie ablaties. Daarnaast hebben we bepaald of de posities van de lekkages in de isolatielijn overeen kwamen met posities van minder contact. Gezien het geringe aantal lekkages kunnen we hierop geen definitief antwoord geven, maar ook deze resultaten suggereren dat er wel een verband is tussen matig contact en het optreden van een lek.

Bij het introduceren van nieuwe technieken in de kliniek is het altijd belangrijk dat de veiligheidsaspecten goed worden onderzocht. In de voorgaande jaren hebben we ons gericht op het onderzoeken van complicaties die kunnen optreden bij radiofrequente ablaties. Met deze onderzoeken hebben we laten zien dat kransslagaderen en zenuwen op het hart niet worden beschadigd door electroporatie ablaties, terwijl het hartweefsel eromheen wel wordt aangedaan. Ook belangrijke zenuwen in de buurt van het hart worden niet beschadigd. Verder hebben we aangetoond dat de longvenen niet krimpen na meerdere electroporatie ablaties. Het hart ligt in de borstkas gedeeltelijk tegen de slokdarm aan. Daarom kan in sommige gevallen de warmte bij radiofrequente ablatie ervoor zorgen dat er een gat ontstaat dat de slokdarm met de linkerboezem verbindt. Als dat gebeurt, zal het bloed uit het hart de slokdarm in stromen. Dit is in bijna alle gevallen dodelijk. In **hoofdstuk 10**, beschrijven we een studie waarin we de electroporatie ablatie direct op de slokdarm uitvoeren. Waar normaal de energie via het hart in de slokdarm komt, en dus de overgebleven energie lager is, krijgt de slokdarm nu de volle lading. In 5 dieren hebben we deze ablaties op de slokdarm uitgevoerd. Op dag 2 en 7 na deze ablaties hebben we endoscopisch naar de binnenkant van de slokdarm gezocht naar schade. Bij de endoscopie op dag 2 waren er kleine blaasjes te zien ter plaatse van de laesie, deze waren echter 5 dagen later verdwenen. Na 60 dagen hebben we de slokdarm histologisch onderzocht op schade. Bij histologische controle waren alleen kleine littekens te zien in de buitenste laag van de slokdarm, de binnenwand was geheel intact. Om uit te zoeken wat de blaasjes precies waren, hebben we 3 dieren aan de studie toegevoegd. Bij deze dieren hebben we 2 dagen na de slokdarmablatie de slokdarm uitgenomen voor histologische controle. De blaasjes bleken in de binnenste laag van de slokdarm te zitten. Onder de blaasjes was reeds nieuwe weefsel gevormd. Deze studie heeft laten zien dat electroporatie ablaties veilig uitgevoerd kunnen worden in de buurt van de slokdarm.

DANKWOORD

Geachte prof.dr. Doevendans, beste Pieter, bedankt voor het vertrouwen dat u in mij had toen u mij in september 2012 aanstelde met de opdracht om de komende 4 maanden iets leuks te bedenken. Dat heeft uiteindelijk geleid tot een promotietraject met niet één maar twee interessante onderwerpen. Gesprekken met u waren altijd 'to the point' en beslissingen werden altijd snel gemaakt. Bedankt voor de begeleiding en de kans die u mij gegeven heeft!

Geachte prof.dr. Chamuleau, beste Steven, in juni 2011 begon ik bij jou en Frebus aan mijn laatste 5^e jaars stage met aansluitend mijn afstudeerstage. Omdat de vrije onderzoeksfeer mij erg aansprak ben ik in september van 2012 met jou als copromotor begonnen aan mijn promotie. Samen hebben we een aantal nieuwe projecten opgestart waarvan de meeste hebben geresulteerd in een hoofdstuk in dit boekje. Daarnaast hebben we samen een aantal mooie valorisatie grants binnen gehaald waar CART-Tech uit voortgekomen is. Verder herinner ik mij natuurlijk de vele gezellige ChamPHD meetings en niet te vergeten avonden in Orlando en Madrid. Richting het einde van mijn promotie ben jij professor geworden en bent daarmee ook gepromoveerd naar de rang van promotor. Steven, bedankt voor alle wijze lessen en begeleiding de afgelopen 5 jaar!

Beste Fred, dr. Wittkamp, nadat jij in november 2012 een presentatie van mij over NOGA-MRI fusie bijwoonde, vertelde jij mij over het ACDC project en de nieuwe hoog frequente generator die eraan kwam. Ik was direct geïnteresseerd en sindsdien bestond mijn promotie uit twee verschillende onderwerpen. Als fysicus met vele jaren ervaring in de elektrofysiologie heb je mij een stuk technische kennis bijgebracht en mij een heel andere blik gegeven op valorisatie van kennis. De afgelopen vier jaar, en met name de laatste paar maanden, heb ik je vaak lastig gevallen met manuscripten die wat input konden gebruiken. Het was een voorrecht om een steentje bij te dragen aan jouw project. Je kennis van het technische elektrofysiologisch veld is uitzonderlijk en ik hoop dat ik nog lang van je mag leren.

Beste Frebus, dr.ir. van Slochteren, lang geleden, in juni 2011 ben ik bij jou en Steven, toen nog phd-student, gestart als 5^e jaars TG-student en aansluitend als eerste TG afstudeerder. Toen ik het jaar daarna als promovendus weer naast je zat, was onze eerste opdracht om naar Kaposvar in Hongarije te gaan, om daar onze nieuwe NOGA-MRI te demonstreren. Eigenlijk ging alles goed, totdat we in het vliegtuig moesten stappen, maar nog aan de koffie zaten. Alles daarna ging een stuk beter en we hebben vele mooie projecten opgezet, met als sluitstuk de CARTBox2 studie. Samen hebben we ook een hele rits studenten begeleid, soms levert "*dat stof tot nadenken*" op. Als copromotor heb je veel invloed gehad op de goede resultaten van de afgelopen jaren, bedankt! Ik hoop dat wij in de toekomst nog veel zullen samenwerken.

Geachte leden van de leescommissie, prof.dr. M.C. Verhaar, prof.dr. W.J.L. Suyker, Prof.dr. E.E. van der Wall, prof.dr. T. Leiner en dr. B.K. Velthuis, graag wil ik u hartelijk danken voor uw bereidheid om zitting te nemen in de beoordelingscommissie van dit proefschrift. Daarnaast wil ik graag, dr. B.K. Velthuis, prof. dr. W.J.L. Suyker, dr. K.P. Loh, prof. dr. ir. M.A. Viergever en prof.

dr. D. van Dijk bedanken voor uw bereidheid om zitting te nemen in de oppositie. In het bijzonder wil ik u, prof.dr.ir C.H. Slump, bedanken dat u ook zitting wil nemen in de oppositie, u heeft namelijk ook zitting gehad in mijn afstudeercommissie op de Universiteit van Twente in 2012.

Mede-ACDC-onderzoekers: Kars, bedankt voor je hulp bij alle experimenten, inzichten, je altijd nuttige commentaren en enthousiasme om nieuwe experimenten op te zetten. Vincent, bedankt voor je hulp bij (en nog steeds) experimenten. Ik heb altijd gedacht dat ik eerder zou promoveren, je hebt me toch verslagen, zij het nipt. Harry, bedankt voor alle technische ondersteuning bij de experimenten. Als er weer eens een kabeltje miste of wij weer een ander apparaat nodig hadden, konden we altijd op jou rekenen.

Paul, Fillipo, Frebus, bedankt voor jullie hulp vanuit CART-Tech met het opzetten en uitvoeren van de CARTBox2 studie en natuurlijk voor de top etentjes bij Meneer Buscourg!

Medeonderzoekers, bedankt voor de lunches, borrels en andere leuke uitstapjes. Anneliene, Arjan, shinen op de ESCI, Bart, Bas, de jongste aanwinst voor de Champie-groep, jouw taak om te zorgen dat de borrelfrequentie hoog genoeg blijft, Cas, Cheyenne, op naar de laatste loodjes! Dirk, organisator in hart en nieren, Sofia was in ieder geval een groot succes! Einar, de manager van onze EK poule, die het EK zonder Nederland toch nog leuk maakte, Freek, wanneer gaan we weer eens naar de golfbaan? Gijs, Ing Han, een leuk weekje Papendal, misschien nog wel een paar golflessen nemen? Iris, avocado bij de lunch is broodnodig als je de hele dag T-toppen aan het vergelijken bent, Jetske, altijd in voor een feestje, Judith, altijd vrolijk, Manon, Mariam, Marloes, Martine, Massieh, Mieke, (meta) Mira, als Bas niet voor de borrels zorgt, moet jij het maar doen, Peter Paul, de altijd (over)enthousiaste collega die nooit ergens niet aan mee doet. En ook niet te vergeten, onze trip naar Miami Beach (en de posterkoker)! Remco, geeft het woord terminaal een geheel nieuwe invulling, bedankt voor de puike organisatie van de onvergetelijke promosci naar St. François, Rik, Roos, hoe staat het inmiddels met je GVB? Sanne, altijd geïnteresseerd, ik herinner me vele nuttige discussies! Sofieke, Stefan, jouw kunsten op de golfbaan had ik niet willen missen, Thijs, de tweede TG'er in de villa, met jou erbij komen we in ieder geval geen vingers, ehho handen tekort. Thomas, binnenkort weer een lobster omlot pakken? Willemien en natuurlijk de 2 Wouters. Voor degene op wie het nog van toepassing is, succes met de rest van de promotie!

Biotechnici, Joyce, Marlijn, Martijn, Grace, Danny en Evelyn, bedankt dat ik altijd kon rekenen op jullie ervaring en handigheid om de experimenten weer tot een goed einde te brengen.

Leonard, Maurits, Bert, René, Ernest, Ben en Wim, bedankt voor jullie hulp met alle elektrotechnische vragen waarmee ik jullie vaak heb lastig gevallen. Ik denk dat we elkaar nog vaak gaan spreken in de toekomst.

Wil en Rolf, bedankt voor jullie hulp met het verkrijgen van gebruikte catheters en allerhande materialen van de HCK. Niels, bedankt voor jouw hulp bij het maken van de MRI scans, een vitaal onderdeel van onze studies. Stijn, bedankt voor jouw hulp met het Noga systeem!

Rutger, bedankt voor de hulp met de dierproeven en het begeleiden van de TG-studenten als medisch begeleider. Aryan, bedankt voor alle hulp met het beoordelen van de coupes, een vitaal onderdeel van vele studies!

Graag zou ik alle TG studenten, Frank, Roos, Tessa, Thijs, Lieke, Jord, Robin, Pien, Eline, Leon en Eliane willen bedanken voor de hulp de afgelopen jaren met het uitvoeren van de experimenten, maar ook voor de nieuwe ideeën die uit jullie stages zijn voortgekomen. Ik wens jullie nog veel succes in de toekomst.

Het stafsecretariaat, Jantine, Sylvia en Tamara voor jullie hulp in de afgelopen jaren. Jantine, bedankt voor jouw hulp met het managen van de eindeloze stroom studenten. Ingrid, in het bijzonder wil ik jou bedanken voor jouw hulp met het managen van allerhande PhD zaken.

Beste Paranimfen, jullie staan natuurlijk ook al in het rijtje van de onderzoekers, maar graag wil ik jullie ook in het bijzonder bedanken voor jullie extra inzet als paranimfen. Beste Ing Han en Peter Paul, de afgelopen jaren hebben we op verschillende vlakken samen gewerkt, allemaal onder de noemer van de stamcelgroep. Deze samenwerking heeft geleid tot een aantal mooie stukjes onderzoek en bijbehorende publicaties. Daarnaast moeten we de talloze borrels, congressen en (weekend)tripjes niet vergeten. Graag wil ik jullie bedanken voor jullie hulp in de laatste fase van mijn promotie!

Beste (schoon) familie en vrienden, bedankt voor jullie interesse in en steun bij mijn promotie. De vele weekendjes weg, vakanties en etentjes hebben mij de laatste jaren veel goed gedaan.

Lieve Familie, Pap, Mam en Yvette, bedankt voor jullie onvoorwaardelijke steun de afgelopen vier jaar tijdens mijn promotie. Jullie waren altijd geïnteresseerd in wat ik allemaal aan het doen was in Utrecht. De weekendjes in Schoonebeek, kerstdagen en de vakantie waren altijd gezellig. Bedankt voor al jullie hulp de afgelopen jaren!

Lieve Michelle, wij hebben elkaar leren kennen tijdens mijn afstudeerjaar, een jaar later, vlak voor het begin van mijn promotie zijn we gaan samenwonen. Nu wonen we alweer ruim twee jaar in ons eigen huis. Jij hebt er de laatste vier jaar, met veel geduld, voor gezorgd dat ik mij volledig kon richten op mijn promotie. Lieve Michelle, bedankt voor al het begrip, tijd, zorg en liefde die je mij gegeven hebt.

LIST OF PUBLICATIONS

van Slochteren FJ, **van Es R**, Koudstaal S, van der Spoel TIG, Sluijter JPG, Verbree J, Pruim RHR, Pluim JPW, Leiner T, Doevendans P a., Chamuleau S A. J: Multimodality infarct identification for optimal image-guided intramyocardial cell injections. *Netherlands Heart Journal* 2014; 22:493–500.

Gho JMIH, **van Es R**, Stathonikos N, Harakalova M, Te Rijdt WP, Suurmeijer AJH, Van Der Heijden JF, De Jonge N, Chamuleau SAJ, De Weger RA., Asselbergs FW, Vink A: High resolution systematic digital histological quantification of cardiac fibrosis and adipose tissue in phospholamban p.Arg14del mutation associated cardiomyopathy. *PLoS ONE* 2014; 9.

Neven, K., Driel, V. Van, Wessel, H. **van, Es, R.** Van, Pré, B. Du, Doevendans, P. A., & Wittkamp, F. (2014). Safety and feasibility of closed chest epicardial catheter ablation using electroporation. *Circulation: Arrhythmia and Electrophysiology*, 7(5), 913–919.

Neven, K., Van Driel, V., Van Wessel, H., **van Es, R.**, Doevendans, P. A., Wittkamp, F. (2014). Epicardial linear electroporation ablation and lesion size. *Heart Rhythm*, 11(8), 1465–1470.

Slochteren, F. J., **Van Es, R.**, Gyöngyösi, M., Spoel, T. I. G., Koudstaal, S., Leiner, T., Doevendans P.A., Chamuleau, S. A. J. (2016). Three dimensional fusion of electromechanical mapping and magnetic resonance imaging for real-time navigation of intramyocardial cell injections in a porcine model of chronic myocardial infarction. *The International Journal of Cardiovascular Imaging*, 1–11.

Neven, K., van Driel, V., van Wessel, H., **van Es, R.**, Doevendans, P. A., Wittkamp, F. (2014). Myocardial Lesion Size After Epicardial Electroporation Catheter Ablation After Subxiphoid Puncture. *Circulation: Arrhythmia and Electrophysiology*, 7(4), 728–733.

van Es, R., van Slochteren, F. J., Jansen of Lorkeers, S. J., Blankena, R., Doevendans, P. A., & Chamuleau, S. A. J. (2016). Real-time correction of respiratory-induced cardiac motion during electro anatomical mapping procedures. *Medical & Biological Engineering & Computing*

van der Broek HT, de Jong L, Doevendans PA, Chamuleau, SAJ, van Slochteren FJ*, **van Es R*** (2016). 3D whole heart myocardial tissue analysis. *J. Vis. Exp.*, (In press)

Mast, T. P., Teske, A. J., Walmsley, J., van der Heijden, J. F., **van Es, R.**, Prinzen, F. W., Delhaas, T., van Veen, T.A., Loh, P., Doevendans, P. A., Cramer, M. J., Lumens, J. (2016). Right ventricular deformation imaging and computer simulation for electromechanical substrate characterization in arrhythmogenic right ventricular cardiomyopathy (ARVC). *J Am Coll Cardiol*, (in press)

van Slochteren FJ, **van Es R**, Chamuleau SAJ, "Cardiac imaging processing for interventions"
U.S. Patent: 20150065855, issued date March 5, 2015.

van Es R, van Slochteren FJ, Meine M, "Method of positioning an interventional device."
Application number: 2016800, Application date May 5, 2016

CURRICULUM VITAE

René van Es was born on March 1st 1987 in Coevorden (The Netherlands). After graduating from his secondary education in 2005, he studied Technical Medicine at Twente University (NL). René received his bachelor's degree in 2009 after which he continued with the master Technical Medicine, Robotics and Imaging. During last 5th year internship he became interested in Cardiology. His final internship, at the department of cardiology of the University Medical Centre Utrecht under supervision of prof. dr. S.A.J. Chamuleau and dr.ir. F.J. van Slochteren, focused on improving the efficacy of stem cell therapy by increasing the accuracy of intramyocardial injections using multimodality imaging. René received his master's degree in Technical Medicine from the University of Twente in 2012. After graduating he started his PhD program at the University Medical Centre Utrecht under the supervision of prof. P.A.F.M. Doevendans, prof. dr. S.A.J. Chamuleau, dr. F.H.M. Wittkampf, and dr.ir. F.J. van Slochteren. His main focus is on improving cardiac regenerative therapy and the development of new technologies to improve cardiac ablation. In the upcoming years, René will continue working in the department cardiology of the University Medical Centre Utrecht.

The first part of the paper discusses the importance of understanding the local context in which a project is implemented. This includes a thorough analysis of the social, cultural, and economic factors that may influence the success or failure of the intervention. It is essential to engage with the community from the outset, ensuring that their voices are heard and their needs are addressed. This participatory approach not only fosters a sense of ownership and commitment among the community members but also allows for the identification of potential challenges and the development of strategies to mitigate them.

The second part of the paper explores the role of leadership in driving change. Effective leaders are those who are able to inspire and motivate others, to set a clear vision, and to create a supportive environment for innovation and growth. They must also be able to build strong relationships and networks, both within the organization and with external stakeholders. Leadership is not a static role; it evolves over time and across different contexts, requiring a high degree of adaptability and resilience.

The third part of the paper examines the importance of monitoring and evaluation in assessing the impact of an intervention. This involves the collection and analysis of data to measure progress, identify areas for improvement, and demonstrate the value of the program. Monitoring and evaluation should be an ongoing process, integrated into the planning and implementation phases of the project. It is crucial to use a variety of methods and tools to gather data, ensuring that the information is both reliable and relevant to the needs of the community.

The fourth part of the paper discusses the challenges and opportunities of implementing a sustainable development strategy. While there are many obstacles, such as limited resources, political instability, and social inequality, there are also many opportunities for innovation and progress. By leveraging the strengths of the community and the support of external partners, it is possible to create a sustainable and inclusive development path that benefits all members of the community.

In conclusion, the paper emphasizes the need for a holistic and participatory approach to development. This involves understanding the local context, engaging the community, and fostering leadership and innovation. By doing so, we can create a more equitable and sustainable world for all.

